

Microscopic foundation of the Eigenstate Thermalization Hypothesis

Dissertation

for the award of the degree
„Doctor rerum naturalium“
of the Georg-August-Universität Göttingen

–

within the doctoral program ProPhys
of the Georg-August University School of Science (GAUSS)

submitted by

Nils O. Abeling
from Husum

Göttingen, 2022

Thesis Committee:

Prof. Dr. Stefan Kehrein

Institut für Theoretische Physik, Georg-August-Universität Göttingen

Prof. Dr. Fabian Heidrich-Meisner

Institut für Theoretische Physik, Georg-August-Universität Göttingen

Priv.-Doz. Dr. Salvatore Manmana

Institut für Theoretische Physik, Georg-August-Universität Göttingen

Members of the Examination Board:

Reviewer: Prof. Dr. Stefan Kehrein

Institut für Theoretische Physik, Georg-August-Universität Göttingen

Second Reviewer: Prof. Dr. Fabian Heidrich-Meisner

Institut für Theoretische Physik, Georg-August-Universität Göttingen

Further members of the Examination Board:

Priv.-Doz. Dr. Salvatore R. Manmana

Institut für Theoretische Physik, Georg-August-Universität Göttingen

Prof. Dr. Matthias Krüger

Institut für Theoretische Physik, Georg-August-Universität Göttingen

Prof. Dr. Stefan Mathias

I. Physikalisches Institut, Georg-August-Universität Göttingen

Prof. Dr. Claus Ropers

IV. Physikalisches Institut, Georg-August-Universität Göttingen

Date of the oral examination: 29.03.2022

Contents

1	Introduction	1
1.1	Classical physics: equilibrium and dynamics	3
1.2	Quantum dynamics: unitarity and non-equilibrium	6
1.2.1	Mathematical formulation of quantum dynamics	6
1.2.2	Inherent quantum features	9
1.2.3	Methods to drive an isolated system to non-equilibrium	12
1.3	Experimental realizations: quantum simulators	12
1.4	Theoretical descriptions of quantum many-body systems	20
1.5	Outline and main results of this work	21
2	Thermalization in isolated systems	23
2.1	Thermalization in classical systems	25
2.2	Thermalization in quantum systems	26
2.2.1	Strong vs. weak thermalization	29
2.2.2	Eigenstate Thermalization Hypothesis (ETH)	30
2.2.3	Semi-classical approach I: Berry's conjecture	32
2.2.4	Random matrix theory and level statistics	33
2.2.5	Deutsch's argument	36
3	Microscopic justification of the ETH	41
3.1	Extending Deutsch's argument	41
3.2	Flow equation method	42
3.2.1	Motivation	43
3.2.2	Mathematical formulation	46
4	Models and methods	49
4.0.1	Second quantization	49
4.1	Model Hamiltonians	51
4.1.1	Hardcore boson model	51
4.1.2	Spinless fermion model	54
4.2	Observables	55
4.2.1	Momentum distribution function	55
4.2.2	Density-density correlation structure factor	55
4.3	Exact diagonalization	56

4.3.1	Symmetries	56
4.3.2	Full representation basis and matrix elements	59
4.4	Measures for localization	61
4.4.1	Inverse participation ratio	61
4.4.2	Shannon entropy	62
4.5	Implementation of the flow equation method	63
4.5.1	Algorithm	63
4.5.2	Implementation and technical details	65
5	Results	67
5.1	Flow and statistics of the Hamiltonian	68
5.1.1	Pre-flow basis transformation into the integrable basis	68
5.1.2	Spectrum and level statistic	70
5.1.3	Progress of flow and convergence	71
5.1.4	Statistical analysis	74
5.1.5	Histograms	76
5.1.6	Normality indicator	77
5.2	Localization of observables	83
5.2.1	Behavior of the observables over the flow	84
5.2.2	Quantifying localization: IPR and Shannon entropy	87
5.2.3	IPR over flow	94
5.2.4	Scaling of the localization measures	96
5.2.5	Summary of the localization scaling analysis	101
5.3	Preflow transformation to the momentum basis	102
5.3.1	Statistical analysis of the Hamiltonian	103
5.3.2	Scaling of the IPR	105
6	Conclusions	107
6.1	Banded pseudo-random Hamiltonian	107
6.2	Few-body structure of the observables	108
6.3	Outlook	109
A	Symmetries and basis construction	111
A.1	Translational symmetry	111
A.1.1	Commutation with the Hamiltonian	114
A.1.2	Matrix elements in the momentum eigenbasis	115
A.2	Reflection symmetry and semi-momentum	116
A.2.1	Commutation with the Hamiltonian	118
A.2.2	Matrix elements in the semi-momentum basis	118
A.3	Particle-hole inversion symmetry	118
A.3.1	Commutation with the Hamiltonian	119
A.4	Observables	120
A.4.1	Momentum distribution function	120
A.4.2	Density-density correlation structure factor	122

A.4.3	Momentum distribution function	123
A.4.4	Density-density correlation structure factor	124
A.5	Implementation	125
A.5.1	Momentum distribution function	125
A.5.2	Density-density correlation structure factor	126
B	Supplementary plots	129
C	Spectral analysis	159
C.1	Unfolding procedure	159
D	Dimensions of symmetry sectors	161
	Bibliography	163
	Acknowledgements	191

Chapter 1

Introduction

The world around us is made up of various, very different states of matter, which display a plethora of properties. Some are known from everyday life like a solid piece of metal used as cutlery or the liquid that is the essential ingredient for life: water. There are other clusters of matter, which are more exotic: gigantic objects like the sun, in which new elements are created through fusion processes, or fascinating alien objects like black holes, which eat up everything. Common to all is the insight that their basic constituents are microscopically small atoms and molecules. Instead of the extreme cases, which are addressed by particle physics or cosmology, condensed matter theory focuses on the intermediate scales of matter. Since it is still macroscopic in size, it follows that a huge number of particles is involved. The progress of science over the last centuries has exposed that matter does not show the behavior of the extensive number of often identical particles, but that it is rather the interaction among them that gives rise to the wealth of emergent macroscopic properties that we observe. The aggregation of mutually interacting degrees of freedom creates a *collective behavior*, which can be radically different from the individual nature. An example is a metal made of many atoms: Whereas a single atom core attracts its electrons restricting their movement, many atoms in a crystalline structure lead to a delocalization of the *valence electrons*, which can propagate freely through the lattice-defining properties like electric current or heat capacity.

The huge number of degrees of freedom, however, renders the mathematical description of matter to be extremely complex. Although it is often possible to write down the microscopic laws of motion for each particle, their solution and the subsequent derivation of the macroscopic behavior are out of reach. For the noble goal to provide a satisfying and universal understanding, it is therefore necessary to find appropriate simplifications to make predictions feasible without neglecting important aspects.

Historically, this was first resolved by *classical thermodynamics*, which focuses on the description of the time-independent *thermodynamic equilibrium* where no macroscopic currents are present. Instead of modeling all microscopic processes, this phenomenological theory describes macroscopic states of matter in an average sense. Moreover, it also allows to take into account the environment, which can also affect the system.

However, when studying thermodynamic processes, one realizes that many states that we observe are in *non-equilibrium*, e. g. the earth, which is in the steady state of being constantly exposed to the energy supplied by the sun or, on small scales, the melting ice cube in the glass of water. Experiments show that non-driven systems in a generic (non-equilibrium) state, like the last example, will eventually relax to and remain in the thermodynamic equilibrium, if one just waits long enough. The transition process is called *thermalization* and is one major topic of this thesis.

In the last century, it was discovered that in certain regimes, namely at very low temperatures or short time scales, the classical description is insufficient and a different, more sophisticated theory is required: quantum mechanics. And although one mostly experiences classical physics in everyday life, it turns out that some aspects of the physical world, like chemical processes, find their origin in quantum mechanics. Moreover, quantum mechanics allows for a successful understanding of fascinating properties of matter like superconductivity.

In the language of quantum mechanics, the description of a many-body system is based on quantum states, which are represented by a wave function and which dynamics are governed by the axiomatic linear Schrödinger equation. However, this does not generally reduce the complexity, but it rather increases it through additional properties like a postulated special symmetry of the wave function. This symmetry originates in the axiomatic *quantum statistics* and affects the behavior in addition to the interaction and the environment. Furthermore, the number of possible states grows exponentially with system size; a fact also named *exponential explosion*. Finally, one observes new phenomena only found in the quantum world like entanglement. Most of the mentioned topics will be discussed briefly in later parts of this thesis.

A major challenge arises when studying *thermalization* in isolated *quantum* systems. Since the quantum language is conceptually different from classical mechanics, the understanding of thermalization in many-body quantum systems requires a new framework. One very prominent concept to understand the thermalization in these systems is the *Eigenstate Thermalization Hypothesis (ETH)*, which will be explained in Section 2.2.2 (Deutsch 1991; Srednicki 1994). However, up until now, there is little analytical evidence supporting the hypothesis or related statements (see also D'Alessio and Polkovnikov (2013)). One successful example is an argument by Deutsch, which is based on random matrices (Deutsch 1991). This thesis addresses the question of thermalization in many-body quantum systems by justifying the ETH from a microscopical point of view. The results presented in this work suggest that the argument by Deutsch can be extended to generic quantum systems providing a strong confirmation of the proposed thermalization mechanism in quantum systems.

The remaining parts of the introduction are organized as follows: the next section briefly introduces major concepts of classical and statistical thermodynamics in classical systems. The goal here is to give a general background of the description of the

dynamics of many-body classical systems, because some concepts can be extended to quantum systems and often form a strong starting point of the understanding. However, to make the differences clear, the part is followed by the corresponding quantum analogue in part 1.2. Thereafter, section 1.3 presents the most important experimental realizations of quantum simulators, which are the basic tools to study the dynamics of many-body systems in the quantum regime. This is followed by section 1.4, which contains an overview of theoretical approaches to quantum many-body theory, which form the base of the mathematical description in this work. Finally, an outline of this thesis and the main results are presented in section 1.5.

1.1 Many-body systems in classical physics: equilibrium and dynamics

The purpose of this section is to give an overview of the understanding of the dynamics in classical systems, which are systems where quantum effects can be neglected. This is particularly necessary for a profound picture of thermalization in these systems (see 2.1). This part begins with the explanation of the macroscopic theory, which also defines the final state of the dynamics, which is the thermodynamic equilibrium. This is followed by the microscopic picture of the underlying theory, which is *statistical thermodynamics*, introducing the important concept of an ensemble. The equilibrium description is contrasted with the approach based on the equations of motion for each particle condensed in the Hamilton formalism.

The most prominent example of a macroscopic approach to matter is the empirical classical thermodynamics as mentioned in the previous part. This theory effectively reduces the extensive number of degrees of freedom to only a handful parameters called *state variables* (like temperature, pressure or volume), which describe a macrostate. Besides, it was found that there is a quantity called *entropy*, which, for isolated systems, grows over time (irreversible process) unless the system never leaves the thermodynamic equilibrium during the unspecified time evolution (reversible process) (Clausius 1856). This was the first time that a distinct direction of time was suggested. Thermodynamics cannot explain how one can derive state variables from the knowledge about the positions and momenta of all particles. Moreover, it was desired to have a microscopic interpretation of entropy. The following development of the atomic gas theory marked the starting point for the formulation of *statistical thermodynamics*. This is a probabilistic approach that connects the microscopic picture to the macroscopic properties via the concept of *phase space* (Gibbs 2014). The phase space allows for a condensed representation of the generalized coordinates $\mathbf{q} = (q_1, q_2, \dots, q_N)$ and canonical momenta $\mathbf{p} = (p_1, p_2, \dots, p_N)$ of N particles as a point (\mathbf{q}, \mathbf{p}) in a high-dimensional space. Each degree of freedom of each particle adds one dimension to the construction. Obviously, a phase point needs to be consistent with the total energy, spatial confinement or other constraints of the system. For simplicity, the system is assumed to be completely isolated from the environment such that neither particles

nor energy can be exchanged. If the system evolves over time, each point in phase space follows a trajectory on the energy hypersurface. The dynamics of the point is determined by the dynamics of each particle, which itself is governed by Hamilton's equations of motion. Thus, it is in principle possible to calculate the state exactly at all times.

The idea of statistical thermodynamics is that the exact initial positions and momenta of all particles cannot be known and that instead a probabilistic interpretation is required. Instead of a single phase point one can assume that there is an entire region of microscopic configurations (microstates) denoted by the phase space density $\rho(\mathbf{q}, \mathbf{p}, t)$. The entire region then evolves via Liouville's equation

$$\frac{\partial}{\partial t} \rho(\mathbf{q}, \mathbf{p}, t) = -\{\rho(\mathbf{q}, \mathbf{p}, t), H(\mathbf{q}, \mathbf{p})\}, \quad (1.1)$$

where $\{\cdot, \cdot\}$ denotes the Poisson bracket (Gibbs 2014; Tolman 1979). The expectation value of any measurable quantity $O(\mathbf{q}, \mathbf{p})$, also called *observable*, is then determined as $\langle O(t) \rangle = \int d\mu \rho(\mathbf{q}, \mathbf{p}, t) O(\mathbf{q}, \mathbf{p})$, where $d\mu = C d\mathbf{q} d\mathbf{p}$ is the measure in phase space with an appropriate constant.

If ρ is constant over time, i. e. in a steady state, it is defined to be in equilibrium. As one can show, this can only happen if it can be expressed in terms of conserved quantities. It is important to note that although ρ does not evolve over time, the particles themselves are in constant motion.

A special equilibrium distribution is the microcanonical *ensemble*, which is defined to be the set of all possible microstates that are consistent with the constraints of the system as mentioned above. If the number of microstates in this set is denoted by W , it is postulated that each point of this set can be assigned an identical probability $1/W$, since this construction contains the least amount of knowledge about the internal interactions ("maximum ignorance"). Interestingly, this postulate can be justified by the *principle of maximum entropy* (Jaynes 1957a,b). In mathematical terms, the microcanonical ensemble is represented by a joint probability density function in phase space and reads

$$\rho_{\text{mc}}(\mathbf{q}, \mathbf{p}) = \frac{1}{W}. \quad (1.2)$$

In a more generic formulation, W is chosen, such that $\int d\mu \rho_{\text{mc}}(\mathbf{q}, \mathbf{p}) = 1$ (see Eq. (2.1)). Beyond the microcanonical ensemble there are other equilibrium ensembles like the canonical ensembles, which also allow heat exchange with an attached bath, and the grandcanonical ensemble, which, on top of heat exchange, includes particle exchange (Gibbs 2014). The three ensembles are the natural extension of thermodynamic equilibrium in the statistical thermodynamics language. They represent the average over many repetitions of identical experiments where only macroscopic variables like the total energy can be controlled. The microscopic details are, however, not precisely specified and vary from one to another. An important and related result is the Maxwell-Boltzmann distribution for a rarefied ideal gas, which can be derived from each ensemble (Maxwell 1860b,a; Boltzmann 1872; Tolman 1979).

A final remark about extending the concept of an ensemble to special non-equilibrium situations: in these cases it is possible to define ensembles that change over time or to take ensembles of non-isolated systems. However, this is not the focus of this thesis. Finally, it remains to connect the microscopic to the macroscopic world. This was achieved by Boltzmann with his famous equation

$$S = k_B \ln W, \quad (1.3)$$

which relates the entropy S to the number of possible microstates of the system in phase space W (Boltzmann 1872, 1866). It also provides an interpretation for the entropy: in ordered systems there are fewer microstates than in completely disordered systems. This led to the prominent conclusion that the entropy is a measure for the disorder in the system.

Boltzmann's entropy equation can be regarded as a special case of the more general entropy formula by Gibbs

$$S = -k_B \sum_i p_i \ln p_i \quad (1.4)$$

by setting $p_i = 1/W$ for all i (Gibbs 2014). The latter equation is also valid for a canonical ensemble when each microstate is weighted with the Gibbs' factor $p_i = e^{-\beta H(\mathbf{q}, \mathbf{p})}/Z$, where β denotes the inverse temperature and Z the partition function.

Having defined the ensembles as the microscopic counterpart to the thermodynamic equilibrium, one is appropriately equipped to study the thermalization process in classical systems in more detail. One aspect is to find out which systems thermalize and which do not. Moreover, one would like to answer the following questions: How is it possible that a phase space density, which depends on time, agrees with an ensemble that is independent of time? Additionally, how can one reconcile the laws of motion, which are time-reversible¹, to a quantity that is irreversible under time and what happens to the huge amount of information about the initial positions and momenta of the particles in the thermalization process?

Historically, the last question is connected to the *arrow of time*, a phrase coined by Eddington in 1927 (Eddington 2012). It describes an apparent direction of time observed in many natural processes: buildings collapse, coffee cups mix and cool and eggs break. But even before, the question of irreversibility was approached by Boltzmann, who formulated his famous H -theorem (Boltzmann 1872). However, this evoked several objections, among them the prominent dispute with Loschmidt (Loschmidt paradoxon) (William Thomson 1874; Loschmidt 1877) and with Poincaré (Sklar 1995). In the modern understanding, thermalization in classical systems is related to dynamical chaos and requires concepts like ergodicity and mixing. Although there is no full proof and some aspects are still unresolved, it is explained in more detail in Section 2.1. That part also presents the notion of integrability, which can be considered as an indicator that shows whether a system thermalizes or not.

¹It is neglected here that the weak interaction violates the CP-invariance.

1.2 Quantum dynamics: unitarity and non-equilibrium

There is a broad consensus that the world of very small scales or times can be described by quantum mechanics. However, this theory contains abstract, non-intuitive concepts that often elude the human experience. The following parts briefly explain the most important notions that are the very core of quantum theory. It starts with the fundamental description of the dynamics of many-body quantum systems. The main difference to the classical case is that the language of quantum theory is based on energy eigenstates instead of phase points. Thereafter, the most important quantum features or phenomena that appear in the theory are introduced.

1.2.1 Mathematical formulation of quantum dynamics

According to the basic axioms of quantum mechanics the description of a physical system takes place in a complex Hilbert space \mathcal{H} . In this space a *pure quantum state* is represented by a ray $|\psi\rangle$. The number of all mutually orthogonal pure states defines the dimension of the Hilbert space and can be finite or infinite. The equation of motion for a pure state is given by the linear Schrödinger equation

$$i\hbar \frac{\partial}{\partial t} |\psi\rangle = H |\psi\rangle \quad (1.5)$$

where H is the many-body Hamiltonian operator of the system and \hbar the reduced Planck constant ([Schrödinger a,b,c,d](#)). In the following, $\hbar = 1$. As any other observable the Hamiltonian is required to be self-adjoint. This ensures that expectation values, which are the ones measured in experiments, are real. If the Hamiltonian is independent of time, the solution of the Schrödinger equation, which defines how a state at time $t = 0$ evolves to time t , is calculated to be

$$|\psi(t)\rangle = e^{-iHt} |\psi(0)\rangle = U(t) |\psi(0)\rangle, \quad (1.6)$$

with the newly defined *time evolution operator* $U(t)$, which is unitary, i. e. $UU^\dagger = \mathbb{1}$, because the Hamiltonian is Hermitian.

Generically, a quantum state $|\Psi\rangle$ does not need to be described by a pure state, but by a mixture of pure states. It is called a *mixed state* and is defined by a *density operator* ρ via

$$\rho = \sum_i p_i |\psi_i\rangle \langle \psi_i|, \quad (1.7)$$

where the p_i are positive-valued fractions that sum up to 1 ($\text{Tr}(\rho) = 1$), and $|\psi_i\rangle \langle \psi_i|$ are the projectors onto the pure state $|\psi_i\rangle$ ([von Neumann 1927](#); [Landau 1927](#); [Dirac 1981](#)). The fractions denote the probabilities to end up in the respective pure state when performing a measurement. If ρ has rank 1 or $\text{Tr}(\rho^2) = 1$, the state is in a pure state. In this sense, the density operator can be interpreted as a statistical ensemble. The time

evolution of the physical system must be reflected by a time-evolved density operator $\rho(t)$. It is determined by the projectors $|\psi_i(t)\rangle\langle\psi_i(t)|$ at later times, which themselves are given by Eq. (1.6), such that $\rho(t) = e^{-iHt}\rho(0)e^{iHt}$. Applying the time derivative to this equation yields the *von-Neumann equation*

$$i\hbar\frac{\partial}{\partial t}\rho(t) = -[\rho(t), H] \quad (1.8)$$

which can be thought of as a quantum analogue to the Liouville equation Eq. (1.1). The correspondence is based on identifying the quantum commutator $\frac{1}{i\hbar}[\cdot, \cdot]$, which is defined as $[A, B] = AB - BA$ with the Poisson bracket $\{\cdot, \cdot\}$. Furthermore, the operator $\rho(t)$ does not depend on additional phase space variables as the classical phase space density function $\rho(\mathbf{q}, \mathbf{p}, t)$, but is defined on an orthogonal basis. According to the principle of maximal entropy, one can then define the microcanonical ensemble as the sum of the projectors to the energy eigenstates of a certain energy window $[E - \Delta E, E + \Delta E]$ centered around the mean total energy $E = \text{Tr}(\rho_{\text{mc}}H)$:

$$\rho_{\text{mc}} = \frac{1}{Z(E, \Delta E)} \sum_{|E_i - E| \leq \Delta E} |E_i\rangle\langle E_i|. \quad (1.9)$$

The number of states in the window $Z(E, \Delta E)$ is required to properly normalize the density operator ($\text{Tr}(\rho_{\text{mc}}) = 1$) and is typically very large. In this sense, one can interpret $1/Z$ as the identical probability and thus the quantum counterpart to $1/W$ in the classical case. As will be explained in part 2.2 it is important in the context of thermalization that the energy window contains an exponentially large number of states for an extensive number of degrees of freedom.

Using the fact that every self-adjoint operator can, in principle, be diagonalized, it is possible to compute the eigenbasis of the Hamiltonian. This basis, which consists of the energy eigenstates, is denoted by

$$H |E_m\rangle = E_m |E_m\rangle \quad (1.10)$$

where $m \in \mathbb{N}_0$ and can be ordered, such that $E_{m+1} \geq E_m$. In this basis the matrix elements of the time-evolved density operator take on the form

$$\rho_{mn}(t) = \langle E_m | \rho(t) | E_n \rangle = \rho_{mn}(0) e^{-i(E_m - E_n)t}. \quad (1.11)$$

Clearly, a pure state will always remain pure. Hence, $\rho(t)$ can never become a thermal density matrix, e. g. of a microcanonical ensemble ρ_{mc} . The von-Neumann equation has important consequences on the dynamics of quantum states: using the cyclic invariance property of the trace operation one can show that the trace of the squared density operator remains constant over time, i. e. $\frac{\partial}{\partial t} \text{Tr}(\rho^2(t)) = 0$. Hence, mixed states remain mixed, whereas pure states remain pure over time. It follows that a pure state can not equilibrate to a thermal state, which is a mixed state, by unitary time evolution. A thorough discussion of these intriguing observations follows in chapter 2.2. However, already von Neumann realized that it is *observables* and not wave functions

that are measured in experiments, such that the study of thermalization needs to focus on those quantities (Neumann 1929).

According to the current interpretation of quantum mechanics a measurement of a quantum state with an observable O projects the quantum state into one of the eigenstates of O (“collapse of the wave function”). The expectation value of an observable for a density operator is calculated as

$$\langle O(t) \rangle = \sum_i p_i \langle \psi_i(t) | O | \psi_i(t) \rangle = \text{Tr}(\rho(t)O), \quad (1.12)$$

where $\langle \psi_i(t) | O | \psi_i(t) \rangle$ is the contribution from each state of the density operator. Performing the trace over the energy eigenbasis this becomes

$$\langle O(t) \rangle = \sum_{m,n} \rho_{mn}(0) e^{-i(E_m - E_n)t} \langle E_m | O | E_n \rangle. \quad (1.13)$$

A special class of observables, namely those that commute with the Hamiltonian, are called *conserved quantities*. Their expectation value is independent of time, which becomes clear by inserting $\rho(t) = e^{-iHt} \rho(0) e^{iHt}$ in Eq. (1.12). If the observable O commutes with the unitary operator, the latter drops out via the cyclic property of the trace.

The generic setting is to consider the non-trivial unitary time evolution of an initial state of the system after a global quench. Although, there are phenomena like recurrences, the observation of time-evolved observables show equilibration. To understand why thermalization in quantum systems requires certain conditions to be met one can start with the time evolution of a generic initial state $|\psi(t=0)\rangle = |\psi_0\rangle$. This state can be expressed in the energy eigenbasis, such that at $t=0$ it reads

$$|\psi(0)\rangle = \sum_m \underbrace{\langle E_m | \psi(0) \rangle}_{c_m} |E_m\rangle. \quad (1.14)$$

In this basis the calculation of the general solution of the Schrödinger equation Eq. (1.6) for $t \geq 0$ becomes

$$|\psi(t)\rangle = e^{-iHt} |\psi\rangle = \sum_m e^{-iE_m t} c_m |E_m\rangle. \quad (1.15)$$

The expectation value of the total energy of this state is given by

$$E = \text{Tr}(\rho H) = \sum_m E_m |c_m|^2 \quad (1.16)$$

with the variance

$$\Delta E^2 = \text{Tr}(\rho(H - E)^2) = \sum_m (E_m^2 |c_m|^2) - E^2 \quad (1.17)$$

that is small compared to E , i. e. $\Delta E \ll E$.

A time-evolved observable in the energy eigenbasis reads

$$O(t) = \langle \psi(t) | O | \psi(t) \rangle = \sum_{m,n} c_m^* c_n e^{i(E_m - E_n)t} O_{mn} \quad (1.18)$$

$$= \sum_m |c_m|^2 O_{mm} + \sum_{m,n \neq m} c_m^* c_n e^{i(E_m - E_n)t} O_{mn} \quad (1.19)$$

where $O_{mn} = \langle E_m | O | E_n \rangle$ denotes the eigenstate expectation value (EEV). Studying this equation in more detail one notices that the time evolution leads to a dephasing among the energy eigenstates (assuming no degeneracies), whereas the diagonal part is constant over time. In an infinite-time average $\langle \cdot \rangle_t$ only the first term, which is defined via the *diagonal ensemble* (DE) where

$$\rho_{\text{DE}} = \bar{\rho} := \lim_{t_0 \rightarrow \infty} \frac{1}{t_0} \int_0^{t_0} \rho(t) dt = \sum_m \rho_{mm} |E_m\rangle \langle E_m|, \quad (1.20)$$

survives, such that

$$\langle O(t) \rangle_t = \sum_m |c_m|^2 O_{mm} = \text{Tr}(\rho_{\text{DE}} O). \quad (1.21)$$

Hereby, it is assumed that no degeneracies are present in the system. Moreover, it is clear that *if* a system thermalizes, it *must* thermalize to the infinite-time average value.

If the system is isolated, one assumes that the corresponding ensemble, the system thermalizes to, is given by the microcanonical ensemble, because all microstates are assumed to have an equal probability (Eq. (1.9)).

It remains to find a quantum mechanical analog to the entropy of the classical case in Eq. (1.4). A common choice is the von Neumann entropy

$$S(\rho) = -\text{Tr}(\rho \ln \rho) = -\sum_i p_i \ln(p_i), \quad (1.22)$$

which vanishes for pure states and is maximal with $S = \ln(\dim(\mathcal{H}))$ for maximally mixed states ($p_i = 1/\dim(\mathcal{H})$ for all i). The latter case can be regarded as a measure for the unpredictability of the system and is the quantum counterpart to Boltzmann's Eq. (1.3).

1.2.2 Inherent quantum features

In this section some of the quantum features that are inherent in the theory are briefly introduced.

Exponential explosion

The major difference between the quantum picture and the classical language is the pivotal insight that the states that describe matter “live” in an exponentially large Hilbert space \mathcal{H} . To give an example one can think of a spin system consisting of N spins, which can either point up or down. The corresponding dimension of the Hilbert space is then given by $\dim(\mathcal{H}) = 2^N$. For macroscopic matter, however, the number of spins is of order 10^{23} and thus $\dim(\mathcal{H}) = 2^{10^{23}}$. This is an incredibly huge number that makes any exact numerical treatment that takes into account every possible state effectively impossible. As a consequence, *exact diagonalization* techniques are limited to a number of lattice sites of 50 depending on the size of the local Hilbert space and the number of symmetries that can be used. This inherent complexity of quantum mechanics is sometimes called *exponential explosion* and requires special approaches like the ones listed in part 1.4.

Superposition

A second fundamental aspect of quantum mechanics is *superposition*. This principle originates from the linearity of the Schrödinger equation (1.5), which defines the dynamics of quantum systems. As a result, linear combinations of solutions of the equation are also solutions. This means that the most general quantum state is a sum of all possible distinct states where each summand has a “weight” given by a complex number. Superposition is the key to the immense power of quantum logics that depend on a mixture of several quantum states, e. g. $|\psi\rangle = a|0\rangle + b|1\rangle$.

Entanglement

The most non-intuitive phenomenon is arguably *entanglement*. It roughly describes the fact that the state of individual particles in composite quantum systems cannot be described independently, but requires the full quantum state. Entanglement has been phrased as the essential resource of quantum computing in the sense that this is the reason why quantum computers outperform classical ones (Steane 1998; Preskill 2000; Nielsen and Chuang 2010).

The combined Hilbert space of composite systems is constructed as the tensor product of the individual Hilbert spaces. For a bipartite system this is given by $\mathcal{H} = \mathcal{H}_A \otimes \mathcal{H}_B$. Each basis state of the composite system has the form $|ij\rangle_{AB} := |i\rangle_A \otimes |j\rangle_B$ such that a generic state $|\psi\rangle_{AB} = \sum_{i,j} c_{ij} |ij\rangle_{AB}$, where the sums run over the respective Hilbert space dimensions of A and B . A state $|\psi\rangle_{AB}$ is called *separable*, if and only if it can be written as the tensor product of states that only live in the respective Hilbert spaces, i. e. $|\psi\rangle_{AB} = |\phi\rangle_A \otimes |\chi\rangle_B$. If this cannot be done, the state is defined to be *entangled*.

An illustrative example for demonstrating entanglement are the four Bell states. The generic state of one qubit is described by $|\phi\rangle = a|0\rangle + b|1\rangle$ (e. g. a spin-1/2 degree of freedom), where a and b are always chosen to normalize $|\psi\rangle$. A generic separable state of the composite system is then given by $|\psi\rangle = (a_A|0\rangle + b_A|1\rangle) \otimes (a_B|0\rangle + b_B|1\rangle)$.

However, the full Hilbert space also contains states like

$$|\psi\rangle = a |01\rangle + b |10\rangle \quad (1.23)$$

$$\text{and } |\psi\rangle = a |00\rangle + b |11\rangle, \quad (1.24)$$

which cannot be constructed from separable states and hence are entangled. Setting $a = 1/\sqrt{2}$ and $b = \pm 1/\sqrt{2}$ yields the four Bell states. These are maximally entangled two-qubit states, which form an orthonormal basis and are also used in the quantum computation context.

To measure the entanglement, it is helpful to first define a special form of the density operator for a pure state in a bipartite system: the reduced density matrix $\rho_A = \text{Tr}_B(|\psi\rangle\langle\psi|_{AB})$, which sums over the basis of system B (“tracing out part B ”). One quantity to measure the entanglement is the von Neumann entropy of one of the reduced density matrices, the so-called *entanglement entropy* (EE):

$$S_{\text{EE}}(\rho_A) = -\text{Tr}(\rho_A \log \rho_A) = -\text{Tr}(\rho_B \log \rho_B) = S_{\text{EE}}(\rho_B). \quad (1.25)$$

For separable states $S_{\text{EE}}(\rho) = 0$, whereas maximally entangled states are identified via $S_{\text{EE}}(\rho) = 1$. For instance, one can immediately derive for the Bell state $|\psi_4\rangle = (|00\rangle + |11\rangle)/\sqrt{2}$ that $\rho_A = \frac{1}{2}(|0\rangle\langle 0| + |1\rangle\langle 1|)$. Taking the trace then yields $S(\rho_A) = 1$. From this follows that the Bell states are maximally entangled. The entanglement entropy for mixed states can also be defined (Horodecki et al. 2001).

An important quantity in this context is the connected correlation function

$$C(O_A, O_B) = \langle (O_A - \langle O_A \rangle) (O_B - \langle O_B \rangle) \rangle, \quad (1.26)$$

which measures the correlation of the fluctuations of observables in the regions A and B around their respective averages. For product states that are not entangled the fluctuations in different regions are completely independent from each other such that this quantity vanishes for all observables.

The most famous controversy connected to entanglement is certainly the EPR paradoxon (Einstein et al. 1935). In this thought experiment two particles initially interact before moving in opposite directions. Since the particles are now entangled, they still depend on each other, although being separated by a huge distance. This is what led the authors to phrase entanglement as “spooky action at a distance”. In their work, the authors tried to show that quantum mechanics is incomplete and that there are additional local degrees of freedom that are hidden. The EPR paradoxon is thought to be resolved by two different approaches. The first explanation is that quantum mechanics contains local hidden variables. However, this was ruled out later by Bell’s famous inequality theorem (Bell 1964; Clauser et al. 1969). Bell’s theorem was confirmed by several experiments without loopholes (Hensen et al. 2015). In the current understanding, the only interpretation that remains states that quantum mechanics is not a locally realistic theory, which means that it is required to describe the system as a whole.

1.2.3 Methods to drive an isolated system into non-equilibrium

In order to study thermalization, it is obvious that the system of choice has to be in non-equilibrium initially. This means that energy or particles need to be pumped into the system (Polkovnikov et al. 2011). This can be done in several ways: quantum quenches, open systems and driven systems. It is important to note that it is possible to create setups, where a system is in non-equilibrium by continuously perturbing it (e. g. by optical pulses like in Mitrano et al. (2016)). These systems cannot be regarded to be isolated. Due to the focus on the thermalization in isolated systems, this shall not be discussed further.

The *quantum quench* is a simple and clean procedure to create non-equilibrium situations, which is not only used theoretically (Calabrese and Cardy 2005, 2006), but has also found its application in many experiments (e. g. Bloch et al. 2008; Mitrano et al. 2016). There are basically three groups of quantum quenches: global, local and geometric quenches (Eisert et al. 2015). A quantum quench is either *local* or *global* depending on the amount of energy that is pumped into the system. Both quench protocols have in common that initially a state is prepared with respect to some Hamiltonian H_0 that depends on several parameters $\lambda = (\lambda_1, \lambda_2, \dots)$. It can be either a pure state (e. g. the ground state) or a mixed state defined by the canonical ensemble $\rho_c = e^{-\beta H_0}$. At time $t = 0$ one or several system's parameters (e. g. the interaction strength among particles) are suddenly changed to new values ("quenched"), which yields the Hamiltonian H . The system then unitarily evolves in time until a measurement is done.

1.3 Experimental realizations of quantum systems: quantum simulators

Just like in classical physics it is often possible to write down the quantum mechanical laws of physics, describing all aspects of a real many-body system including all present particles and interactions. However, the equations are usually too complex to tackle. For this reason, the paradigmatic approach is to analyze an idealized model of the real system (e. g. by ignoring relativistic effects). Even then, though, analytical solutions are rare and often impossible for most cases and higher dimensions. A possible alternative is to compute properties with numerical techniques. This path has been thriving for the past decades due to the enormous growth of (classical) computer power. However, due to the immense complexity, which naturally accompanies an exponentially large Hilbert space, a straightforward exact diagonalization routine that includes all states is often simply not feasible for larger systems on a classical computer (even in one dimension).

The obvious solution is to invent new methods and algorithms that focus only on the relevant physics while neglecting other aspects. Some of the methods are introduced in part 1.4. As a consequence of the special purpose the methods are designed for, they can encounter problems in different regimes. For example, the approach that relies on taking into account only the most important states is limited by the entanglement

(e. g. time-dependent Density Matrix Renormalization Group (tDMRG) (Daley et al. 2004b; White and Feiguin 2004; Vidal 2004)). For approximation methods that treat more complex systems, the question always arises how accurately the obtained results describe the desired models (e. g. Density Functional Theory (DFT) (Verma and Truhlar 2020)).

The most universal option in computing generic quantum systems would be to leave the realm of classical computation and to use the benefits of *quantum computation* instead. This has already been pointed out in the early 1980's (Benioff 1980; Manin 1980; Feynman 1982). Of course, a universal quantum computer as devised by Deutsch and Penrose (1985), Deutsch and Jozsa (1992) and Lloyd (1996) would meet the needs, because it consists of a series of quantum gates that allow for the encoding of any quantum state and the implementation of any desired model Hamiltonian. This also includes non-local Hamiltonians (Dodd et al. 2002; Masanes et al. 2002; Bennett et al. 2002). Therefore, this machinery is often called to be *digital* in reference to classical computers. In addition, it has been suggested that a universal quantum computer would be a very powerful tool, outperforming classical counterparts in many ways (Deutsch and Jozsa 1992; Shor 1994; Grover 1997), yet this is work in progress.

The technological precursor of the universal quantum computer is the *analog quantum simulator*, and it is often sufficient for the desired purposes (Abrams and Lloyd 1997; Somma et al. 2002). A quantum simulator describes a table-top experiment with a highly controllable system, which Hamiltonian emulates a desired model Hamiltonian (Buluta and Nori 2009). The underlying trick is that there is map between the two Hamiltonians, such that one can study the quantum effects of a model by simulating another one in experiment, e. g. atoms in a magnified lattice can simulate quantum magnetism. The advantage of quantum simulators in contrast to the universal quantum computer is certainly the fact that no error correction and less accuracy is needed (Buluta and Nori 2009). Nevertheless, the challenges for an experimental realization are high: to ensure coherent dynamics it is required to prevent the system from energy loss and dephasing. Consequently, one needs to maintain near-perfect isolation from the surrounding environment and very low temperatures. Moreover, a precise handling of the system's parameters is essential in order to perform quantum quenches or to do other manipulations like the preparation of the initial state in the simulator. Equally important is the extraction of the desired information out of the system through a specifically tailored measurement process. Many of these demanding technical requirements for the realization of quantum simulators have been solved over the past decades such that, nowadays, there are plenty of different experiments (see e. g. reviews Buluta and Nori 2009; Ladd et al. 2010; Georgescu et al. 2014). They range from all-optical setups (O'Brien 2007), experiments using NMR (Somaroo et al. 1999; Du et al. 2010), quantum dots (Manousakis 2002) to superconducting circuits (van Oudenaarden and Mooij 1996).

The last two classes both use electromagnetic fields and laser cooling to confine the degrees of freedom, which are ions or atoms, respectively. The main difference is the depth of the trapping potential, which is either the strong Coulomb interaction or a shallow laser-induced dipole interaction as explained in the following.

The general concept to entrap ions with electromagnetic fields is known under the name of *ion traps*. It has been proposed in several forms (Cirac and Zoller 1995; Poyatos et al. 1996; Porras and Cirac 2004; Schmied et al. 2008; Blatt and Roos 2012), some of which have been realized (for a list see e.g. Wineland et al. (1998)). The general idea is to entrap ions using electromagnetic fields, e.g. with a combination of static electric and magnetic fields (Wineland et al. 1983) or rf-fields (Dehmelt 1968, 1969). While the strong Coulomb interaction confines the ions, they are cooled down by lasers in various ways, which are explained in more detail below (Wineland et al. 1978; Neuhauser et al. 1978). This setting offers a precise control that also allows for quantum information processing (Monroe et al. 1995; Blatt and Wineland 2008; Häffner et al. 2008). More recent advances have demonstrated that it is possible to study the time evolution of different observables to learn, e.g., about the spreading of entanglement in ion crystals (Kim et al. 2009; Jurcevic et al. 2014). Other phenomena that can be observed are dynamical quantum phase transitions (Jurcevic et al. 2017) and discrete time crystals (Zhang et al. 2017).

Beyond ions, it is also possible to entrap atoms in *ultracold atomic gas* experiments. In contrast to ion traps the neutral atoms are not trapped by rather strong Coulomb forces, but through weaker radiation-pressure traps (Pritchard et al. 1986; Raab et al. 1987), magnetic traps (Migdall et al. 1985; Bergeman et al. 1987) or optical traps (Bjorkholm et al. 1978; Chu et al. 1986). The last of the mentioned mechanisms yields the shallowest potentials and is thus able to reach the lowest temperatures (Grimm et al. 2000). In the following, it is explained how this technique can be used to create a regular potential energy landscape, named *optical lattice*. Ultracold atomic gas experiments have proven to be very successful, which is why various reviews especially focus on this concept e.g. Lewenstein et al. (2007); Bloch et al. (2008); Cazalilla et al. (2011); Bloch et al. (2012); Langen et al. (2015) and Gross and Bloch (2017).

The following part gives an overview of the general setup of the experiment, how the entrapping works, how manipulations are done and, finally, what measurements and phenomena can be realized with the present knowledge.

The idea to entrap atoms in an optical potential was introduced in the 60s (Askar'yan 1962; Letokhov 1968), initially in the context of laser spectroscopy of a trapped single atom (Letokhov 1975). The general idea is as explained in the next paragraph (following Grimm et al. (2000)).

If an atom is exposed to light, a small oscillating dipole moment is induced, proportional to the complex polarizability. This dipole now interacts with the light yielding an interaction potential, which is proportional to the field intensity of the driving electric field of the light and to the real-part of the polarizability. Moreover, the gradient of the potential defines a conservative force on the dipole. However, the atom is also absorbing energy proportional to the imaginary-part of the polarizability. This can be interpreted as a photon scattering process and leads to dipole radiation due to spontaneously emitted photons. The interaction potential and the scattering rate are the defining quantities of the atom in the light field. By calculating the polarizability both quantities can be rewritten with respect to the field intensity and

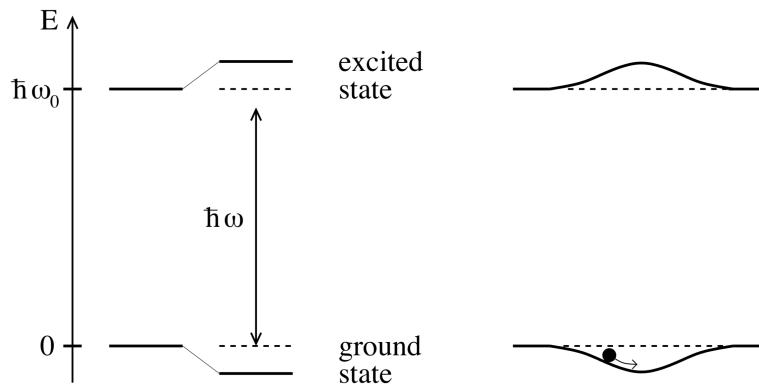


Figure 1.1: Left-hand side: Light shifts induced by a red-detuned laser for a two-level system. The ground state is shifted down and the excited state up. Right-hand side: A Gaussian laser beam creates a potential well, which can trap an atom. Reprinted from [Grimm et al. \(2000\)](#), with permission from Elsevier.

the difference of the driving light frequency to the frequency of the optical transition. If this difference is negative (so-called *red-detuned* light), the interaction minima are found to be at the locations of the intensity maxima, therefore “pulling” the atoms into the light field. In order to determine the effect of the laser light on the energy levels of a more complicated atom one can perform a second-order time-independent perturbation theory for non-degenerate states ([Grimm et al. 2000](#)). In a two-level system, this leads to a shift in the ground state and excited state with different signs (see Fig. 1.1 for red-detuned light), which is exactly given by the interaction potential. This is called “light shift” or “ac Stark shift” and helps to confine the atoms in the light induced trap by lowering the corresponding energies (in a red-detuning setting). The choice of the atom is defined by the ability to be strongly polarized in order to yield a convenient spectral range, which is why one usually prefers Alkali metals ([Grimm et al. 2000](#)). However, the trapping potential of a simple laser beam is usually too weak to confine an atom in the potential energy landscape. Therefore, different trapping techniques using several beams have been envisioned, one of them the “standing-wave” setting. In this setting two counter-propagating laser beams interfere to create standing light patterns, which offer extremely tight traps for the atoms and which can be thought of as representing a “light crystal” ([Grimm et al. 2000](#)).

Before the atoms can be confined in the optical lattice, it is necessary to cool them down. This is, because the thermal energy of room-temperature atoms is orders of magnitude larger than the trapping potential ([Grimm et al. 2000](#)). A necessary requirement for the realization of ultracold atomic gases was therefore the successful development of effective cooling mechanisms ([Hänsch and Schawlow 1975](#)). To achieve a low enough temperature several different cooling processes are successively performed for the preparation of an ultracold atomic gas. Usually, it begins with Doppler-cooling and following by the combination of evaporative cooling and

laser cooling. The term “ultracold” usually describes temperatures of $T < 1\text{mK}$ as e. g. in ultracold photoassociation spectroscopy experiments (Jones et al. 2006). It corresponds to a situation where only s-wave scattering can occur. Nowadays, it is even possible to achieve temperatures $T < 10\text{pK}$ (Bloch et al. 2012). The two most important parameters of optical lattices are the well depth and the geometry, which can be tuned precisely. This provides a huge amount of versatility: it is easy to change the geometry or the effective dimension of the system, the disorder or the depth as demonstrated first by Greiner et al. (2002a). The laser trapping allows for one-dimensional, two-dimensional and three-dimensional lattices (Köhl et al. 2005) and also offer to set up systems with weak or strong interaction. They can even be adjusted, so that there is an enormously strong effective magnetic field (Goldman et al. 2016).

The number of models that ultracold atomic gases are able to simulate is large. In the late 1990s, Jaksch et al. (1998) demonstrated that dilute ultracold atomic gases confined in an optical lattice are able to approximately simulate the dynamics of the Bose-Hubbard lattice model under certain conditions, which are discussed in more detail below (Hubbard and Flowers 1963; Kanamori 1963; Gutzwiller 1963). The Bose-Hubbard model is a variant of the original Hubbard model, but with spinless bosons instead of fermions as the fundamental particles. The Hamiltonian reads

$$H = -t \sum_{\langle i,j \rangle} b_{i+1}^\dagger b_j + \frac{U}{2} \sum_i n_i(n_i - 1) - \mu \sum_i n_i, \quad (1.27)$$

where $\langle i, j \rangle$ denotes the sum over all lattice sites i and all of its neighbors j . The behavior of this model is defined by the structure of the lattice and the size and sign of the ratio of the hopping parameter t to the density-density interaction strength U , namely t/U . If one assumes translational invariance, the hopping parameter t is identical for every site. One important phenomenon that is captured in a Bose-Hubbard model is the Mott-superfluid transition (Fisher et al. 1989; Tasaki 1998). If the ratio t/U is very large, the kinetic part dominates and the bosons can move, whereas if it is small enough, the interaction restrains the particles from propagating and the system is insulating. A first major achievement in the development of ultracold atomic gases, which also served as a proof of principle, was that Greiner et al. (2002a) were able to show the Mott-superfluid transition experimentally after it had been proposed by Jaksch et al. (1998).

In the following years, also dynamical quantities like the effect of damping on the transport were studied (Fertig et al. 2005). Moreover, the techniques were improved and refined with various quench protocols and parameter tunings. For example, it has been developed to employ a global quench from a shallow to a deep lattice (Greiner et al. 2002b; Sebby-Strabley et al. 2007) and to vary the lattice depth in a soft-core boson model (Tuchman et al. 2006).

In general, it was suggested that optical lattices can be used to simulate a wide range of condensed matter systems (Lewenstein et al. 2007) and even build universal quantum computers (Brennen et al. 1999; Jané et al. 2003). One group has proposed to

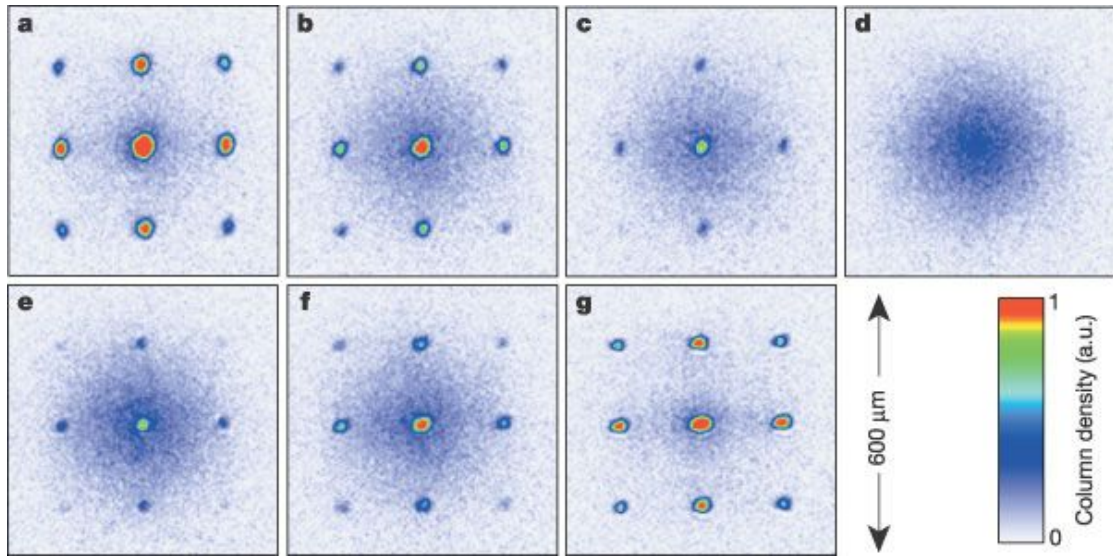


Figure 1.2: Collapse and revival experiment in a Bose-Einstein condensate. The figure shows the dynamical evolution, obtained by time of flight measurements, of the matter wave interference pattern after a quench, which increases the depth of the potential well. After some time, the interference pattern is seen to come to its initial state (revival). From Greiner et al. (2002b). Reprinted with permission from Springer Nature Publishing AG.

realize quantum logic gates using ultracold atomic gases in optical lattices (Brennen et al. 1999). However, the research is not restricted to bosonic lattice systems, but also fermionic lattices can be realized (Esslinger 2010; Schreiber et al. 2015). If the fundamental particles are fermions, i.e. the original Hubbard model, phenomena like magnetism and superconductivity can be studied (Esslinger 2010). If the depth of the potential wells is large enough, it is also possible to see the antiferromagnetic Néel state (Koetsier et al. 2008). Moreover, one can add the interaction among the particles in order to get an interacting Fermi gas in an optical lattice and study Mott Physics in fermionic atoms (Jördens et al. 2008; Schneider et al. 2008).

Not all fundamental questions related to thermalization can be answered by ultracold atoms on a lattice. Some of them are addressed using models like a one-dimensional Bose gases in continuum. Here, the setting allows for the study of the time evolution of the system, e.g. to analyze the relaxation in these models, which shows different regimes (Hofferberth et al. 2007). Other experiments focus on the relaxation after a rapid split of a 1D Bose gas and suggest that the final state is a *prethermal* state, representable by a *Generalized Gibbs Ensemble (GGE)* (Gring et al. 2012), and how prethermal correlations emerge (Langen et al. 2013).

Other experiments study the relaxation of observables (Trotzky et al. 2012; Kaufman et al. 2016) (see Fig. 1.3). Famous examples for cases, where no thermalization was seen, is the collapse-and-revival experiment (Greiner et al. 2002b) (see Fig. 1.2) or the

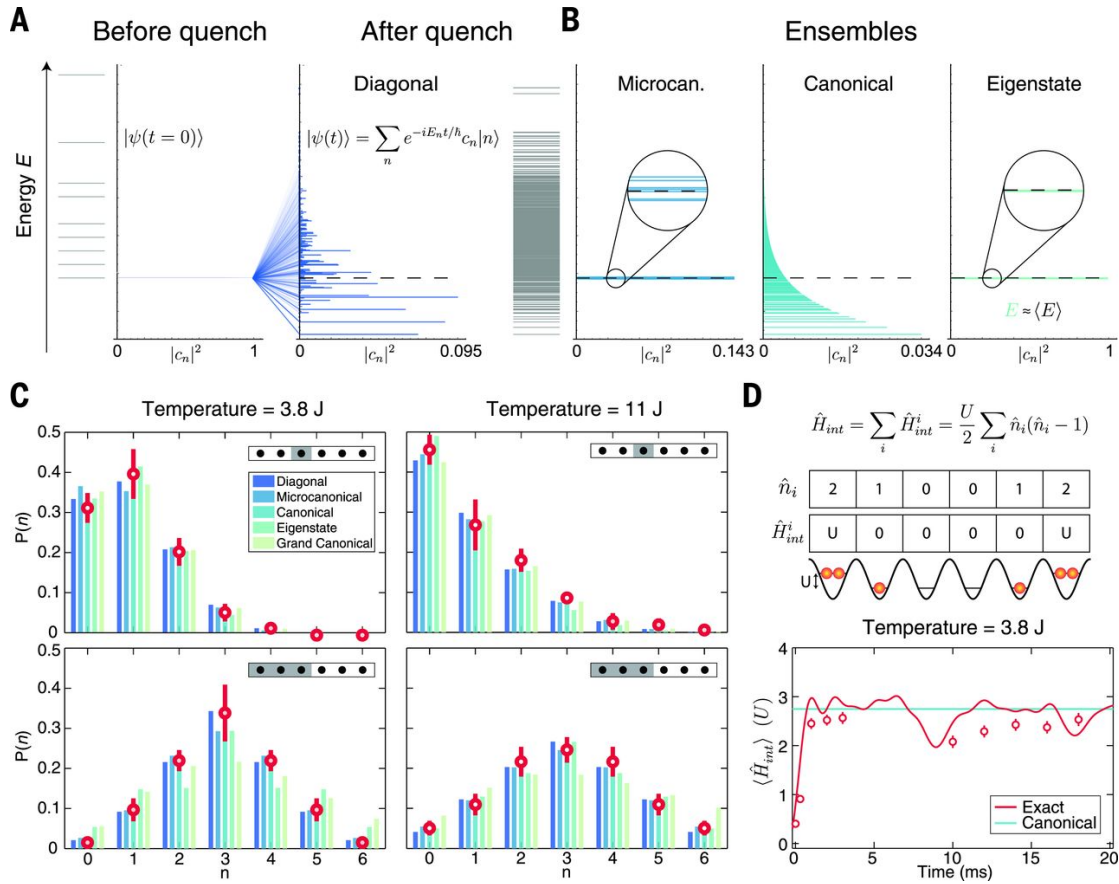


Figure 1.3: Analysis of local observables in a state after a global quench. (A) The ground state of the initial system quenches to a large number of eigenstates of the new Hamiltonian. The system is then evolved. (B) Measures show that the expectation value of observables agrees with the corresponding statistical ensembles. (C) The number statistics suggest thermalization for several temperatures. (D) The interaction energy is found to thermalize in agreement with the numerical simulation. From [Kaufman et al. \(2016\)](#). Reprinted with permission from AAAS.

experiment with a “quantum Newton’s cradle” in Fig. 1.4. The observed revivals are attributed to the system being close to an integrable point. The conserved quantities prevent the system from thermalizing.

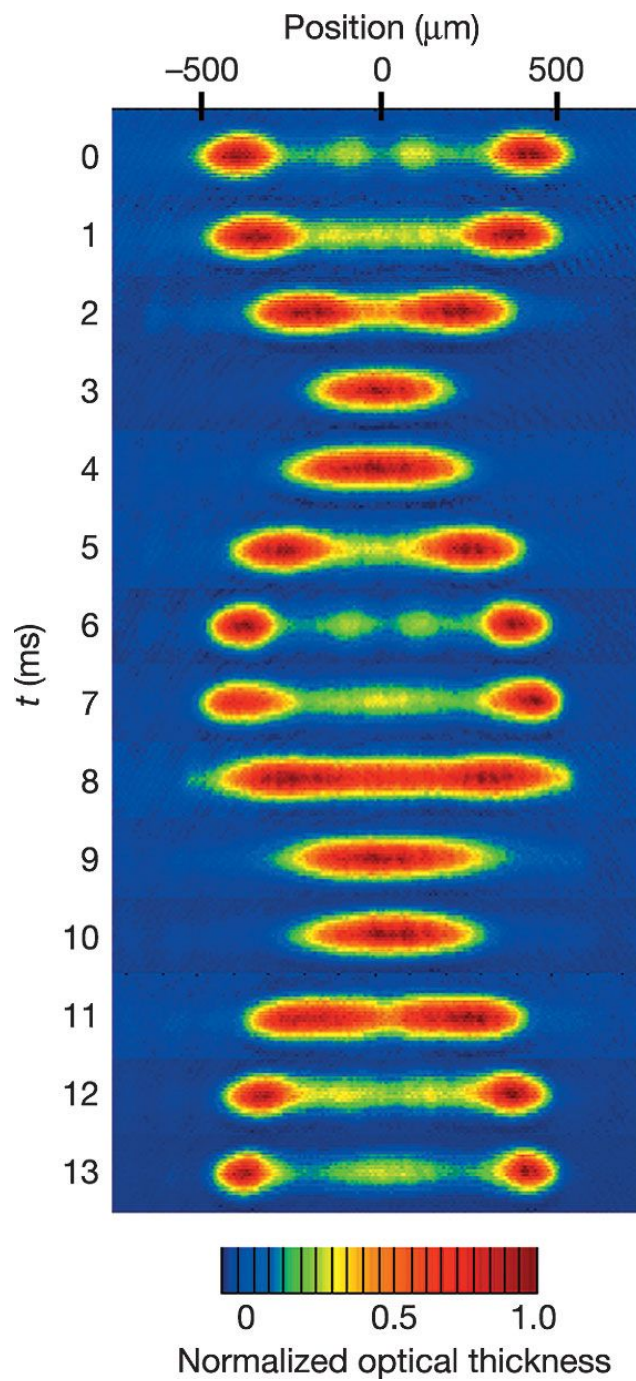


Figure 1.4: A quantum Newton's cradle. In this experiment, the momentum distribution is measured using time-of-flight adsorption images. It does not show any sign of thermalization due to the integrability of the system. From [Kinoshita et al. \(2006\)](#). Reprinted with permission from Springer Nature.

1.4 Theoretical descriptions of quantum many-body systems

As explained before, the theoretical description of a quantum many-body system is often very challenging. To render the problem more feasible, one can simplify the system to an effective model, which is valid in the scale that contains the relevant physics. In general, it is most desirable to find an analytical solution, but this is only possible for a few systems. And almost all the solvable models are defined over one-dimensional lattices.

In the following, a short list of methods, which are employed to study different physical phenomena in quantum systems, is given.

Analytical methods for quantum many-body systems at non-equilibrium are challenging. As mentioned before, there is the class of integrable models (solvable models), which are models that have an extensive number of conserved quantities, which can be exploited to find an explicit or implicit analytical solution (Bethe 1931). Another analytic method is the Keldysh formalism, which allows for the derivation of quantum kinetic equations (Kamenev and Andreev 1999). With the progress in the development of modern computers numerical methods have seen wide application. A method, which does not make any approximations, is the exact diagonalization technique (ED). In this method, the entire Hamiltonian is constructed and diagonalized such that all the eigenenergies and eigenstates are available. Using these, all desired properties can be calculated. The backside of this method is that only small systems are feasible, because the exponential growth of the Hilbert space leads to challenges with disk space and computer time. The exact diagonalization method is used in this work and presented in detail in Chapter 4. Other numerical methods are the Density Functional Theory (DFT), which aims at computing complex crystal structures (Hohenberg and Kohn 1964; Kohn and Sham 1965) or the Density Matrix Renormalization Group technique (DMRG) to model mostly ground state properties (White 1992, 1993; Schollwöck 2011; Manmana et al. 2005; Schollwöck 2005). While the former method can include assumptions, which are hard to check, the latter method suffers from the constraint that in time-dependent calculations it is hard to reach long times due to the growth of the entanglement in the system (Daley et al. 2004a; White and Feiguin 2004; Vidal 2004; Manmana et al. 2007). Another class of methods are stochastic methods like Quantum Monte Carlo, which has been successfully applied for different models (McMillan 1965; Suzuki 1993; Foulkes et al. 2001; Kolorenč and Mitas 2011). However, since this method may suffer from the infamous sign problem, which limits the accessible times (Troyer and Wiese 2005), the application is more successfully for bosons. Overall, it must be decided on a case by case basis, which method serves the best.

1.5 Outline and main results of this work

This thesis addresses the question of thermalization in closed quantum many-body systems. It answers the question whether it is possible to extend the reasoning of Deutsch to generic microscopic many-body Hamiltonians (Deutsch 1991). The extensive numerical analysis presented in this work supports the hypothesis that this is indeed possible.

The remainder of this thesis is organized as follows: The next chapter covers the theoretical background and previous achievements in the context of thermalization in closed systems. This starts from the treatment of classical systems and the definition of ergodicity, continues with semi-classical approaches and concludes with an explanation of the Eigenstate Thermalization Hypothesis and Deutsch's work. Following this, Chapter 3 states the main idea and discusses what observations are necessary to justify it. In addition, the method, which is applied to address the problem is outlined. In Chapter 4 the considered model and its representation is presented. It is followed by an introduction of the various algorithms to solve the flow equation and its implementations. Finally, it treats the exact diagonalization procedure and exploited symmetries. The main results of this work are then presented in Chapter 5 which is divided into a part about the Hamiltonian and a part about the observables. Finally, this work concludes with Chapter 6, which discusses the findings and suggests future projects.

Chapter 2

Thermalization in isolated systems

For the purposes of this thesis, “Thermalization” is defined to be the process of equilibration of an isolated system at non-equilibrium to a thermal state. The thermal state can be understood as the asymptotic state, which can be described by only a few macroscopic variables like the total energy. Other definitions define the thermal state to be the state, which is described by the means of statistical physics.

Thermalization is a very intriguing phenomenon, because, on first sight, it touches the very foundations of physics. The main motivation for the development of physics is to obtain the ability to predict a system’s behavior in the future from knowing its current state. In this sense, it is widely accepted that, if the laws of physics are correct and all relevant microscopic interactions and processes within the system and with its environment are taken into account, the initial knowledge is enough to make predictions about the *time evolution* of the system. Despite the technical impossibility to solve equations for a macroscopic piece of matter with 10^{23} atoms or particles, it is believed that, in principle, the physics are correctly described.

It turns out, though, that measurements of macroscopic properties (*observables*) do not depend on the precise knowledge of all microscopic constituents before the experiment starts. A box of particles, where all particles are confined to one half, will mix *irreversibly* to a state with an isotropic density over time, even, if one repeats the exact experiment with some or even all particles moved slightly. In general, one observes that, if an experiment runs longer and a thermal state has been reached, it is not possible anymore to find out anything about the initial state except for a few conserved quantities like the total energy. Macroscopically, it seems as if the system has *forgotten* the information about the initial state. It is the independence of the microscopic details of the initial state, which leads to an identical behavior on the macroscopic scale after thermalization. This observation contains the essence of thermalization and shows the close connection to *irreversibility* and the Second Law of Thermodynamics, which, in rudimentary terms, defines a direction of the time flow.

However, the process of thermalization in quantum systems has not been satisfactorily understood, yet. Historically, it remained a mystery for long times what systems do thermalize or what do not. To understand this in more detail one usually begins by

analyzing the universal behavior of the dynamics, e. g. after a quantum quench, and what properties the equilibrated state has, if there is any (Polkovnikov et al. 2011). Any thorough understanding of thermalization must eventually explain why some systems, like the ones that feature many body localization (MBL) do not thermalize, whereas other systems seem to do so (Geraedts et al. 2016). In this sense, it is the goal to have an unambiguous method to clearly distinguish both classes (Deutsch 2018).

The thermal state, which, if the system thermalizes, defines the asymptotic endpoint of the time evolution, depends on the degree of isolation of the environment. The most isolated thermal state is given by the microcanonical ensemble, where neither energy nor particles can be exchanged with the surrounding world. If a bath is added, such that energy can move from or to the system, the corresponding ensemble is given by the canonical ensemble. Finally, an additional particle exchange leads to an asymptotic behavior as given by the grand canonical ensemble.

To understand thermalization in its most profound case one is usually interested in the completely isolated case as predicted by the microcanonical ensemble. This is, because, for a system *with* an attached bath, one could ask how thermalization occurs for the extended system that consists of the initial system *plus* the bath and thus one would end up with an isolated system again.

Although any experiment in the real world will always be connected to its environment, because perfect isolation is impossible, this thesis only treats the latter case of perfectly isolated systems. Finally, if thermalization is understood for the isolated system, it is, in general, possible to reconstitute the other two cases by splitting the system into parts and treating one of them as the bath.

Although the concepts for understanding thermalization in isolated classical or quantum systems share similarities, they also display differences. One major difference concerns the “loss of information”: In the classical treatment the system initially contains much information about the degrees of freedom (e. g. particle positions and velocities). The description of a thermal state, however, only requires few parameters like the total energy. It follows that over the process of thermalization the system “loses” information, but the question remains how this is possible. One widely accepted explanation involves the concepts of ergodicity and mixing.

In quantum mechanics the loss of information corresponds to the independence of the thermal state from the initial preparation. Many different preparations yield an identical thermal state after a long time evolution. Since ergodicity and mixing are not concepts, which can be straightforwardly extended to genuine quantum systems, the major question arises, how this can be understood. Hence, one finds that the essential questions of thermalization are how a thermal state can be reached through a unitary time evolution, which is time-reversal invariant, and what systems do thermalize and what do not.

This consideration hints at the fact that the description of thermalization is fundamentally different in the classical and quantum regime, because the underlying mathematical formulation bases on an entirely different foundation. In classical

systems, the thermal state is believed to be formed over the course of time, whereas in quantum systems it must be encoded in the energy eigenstates. And although the understanding is far from complete for both cases, the next two parts are intended to give an overview about some of the similarities and differences when studying thermalization in the classical and quantum regime (Jaynes 1957a).

There are many reviews and books about this topic which discuss the topic in varying elaborateness, e.g. Balescu (1975); Reichl (1980); Wallis and Gutzwiller (1990); Balian et al. (2006); Uffink (2006); Gallavotti (2013) for classical systems and e.g. Polkovnikov et al. (2011); Eisert et al. (2015); Gogolin and Eisert (2016); D'Alessio et al. (2016) for quantum systems. The following parts combine and summarize the content of some of them.

2.1 Thermalization in classical systems

In classical systems, thermalization is related to chaos, ergodicity and mixing (Lebowitz and Penrose 1973; Lichtenberg and Lieberman 1992; Cvitanovic et al. 2005; Singh 2013). This topic, however, remains full of controversies and disagreements. This brief section is intended to present these concepts to better understand the differences and similarities to the quantum case, which understanding is heavily motivated by its classical counterpart. To do this one imagines a classical situation: particles in an isolated container. The only constraints are the spatial borders and the conservation of the total energy. The interaction among the particles is governed by an idealized Hamiltonian $H(\mathbf{p}, \mathbf{q})$, which depends on the canonical or generalized coordinates \mathbf{q} and conjugated momenta \mathbf{p} of all involved particles. The initial state of the system is then defined by a point in the phase space. The Hamiltonian governs how this point evolves in time under the given constraints. Statistical physics then provides the procedure for a probabilistic analysis: one defines a fictitious microcanonical ensemble as a joint probability density function in phase space. It includes all points in phase space that obey the constraints and every member of the ensemble is assumed to have the identical probability, if it falls within the energy constraint. This is to ensure that the average value stays constant over time. As it turns out, this construction agrees very well with experiments. The reason for this remains unclear so far. Two different lines of thoughts have been proposed to explain the underlying physics. One is based on *dynamical chaos* and *ergodicity* and the other one on a *typicality argument* (D'Alessio et al. 2016).

The first is based on the concept on *ergodicity*, namely in the form of the *ergodic hypothesis* (Penrose 2005). The ergodic hypothesis states that every possible region of the phase space will be covered over the course of the dynamics and that the time spent in each region is proportional to its volume. It follows that the time average is equal to the ensemble average. For a few systems this way of reasoning was proved, e.g. the Sinai billiard (Sinai 1963, 1970) and the Bunimovich stadium (Bunimovich 1979) (see Fig. 2.1). However, for other systems the ergodic hypothesis is not fulfilled. These

systems have an extensive number of conserved quantities and are called *integrable* systems.

The second explanation is called the *typicality argument*. If one assumes that all microstates in the set, which yields an identical macroscopic observation, have an identical probability, then one can say that the number of *typical* states is vastly larger than the number of *atypical* states. An example for an atypical state is the state, where all particles in a box are confined to one side (D'Alessio et al. 2016). As a consequence, one would often see atypical states to evolve to typical states.

To get a more general formulation the construction includes a range of total energies of width $2\Delta E$ around the peak E_0 .

$$\rho_{\text{mc}}(\mathbf{q}, \mathbf{p}) = \frac{1}{h^N C} \frac{1}{W} f\left(\frac{H - E_0}{2\Delta E}\right) \quad (2.1)$$

where $f(x)$ is a sharply peaked function with width $2\Delta E$, H the Hamiltonian of the system which returns the total energy, h a constant which defines the volume of a single phase point and C an over-counting factor. With this definition, it is possible to study the expectation value of a classical *observable* $O(\mathbf{q}, \mathbf{p})$ with respect to the ensemble. The so-called *ensemble average* $\langle \cdot \rangle_S$ is given as the average over the entire set of phase points of the ensemble

$$\langle O(\mathbf{q}, \mathbf{p}) \rangle_S = \int O(\mathbf{q}, \mathbf{p}) \rho(\mathbf{q}, \mathbf{p}) d\mathbf{q} d\mathbf{p} \quad (2.2)$$

The *ergodic hypothesis* then states that *Ergodicity* means that for most initial states the long-time average covers the phase space uniformly (Boltzmann 1872; Ehrenfest and Ehrenfest 2002). From this follows that the infinite-time average "equals" the statistical prediction, which is given by the average over many initial states (Gogolin and Eisert 2016). Other motivation for the ergodic hypothesis is that almost all microscopic states lead to the same values of the macroscopic observables. This means that different configurations in phase space do not differ in measurements, although they contain microscopic variations. Despite these successes, several problems have not been resolved: experiments seem to thermalize much faster than the exponential amount of time needed to explore all regions of the phase space. Secondly, the ergodic hypothesis makes statements about long-time averages instead of instants in time after a long-time. This is sometimes called thermalization in a *weak sense*.

2.2 Thermalization in quantum systems

Quantum systems are fundamentally different from classical systems. It is therefore not at all obvious, whether and how the concepts of thermalization in classical systems translate to the quantum case. Since thermalization in classical systems is understood

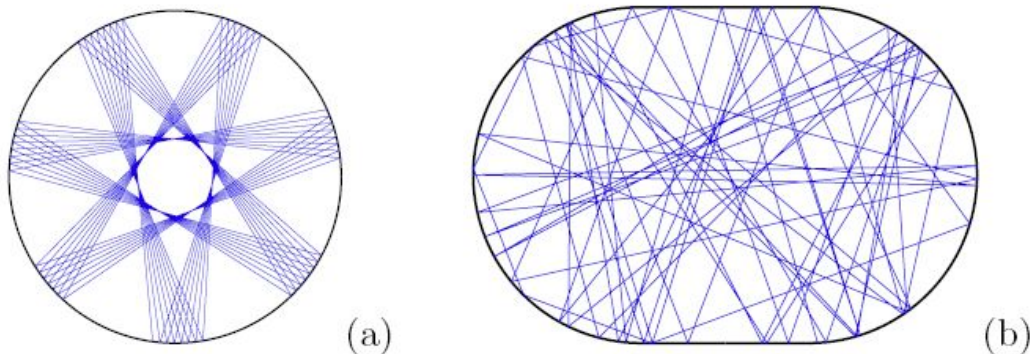


Figure 2.1: Classical trajectories of a billiard moving inside of two different two-dimensional cavities. **(a)** If the shape of the cavity is circular there are two conserved quantities: the total energy and the angular momentum. Since the number of integrals of motion matches the number of degrees of freedom the system is said to be *integrable*. It follows that the uniform population of the phase space is prevented. The system is regular and *non-ergodic*.

(b) If the shape of the cavity is the Bunimovich stadium, there is no additional integral of motion such that the model is *non-integrable*. All phase space points with a matching total energy are evenly covered over time. The system is chaotic and *ergodic* (Bunimovich 1979). Reprinted from Stöckmann (2010).

with the concept of ergodicity and deterministic chaos, the attempt to extend these notions to quantum systems seems natural. However, as will be explained in the following, it is not immediately clear how to define *quantum ergodicity* or how to define *quantum chaos*. The main difference between classical and quantum systems resides in the respective definitions of a microstate and the phase space. A point in the classical phase space, which is denoted as a microstate, is described by generalized coordinates and conjugated momenta of all involved degrees of freedom. Quantum systems on the other hand obey Heisenberg's *uncertainty relation*, which states that no simultaneous measurements of the positions and momenta are possible with arbitrary precision. As a consequence, a point in phase space is not well defined and therefore the canonical phase space does not exist. One attempt to fix this is to construct a semi-classical phase space of eigenstates of the Hamiltonian instead. This is known as the "Wigner-Weyl formalism" and explained in more detail in Section 2.2.3. While it offers more insight into the thermalization processes in quantum systems that do have a classical limit pendant, it does not provide an understanding of genuine quantum systems, where the classical limit is not known.

As it turns out, a possible solution to this, which also finds plausible arguments, is that the thermal properties are encoded in each eigenstate. This is the main idea of the Eigenstate Thermalization Hypothesis and is explained in more detail in Section 2.2.2. Overall, it remains an intriguing question how a quantum state, defined by a wave function, can be explained to thermalize. It has already been pointed out by Neumann (1929) that one should rather study observables, i. e. the operators describing a

measurement, which act on a quantum state as becomes clear in the later chapters.

Interestingly, it turns out that this question not only appears in the research of condensed matter (Kollath et al. 2007; Eckstein et al. 2009; Moeckel and Kehrein 2010), but also in other fields like cosmology (Kofman et al. 1996; Podolsky et al. 2006) and high-energy physics (Berges et al. 2004; Braun-Munzinger et al. 2001).

The generic setting is to consider the non-trivial unitary time evolution of an initial state of the system after a global quench. Although there are phenomena like recurrences, the study of time-evolved observables show equilibration. To understand why thermalization in quantum systems requires certain conditions to be met, one can start with the time evolution of an isolated pure state. Every finite dimensional Hamiltonian can, in principle, be brought into a diagonal form, if the chosen basis consists of the energy eigenstates.

$$H |E_m\rangle = E_m |E_m\rangle \quad (2.3)$$

$$H = \sum_m E_m |E_m\rangle \langle E_m| \quad (2.4)$$

If this basis is used to express any quantum state $|\psi\rangle$ at time $t = 0$ via

$$|\psi(0)\rangle = \sum_m \underbrace{\langle E_m|\psi(0)\rangle}_{c_m} |E_m\rangle, \quad (2.5)$$

the calculation of the general solution of the Schrödinger equation (Eq. (1.6)) for $t \geq 0$ is trivial:

$$|\psi(t)\rangle = e^{-iHt} |\psi\rangle = \sum_m e^{-iE_m t} c_m |E_m\rangle. \quad (2.6)$$

It is evident that the density matrix $\rho(t) = |\psi(t)\rangle\langle\psi(t)|$ will always remain pure ($\rho^2(t) = \rho(t)$) at all times. Hence, $\rho(t)$ can never become a thermal density matrix of the appropriate ensemble ρ_{mc} . However, already von Neumann realized that it is *observables* and not wave functions that are measured in experiments, such that the study of thermalization needs to focus on those quantities (Neumann 1929). A time-evolved observable in the energy eigenbasis reads

$$O(t) = \langle\psi(t)|O|\psi(t)\rangle = \sum_{m,n} c_m^* c_n e^{i(E_m - E_n)t} O_{mn} \quad (2.7)$$

$$= \sum_m |c_m|^2 O_{mm} + \sum_{m,n \neq m} c_m^* c_n e^{i(E_m - E_n)t} O_{mn} \quad (2.8)$$

where $O_{mn} = \langle E_m|O|E_n\rangle$ denotes the EEV. Studying this equation in more detail, one notices that the time evolution leads to a dephasing among the energy eigenstates (assuming no degeneracies), whereas the diagonal part is constant over time. In a long-time average $\langle \cdot \rangle_t$ only the first term, which is defined via the *DE* where

$$\rho_{\text{DE}} := \lim_{t_0 \rightarrow \infty} \frac{1}{t_0} \int_0^{t_0} \rho(t) dt = \sum_m \rho_{mm} |E_m\rangle \langle E_m|, \quad (2.9)$$

survives, such that

$$\langle O(t) \rangle_t = \sum_m |c_m|^2 O_{mm} = \text{Tr}(\rho_{\text{DE}} O). \quad (2.10)$$

Hereby, it is assumed that no degeneracies are present in the system. Moreover, it is clear that *if* a system thermalizes, it *must* thermalize to the long-time average value. An observable is defined to thermalize, if the average expectation value of this observable matches the microcanonical ensemble value after some time *and* if it then stays close to it for most later times. From Eq. (2.8), it becomes clear that this can only be achieved, if the diagonal matrix elements agree with the microcanonical ensemble and if the off-diagonal matrix elements are quasi vanished. It is immediately clear, though, that the diagonal ensemble strongly depends on the initial, state via the coefficients c_m . This is a major difference to the classical picture, where the time average only depends on the total energy. Hence, it remains to be explained how the diagonal ensemble can agree to the microcanonical ensemble, which is independent of the initial state (Rigol et al. 2008). This is the major question of thermalization in quantum systems. Several ways of thought have been proposed; some are presented in Section 2.2. The most promising ideas have culminated in the *Eigenstate Thermalization Hypothesis (ETH)*, which is explained in the next section. As it turns out, the hypothesis requires an exponentially small average level spacing as it is present in systems with an extensive number of degrees of freedom (Deutsch 2018).

Finally, there remains another major difference between classical and quantum systems: in quantum systems not every generic observable will thermalize. This can easily be seen by considering the projection operator onto an energy eigenstate, which does commute with the Hamiltonian. Therefore, it is a constant of motion as any other function of the Hamiltonian. This can also be seen from the set of coefficients $c_m = \langle E_m | \psi(0) \rangle$, which appear in the time-evolved state in Eq.(2.6). Analogously to classical conserved quantities, they will not change over time even in classically chaotic systems. In other words, there are many additional integrals of motion, which do not appear in the classical case.

2.2.1 Strong vs. weak thermalization

It turns out that, in quantum systems, thermalization can happen without time-averaging (Srednicki 1994). It follows that it is important to distinguish two different situations. The first one, which is called *strong thermalization*, means that the observable evaluated after a long time

$$O(t) \rightarrow O_{\text{micro}} \quad (2.11)$$

thermalizes, i. e. agrees with the microcanonical ensemble value, and remains close to it for most times (recurrences at exponentially long (in the number of degrees of freedom) times are not relevant in macroscopic systems. This is what is mostly seen

in experiments (D'Alessio et al. 2016). The other case is called *weak thermalization*, which only makes statements about the long-time average

$$\bar{O}(t) := \lim_{t_0 \rightarrow \infty} \frac{1}{t_0} \int_0^{t_0} dt O(t) \rightarrow O_{\text{micro}}. \quad (2.12)$$

Strong thermalization implies weak thermalization.

2.2.2 Eigenstate Thermalization Hypothesis (ETH)

Historically, it was Neumann (1932), who studied the thermalization in generic quantum systems first and who pointed out that it is observables, which one must analyze. The analytic calculation for the time-evolved observable yields Eq. (2.12). Therefore, it becomes clear that thermalization can only occur if the diagonal ensemble average equals the microcanonical ensemble and the off-diagonal contributions are negligible. This, however, leads to questions that need to be answered, e. g. how the information of the initial state encoded in the c_m can be “lost”? Secondly, in many-body systems with an exponentially small level spacing, how long does one have to wait until the fluctuations average out (D'Alessio et al. 2016)?

A major development in the understanding of quantum thermalization was the ansatz for the mechanism behind it. It was achieved by Deutsch (1991) and then Srednicki (1994, 1996, 1999). Their culminated in the ansatz, which known under the name Eigenstate Thermalization Hypothesis (ETH), and which comes in a mathematically very precise form. It states that the matrix elements of observables in the eigenbasis of a Hamiltonian H are given by

$$O_{mn} = \langle E_m | O | E_n \rangle = O(\bar{E})\delta_{mn} + e^{-S(\bar{E})/2} f_O(\bar{E}, \omega) R_{mn}, \quad (2.13)$$

where $\bar{E} = (E_m + E_n)/2$ denotes the average, $\omega = E_n - E_m$ the difference of the eigenstates and $S(\bar{E})$ is the thermodynamic entropy at energy \bar{E} (which scales linear with system size) (D'Alessio et al. 2016). Furthermore, the two functions $O(\bar{E})$ and $f_O(\bar{E}, \omega)$ are smooth functions, and $O(\bar{E})$ agrees with the microcanonical expectation value. Lastly, R_{mn} is a random number with zero mean and unit variance.

It is believed that ETH holds for few-body observables (Rigol et al. 2008; Biroli et al. 2010; Rigol and Srednicki 2012) (see also (Hosur and Qi 2016)). Some authors argue that ETH holds for all observables, if the support of the observable is small compared to the system size (Garrison and Grover 2018). The conjecture corresponds to saying that the reduced density matrix of a high-energy eigenstate, where the complement of the operator's support has been traced out, is given by the density operator of a canonical (or in some cases microcanonical) ensemble at the same energy (Garrison and Grover 2018). It follows that a single high-energy eigenstate already encodes all thermodynamical properties of the system at that temperature. In other words, in the intuitive picture, one can understand thermalization as the effect that the subregion of a few-body operator is thermalized by the the rest of the system, which acts as the

environment.

ETH implies that the expectation values of few-body observables in isolated quantum systems at non-equilibrium relax to the value, which is predicted by statistical physics (D'Alessio et al. 2016). Inserting the ansatz Eq. (2.13) into Eq. (2.8) and the definition of the microcanonical ensemble shows that both side agree:

$$\langle O(t) \rangle_t \approx O(\langle E \rangle) \approx \langle O \rangle_{mc}, \quad (2.14)$$

Moreover, the form of the off-diagonal matrix elements assures that the fluctuations remain small. ETH can also be used to solve the paradox, how the information about the initial state can be lost in a unitary time-evolution. The solution is that the information is not lost, but it is spread over the entire system, which makes it inaccessible for local measurements. Small subsystem, however, can thermalize, because the remainder of the isolated system acts as the reservoir. ETH implies that the initial state has already thermal properties on the level of the energy eigenstates. This was phrased as “every eigenstate is thermal” (Srednicki 1999). For a window of many eigenstates, one then basically can define an ensemble of single state energy eigenstates (Nandkishore and Huse 2015).

ETH has been successfully verified for a variety of discrete quantum systems in 1D systems (Rigol et al. 2008; Rigol 2009b; Santos and Rigol 2010b; Rigol and Santos 2010; Steinigeweg et al. 2013; Ikeda et al. 2011; Dubey et al. 2012; Beugeling et al. 2014), 2D systems (Mondaini et al. 2016) and for semi-classical systems (Feingold and Peres 1986a; Feingold et al. 1989a). The earliest numerical results were obtained by Jensen and Shankar (1985) for quantum spin systems (later also (Bohigas et al. 1984)). However, the strong limitations in the computing power and memory available at that time only allowed for small system sizes and hence a clear understanding of the difference of integrable and non-integrable systems was not possible. More recent numerics are not only able to clearly distinguish the two cases, but they also seem to indicate that strong ETH is valid (Kim et al. 2014).

The systems, which are not expected to thermalize, fall into two groups: integrable systems and systems, which show Many-Body Localization (MBL). Integrable systems have an extensive number of conserved quantities, which prevent thermalization, such that they equilibrate to the GGE instead (Rigol et al. 2007; Cassidy et al. 2011; Caux and Essler 2013)). Therefore, integrable systems do not fulfill ETH. The other group are systems, which show Many-Body Localization (MBL). This is partially understood for fully MBL (FMBL) by the construction of conserved charges (Serbyn et al. 2013a,b; Huse et al. 2014). For systems, which show weak disorder, however, ETH seems to be valid (Pal and Huse 2010).

It is helpful to compare Eq. (2.13) to the prediction of a full random Hamiltonian matrix of dimension \mathcal{D} . If the Hamiltonian is fully random, its eigenstates consist of Gaussian distributed entries, which as a whole fulfill the orthonormality condition. The expression for the matrix elements of a local observable is then found to be

$$O_{mn} \approx \delta_{mn} \frac{1}{\mathcal{D}} \sum_i O_i + \sqrt{\frac{O^2}{\mathcal{D}}} R_{mn}, \quad (2.15)$$

where R_{mn} denotes a random number with a vanishing average and unit variance (variance is 2 if the Hamiltonian is drawn from the GOE, see below). By comparing this expression with Eq. (2.13), it is clear that the radical fully random ansatz is extreme in the way that the diagonal ensemble value does not depend on the index m and that therefore the thermalization is reached, because the average of the observable can be pulled out of the sum in Eq. (2.10) and the dependence on the initial state vanishes.

2.2.3 Semi-classical approach I: Berry's conjecture

Important works in the topic of thermalization have been the semi-classical approaches (Berry 1977b,a; Srednicki 1994). Their aim is to use the understanding of classical chaos to understand the chaos in quantum physics. The main idea is to extend the concept of phase space to the quantum world, which has been in the 1940's (Groenewold 1946; Moyal 1949). Both approaches base on ideas first put forward by Weyl and Wigner, which is why this formalism is called Wigner-Weyl formalism (Weyl 1927; Wigner 1932). The important quantity is the Wigner function, which is the Wigner-Weyl transformation of the density operator. It plays the role of the probability distribution in phase space (Polkovnikov 2010). For a pure state, one finds

$$W(\mathbf{x}, \mathbf{p}) = \frac{1}{(2\pi\hbar)^{3N}} \int d^{3N}\xi \psi^* \left(\mathbf{x} + \frac{\xi}{2} \right) \psi \left(\mathbf{x} - \frac{\xi}{2} \right) \exp \left[-i \frac{\mathbf{p}\xi}{2} \right], \quad (2.16)$$

with \mathbf{x}, \mathbf{p} are the coordinates and momenta of the N particles, which span the $6N$ -dimensional phase space (D'Alessio et al. 2016). Using Eq. (2.16), one can calculate expectation value for observables via

$$\langle O \rangle = \int d^{3N}x d^{3N}p O_W(\mathbf{x}, \mathbf{p}) W(\mathbf{x}, \mathbf{p}), \quad (2.17)$$

where O_W is the Wigner-Weyl transform of the Observable (D'Alessio et al. 2016)

$$O_W(\mathbf{x}, \mathbf{p}) = \frac{1}{(2\pi\hbar)^{3N}} \int d^{3N}\xi \left\langle \mathbf{x} - \frac{\xi}{2} \left| O \right| \mathbf{x} + \frac{\xi}{2} \right\rangle \exp \left[-i \frac{\mathbf{p}\xi}{2} \right]. \quad (2.18)$$

Berry's conjecture now states that the high-energy wave functions in a time-reversal invariant and ergodic system, i. e. where the classical counterpart is chaotic, are superpositions of random plane waves

$$\left\langle \psi^* \left(\mathbf{x} - \frac{\mathbf{s}}{2} \right) \psi \left(\mathbf{x} + \frac{\mathbf{s}}{2} \right) \right\rangle = \frac{1}{\Omega} \int d^{3N}p \exp \left[\frac{i}{\hbar} \mathbf{p}\mathbf{x} \right] \delta(E - H(\mathbf{x}, \mathbf{p})), \quad (2.19)$$

where $H(\mathbf{x}, \mathbf{p})$ is the classical Hamiltonian, E the energy of the eigenstate and $\Omega = \int d\mathbf{x} d\mathbf{p} \delta(E - H(\mathbf{x}, \mathbf{p}))$ (Berry 1977b). Using this expression in Eq. (2.17) means taking the ensemble average over eigenstates, which condenses to the microcanonical average. This can be regarded, in essence, as a semi-classical version of the ETH.

One famous application of Berry's conjecture was the analytical thermalization study of Srednicki (1994) for a hard sphere gas, who was able to demonstrate thermalization and to derive the Maxwell-Boltzmann, Fermi-Dirac or Bose-Einstein distribution, depending on the symmetries.

2.2.4 Random matrix theory and level statistics

A field that is nowadays widely applied in physics and, in particular, in the context of thermalization and the study of chaotic behavior is random matrix theory (RMT) (Forrester et al. 2003). The quintessential paradigm is that a real deterministic system is modeled by the average behavior of an *ensemble* of random matrices, which are formed according to a set of parameters to display certain statistical properties.

A fundamental cornerstone of quantum mechanics by Wigner states that any symmetry operator of a Hamiltonian is either unitary or antiunitary (Wigner 1931). A very important example for the latter is certainly the time reversal operation¹. This understanding was used to define the two major types of a random matrix ensemble (RME), i. e. a matrix which elements are random variables, which are the *invariant RME* and the *non-invariant RME* (Leitner and Cederbaum 1993). The first is invariant under basis transformations $H \rightarrow UHU^{-1}$ with a real orthogonal matrix U , which is why their probability density is given as $p(H) \propto \exp(-\text{Tr } V(H))$, where $V(H)$ is an arbitrary function, which is analytic in $H = 0$. One important version of this is given by

$$p(H_{ij}) = A \exp\left(-\frac{1}{4a} \left(\sum_i H_{ii}^2 + 2 \sum_{i<j} H_{ij}^2 \right)\right) \quad (2.20)$$

and denotes the famous Gaussian orthogonal ensemble (GOE) defined by Wigner and Dyson (also called Wigner-Dyson ensemble) (Mehta 2004). All H_{ij} , $k \leq j$ are statistically independent random variables, which are Gaussian distributed, i. e. $H_{ij}, H_{ii} \sim \mathcal{N}(\mu, \sigma^2)$, where $\mathcal{N}(\mu, \sigma^2)$ denotes the Gaussian (or normal) distribution with mean μ and variance σ^2 and a corresponding probability density function (PDF) $f(x) = 1/(\sigma\sqrt{2\pi}) \exp[-(x - \mu)^2/(2\sigma^2)]$. For different symmetries of H , i. e. hermiticity or self-duality one finds the corresponding Gaussian unitary ensemble or Gaussian symplectic ensemble (Tao 2012). Since the ensemble is invariant under basis transformations, one can bring the matrix H to diagonal form and express the probability density solely by the eigenvalues. One can derive the famous semi-circle law, which is given as the probability density distribution for the eigenvalues and reads

$$\sigma(x) = \frac{1}{2\pi} \sqrt{4 - x^2}. \quad (2.21)$$

Historically, this type of random matrices has first been devised for its use in multivariate statistics by Wishart (1928). The first application in physics, which later led to the name, was the seminal work by Wigner, who suggested that the energy level spacings in the spectra of heavy nuclei can be modeled by those of random matrices (Wigner 1951b; Lane et al. 1955). He realized that in the low-energy part of the spectrum, the complete picture is often desired, whereas in the high energy

¹This can be seen from the canonical commutator $[x, p] = i\hbar$, which is preserved under time reversal. Since a time reversal operation changes the sign of the momentum and leaves the position untouched, an additional complex conjugation is required to assure the invariance.

region, where density is high, it is sufficient to focus on statistical properties such that random matrices become viable (Wigner 1957b). He and others subsequently developed an extensive theory, which is nowadays known under the term RMT (see also the books on random matrix theory by Mehta (2004); Edelman and Rao (2005) and Tao (2012)).

Random matrix theory is a valid description of a real, i. e. deterministic, physical system, because the correlation between the "true" matrix elements of the Hamiltonian and the components of the initial wave function are negligible (Borgonovi et al. 2016). If the local level density is high enough, the superposition of neighboring energy eigenstates in the mean-field basis becomes complicated enough that a statistical description reveals universal features.

Beyond the aforementioned heavy nuclei, complex atoms (Porter and Rosenzweig 1960; Camarda and Georgopoulos 1983) and many-electron molecules (Haller et al. 1983), connections between random matrix theory and other topics of condensed matter theory have been successfully established, e. g. in the study of conductivity in disordered metals or of elastodynamic properties of structured materials (Mehta 2004) or in the form of a banded random matrix to study quantum chaos in the quantum-kicked rotor model (Izrailev 1990). Moreover, it has also been related to more exotic areas like the zeros of the Riemann ζ -function and two-dimensional quantum gravity (Forrester et al. 2003). Later on, it was Balian, who derived the Gaussian random matrix ensembles from minimizing the information entropy (Balian 1968).

Level statistics

In his seminal paper, Wigner found that the statistical analysis of the spectra ("level statistics") of certain random matrices offers a feasible way to describe the nuclei with their huge number of energy levels from a theoretical point (Wigner 1951a, 1955, 1957a). Wigner designed the random matrix as the sum of two parts: The equally spaced diagonal part is thought of describing the non-interacting nucleons in the heavy nuclei in the mean-field representation, whereas the off-diagonal banded part introduces the interaction between them. In this way, the banded Wigner matrix was invented. While the choice that H_{ij} are statistically independent is artificial, the second condition, that all $p(H_{ij})$ are invariant under basis transformation, i. e. $H \rightarrow U^{-1}HU$, is natural, because it gives all kinds of interactions equal weight (Dyson 1962d). 1 year after Wigner, the assumption for the level spacing on the diagonal of unperturbed was extended from constant (Wigner) to Poissonian distributed (Gurevich and Pevsner 1956). To describe the distribution of the spacing of neighboring levels Wigner derived the famous *Wigner surmise* (or Wigner-Dyson distribution), which reads

$$p_W(s) = \frac{\pi s}{2} e^{-\frac{\pi s^2}{4}}, \quad (2.22)$$

where $s = S/D$ is a level spacing S divided by the mean distance between levels D (Wigner 1957b). The key feature of Eq. (2.22) is the *level repulsion*. This means that for

small $s \rightarrow 0$ also $p_W(s) \rightarrow 0$. Dyson connected the Gaussian random matrix ensembles to the integrability of a model (Dyson 1962b,c). Later, the GOE predictions have been compared in detail with different experimental data of compound-nucleus resonances and found to agree satisfyingly, both showing the level repulsion (Haq et al. 1982; Bohigas et al. 1983). Moreover, it was shown that the level statistic as predicted by the GOE (Wigner-Dyson distribution) is consistent with the level statistic of the quantum Sinai's billiard demonstrating the universality of RMT also for a small number of degrees of freedom (Bohigas et al. 1984) (later also atomic levels have been analyzed (Rosenzweig and Porter 1960; Camarda and Georgopoulos 1983)). On the other hand, it has been shown for integrable systems with more than one degree of freedom that the level spacings are expected to be uncorrelated with a Poissonian distribution (Berry et al. 1977). Nowadays, the level statistics is the main indicator for the lack of integrability (Santos and Rigol 2010b). Level repulsion has also been demonstrated for quantum versions of the stadium (McDonald and Kaufman 1979) and Sinai billiard (Berry 1981), which are known to be chaotic classically.

Wigner's ansatz to model a system has not changed. Usually one designs the Hamiltonian to consist of an integrable system H_0 , to which an integrability-breaking term H_1 , which consists of random variables, is added:

$$H = H_0 + H_1 \quad (2.23)$$

The added *perturbation* H_1 can have different forms and properties. It can be described by a full or banded random matrix, sparse or not sparse, and can have a vanishing (quantum kicked rotor, (Izrailev 1988)) or non-vanishing diagonal (Feingold et al. 1991).

Banded random matrices have the advantage that they are thought to describe typical realistic models, because there is no infinite rank of inter-particle interaction (there is a maximal number $n < \infty$ of n -body interaction terms) (Izrailev 1995, 1990). Therefore, the eigenstates do not spread over the entire basis of H_0 . Full random matrix, however, can be regarded as an extension to banded random matrix theory (Bohigas 1991). Their description of real world models is hindered, because the level density has the nonphysical semicircle form. In the late 1990's Feingold et al. (1989b) showed how, for few-body Hamiltonians, banded random matrices appear in a semiclassical picture. In the following, this insight was extended to explain how semi-classical constraints create a level statistic, which assumes the Brody distribution, thereby connecting the banded random matrices with integrability (Feingold et al. 1991).

The idea was refined by many contributors to the important insight that the Hamiltonian in a "non-fine-tuned" basis looks random - a result, which predates the basic assumption of Deutsch's argument (see Section 2.2.5) (Porter and Rosenzweig 1960; Dyson 1962d,a,b). It is important to note that Wigner considered a genuinely quantum system and not a semi-classical limit.

Random matrix theory has allowed for a deeper understanding of the level statistics of many-body quantum systems. It showed that the analysis of the level statistics provides many insights about the system of study. In a system, where the matrix ele-

ments of the corresponding Hamiltonian are Gaussian distributed, the distribution of the level spacings features two generic properties: (1) it decays as a Gaussian for large energy spacings and (2) it features the so-called "level repulsion", i. e. the probability of two energy levels being very close together drops to 0.

Random matrix theory can also be used to determine the onset of quantum chaos (Bor-gonovi et al. 2016). In particular, it has been found that the distribution of the spacings of the energy eigenvalues ("energy levels"), also called "level statistic", is an immediate indicator for integrability and hence the question, whether the system thermalizes or not. They have been studied and compared to experimental data of realistic systems, for which they have served as a reference. To get the full understanding of the onset of thermalization, however, one needs to focus on the structure of the eigenstates. Hence, the level statistic can be thought of as a condensed version of the complementary information stored in the eigenstates.

2.2.5 Deutsch's argument

This part summarizes the reasoning by J. Deutsch, in this thesis also called *Deutsch's argument*, as published by Deutsch (1991). Extensive notes containing all the calculations have never been published, but are accessible online on his [website](#).

Historically, Deutsch's approach is the first analytic result in the context of ETH, even before the hypothesis was given a name. It is motivated by finding an analogue to classical ergodicity for quantum systems. However, in his work, Deutsch is not interested in establishing a semi-classical argument, but instead aims at considering genuine isolated quantum systems. Nevertheless, the terminology and the way of thinking is often based on the classical treatment of thermalization. More specifically, Deutsch asks what quantum analogue of ergodicity and chaos can be defined that ensure thermalization in generic, non-integrable systems. Moreover, he emphasizes that it is essential that any concept of the thermalization process must be able to distinguish these systems from integrable systems, which are thought to equilibrate differently (see GGE) (Deutsch 2018). His argument can be regarded as combining the concept of a random matrix

The case Deutsch considers is motivated by an *ideal gas*, where small random interactions are added. Classically, an ideal gas will not thermalize, because there are no interactions among the gas particles. However, by increasing their diameter to a finite value it can be assured that the entire phase space is covered over time, which leads to ergodicity and finally thermalization (see Section 2.1).

Deutsch's approach follows the same track by modeling the quantum system to consist of a diagonal integrable part ("ideal gas"), which describes the kinetic energy or "hopping" of particles, and a small perturbation, which is supposed to represent the interaction. This interaction is added in the form of a banded random matrix and renders the system to be non-integrable (Deutsch 2018). In the following analysis, he then shows that under certain conditions generic observables thermalize, i. e. agree to their microcanonical expectation values, if one averages over many different realizations of random matrices. As will be explained below, it turns out to be essential

to assume that the number of degrees of freedom is huge such that the level spacing is sufficiently small. Deutsch's argument has been refined by [Nation and Porras \(2018\)](#) and further extended by Reimann through several works ([Reimann 2015](#); [Reimann and Dabelow 2021](#)). The following part explains Deutsch's argument in greater detail.

In his paper [Deutsch \(1991\)](#) studies the question of thermalization for observables, since these are the quantities that are measured in experiments, as explained before. Instead of talking about thermalization, Deutsch uses the phrase "ergodicity", which he defines to mean that the expectation value of a time-averaged observable O agrees with the microcanonical ensemble value. Deutsch defines "ergodicity" by the agreement between the time average of the expectation value of an operator and the expectation value over a small energy window defined by the function $\Delta(E, E_m)$, which is sharply peaked where $E = \langle E_m | H | E_m \rangle$. The definition reads

$$\langle \langle \psi | O | \psi \rangle \rangle_t = \sum_m \Delta(E, E_m) O_{mm} \quad (2.24)$$

with the eigenstate expectation value $O_{mn} = \langle E_m | O | E_m \rangle$ as in Eq. (2.8). This is the essential equation, which one would like to derive.

The ansatz by Deutsch can be regarded as being motivated by earlier works using random matrices by Wigner and others (see Section 2.2.4) and by the semi-classical arguments, which experienced a lot of numerical evidence ([Berry 1977b](#); [Feingold and Peres 1986a](#); [Feingold et al. 1989a](#)). Like in the previous chapter, the assumption, which Deutsch makes, is that the model Hamiltonian H consists of a non-ergodic, integrable part H_0 , which, e. g., contains the hopping or kinetic energy of a large number of non-interacting particles ("ideal gas"), and an additional banded random contribution H_1 , which is a real symmetric matrix. Overall, he defines the Hamiltonian to be

$$H = H_0 + H_1 \quad (2.25)$$

The integrable part H_0 has a mean level spacing of ϵ . The H_1 part is introduced to make the system ergodic (in the sense of "non-integrable") and can be regarded as modeling the interaction among the particles (e. g. two-body interaction) ([Deutsch 2018](#)). However, instead of doing this in an explicit manner, Deutsch assumes a real symmetric matrix with its elements randomly taken from a GOE with zero mean and a variance σ^2 ([Reimann and Dabelow 2021](#)). In the integrable basis $|E_n^0\rangle$ the matrix elements of the integrability-breaking interaction term are given as

$$h_{mn} = \langle E_m^0 | H_1 | E_n^0 \rangle. \quad (2.26)$$

It is assumed that $h_{mn} \propto \exp(-\beta |E_m^0 - E_n^0|)$ for $\beta |E_m - E_n| \gg 1$. This can be motivated by semi-classical phase space arguments (see [Deutsch \(1991\)](#) and Appendix B in the corresponding unpublished notes) and is an often used way to mimic short-range interaction. It is important to note that the matrix elements are known and fixed, but sampled from the mentioned random ensemble. This idea follows along the lines of previous papers ([Berry 1977b](#); [Feingold and Peres 1986b](#); [Feingold et al. 1989a](#)).

The perturbation H_1 has the effect of mixing eigenstates of H_0 , which are close in energy. Even for a very small window, there will be an exponentially large number of eigenstates, which mix (Reimann and Dabelow 2021), so that one expects that the perturbation could be made smaller than the average level spacing of H_0 and still have a large effect. The assumption now is that the two basis of eigenstates mix in a small energy window with random phases. This is motivated by the work in the semi-classical realm of Berry (1977b), who conjectured that the eigenstates of H in the basis that diagonalizes H_0 are random superpositions. As phrased by Deutsch (2018): The typical eigenstate of a non-integrable system is the random superposition of integrable states in some narrow energy shell, such that with

$$|E_m\rangle = \sum_n c_{mn} |E_n^0\rangle, \quad (2.27)$$

the overlaps $c_{mn} = \langle E_m | E_n^0 \rangle$ are random, because H_1 is random. The ingenuity of Deutsch is that he was able to calculate the probability distribution for the elements c_{mn} and he showed that they are given by the Lorentzian

$$\Lambda(m, n) = \frac{1}{\pi} \frac{\pi \sigma^2 / \epsilon}{(m - n)^2 + \pi^2 \sigma^4 / \epsilon^2}, \quad (2.28)$$

such that

$$\langle c_{mn} c_{ij} \rangle_{\text{rand}} = \delta_{mi} \delta_{nj} \Lambda(m, n), \quad (2.29)$$

(see (Deutsch 1991; Deutsch; Reimann and Dabelow 2021)). To do this he assumed that the overlaps are statistically independent Gaussian random variables.

Then, under the assumption of self-averaging, one can express the EEVs of an observable in the basis of H as

$$\langle E_m | O | E_m \rangle = O_{mm} = \sum_{i,j} c_{mi} c_{mj} O_{ij}^0 \approx \sum_i \Lambda(m, i) O_{ii}^0, \quad (2.30)$$

which implies a smoothing of neighboring diagonal elements O_{mm} just as in the ETH (Deutsch 1991; D'Alessio and Polkovnikov 2013). O_{nn}^0 denote the EEV of the unperturbed system.

The question is, whether the Deutsch argument can provide the ETH prediction for off-diagonal matrix, as well. Since they average to 0, it is better to study the square modulus

$$|O_{mn}|_{m \neq n}^2 = \sum_{i,j} c_{mi} c_{ni} c_{mj} c_{nj} O_{ii}^0 O_{jj}^0. \quad (2.31)$$

Then, one finds that only some terms survive the double sum and it reads

$$|O_{mn}|_{m \neq n}^2 = \sum_{i,j} |c_{mi}|^2 |c_{ni}|^2 (O_{ii}^0)^2 \approx \sum_i \Lambda(m, i) \Lambda(n, i) (O_{ii}^0)^2, \quad (2.32)$$

which matches the ETH assumption (Reimann and Dabelow 2021). The above equation is only true, if one assumes uncorrelated coefficients c_{mi} , this condition, however, can be relaxed (Nation and Porras 2018).

With these results, one can finally tackle the time-evolution of an initial state, i. e. Eq. (2.24). Before studying the generic case for any initial state, the calculation focuses on the time evolution of an eigenstate of H : Since Eq. (2.10) predicts that the infinite time average is given by the diagonal ensemble, one can insert the Lorentzian into this equation and obtains the microcanonical average. Finally, one can use the sharply peaked property of Δ in Eq. (2.24) together with ?? to show the thermalization of the generic initial state. Interestingly, a similar result as Deutsch's has been derived by Wigner decades earlier (Wigner 1955; Reimann and Dabelow 2021). Finally, it remains to emphasize that his approach is special, because it is an ansatz, simple enough to be analytically tractable, that still allows for non-trivial results.

Furthermore, there is another numerical study addressing the question of thermalization in small Hubbard lattices, which show that the Hamiltonian can be modeled as a banded matrix (Genway et al. 2012).

Chapter 3

Microscopic justification of the Eigenstate Thermalization Hypothesis

This chapter explains the main goal of this thesis. Motivated by the findings of Deutsch as outlined in part 2.2.5 the idea is to extend the argument to generic microscopic Hamiltonians. This requires a thorough study of the Hamiltonian and few-body observables, which are accessible in experiments for different systems. The next part contains the main line of thought and how the theory can be verified by the results. It is followed by a brief explanation of the applied method: the *flow equation approach*.

3.1 Extending Deutsch's argument

In Section 2.2.5 the reasoning of Deutsch was presented in detail. The argumental chain, on which he builds up the analytical arguments for thermalization, base on the assumption that the Hamiltonian has the form of a banded random matrix (Deutsch 1991). He was then able to demonstrate that, for a large class of operators, thermalization can be shown (Deutsch 1991).

The hypothesis is that Deutsch's argument with the random matrix ansatz holds for a generic non-random quantum system defined by a microscopic Hamiltonian. However, to find general analytic arguments is a very hard problem. To quote P. Reimann: "Providing a more rigorous justification of this well-established common lore in random matrix theory is a long-standing, very difficult task [...]" (Reimann and Dabelow 2021). This project tries to justify the assumptions made by Deutsch in his argument using a numerical ansatz.

The idea of this project is that any Hamiltonian representing a generic system, which is usually set up in a designated basis (e. g. spatial basis), can be unitarily transformed to a different basis, in which it takes on a form as imagined by Deutsch. More precisely, the idea is that the Hamiltonian in the new basis takes on a banded form

with matrix elements that appear *as if* they were drawn from a Gaussian ensemble. In other words, it must be ensured that the matrix elements are pseudo-random with the demanded properties. It is, of course, possible to use a random unitary transformation to introduce the randomness in the Hamiltonian, but this does not lead to the banded form (see Fig. 5.4 in Chapter 5). So the first main challenge is to find a transformation, which has the desired effect on the Hamiltonian.

The second part of the argument deals with observables. Since it is believed that only few-body observables fulfill the ETH, which is the main concept of quantum thermalization, it is important to verify that the basis, which brings the Hamiltonian to a banded form, does not “destroy” few-body property of the observables. In order to do that, the scaling of the occupied phase space is analyzed for different lattice sizes in the new basis. If it shows a non-extensive behavior, one would conclude that few-body still look “few-body” in the changed basis.

The reasoning is that if both conditions, i. e. the banded “random” structure of the Hamiltonian and the “few-bodiedness” of the thermalizing observables, are fulfilled, then it is possible to apply Deutsch’s argument. By doing so, one would have shown that the system is indeed thermalizing.

This project addresses this question by testing the above requirements for a 1D hardcore model numerically. If it was fulfilled for this system, this would support the hypothesis that it is indeed true for generic Hamiltonians. The next step would be to think about *analytic* arguments supporting this, although it is not clear, whether this is actually achievable, at all.

The model, which is used, “lives” on a one-dimensional lattice with a two-dimensional local Hilbert space (like spin-1/2 models) in order to keep the Hilbert space at a manageable size (see exponential growth as explained in the introduction). Moreover, all possible symmetries, which are present in the system are taken into account to further reduce the Hilbert space dimension and for other reasons, which are described later.

To test the idea, which is outlined in the previous part, one needs a method to find the desired basis with the required properties. The method must not change the spectrum of the Hamiltonian, therefore it needs to be a unitary transformation. One straightforward way would be to create a random unitary matrix, because this assures that the matrix elements will look completely random. However, it is very unlikely that this choice will meet the other requirements, because it will generally neither lead to a banded form, nor conserve the few-body property of the observables.

A method that seems promising is the *flow equation method*, which uses continuous unitary transformations (CUTs). This method, which leads to a band-diagonalization of the Hamiltonian matrix H , is introduced in the following section.

3.2 Flow equation method

This part treats the flow equation method, which is the method of choice used to bring the tested Hamiltonians into a band-diagonal form.

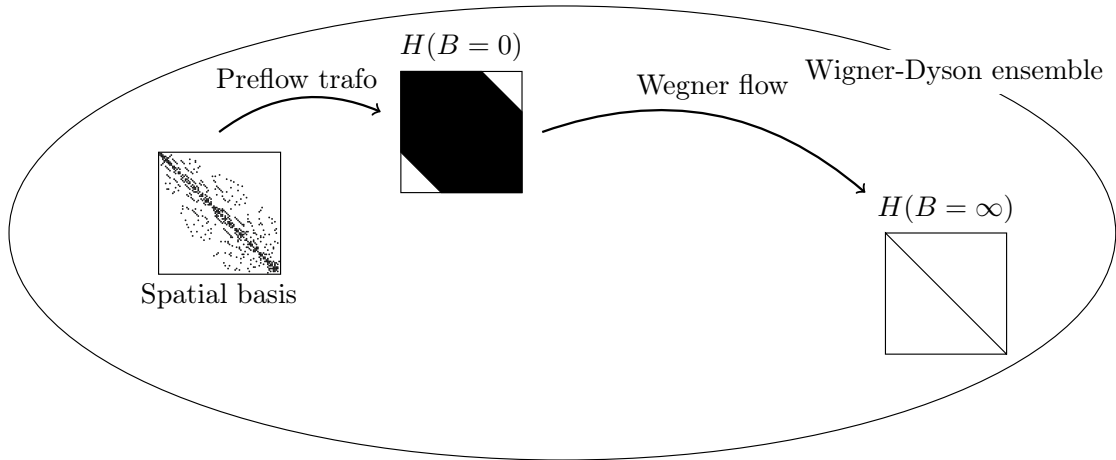


Figure 3.1: Schematic depiction of the Wegner flow creating a more band-diagonal Hamiltonian. The Wigner-Dyson ensemble contains all Hamiltonian matrices, which can be reached via unitary transformations and which therefore share the identical level spacing statistic. The matrix in the spatial basis, at $B = 0$ and at $B = \infty$ are rare occurrences, since they can only be found with a vanishing measure, whereas most matrices have a full random matrix form. The regular Wegner flow as defined by the flow equation band-diagonalizes a matrix by construction until the fully diagonalized form ($B = \infty$) is reached. The statistical properties of the Hamiltonian H over the flow are studied and compared to Deutsch’s requirements. Moreover, four observables are created, transformed in the corresponding flow basis, and analyzed, whether they retain their few-body structure throughout the flow.

3.2.1 Motivation

The underlying motivation for the development of the flow equation method is identical to the other approaches described in chapter 1.4: the attempt to reduce the complexity of complicated condensed matter systems in order to make statements about their physical nature and understand observed phenomena. Within this group, it falls into the category of perturbative analytical approaches, more precisely into the subcategory of *renormalization schemes* (Kehrein 2007). The motivation for the development of these techniques stems from the fact that there can be all kinds of energy scales present in a complex condensed matter system as already mentioned in the introduction. They can be apart by several orders of magnitude, which makes it difficult to treat the problem in its entirety. The optimal way, of course, would be to solve the Hamiltonian, i. e. to bring it into the diagonal form. Then all eigenstates and their energies would be available. However, in many cases, this is not feasible. Another way is to focus on the relevant energy scales and “integrate out” the unimportant ones, also called *energy scale separation* to successively reduce the maximal energy scale, given by the cutoff Λ_{RG} , down to the relevant energy scale (see Kehrein (2007)). This renormalization process creates a new *effective* model with a decreased maximal energy scale, which still shows the same physics as the original

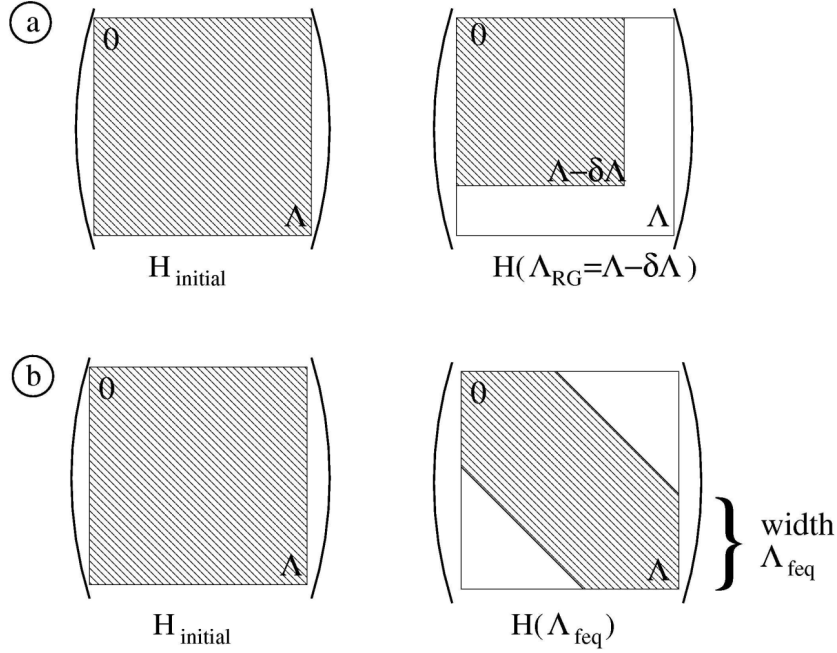


Figure 3.2: Different rescaling procedures shown by their effect on a many-particle Hamiltonian H . The matrix is initially sorted in ascending order according to the single-particle energies on the main diagonal. **(a)** The usual renormalization integrates out degrees of freedom with high energies reducing the Hilbert space to the new UV-cutoff $\Lambda_{\text{RG}} = \Lambda - \delta\Lambda$. **(b)** The flow equation defines an alternative scaling method, which successively eliminates large energy *differences* and results in a band-like structure with a band width Λ_{feq} (defined in Eq. (3.14)). Taken with permission from the monograph written by [Kehrein \(2007\)](#).

model.

One simple example was given by [Kehrein \(2007\)](#) and describes an impurity scattering model in an electron gas with a point-like interaction strength. In a discretized form (a fixed number of states) the corresponding Hamiltonian matrix takes on a solvable quadratic form of $c_k^\dagger c_{k'}$ -terms, which describes the scattering of plain waves. As a consequence, it can be casted into matrix form as depicted in Fig. 3.2 on the left. The entire matrix can be sorted according to the diagonal that contains the kinetic energy. The off-diagonal matrix elements contain the scattering terms, which are proportional to the interaction strength (grey shaded areas indicate non-vanishing terms). The conventional rescaling or renormalization is shown in the top row in Fig. 3.2. The procedure treats the initial interaction or coupling strength in a perturbative way. This makes it possible to integrate out the degrees of freedom with the highest energies, yielding a reduced cutoff Λ_{RG} . In the process the coupling or interaction strength changes as defined by a scaling equation. One ends up with a reduced Hilbert space, which still correctly describes the low-energy physics of the model ([Kehrein 2007](#)).

The idea for the flow equation follows the same line of thought. Instead of integrating out degrees of freedom with high single-particle energies as before, the flow equation formalism is designed to successively eliminate matrix elements, which correspond to large energy transfers. To derive the equation, which defines the flow, one can start from the initial goal: to find a unitary transformation U , which changes the initial basis to a different one, in which the Hamiltonian takes on a more diagonal form. This method eliminates matrix elements, which couple states with large energy differences. In matrix form this corresponds to a band-diagonalization of the Hamiltonian matrix H , if the initial diagonal is ordered.

The flow equation method is named after its defining differential equation

$$\frac{dH}{dB} = [\eta(B), H(B)], \quad (3.1)$$

which introduces the flow parameter B and the generator $\eta(B)$. The canonical choice is to use the Wegner-Wilson-Glazek (WWG) generator, which is basically a method of steepest descent and leads to a high speed of band-diagonalization (Wegner; Glazek and Wilson 1993). It is given by $\eta(B) = [H_{\text{diag}}(B), H_{\text{int}}(B)]$ and is used in this work. Here, H_{diag} denotes the diagonal of $H(B)$, while H_{int} describes the off-diagonal part. However, the generator can be defined in other ways with varying properties (Hénon 1974; White 2002; Morris et al. 2015; Savitz and Refael 2017). The flow runs from $B = 0$ to $B = \infty$, which is when the Hamiltonian is completely diagonalized and thus $\eta(B = \infty) = 0$.

Closely related to the flow equation is the differential equation, which describes the corresponding unitary transformation $U(B)$ that connects the initial Hamiltonian with its transformed version via the similarity relation $H(B) = U(B)H(0)U^\dagger(B)$. It is given as

$$\frac{dU}{dB} = \eta(B)U(B). \quad (3.2)$$

The unitary matrix $U(B)$ as the basis transformation matrix is also used to transform other observables into the new basis and hence completes the picture. The flow equation method is explained in detail in chapter 3.2.2.

With the flow equation method at hand, the project's goals can be approached. By continuously transforming the Hamiltonian, it steadily becomes more diagonal creating the required band structure. Since the numerics are exact and contain all matrix elements, the matrix elements can be analyzed with regard to the degree of randomness and their distribution. Furthermore, the unitary matrix $U(B)$ makes it possible to compute any observable in the new basis and allows for the study of "few-bodiedness" with various tools. The mathematical details of the flow equation method are outlined in the next chapter.

3.2.2 Mathematical formulation

In other words, one would like to perform a unitary transformation such that $H' = UHU^\dagger$ is more band diagonal. Since any unitary can be rewritten as $U = e^\eta$, where η denotes an anti-hermitian matrix ($\eta^\dagger = -\eta$), one can expand the exponential to yield

$$U = e^\eta = 1 + \eta - \frac{1}{2}\eta^2 + \dots \quad (3.3)$$

For a very small transformation $\Delta B\eta$ it is sufficient to include only the zeroth and first order terms and the transformed Hamiltonian becomes

$$H' = (1 + \Delta B\eta)H(1 - \Delta B\eta) = H + \Delta B [\eta H - H\eta]. \quad (3.4)$$

This equation can be rewritten to

$$\frac{H' - H}{\Delta B} = [\eta, H], \quad (3.5)$$

which is the flow equation Eq. (3.1) in the infinitesimal limit $\Delta B \rightarrow dB$.

For the implementation several matrices are required. It is useful to focus on the matrix elements, before zooming out again to full matrices. To begin with it is useful to start with the flow equations and write them in terms of concrete matrix elements. The procedure and notation here closely follows [Savitz and Refael \(2017\)](#). First, the diagonal and off-diagonal parts of the Hamiltonian are defined:

$$D_a := H_{aa} \quad (3.6)$$

$$J_{ab} := H_{ab} \quad a \neq b \quad (3.7)$$

with $J_{ab} = J_{ba}$. Additionally, one can define $X_{ab} := \frac{1}{2}(D_a - D_b)$. Obviously, $X_{aa} = 0$ and $X_{ab} = -X_{ba}$. For matrix elements the WWG-flow reads

$$\dot{\eta}_{ab} = [H_{\text{diag}}, H]_{ab} = (H_{aa} - H_{bb})H_{ab} = 2X_{ab}J_{ab} \quad (3.8)$$

$$\dot{H}_{ab} = [\eta, H]_{ab} = \sum_c (\eta_{ac}H_{cb} - H_{ac}\eta_{cb}) \quad (3.9)$$

If $a = b$, this simplifies to

$$\dot{D}_a = 2 \sum_{c \neq a} \eta_{ac}J_{ca}, \quad (3.10)$$

whereas for $a \neq b$ terms with η_{aa} vanish, such that

$$\dot{J}_{ab} = -4X_{ab}^2J_{ab} + \sum_{c \neq a,b} (\eta_{ac}J_{cb} - J_{ac}\eta_{cb}) \quad (3.11)$$

$$= -4X_{ab}^2J_{ab} + 2 \sum_{c \neq a,b} (X_{ac} + X_{bc})J_{ac}J_{cb} \quad (3.12)$$

Eq. (3.12) can be solved by first-order perturbation theory. If $|J_{ab}| \ll |X_{ab}| = |H_{aa} - H_{bb}|$, the second term can be neglected and one finds the linearized solution

$$J_{ab}(B) \approx J_{ab}(0)e^{-B|H_{aa}(B)-H_{bb}(B)|^2}. \quad (3.13)$$

It follows that the off-diagonal matrix elements decay exponentially, if the difference of their respective diagonal matrix elements is large. Since the basis of the initial Hamiltonian matrix is chosen to be the integrable basis (momentum basis), i. e. the basis where H is diagonal if $V_2 = 0$ ($V_1 = V_2 = 0$), the flow will successively remove all the off-diagonal elements with increasing flow, until only the diagonal is left in the limit $B \rightarrow \infty$. Moreover, one can estimate that elements, where this difference X_{ab} fulfills

$$X_{ab} = |H_{aa} - H_{bb}| < \Lambda_{\text{feq}} := \frac{1}{\sqrt{B}} \quad (3.14)$$

have not decayed significantly (or mostly by approximately $1/e$). This in turn defines the width of the band in Fig. 3.2.

For With these equations the first derivative is given by

$$\dot{\eta}_{ab} = [\dot{H}_{\text{diag}}, H]_{ab} + [H_{\text{diag}}, \dot{H}]_{ab} = 2 \sum_c (\eta_{ac} H_{ca} H_{ab} - H_{ab} \eta_{bc} H_{cb}) \quad (3.15)$$

$$+ \sum_c (H_{aa} \eta_{ac} H_{cb} - H_{aa} H_{ac} \eta_{cb} - \eta_{ac} H_{cb} H_{bb} + H_{ac} \eta_{cb} H_{bb}) \quad (3.16)$$

Not only η is required, but all of the following derivatives are needed for the numerical implementation:

$$\eta = [H_{\text{diag}}, H] \quad (3.17)$$

$$\dot{H} = [\eta, H] \quad (3.18)$$

$$\dot{\eta} = [\dot{H}_{\text{diag}}, H] + [H_{\text{diag}}, \dot{H}] \quad (3.19)$$

$$\ddot{H} = [\dot{\eta}, H] + [\eta, \dot{H}] \quad (3.20)$$

$$\ddot{\eta} = [\ddot{H}_{\text{diag}}, H] + 2[\dot{H}_{\text{diag}}, \dot{H}] + [H_{\text{diag}}, \ddot{H}] \quad (3.21)$$

This results from the fact that the explicit algorithm used, the Stable Unitary Integrator (SUI), approximates an exponential in Eq. (4.36). The flow equation can be simplified to

$$\begin{aligned} \frac{dH}{dB} &= H_{\text{diag}} H H - H H_{\text{diag}} H - H H_{\text{diag}} H + H H H_{\text{diag}} \\ &= H_{\text{diag}} H H - 2 H H_{\text{diag}} H + H H H_{\text{diag}} \end{aligned} \quad (3.22)$$

where numerically H_{diag} is always given by the diagonal of the current matrix $H(B)$. The calculation of the corresponding unitary transformation $U(B)$ which is defined as

$$U(B) = T_B \exp \left(\int_0^B dB' \eta(B') \right) \quad (3.23)$$

can be done via Eq. (3.2). The flow eventually completely diagonalizes H such that

$$H_{ij}(B = \infty) = D_i(B = \infty) \quad (3.24)$$

with $D_i(B = \infty) = E_i$ denoting the i -th eigenvalue.

$$\dot{U} = \eta U \quad (3.25)$$

Another way of writing Eq. (3.1) is

$$H(B) = e^{\eta(B)} H(0) e^{-\eta(B)} \quad (3.26)$$

where $\eta(B) = -\eta^\dagger(B)$ denotes the anti-hermitean generator.

Since the flow eventually diagonalizes H it is possible to write $H(B) = U(B)H(0)U^\dagger(B)$ in terms of the eigenvalues of H : $H_{ij}(B = \infty) = \delta_{ij}E_i$. Using the property that the trace is invariant under cyclic permutations and thus invariant under unitary basis transformations it is possible to transform $H(B = \infty)$ into any basis, i. e. into each basis of the flow. Hence, one finds that the sum over the eigenvalues is conserved over the course of the flow:

$$\sum_i E_i = \text{Tr}(H(B = \infty)) = \text{Tr}(U(B \rightarrow \infty)H(B)U^\dagger(B \rightarrow \infty)) = \text{Tr}(H(B)) \quad (3.27)$$

Using the property that a trace is invariant under unitary transformations it turns out that all integer powers of the Hamiltonian are conserved throughout the flow:

$$\begin{aligned} \text{Tr}(H^p(B = \infty)) &= \sum_i E_i^p = \text{Tr}(H^p(B)) = \text{Tr}((U(B \rightarrow \infty)H^p(B)U^\dagger(B \rightarrow \infty))^p) \\ &= \text{Tr}(U(B)H^p(0)U^\dagger(B)) = \end{aligned} \quad (3.28)$$

Mean of diagonal elements I_1/n is conserved:

$$I_1 := \sum_i E_i = \sum_i D_i(B) = \text{Tr}(H(B)) \quad (3.29)$$

I_2 is the Frobenius norm of the Hamiltonian H squared:

$$I_2 := I_2^D + I_2^J = \sum_i E_i^2 = \sum_{i,j} |H_{ij}(B)|^2 = \text{Tr}(H^2(B)) \quad (3.30)$$

being conserved follows that

$$\frac{dI_2^D}{dB} = -\frac{dI_2^J}{dB}. \quad (3.31)$$

So if all off-diagonal matrix elements decrease in size, the diagonal must grow. More information on the Stable Unitary Integrator and the implementation of the flow equation can be found in [Buono and Lopez \(1999\)](#), [Savitz and Refael \(2017\)](#), [Thomson and Schiró \(2018\)](#).

Chapter 4

Models and methods

This chapter introduces the models, which are studied in this project, and the basic description, which is the binary representation in the occupation number basis.

Real materials are simplified in order to be tractable for analytical or numerical calculations. In nature, most materials have an extensive number ($\approx 10^{23}$) particles and an isotropic mutual interaction among them. However, this is still beyond a possible calculation, because the Hilbert space scales exponentially with the particle number. Moreover, it is too complicated to model the different ranges of interactions such that it is required to be simplified. A common approximation is to represent the crystal structure by a lattice and to restrict the analysis to one dimension, which is also the choice in this work. Moreover, the interaction is reduced to only nearest-neighbor (NN) or next-to-nearest-neighbor (NNN) interaction.

As in most many-body studies the *occupation number representation* (also *second quantization*) is used throughout the entire work. This formalism assures the correct (anti-)symmetrization of states intrinsically and thereby makes all calculations simpler and more comprehensible.

4.0.1 Second quantization

In the formalism any N -particle many-body state $|\psi\rangle$ of a finite one-dimensional lattice with L sites is given by

$$|\psi\rangle = \sum_{\substack{n_j=0 \forall j \\ \sum n_j=N}} c_{n_1, n_2, \dots} |n_1, n_2, \dots, n_L\rangle \quad (4.1)$$

where the $n_j = c_j^\dagger c_j$ ($b_j^\dagger b_j$) denote the occupation numbers (i. e. number of particles) at site j for fermions (bosons). For fermions, it is famously known by *Pauli's exclusion principle* that only one fermion is allowed per state. Since in this work the fermions are considered to be *spinless*, this principle manifests itself in a bounded local energy density, i. e. the occupation numbers n_j in Eq. (4.1) can only be 0 or 1. This is different in a generic bosonic model, where the local occupation numbers are unconstrained. To reduce the complexity of the boson site occupations to the fermionic case the bosons

can be made *hardcore* (Matsubara and Matsuda 1956). Hardcore bosons are defined to be *impenetrable* and have an altered commutation relation for identical indices which resembles the fermionic canonical anti-commutation relation:

$$\text{Fermions: } \{c_i^\dagger, c_j\} = \delta_{ij} \quad \{c_i, c_j\} = \{c_i^\dagger, c_j^\dagger\} = 0 \quad (4.2)$$

$$\begin{aligned} \text{Hardcore bosons: } [b_i^\dagger, b_j] = 0 \quad [b_i, b_j] = [b_i^\dagger, b_j^\dagger] = 0 \quad i \neq j \quad (4.3) \\ \{b_i^\dagger, b_i\} = 1 \quad \{b_i, b_i\} = \{b_i^\dagger, b_i^\dagger\} = 0 \quad i = j \end{aligned}$$

In other words, it is $[b_i, b_j^\dagger] = \delta_{ij}(1 - 2n_i)$. It follows that hardcore bosons behave like bosons (i. e. they commute for different lattice sites), but they do not occupy a site with more than one particle. In other words, the spatial creation and annihilation operators for both fermions and hardcore bosons are defined in the same way:

$$\text{Fermions: } c_j |0_j\rangle = 0 \quad c_j^\dagger |0_j\rangle = |1_j\rangle \quad c_j |1_j\rangle = |0_j\rangle \quad (4.4)$$

$$\text{Hardcore bosons: } b_j |0_j\rangle = 0 \quad b_j^\dagger |0_j\rangle = |1_j\rangle \quad b_j |1_j\rangle = |0_j\rangle \quad (4.5)$$

It is the “binary behavior”, which vastly reduces the Hilbert space dimension and why it becomes feasible to perform exact diagonalization studies (see Section 4.3).

Having defined the creation operators the basis or Fock states on the right hand side of Eq. (4.1), which span the Fock space, can be defined. A Fock state is given by

$$|n_1, n_2, \dots, n_L\rangle = \prod_j (a_j^\dagger)^{n_j} |0\rangle = (a_1^\dagger)^{n_1} (a_2^\dagger)^{n_2} \dots (a_L^\dagger)^{n_L} |0\rangle \quad (4.6)$$

where a_j^\dagger creates a particle at site j , i. e. $a_j^\dagger = c_j^\dagger$ (b_j^\dagger) creates a fermion (hardcore boson) ($|0\rangle = \prod_j |0_j\rangle$ denotes the vacuum). The order of the a_j^\dagger -operators is a convention, which is fixed for the rest of the calculation. A properly ordered state is called *normal ordered*. It only plays a role for fermions, because bosons and spins on different lattice sites commute. In the following the notation solely focuses on fermions, because the hardcore bosonic case is analogous, only without the fermionic sign factors. The action of the ladder operators on a basis state is then

$$c_j^\dagger |n_1, n_2, \dots, n_L\rangle = \begin{cases} (-1)^{\sum_{l<j} n_l} |n_1, n_2, \dots, 1_j, \dots, n_L\rangle & \text{if } n_j = 0 \\ 0 & \text{if } n_j = 1 \end{cases} \quad (4.7a)$$

$$c_j |n_1, n_2, \dots, n_L\rangle = \begin{cases} (-1)^{\sum_{l<j} n_l} |n_1, n_2, \dots, 0_j, \dots, n_L\rangle & \text{if } n_j = 1 \\ 0 & \text{if } n_j = 0 \end{cases} \quad (4.7b)$$

The sign factor in front of the state appears because of the anticommutation relation and only occurs for fermions.

4.1 Model Hamiltonians

This project studies the question, if or to what extent any generic Hamiltonian, can be brought to a banded form, which is identifiable with a banded random matrix, while preserving the few-body structure of physical observables. This hypothesis, which is outlined in Chapter 3, is analyzed numerically with a model Hamiltonians, which, in the easiest form, can be formulated using hard-core bosons or spinless fermions. Both options are closely related, yet different as explained in the following. The Hamiltonian is defined on a one-dimensional lattice of L sites and contains a kinetic term defined by the nearest neighbor (NN) and next-to-nearest neighbor (NNN) hopping amplitudes t_1 and t_2 and an interaction term, which describes a NN and NNN repulsive density-density interaction proportional to strengths V_1 and V_2 ($V_1, V_2 \geq 0$).

Although the models seem basic with only hopping between close sites and a simple form of interaction, it features a gapless superfluid phase for $V_2 < 2$ (and $t_1 = V_1 = 1$) and a gapped insulator phase for $V_2 > 2$ with the critical point at $V_2 = 2$ (Zhuravlev et al. 1997). This richness coupled with its simplicity is why it has become paradigmatic in exact diagonalization studies. The version, which is considered in this work, is also discussed e. g. in Refs. Rigol (2009a) and Santos and Rigol (2010b) in the context of quantum chaos and thermalization. It is given in general operators a_j^\dagger and a_j by

$$H = -t_1 \sum_{j=1}^L (a_{j+1}^\dagger a_j + a_j^\dagger a_{j+1}) - t_2 \sum_{j=1}^L (a_{j+2}^\dagger a_j + a_j^\dagger a_{j+2}) + V_1 \sum_{j=1}^L \left(n_j - \frac{1}{2}\right) \left(n_{j+1} - \frac{1}{2}\right) + V_2 \sum_{j=1}^L \left(n_j - \frac{1}{2}\right) \left(n_{j+2} - \frac{1}{2}\right). \quad (4.8)$$

The Hamiltonian in Eq. (4.8) has the property that it conserves the total number of particles, because the creation and annihilation operators appear in each term each either once or twice (see also Section 4.3.1). Other properties depend on the type of the fundamental particles, the boundary conditions and system parameters. They are discussed in more detail in the following sections.

4.1.1 Hardcore boson model

If the fundamental particles are hardcore bosons, i. e. the creation and annihilation operators are b_j^\dagger and b_j , respectively, the model is called the *hardcore boson model* (abbreviated as HCB). For this model two different boundary conditions are discussed: periodic boundary conditions and open boundary conditions.

Hardcore bosons model with periodic boundary conditions

If the boundary conditions are assumed to be periodic, i. e. $b_{j+L}^\dagger = b_j^\dagger$ (abbreviated as PBC) the Hamiltonian takes on a form, which has already been studied extensively in Refs. Rigol (2009a,b); Rigol and Santos (2010); Santos and Rigol (2010a,b) (and supplementary material). In the following, the energy scale is set by fixing $t_1 = 1$ and $V_1 = 1$,

if not mentioned otherwise.

If $t_2 = 0$ and $V_2 = 0$, the Hamiltonian is integrable through the Bethe ansatz (Bethe 1931). Therefore, the terms proportional to t_2 and V_2 are also called the *integrability breaking* terms. For $t_2 = 0$ and $V_2 < 2$ the model describes a Luttinger liquid and features a metal-insulator transition at $V_2^{\text{crit}} = 2$ and half-filling (Des Cloizeaux and Gaudin 1966; Yang and Yang 1966). It is found that in the metallic phase the ground state is a gapless superfluid, whereas it is a gapped charge-density-wave insulator for $V_2 \geq 2$ (Zhuravlev et al. 1997). The critical value depends on the filling, such that the metal-insulator transition shifts to higher values of V_1 and V_2 for smaller fillings and disappears completely otherwise (e. g. for $N = L/3$, $V_1 < 3$ and $V_2 > 0$) (Zhuravlev et al. 1997; Schmitteckert and Werner 2004). In its generic form with $t_2 > 0$ and $V_2 > 0$, the system is more complicated and additional phases can appear (Schmitteckert and Werner 2004).

The hard-core boson model has been verified to fulfill the ETH numerically (Santos and Rigol 2010a). In particular, the study of localization measures has been used in this model, mostly to study the degree of complexity of energy eigenstates in a particular basis. Santos and Rigol (2010b) have suggested that the smoothness of the localization measures of the overlaps $\langle \phi_i | E_n \rangle$ for a fixed n over all basis states i might serve as an indicator for quantum chaos. In particular, it has been shown that the localization measures vary depending on the size of V_2 . If $V_2 = 0$, the system is integrable and the localization measures fluctuate for neighboring eigenstates heavily as expected (Santos and Rigol 2010b). For $V_2 > 0$, but not too large, there is a smooth behavior with respect to the energy of the eigenstates showing delocalization in the center of the spectrum. On the other hand, if V_2 is very large, bands are formed and the localization measures signal delocalization in the momentum basis. With periodic boundary conditions the Hamiltonian in Eq. (4.8) becomes invariant under translations, which allows for the decomposition of the Hilbert space into different crystal momentum sectors (see Section 4.3.1). Other symmetries of the Hamiltonian are the space inversion or reflection symmetry, if the total momentum is $k = 0$ or $k = \pi$, and the particle-hole exchange symmetry at half-filling, i. e. $N = L/2$ (see Section 4.3.1 and Section 4.3.1). If $t_2 = 0$, the hardcore boson model can be mapped onto the spinless fermion model (see Section 4.1.2) via the Jordan-Wigner transformation $b_j^\dagger = e^{i\Phi_j} c_j^\dagger$, $b_j = e^{-i\Phi_j} c_j$, where the phase $\Phi_j = \pi \sum_{l=1}^{j-1} c_l^\dagger c_l$ depends on all occupation numbers left of the current position (Jordan and Wigner 1928; Lieb et al. 1961). It is obvious that this "Jordan-Wigner string" does not change the densities n_j , it introduces, however, a phase factor due to the hopping over the boundary. One finds that

$$\begin{aligned}
H_{\text{HCB}} &= -t_1 \sum_{j=1}^{L-1} \left(c_j^\dagger c_{j+1} + c_{j+1}^\dagger c_j \right) - t_1 \left(e^{i\Phi_{L-1}} c_L^\dagger c_1 + c_1^\dagger e^{-i\Phi_{L-1}} c_L \right) \\
&\quad + V_1 \sum_{j=1}^L \left(n_j - \frac{1}{2} \right) \left(n_{j+1} - \frac{1}{2} \right) + V_2 \sum_{j=1}^L \left(n_j - \frac{1}{2} \right) \left(n_{j+2} - \frac{1}{2} \right) \\
&= H_{\text{SLF}} + t_1 \left(\pm 1 \mp e^{i\pi(N_f-1)} \right) \left(c_L^\dagger c_1 + c_1^\dagger c_L \right)
\end{aligned} \tag{4.9}$$

The sign in front of the 1 indicates the fermionic boundary conditions of the SLF model, where '+' means PBC and '-' means APBC, and the sign in front of the exponential depends on the boundary conditions of the HCB model, where '-' means PBC and '+' means APBC. The mapping is valid, if the second term in Eq. (4.9) vanishes, which hence depends on the boundary conditions of both models. If the same boundary conditions are imposed on both models, i. e. both have either PBC or APBC, the number of fermions N_f needs to be odd. Likewise, if the boundary conditions are different and N_f is even, the mapping is also fulfilled. In other words, if $N_b = N_f$ is odd, one can assume identical boundary conditions, e. g. both have PBC, whereas for $N_b = N_f$ even the boundary conditions need to be different.

Although the Jordan-Wigner transformation identifies the Hamiltonians with each other and even shows that their spectra is identical in the thermodynamic limit, observables, which depend on off-diagonal terms, differ in general (e. g. the momentum distribution function in Section 4.2.1).

Finally, it is possible to relate the HCB model to the XXZ model, which describes spin-1/2 degrees of freedom on a lattice. Since a spin at site j is either up ($S_j^z = \uparrow$) or down ($S_j^z = \downarrow$), it can be mapped to the occupation number representation with a trivial version of the Holstein-Primakoff transformation (Holstein and Primakoff 1940). It is given as

$$S_j^z = n_j - 1/2 \quad (4.10a)$$

$$S_j^+ = S_j^x + iS_j^y = b_j^\dagger \quad (4.10b)$$

$$S_j^- = S_j^x - iS_j^y = b_j \quad (4.10c)$$

with the usual spin-flip operators S_j^+ and S_j^- . Since spins on different lattice sites commute, spin-1/2 degrees of freedom are naturally related to hardcore bosons instead of fermions, for which a Jordan-Wigner transformation would suffice. With the transformation in Eq. (4.10) it is straightforward to map the HCB Hamiltonian to a generic XXZ chain as defined by Santos et al. (2012a) (but now with PBC) by setting $t_1 = -J/2$, $V_1 = \mu J$, $t_2 = -\lambda J/2$ and $V_2 = \lambda J\mu$. This corresponds to a HCB model, where $t_2 = -V_1/2$ and $V_2 = \mu V_1$.

Hardcore boson model with open boundary conditions

Another possibility for the hardcore boson model is to impose open-boundary conditions (OBC). In that case, the Hamiltonian remains basically the same and only the sums are adjusted to not go around the boundary, e. g. the NNN-contribution runs only from $j = 1$ to $j = L - 2$. Moreover, since the chain is open, one cannot simply exploit the translation invariance. Therefore, it is required to break this symmetry in order to avoid degeneracies. This is done by adding a small on-site potential proportional to ϵ on only one lattice site (chosen to be on the first site). This also destroys the space inversion symmetry. The Hamiltonian, which is described and studied in Ref. Santos et al. (2012b), then reads

$$\begin{aligned}
 H = & \epsilon \left(n_1 - \frac{1}{2} \right) - t_1 \sum_{j=1}^{L-1} (b_j^\dagger b_{j+1} + b_{j+1}^\dagger b_j) - t_2 \sum_{j=1}^{L-2} (b_j^\dagger b_{j+2} + b_{j+2}^\dagger b_j) \\
 & + V_1 \sum_{j=1}^{L-1} \left(n_j - \frac{1}{2} \right) \left(n_{j+1} - \frac{1}{2} \right) + V_2 \sum_{j=1}^{L-2} \left(n_j - \frac{1}{2} \right) \left(n_{j+2} - \frac{1}{2} \right). \quad (4.11)
 \end{aligned}$$

It is planned to use this model in a future study.

4.1.2 Spinless fermion model

The system defined via interactions and hoppings as in Eq. (4.8) can be filled with spinless fermions, as well. If the fundamental particles are spinless fermions, i. e. the creation and annihilation operators are c_j^\dagger and c_j , respectively, the model is called the *spinless fermion model* (abbreviated as SLF). For this model the boundary conditions are assumed to be periodic, i. e. $c_{j+L}^\dagger = c_j^\dagger$ (abbreviated as PBC).

The SLF model shares most of its properties with its HCB counterpart in Section 4.1.1: it features the translational, space inversion and particle-hole exchange symmetry and, if $t_2 = V_2 = 0$, it is Bethe integrable (Yang and Yang 1966).

Furthermore, if $t_2 = 0$, the Jordan-Wigner transformation as defined in Section 4.1.1 can be inverted such that the spinless fermion version of Eq. (4.8) can be mapped to its hardcore boson counterpart. If $t_2 > 0$, this mapping changes to a different type of hardcore boson model. In addition, this destroys the particle-hole exchange symmetry, which is present in the hardcore boson case for any t_2 .

Another difference is that although some observables in the fermionic case like the kinetic or interaction energy can be matched to their HCB analogue, other observables like the momentum distribution function strongly depend on the fermionic anticommutation sign and behave therefore differently (see also Section 4.2). The results for this model, however, are not included here.

4.2 Observables

The observables need to be set up in the same basis as the initial Hamiltonian in order to be properly transformed into a new basis. Therefore, it is required that they have the same symmetries as the Hamiltonian (see Section 4.3.1). Two natural observables are the kinetic energy K and the interaction energy I . While the first is defined as the non-interacting "hopping" part of the Hamiltonian, the latter consists of the remainder, i. e. the terms proportional to V_1 and V_2 . They are both *local* observables, in the sense that they do not describe long-range hoppings or interactions on the lattice. They differ in the fact that the kinetic energy is a one-body observable, whereas the interaction energy is a two-body observable. Together with the momentum distribution function and the density-density correlation structure factor, which are non-local one-body and two-body observables, this set represents the first choice to cover aspects of generic observables.

4.2.1 Momentum distribution function

The momentum distribution function $n(k)$ is the Fourier transform of the one-particle correlation operator $\rho_{lm} = c_l^\dagger c_m$ and a non-local one-body observable. Sometimes, it is also called mode occupation, because it measures what modes are occupied or not. The operator, which is often measured in time-of-flight experiments with ultracold atomic gases (see Section 1.3), is defined as

$$n(k) = a_k^\dagger a_k = \frac{1}{L} \sum_{l,m=1}^L e^{ik(l-m)} a_l^\dagger a_m. \quad (4.12)$$

However, since $n(k)$ has a designated direction, it does not commute with the reflection operator. In order to use the reflection symmetry, the observable, which is analyzed in Chapter 5, combines $n(k)$ and $n(-k)$ to

$$n^{\text{sym}}(k) = \frac{1}{2}(n(k) + n(-k)). \quad (4.13)$$

In this work only $n(k=0)$ is analyzed, such that the symmetrization is not necessary. In the case of hardcore bosons, the symmetrized observable also commutes with the particle-hole exchange operator as can be seen in Appendix A.4.1.

4.2.2 Density-density correlation structure factor

The density-density correlation structure factor is a two-body non-local operator, which is given by the Fourier transform of the density-density correlation operator $N_{lm} = n_l n_m$, i. e. the product of two occupation number (density) operators at positions l and m . In mathematical terms it reads

$$N(k) = \frac{1}{L} \sum_{l,m=1}^L e^{ik(l-m)} n_l n_m. \quad (4.14)$$

4.3 Exact diagonalization

This section contains the procedure of implementing a finite lattice Hamiltonian with a binary local Hilbert space on a computer. Since the number of states grows exponentially with the system size, i. e. with $\sim 2^L$, it is, in general, not feasible to study lattices, which are larger than ~ 16 sites. One way to circumvent this is to use all available symmetries to split the Hilbert space into smaller parts. Each sector is then defined by a set of quantum numbers and can be studied independently. This procedure, which is described in the following section and more detailed in Appendix A, leads to the basis, which is summarized in Section 4.3.2.

4.3.1 Symmetries

A symmetry in quantum mechanics is defined to be a transformation, which does not change the outcome of a measurement. In this context, this requires the symmetry generating operator to commute with the Hamiltonian and to be unitary. One can then find a simultaneous eigenbasis, which allows the break up of the entire Hilbert space into sectors of the corresponding set of commuting operators. Each sector is identified by a set of corresponding quantum numbers. If the basis is changed into one, which takes into account all symmetries, the independent blocks become small in contrast to the full Hilbert space. As a result, it becomes possible to perform the continuous unitary transformation flow on each block each represented by a different matrix.

The usage of symmetries in combination with exact diagonalization is a widespread technique, e. g. when studying the Eigenstate Thermalization Hypothesis in different lattice systems (Rigol 2009a; Santos and Rigol 2010b; Rigol and Srednicki 2012; Santos et al. 2012b). In many cases, however, not all, but only some symmetries of the Hamiltonian are used, e. g. one considers only the translational symmetry while breaking or ignoring the space inversion symmetry (parity) and the particle-hole exchange symmetry (by not considering half-filling and a momentum sector with $k \neq 0$). As a consequence, the size of the Hamiltonian (dimension of the biggest symmetry sectors) remains rather huge for lattice sizes like $L = 20$ and 22 . For the previously mentioned works this is not a problem, though, since it is only required to diagonalize the Hamiltonian once to obtain all the necessary information (eigenvalues and -vectors).

In this work the goal is to band-diagonalize the Hamiltonian with the flow equation method which requires many recurrent matrix-matrix multiplications, which are costly for large matrices. It is, of course, desirable to make statements about systems with lattice sizes as large as possible. Preferably, the sizes are comparable to the ones considered in the literature. In order to achieve that all possible symmetries are taken into account to reduce the size of the symmetry blocks as far as possible. Another reason is that the flow does not differentiate between degenerate states, i. e. off-diagonal matrix elements will remain persistent, since matrix elements decay approximately with $\sim \exp(-B(H_{ii} - H_{jj})^2)$ (see below).

The symmetries are the conservation of particle number (total spin) and the invari-

ance under lattice translations, space inversion (or reflection) and the particle-hole exchange (spin-flip). In the following part it is explained in detail how the symmetries of the systems are used to reduce the effective Hilbert space dimension significantly. It is based on the recipe provided by [Sandvik \(2010\)](#).

Particle number conservation

The first simplification is that the particle number given by

$$N = \sum_{j=1}^L n_j \quad (4.15)$$

is conserved by the Hamiltonian, i. e. $[H, N] = 0$ (for XXZ model: the number of particles is interpreted to be the number of \uparrow -spins, such that one can define the derived quantity named magnetization $M = 2N - L$). As it turns out, the fact that the total particle number does not change is directly visible from the expression, which defines the Hamiltonian: The kinetic energy part describes the hopping of particles, i. e. a particle is annihilated at some site and created at another. Since the interaction part only counts neighboring particles, the total number of particles is entirely untouched. Mathematically speaking, this constant of motion reflects the $U(1)$ -symmetry of the Hamiltonian, which can be seen by multiplying the creation and annihilation operators in the Hamiltonian by a phase factor, i. e. $(a_j^\dagger, a_j) \rightarrow (e^{i\phi} a_j^\dagger, e^{-i\phi} a_j)$. It follows that the full Hamiltonian splits into different particle number (magnetization) sectors, which do not interact with each other. This is why the first simplification is to use the basis, where all states belong to the subspace of the Fock space with a chosen particle number N (or magnetization).

Translational symmetry

A major reduction of complexity happens by exploiting the translational symmetry of the Hamiltonian, if periodic boundary conditions (PBC), i. e. $a_{L+1}^\dagger = a_1^\dagger$, are imposed. The translational symmetry means that the Hamiltonian remains unchanged, if all operators are shifted according to $(a_j^\dagger, a_j) \rightarrow (a_{j+1}^\dagger, a_{j+1})$. In other words, it is *invariant* under translations and commutes with the translation operator \mathcal{T} , which shifts the lattice sites by one to the right:

$$\mathcal{T} |n_1, n_2, \dots, n_L\rangle = s_{\mathcal{T}}^{n_L} |n_L, n_1, \dots, n_{L-1}\rangle. \quad (4.16)$$

The sign factor $s_{\mathcal{T}} = (-1)^{(N-1)}$ only appears, if the particles are fermions and ensures that the state remains normal ordered when a fermion moves across the (periodic) boundary. It will introduce the sign, which is needed to hop the fermion over the remaining $N - 1$ fermions to the leftmost site. It is important to notice that $s_{\mathcal{T}}$ does not show up, if $n_L = 0$. Moreover, if N is odd, the hopping fermion permutes $N - 1$ times, which is then an even number, such that it is always 1. Therefore, in order to make the calculation easier in the case of fermions, one could use an odd number of

fermions in the system to return to the hardcore boson case (see Section 4.1.1). Finally, it is clear that \mathcal{T} is unitary, because the scalar product of two arbitrary states remains the same, if the basis is shifted for both states equally, i. e. $\langle \mathcal{T}\varphi | \mathcal{T}\psi \rangle = \langle \varphi | \psi \rangle$.

In order to find the eigenbasis one can show¹ that L shifts by 1 return the state to itself, hence $\mathcal{T}^L = 1$. It follows that the eigenvalues of \mathcal{T} are all lying on the unit circle and that the eigenvectors $|a(k)\rangle$ are defined by

$$\mathcal{T} |a(k)\rangle = e^{ik} |a(k)\rangle \quad (4.17)$$

$$\text{where } k = \frac{2\pi}{L}m \text{ and } m \in \mathbb{Z}. \quad (4.18)$$

The values for m are chosen to be $-\frac{L}{2} < m \leq \frac{L}{2}$ for L even, such that $k \in (-\pi, \pi]$, and $-\frac{L-1}{2} \leq m \leq \frac{L-1}{2}$ for L odd, such that $k \in (-\pi, \pi)$. The variable k is interpreted as (*crystal*) *momentum*, because it is possible to define the momentum operator Π , which generates the translations and fulfills $e^{i\Pi} = \mathcal{T}$ (Essler et al. 2005).

Finally, it remains to be shown that the translation operator commutes with the Hamiltonian, i. e. $[H, \mathcal{T}] = 0$. Only then the eigenbasis of \mathcal{T} can be used as a simultaneous eigenbasis of both the translation operator and the Hamiltonian. Since the transformation of the Hamiltonian with the translation operator just induces a shift in the indices (see Eq. (A.3) in Appendix A.1), it is straight forward to realize that a simple renaming of the indices together with the periodic boundary conditions map the Hamiltonian onto itself. Thus, it follows that the Hamiltonian indeed splits up into different momentum sectors each with a basis set identified by the momentum k . The calculation of the expression for this set, i. e. $|a(k)\rangle$, yields Eq. (A.4) and is described in more detail in Appendix A.1. Numerically, the Hamiltonian is implemented in matrix form, which elements are determined by the action of H on a basis momentum state $|a(k)\rangle$ as explained in Appendix A.1.2.

Reflection symmetry

The reflection symmetry (sometimes called space inversion symmetry) describes the transformation of a spatial coordinate into its mirror image by flipping its sign. The defining operator is the parity operator \mathcal{P} , which swaps the positions from $j \rightarrow L-j+1$. It is given as:

$$\mathcal{P} |n_1, n_2, \dots, n_L\rangle = s_{\mathcal{P}} |n_L, n_{L-1}, \dots, n_1\rangle. \quad (4.19)$$

with the fermionic sign factor $s_{\mathcal{P}} = (-1)^{N(N-1)/2}$. It is clear that the action of \mathcal{P}^2 returns a state to itself ($s_{\mathcal{P}}^2 = 1$, because $N(N-1)$ is always even), which means that the eigenvalues must be $p = \pm 1$. Furthermore, \mathcal{P} is unitary, because the scalar product between two arbitrary states does not change, if both basis are reflected with respect to the boundary.

¹In the case of fermions there are N sign factors, which each yield a minus sign such that the overall sign factor will be $(-1)^{N(N-1)}$, which is always 1.

In order to use the reflection symmetry in combination with the translational symmetry, one needs to find a simultaneous eigenbasis for both \mathcal{T} and \mathcal{P} . It is not possible to simply take the eigenbasis of the translation operator, though, because the two symmetry operators do not generally commute. This can be seen from

$$\begin{aligned}\mathcal{P}\mathcal{T} |n_1, \dots, n_L\rangle &= \mathcal{P} s_{\mathcal{T}}^{n_L} |n_L, n_1, \dots, n_{L-1}\rangle = s_{\mathcal{T}}^{n_L} s_{\mathcal{P}} |n_{L-1}, \dots, n_1, n_L\rangle \\ &= \mathcal{T}^\dagger s_{\mathcal{P}} |n_L, \dots, n_1\rangle = \mathcal{T}^\dagger \mathcal{P} |n_1, \dots, n_L\rangle,\end{aligned}$$

i. e. $\mathcal{P}\mathcal{T} = \mathcal{T}^\dagger \mathcal{P}$. However, for the eigenstates with momenta $k = 0$ and $k = \pi$, which do not have a designated direction, both operators do commute. This is the motivation to construct *semi-momentum* states by combining positive and negative k -blocks by both adding ($\sigma = 1$) and subtracting ($\sigma = -1$) states with $\pm k$ from another. As a result, one finds semi-momentum² states $|a(k, p)\rangle$, for which $\mathcal{P} |a(k, p)\rangle = p |a(k, p)\rangle$ and $[\mathcal{P}, \mathcal{T}] = 0$ holds. Finally, it remains to show that $[H, \mathcal{P}] = 0$. A complete derivation is given in part A.2.

Particle-hole symmetry

At half-filling, i. e. $N = L/2$, an even number of lattice sites L and no NNN hopping (i. e. $t_2 = 0$) the systems can feature the particle-hole symmetry, i. e. the Hamiltonian is invariant under the transformation, which exchanges $a_j^\dagger \rightarrow (-1)^j a_j$ and vice-versa. The minus sign is only present in the case of fermions and assures the correct order of the terms. The action on a Fock state is simply

$$\mathcal{Z} |n_1, n_2, \dots, n_L\rangle = |1 - n_1, 1 - n_2, \dots, 1 - n_L\rangle, \quad (4.20)$$

because the sign factor can be determined to be 1 (see Appendix A.3).

4.3.2 Full representation basis and matrix elements

The final basis depends on the combination of symmetries, which are taken into account. The Hamiltonian is complex, if only the translational symmetry is considered as can be seen in Eq. (A.13). If all symmetries are taken into account, the final basis is chosen such that a basis state is given by all translations, space inversions and particle-hole exchanges (if applicable) and all combinations thereof of a chosen reference state $|a\rangle$:

$$|a^\sigma(k, p, z)\rangle = \frac{1}{\sqrt{L_a^\sigma}} \sum_{r=0}^{L-1} C_k^\sigma(r) (1 + p\mathcal{P})(1 + z\mathcal{Z})\mathcal{T}^r |a\rangle \quad (4.21)$$

The action of this state on an operator O , which commutes with all symmetry operators is then

$$O |a^\sigma(k, p, z)\rangle = \frac{1}{\sqrt{L_a^\sigma}} \sum_{r=0}^{L-1} C_k^\sigma(r) (1 + p\mathcal{P})(1 + z\mathcal{Z})\mathcal{T}^r O |a\rangle \quad (4.22)$$

²In the following no distinction is made between the semi-momentum $0 < k < \pi$ and the conventional crystal momentum $k = 0, \pi$, such that $0 \leq k \leq \pi$.

and therefore defined by the action on the reference state $O|a\rangle$. Generally, the operators have the form

$$O = \sum_{s=0}^{L-1} o_s, \quad (4.23)$$

where o_s only acts on the lattice site s and $o_{s=0}$ contains the part, which does not change $|a\rangle$, at all.

$$\begin{array}{llll} \mathcal{T}^m \mathcal{P} |a\rangle \neq |a\rangle & \mathcal{T}^m \mathcal{Z} |a\rangle \neq |a\rangle & \mathcal{T}^m \mathcal{P} \mathcal{Z} |a\rangle \neq |a\rangle & c = 1 \\ \mathcal{T}^m \mathcal{P} |a\rangle = |a\rangle & \mathcal{T}^m \mathcal{Z} |a\rangle \neq |a\rangle & \mathcal{T}^m \mathcal{P} \mathcal{Z} |a\rangle \neq |a\rangle & c = 2 \\ \mathcal{T}^m \mathcal{P} |a\rangle \neq |a\rangle & \mathcal{T}^m \mathcal{Z} |a\rangle = |a\rangle & \mathcal{T}^m \mathcal{P} \mathcal{Z} |a\rangle \neq |a\rangle & c = 3 \\ \mathcal{T}^m \mathcal{P} |a\rangle \neq |a\rangle & \mathcal{T}^m \mathcal{Z} |a\rangle \neq |a\rangle & \mathcal{T}^m \mathcal{P} \mathcal{Z} |a\rangle = |a\rangle & c = 4 \\ \mathcal{T}^m \mathcal{P} |a\rangle = |a\rangle & \mathcal{T}^m \mathcal{Z} |a\rangle = |a\rangle & \mathcal{T}^m \mathcal{P} \mathcal{Z} |a\rangle = |a\rangle & c = 5 \end{array} \quad (4.24)$$

$$L_a^\sigma = \frac{2L^2}{R_a g_k} \times \begin{cases} 1 & c = 1 \\ 1 + \sigma p \cos(km) & c = 2 \\ 1 + z \cos(km) & c = 3 \\ 1 + \sigma p z \cos(km) & c = 4 \\ (1 + \sigma p \cos(km))(1 + z \cos(kn)) & c = 5 \end{cases} \quad (4.25)$$

The matrix elements are then calculated to be

$$\langle b_j^\sigma(k, p, z) | O_j | a^\sigma(k, p, z) \rangle = o_j(a) (\sigma p)^{q_j} z^{g_j} \sqrt{\frac{L_{b_j}^\tau}{L_a^\sigma}} \begin{cases} \cos(kl_j) & c = 1, 3 \\ \frac{\cos(kl_j) + \sigma p \cos(k(l_j - m))}{1 + \sigma p \cos(km)} & c = 2, 5 \\ \frac{\cos(kl_j) + \sigma p z \cos(k(l_j - m))}{1 + \sigma p z \cos(km)} & c = 4 \end{cases} \quad (4.26)$$

$$\langle b_j^{-\sigma}(k, p, z) | O_j | a^\sigma(k, p, z) \rangle = o_j(a) (\sigma p)^{q_j} z^{g_j} \sqrt{\frac{L_{b_j}^\tau}{L_a^\sigma}} \begin{cases} -\sin(kl_j) & c = 1, 3 \\ \frac{-\sigma \sin(kl_j) + p \sin(k(l_j - m))}{1 - \sigma p \cos(km)} & c = 2, 5 \\ \frac{-\sigma \sin(kl_j) + p z \sin(k(l_j - m))}{1 - \sigma p z \cos(km)} & c = 4 \end{cases} \quad (4.27)$$

4.4 Measures for localization

The hypothesis of this work is that observables retain their few-body property, where the Hamiltonian appears to be drawn from an ensemble of banded random matrices. “Few-bodiedness” is a different concept than “locality (in a specific basis)” and only quantifiable through the comparison of different lattice sizes. A few-body observable is defined in Section 2.2.2 and means an observable, where all contributing terms are n -body operator with n being not extensive with respect to the system size L , i.e. $n \ll L$ (D’Alessio and Polkovnikov 2013). This property can be verified by analyzing the scaling of “locality measures” over lattice size. A locality measure is usually a quantity that addresses states. It measures how many states of a chosen basis are required to describe the state entirely. If the number is small, the state is said to be local with respect to the chosen basis. Observables can be completely local in one basis and delocalized in another, e.g. the kinetic energy is local in momentum space, whereas it is delocalized in the spatial basis. However, by analyzing the localization in a specific basis over different lattice sizes, it is possible to measure how much of the Hilbert space is required to correctly express the observable. If the *scaling* shows that a constant or growing fraction of the Hilbert space is occupied, then the observable is defined to not have a few-body structure. In other words, if the locality measure does not scale extensively with respect to the lattice size, the observable is considered to be of the few-body type. In this sense, the “few-bodiedness” can be understood as “locality in the Hilbert space”, which is why the term “locality” is used.

In the following two measures for localization are presented. They are generalized to quantities that measure the locality of observables.

4.4.1 Inverse participation ratio

One important tool to measure the localization of a state with respect to a given basis is the *participation ratio*. It is given by the sum over the entire Hilbert space of all the overlaps of the state with a basis state to the power 4. Historically, it was first introduced for the study of atomic vibrations by Bell and Dean (1970). Nowadays, its inverse, the *inverse participation ratio* (IPR), is chosen more often to quantify the spreading of a state over a basis (Edwards and Thouless 1972; Wegner 1980; de Forcrand 2007).

The inverse participation ratio (IPR) in the classical sense is a measure for how localized a state $|\psi\rangle$ is with respect to a chosen basis $|i\rangle$. The usual definition reads

$$\text{IPR} := \frac{\sum_i |\langle i|\psi\rangle|^4}{\left(\sum_i |\langle i|\psi\rangle|^2\right)^2} \quad (4.28)$$

where the sum runs over the entire Hilbert space. This definition, which also works for unnormalized states $|\psi\rangle$, simplifies to the known form $\text{IPR} = \sum_i |\langle i|\psi\rangle|^4$ for normalized states. The IPR attains its maximal value 1, if $|\psi\rangle$ exactly matches a single basis state. Hence, this value describes perfect *localization*. Contrarily, if $|\psi\rangle$ is spread over all

basis states evenly, i. e. *delocalizes* entirely, $|\langle i|\psi\rangle| = C$ where C denotes a constant, the IPR becomes minimal with $1/D$, where $D = \dim(\mathcal{H})$ denotes the corresponding Hilbert space dimension.

The traditional definition of the IPR in Eq. (4.28) considers states, however it is possible to extend this definition to work with operators. The IPR for an operator O in matrix form is defined via its matrix elements $O_{ij} = \langle i|O|j\rangle$ in a specific basis $|i\rangle$ to be

$$\text{IPR}(O_j) := \frac{\sum_i |O_{ij}|^4}{(\sum_i |O_{ij}|^2)^2}. \quad (4.29)$$

Again, the denominator assures proper normalization. This can be done for all indices j , i. e. over the entire spectrum yielding a full picture of the localization at different energies. The IPR for operators behave analogously to the traditional IPR. The maximal value of the IPR is 1 and occurs, if only one $|O_{i'j}| > 0$ while $|O_{ij}| = 0$ for all other $i \neq i'$. Thus, this situation corresponds to a perfect localization of the operator. Generally, localization means that only very few basis states are needed to describe the operator correctly. In a physical picture this means that the operator does not mix the states in the chosen basis much and that the eigenstates of O are a superposition of only a few basis states. Like in the previous case, the minimal value is the reciprocal dimension of the Hilbert space $\dim(\mathcal{H})^{-1}$ and can only be reached if all O_{ij} are equal in size, i. e. if $|O_{ij}| = C$ where C describes a constant. Physically, this situation describes the delocalization of the operator over all basis states.

The IPR of random numbers distributed according to the GOE is given by $D/3$ and offers the comparison to yet another important case (Zelevinsky et al. 1996). The IPR is often used in to probe the localization, mostly to study the localization in the integrable (mean-field) basis or in the momentum basis (Santos and Rigol 2010b; Rigol and Santos 2010; Santos and Rigol 2010a).

4.4.2 Shannon entropy

The Shannon entropy is another quantity, which is sometimes used to measure the localization of states in a specific basis $|\phi_j\rangle$:

$$S_\alpha = - \sum_{j=1}^D |\langle \phi_j | \psi_\alpha \rangle|^2 \ln |\langle \phi_j | \psi_\alpha \rangle|^2 \quad (4.30)$$

It is $S_{\text{GOE}} \sim \ln(0.48D_k)$ for a random matrix from the GOE. The definition for observables can be done as

$$S_i = - \sum_{j=1}^D \frac{|O_{ij}|^2}{\sum_j |O_{ij}|^2} \ln \frac{|O_{ij}|^2}{\sum_j |O_{ij}|^2} \quad (4.31)$$

The values of the Shannon entropy are in a way reciprocal to the IPR, because a small S_i indicates localization with the extreme case of full localization, i. e. only one element at

$S_i = 0$. On the other hand, if $O_{ij} = C$, for all j , one finds that $S_i = \ln D$ and the system displays perfect delocalization. In some cases the IPR and the Shannon entropy are combined into the “structural entropy” $S_{\text{str}} = S - \ln \text{IPR}$ (Santos and Rigol 2010a; Pipek and Varga 1992). This is summarized in Table 4.1.

Measure	localized	random matrix	delocalized
IPR	1	$3/D$	$1/D$
Shannon entr.	0	$\ln(0.48D)$	$\ln D$

Table 4.1: Extrema values for the measures for delocalization. The value for a random matrix is in between fully localized and delocalized (D denotes the dimension of the corresponding Hilbert space) (Izrailev 1990; Zelevinsky et al. 1996).

4.5 Implementation of the flow equation method

This section describes the algorithm to solve the flow equation with the Wegner-Wilson-Glazek generator (WWG), given by Eq. (3.1) and Eq. (3.2), numerically. In addition, some details of the implementation are provided.

The straightforward way to solve these equations numerically would be a 4+1-order (or even 8th-order) Runge-Kutta (RK) solver with an adaptive stepsize based on the Dormand-Prince method (Press et al. 2007; Dormand and Prince 1980). After each integration step $H(B)$ is used to compute the unitary matrix $U(B)$ via Eq. (3.2). Although the error of an n th-order RK solver grows with $\mathcal{O}(h^{n+1})$, the method suffers from other difficulties and drawbacks (Savitz and Refael 2017). One problem is that simple RK-algorithms lose the unitarity property of U over the course of the flow. This leads to a growing error, until $H(B)$ does not obey the similarity relation anymore (to a given precision).

Another problem is the so-called “stiffness” of the WWG-flow: Any off-diagonal matrix element decays exponentially depending on the difference of its respective diagonal matrix elements. It follows that off-diagonal matrix elements where the diagonal correspondents are close by rotate out only after an exponentially long flow. One way to circumvent the slow decay is to implement other flows like the *uniform tangent decay flow* as developed by Savitz and Refael (2017). Although this algorithm represents an alternative method to understand the main questions of this project, this work is solely using the WWG-flow.

4.5.1 Algorithm

The first problem concerning the loss of unitarity can be circumvented by choosing a specifically designed algorithm, which preserves the unitarity (Shadwick and Buell 1997). The group of integrators, which does that, are called *unitary integrators* and will be explained in the following (Savitz and Refael 2017). The algorithm focuses on breaking down the flow to small integration steps and approximating each of them

independently (Shadwick and Buell 1997). This basically corresponds to simply taking the first-order forward Euler integrator. Therefore, the flow is restricted to a very small rotation from $B \rightarrow B + \Delta B$ ($\Delta B \ll 1$), i. e.

$$H(B + \Delta B) = e^{\Delta B \eta(B)} H(B) e^{-\Delta B \eta(B)}. \quad (4.32)$$

Accordingly, the unitary transformation in Eq. (3.23) is given by

$$U(B \rightarrow B + \Delta B) = T_B \exp \left(\int_B^{B+\Delta B} dB' \eta(B') \right) \approx \exp (\Delta B \eta(B)), \quad (4.33)$$

because $\eta(B')$ is assumed to be constant and equal to the initial value $\eta(B)$ in the interval $[B, B + \Delta B]$. Instead of assuming that η is constant, one can also include higher order terms from the Taylor expansion about B , which is given by

$$\eta(B') \approx \eta(B) + \dot{\eta}(B)(B' - B) + \frac{1}{2} \ddot{\eta}(B)(B' - B)^2 + \mathcal{O}((B' - B)^3) \quad (4.34)$$

where $\dot{\eta}$ and $\ddot{\eta}$ denote the first and second derivative of η with respect to B . After inserting the higher order terms into Eq. (4.34) one finds

$$\begin{aligned} U(B \rightarrow B + \Delta B) &= T_B \exp \left(\int_B^{B+\Delta B} dB' (\eta(B) + \dot{\eta}(B)(B' - B) + \frac{1}{2} \ddot{\eta}(B)(B' - B)^2) \right) \\ &= T_B \exp \left(\eta(B) \Delta B + \frac{1}{2} \dot{\eta}(B) \Delta B^2 + \frac{1}{6} \ddot{\eta}(B) \Delta B^3 \right) \\ &\approx \exp (\Delta B \zeta(\Delta B)) \end{aligned} \quad (4.35)$$

where the B -ordering was approximated by a Magnus expansion and

$$\zeta(\Delta B) = \eta(B) + \frac{1}{2} \dot{\eta}(B) \Delta B + \frac{1}{12} (2\ddot{\eta}(B) - [\eta(B), \dot{\eta}(B)]) \Delta B^2. \quad (4.36)$$

Finally, it remains to compute the exponential of a matrix in Eq. (4.35) which can be quite difficult (Moler and Van Loan 2003). The simplest method which just sums the (Taylor) series expansion terms is disadvantageous, because it creates truncation errors and can lead to dangerous "cancellation catastrophies" which origin in the chosen arithmetic of the computer (cf. "round-off errors") (Moler and Van Loan 2003).

Another method is the "scaling and squaring" algorithm which is most widely used in linear algebra libraries. It basically splits the exponential into $e^A = (e^{A/j})^j$ with j being the smallest even number for which $\|A\|/j < 1$. Then, $e^{A/j}$ is computed with either the series expansion method or the Padé approximation (e. g. `expmat`-function in ARMADILLO or `expm`-function in MATLAB) (Blanes et al. 2009).

The Padé approximation of order (p, q) is defined by

$$e^A \approx R_{pq}(A) = [D_{pq}(A)]^{-1} N_{pq}(A) \quad (4.37)$$

with

$$N_{pq}(A) = \sum_{j=0}^p \frac{(p+q-j)! p!}{(p+q)! j! (p-j)!} A^j \quad (4.38)$$

and

$$D_{pq}(A) = \sum_{j=0}^q \frac{(p+q-j)! q!}{(p+q)! j! (q-j)!} (-A)^j. \quad (4.39)$$

It can be used whenever $\|A\|$ is not too big. Since ΔB is small and thus $\|\Delta B \eta\|$, the exponential is simplified using the corresponding (2,2)-Padé approximant (Blanes et al. 2009):

$$e^{\Delta B \zeta(B)} \approx \frac{12 + 6\Delta B \zeta(\Delta B) + \Delta B^2 \zeta^2(\Delta B)}{12 - 6\Delta B \zeta(\Delta B) + \Delta B^2 \zeta^2(\Delta B)}. \quad (4.40)$$

4.5.2 Implementation and technical details

This section deals with the implementation and its technical details.

It explains how a Fock state as in Eq. (4.6) with a binary local Hilbert space is represented in the exact diagonalization formalism. Since all considered systems have a binary local (site) basis, i. e. 0 or 1 (or spin up or down), it is possible to identify a state with an integer s over its representation in the dual basis as a bitstring via

$$|n_1, n_2, \dots, n_L\rangle \cong [n_1 n_2 \dots n_L]_2 = \sum_{j=1}^L n_j 2^{L-j} = s, \quad (4.41)$$

e. g. $c_2^\dagger c_3^\dagger c_5^\dagger c_7^\dagger |0\rangle = |0110101\rangle = [1010110]_2 = 86$. It is important to note that the bitstring ordering is defined to have the reverted order of the site ordering (from right to left). This convention is chosen in order to connect the binary integer representation, which starts at the right end to the lattice site numbering, which is from left to right. Any operation on the particles or spins like creation, annihilation or swapping of particles or spins can then be implemented straightforwardly. A swapping operation on the state above like $(c_4^\dagger c_3 + c_3^\dagger c_4) |0110101\rangle = (c_4^\dagger c_3 + c_3^\dagger c_4) c_2^\dagger c_3^\dagger c_5^\dagger c_7^\dagger |0\rangle = c_2^\dagger c_4^\dagger c_3 c_3^\dagger c_5^\dagger c_7^\dagger |0\rangle + 0 = c_2^\dagger c_4^\dagger c_5^\dagger c_7^\dagger |0\rangle = |0101101\rangle$ is translated into a bitswap $[1010110]_2 \xleftrightarrow{\leftrightarrow} [1011010]_2 = 90$. It becomes more difficult, though, if the hopping is over the boundaries, and there is an even number of fermions. Then an additional minus sign might be needed in order to reorder the creation operators in the correct way. Since for this work, only the results for hard-core bosons are presented, this is not discussed here.

Technical details

In order to benefit from a simplified syntax the library ARMADILLO is used, but just as a wrapper (Sanderson and Curtin 2016; Eddelbuettel and Sanderson 2014). The written

code of the programs used to produce and analyze the data, as well supplementary files and scripts can be accessed via https://gitlab.gwdg.de/stefan-kehrein-condensed-matter-theory/nils-abeling/flow_equation_project. Processed data and data used for the plots can be found under https://gitlab.gwdg.de/stefan-kehrein-condensed-matter-theory/nils-abeling/flow_equation_data. To get access to any of the repositories please ask Stefan Kehrein via email to stefan.kehrein@theorie.physik.uni-goettingen.de.

Chapter 5

Results

This chapter contains the main results of this thesis. It is divided into different parts. The first part addresses the study of the structure and statistical properties of the Hamiltonian over the flow. The second part contains the discussion of the behavior of the four observables defined in Section 4.2 and the projection operator over the flow and treats the question, whether the few-body structure of the observables is retained throughout the flow (see Chapter 3).

In addition, most results obtained from the directed regular flow (“Wegner flow”), which is defined by the flow equation in Eq. (3.2), are compared with the results from a random unitary transformation. This means that the Hamiltonian and the observables at $B = 0$ are transformed with the random unitary matrix U_{rand} into a random basis, i. e. $H_{\text{rand}} = U_{\text{rand}}H(B = 0)U_{\text{rand}}^\dagger$ and likewise for an observable.

The model is the hardcore boson model as given in Eq. (4.8) with parameters $t = 1.0$, $V_1 = 1.0$, $V_2 = 0.96$ (non-integrable) and periodic boundary conditions. The next-to-nearest-neighbor interaction parameter V_2 is chosen to allow for a comparison with the literature in Santos and Rigol (2010a) and to be able to study the behavior in steps of 0.12 (not shown here). The system sizes are chosen to be $L = 16$ (usually depicted with the color green), 18 (red), 20 (blue) and 22 (purple) and the number of bosons is set that the system is half-filled. For $L = 22$ only the symmetry sectors $k = 0, \pi$ are taken into account, because the other symmetry sectors are computationally not feasible. A preflow basis transformation is the initial transformation before the regular (“Wegner”) flow. Two different preflow basis transformations are discussed: the first is the transformation into the “integrable” part of the Hamiltonian (“mean-field basis”). It is defined as the basis, which diagonalizes the integrable version of the Hamiltonian, i. e. where $t = V_1 = 1.0$ and $V_2 = 0$. The second preflow basis transformation is the momentum basis, which is the basis where the kinetic part of the Hamiltonian is diagonal, i. e. $t = 1$ and $V_1 = V_2 = 0$. The results for the latter case are presented in Section 5.3.

The algorithm to solve the flow equations is the stable unitary integrator as described in Section 4.5. The stepsize is chosen to be $\Delta B = 0.001$ and constant.

In the following, matrices are depicted with a logarithmic color scale from negative (blue) to positive (red) with white indicating matrix elements smaller than 10^{-7} . This

ensures that off-diagonal matrix elements, which can be several orders of magnitude smaller than the dominating diagonal matrix elements, are still visible. The position of the matrix elements is usually depicted depending not on their indices (m, n) , but on the “eigenenergy per site” $(E_m/L, E_n/L)$. All small rectangles, which represent the matrix elements in the plot, are enlarged until they touch a neighboring site. Therefore, there are larger rectangles in areas where the spectrum is less dense, i. e. close to the borders. A matrix element can be thought of as residing in the center of a rectangle. This decision allows comparisons of different system sizes, because the energy per site (or energy density) is the defining quantity.

The results in the following chapters are mostly depicted in two groups: the symmetry sectors, where $k = 0$ or $k = \pi$ and the other ones, i. e. $k \neq 0, \pi$. The other quantum numbers like the parity p and particle-hole symmetry z are all considered, such that the group of $k = 0, \pi$ contains the combinations $(k, p, z) = (0, \pm 1, \pm 1)$ and $(\pi, \pm 1, \pm 1)$, while $k \neq 0, \pi$ consists of $(1, 1, \pm 1), \dots, (L/2 - 1, 1, \pm 1)$ (see Section 4.3.1). This is done, because the dimensions of the Hilbert spaces of the two groups do differ strongly (Table D.1). Since a state can delocalize more in a larger Hilbert space, this is a common technique (Santos and Rigol 2010a).

5.1 Flow and statistics of the Hamiltonian

This part addresses the Hamiltonian matrix, which is the main protagonist of the flow. The following analysis begins by explaining how and why a basis transformation is performed before the flow. After that, the level statistic of the Hamiltonian is shown in order to demonstrate that the system with the chosen parameters indeed describes a non-integrable model. This part is followed by the statistical analysis in Section 5.1.5, which examines, in what ways the Hamiltonian can be regarded as a random matrix in a different basis.

5.1.1 Pre-flow basis transformation into the integrable basis

Initially, the Hamiltonian is set up in the spatial basis as described in Section 4.3.2 and is shown in Fig. 5.1a. One immediately notices that it is only sparsely populated on the off-diagonals with a dominating main diagonal. This, of course, results from the interaction terms being diagonal in the spatial basis, whereas the hopping terms can lead to an overlap of different states. Before the flow starts the Hamiltonian matrix is transformed to a different basis. This is done to match the requirements in Deutsch’s argument (see Section 2.2.5), who assumed in Eq. (2.25) that

$$H = H_0 + H_1,$$

where H_0 describes the integrable part and H_1 is the interaction, which creates the “quantum ergodicity” (Deutsch 1991). There are three important basis: the spatial or site basis, which becomes important when studying spatial localization. It is the basis, which is used to set up the Hamiltonian with the Exact Diagonalization technique.

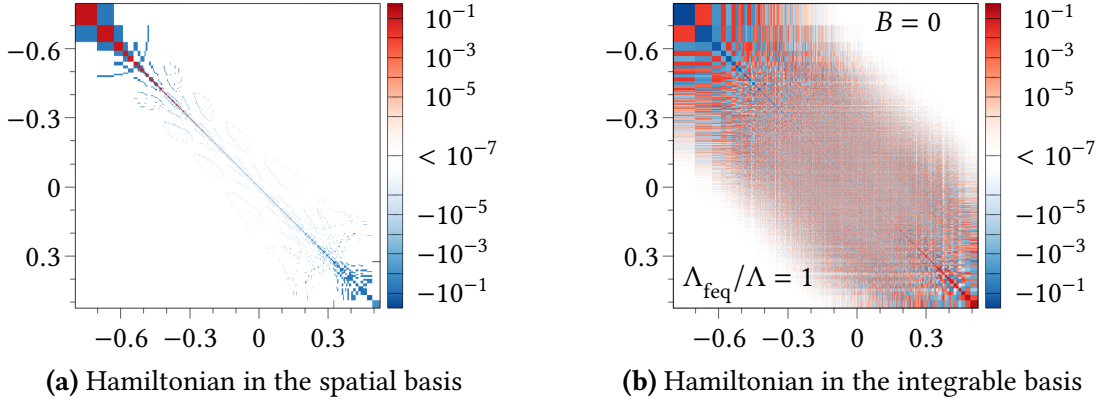


Figure 5.1: The pre-flow basis transformation into the integrable basis. **(a)** The Hamiltonian matrix for a hardcore boson system with $t = 1$, $V_1 = 1$ and $V_2 = 0.96$ of the symmetry sector $(k, p, z) = (0, 1, 1)$ and a lattice size $L = 18$. On both axis the index is mapped to the corresponding “eigenenergy per site”, i. e. $n \rightarrow E_n/L$. Only few non-vanishing values can be seen compared to the size of the matrix, which shows the sparsity of the Hamiltonian in the spatial basis. Due to the negative sign in front of t in Eq. (4.8) all off-diagonal matrix elements are negative. **(b)** The Hamiltonian matrix after the transformation to the mean-field basis, which diagonalizes the integrable Hamiltonian that only contains the terms ($t = V_1 = 1$, $V_2 = 0$). The matrix is densely populated. All off-diagonal matrix elements are by construction proportional to V_2 .

Other options are the momentum basis, which is relevant if V_2 is large, or the integrable basis, i. e. the basis formed by the eigenstates of the Hamiltonian when $V_2 = 0$ (Santos and Rigol 2010b). In this case, the model becomes Bethe integrable, such that the basis can be denoted as the “mean-field” basis (Santos and Rigol 2010a). It is assumed to be the best choice to distinguish global from local behavior (Zelevinsky et al. 1996). This integrable basis is the one, which is mainly used in this work. After a transformation the entire Hamiltonian is sorted in the way, which sorts the main diagonal in ascending order, to both match the conditions in Deutsch’s argument and to provide a more precise understanding when studying the exponential decay of each matrix element (see below). The resulting Hamiltonian for the integrable preflow basis is depicted in Fig. 5.1b and marks the start of the flow ($B = 0$). Due to the transformation in the integrable basis, it follows that all off-diagonal matrix elements must be proportional to the next-to-nearest neighbor (NNN) interaction V_2 . Since it breaks the integrability, it is also known as the “integrability breaking” term.

In Section 5.3 the analysis is repeated, but this time for the flow starting in the momentum basis, i. e. the basis where the hopping part of the Hamiltonian (proportional to t_1) is diagonal (Santos and Rigol 2010a). It follows that the off-diagonal part is only given by the density-density interaction (NN and NNN, proportional to V_1 and V_2 , respectively).

In matrix plots two variables shown are the flow variable B and $\Lambda_{\text{feq}}/\Lambda$. The latter

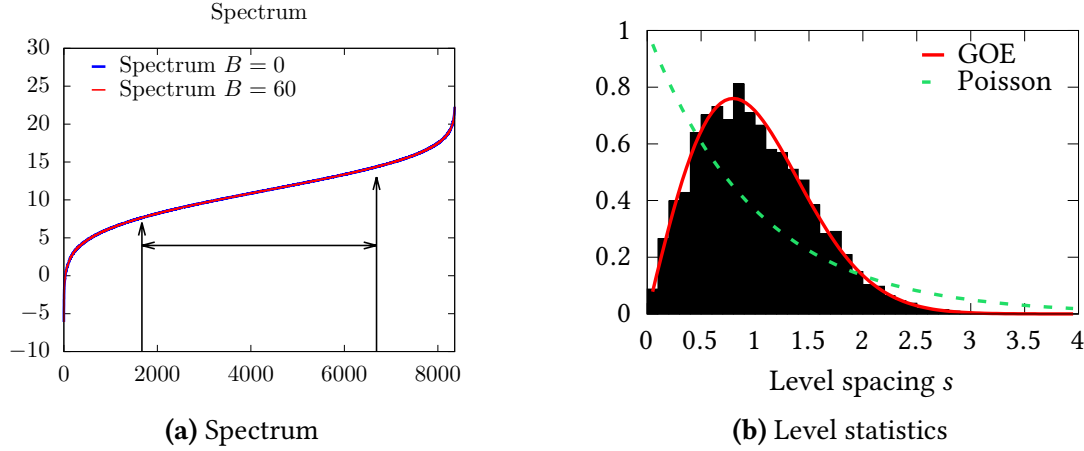


Figure 5.2: (a) Spectrum of the Hamiltonian. Since the flow equation applies unitary transformations, the spectrum does not change. The center area (i. e. with 20% cutoff on both ends) between the arrows is the bulk of the spectrum, which the following analysis focuses on. (b) Statistic over the spacings of the energy eigenvalues (level statistic) in the center of the spectrum (20% cutoff at both ends). The degree of the fitting polynomial of the unfolding procedure (see Appendix C.1) is chosen to be 13 and the binsize is 0.1. The histogram agrees with the Wigner surmise (solid red line), which approximately describes the level statistic of a matrix from the GOE. This also serves as the indicator for the non-integrability (see Section 2.2.4). If a system is integrable, it is expected to follow the Poissonian prediction (blue dashed line).

denotes the fraction of the matrix that still needs to be “rotated out” by the flow and is explained in the next Section (see also Section 3.2.2).

5.1.2 Spectrum and level statistic

This part addresses spectral properties of the Hamiltonian. By analyzing the spectrum it is possible to check, whether the implemented flow equation method is indeed unitary, and to specify the “bulk region”, which is the region that is studied in the consecutive parts. Fig. 5.2a shows the spectrum (i. e. the sorted eigenvalues) for the given Hamiltonian for $L = 22$ in the symmetry sector $(k, p, z) = (0, 1, 1)$. By comparing the spectra for $B = 0$ and $B = 60$, one immediately notices that the flow conserves the full spectrum and is thus unitary. A more detailed check reveals that the level of error in the center of the spectrum is approximately $< 2 \times 10^{-12}$ for the chosen flow integration step size. The figure also shows two black arrows, which define the border of the “bulk region”. This is the section of the spectrum where the eigenvalues are densely distributed without any sudden jumps or other anomalies. For the statistical analysis, this region, i. e. the central 60%, is analyzed. The right figure 5.2b shows the level statistics of the bulk. It approaches the Wigner-Dyson surmise and indicates the non-integrability due to the non-vanishing next-to-neighbor (NNN) interaction called level-repulsion (see Section 2.2.4).

5.1.3 Progress of flow and convergence

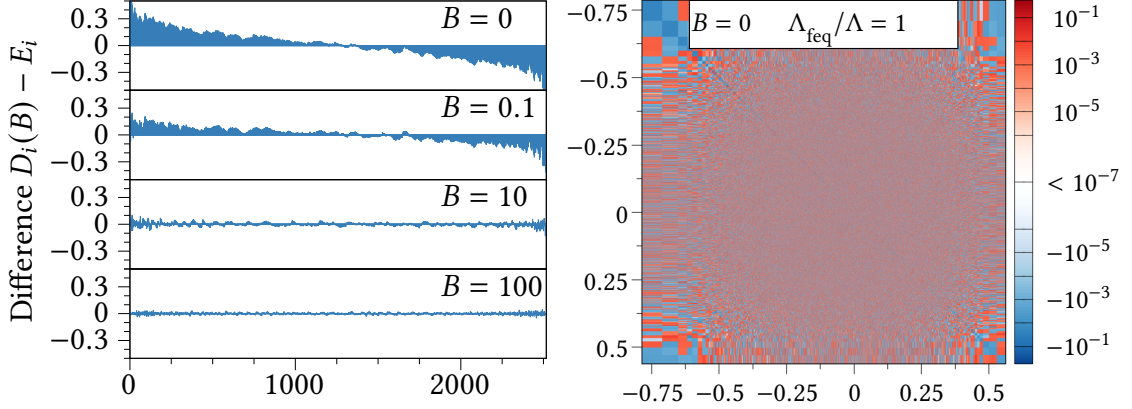


Figure 5.3: Differences between the diagonal elements D_i of the sorted Hamiltonians Fig. 5.1b, when transformed by a random unitary matrix in Fig. 5.6 and the corresponding eigenvalues E_i for different points in the flow. $(k, p, z) = (1, 0, 0)$ and $L = 20$.

Figure 5.4: The Hamiltonian matrix as in Fig. 5.1b, when transformed by a random unitary matrix, for the symmetry sector $(k, p, z) = (1, 0, 0)$ and $L = 20$.

The focus of this section is to examine the flow in more detail. The aim is to understand how the flow changes the Hamiltonian and to measure the effects of the convergence. The action of the flow on the Hamiltonian of the hardcore boson model is depicted in Fig. 5.6. The initial matrix is the Hamiltonian in the sorted integrable basis, such that the diagonal is increasing in size. Using Eq. (3.14) a ratio $\Lambda_{\text{feq}}/\Lambda$ is defined, which can be interpreted as a measure for the approximated fraction of the matrix that still needs to be eliminated (“rotated out”) before reaching the purely diagonal Hamiltonian. The Λ_{feq} can be identified via Eq. (3.14) to the reduced energy bandwidth. Using this definition, it is possible to compute lines, which indicate the matrix elements that have decayed to a chosen fraction of their initial size. In Fig. 5.6 solid (dashed) black lines are included to indicate a decay to $1/3$ ($1/100$) of the initial value.

When studying the Hamiltonian over the course of the flow in Fig. 5.6, it is striking how fast it converges to the diagonal. At $B = 0.01$ (Section 5.1.3), which corresponds to only 10 integration steps, already more than half of the matrix has been eliminated. This can be explained by the huge difference in the corresponding diagonal matrix elements, which define a very fast decay, because $H_{ij}(B)$ behaves approximately as $H_{ij}(B) \propto \exp(-B(H_{ii} - H_{jj})^2)$ (see Eq. (3.13)). At $B = 10$ less than 1.5% of subdiagonals have values, which contribute significantly. However, since for a matrix element close to the main diagonal the difference in the diagonal elements is exponentially small, they take exponentially long to rotate out. The longest flow that is feasible to reach numerically is $B = 100$, where the matrix consists of the closest 0.4% of subdiagonals. Although it is not possible to reach $B = \infty$ from the start of the flow, it can, however, be done via diagonalization of the initial Hamiltonian, because the approach is based on exact diagonalization. In other words, a straight forward diagonalization allows for the study of the Hamiltonian at $B = \infty$, which is depicted in Section 5.1.3, which is, of

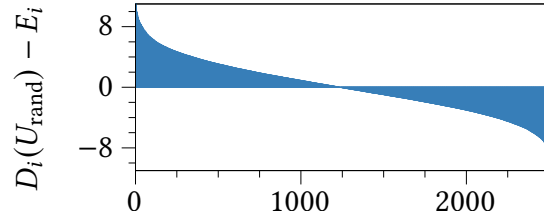


Figure 5.5: Differences between D_i of the sorted Hamiltonian in a random basis in Fig. 5.4 and the corresponding eigenvalue E_i .

course, diagonal in its eigenbasis.

Figure 5.6 is ideal to understand that the Wegner flow has the property of “band-diagonalization”. A transformation via a random unitary leads to a random Hamiltonian, which has a thoroughly different appearance as can be seen in Fig. 5.4. In the next chapters the results for the Wegner flow are compared with the transformation of a true random unitary matrix in order to show the similarities and differences.

Since the Hamiltonian $H(B = \infty)$ only consists of the eigenvalues on the diagonal, it can be concluded that the diagonal matrix elements D_n of the sorted Hamiltonian converge as $D_n(B) \rightarrow D_n(B = \infty) = E_n$ (after sorting). This behavior is studied in Fig. 5.3, where the difference $D_i(B) - E_i$ is plotted versus the index of the Hamiltonian matrix ($L = 20$, $(k, p, z) = (0, 1, 1)$). It shows that after 100 integration steps, at $B = 0.1$, the difference is already smaller than 0.1 in the bulk of the spectrum. At later flows, though, when the Hamiltonian is narrowly banded and the remaining subdiagonals are very close to the diagonal, it becomes exponentially hard to band-diagonalize further. In a physical picture, this means that it is hard to eliminate interaction matrix elements, which only transfer small amounts of energy. Hence, the flow is not making much progress, anymore, and the convergence of $D_n \rightarrow E_n$ seems stopped. Since all the diagonal matrix elements D_n represent the eigenvalues of the “unperturbed” Hamiltonian H_0 in Deutsch’s picture, they are used as a point of reference in a similar way as Deutsch did. Therefore, one can define the eigenbasis of the unperturbed Hamiltonian at flow B via $H_0(B) |D_n(B)\rangle = D_n(B) |D_n(B)\rangle$. If $B = \infty$, the eigenbasis of the current flow becomes the eigenbasis of the full Hamiltonian H . It follows that the matrix elements of the full Hamiltonian $H(B)$ are given by

$$\langle D_m(B) | H(B) | D_n(B) \rangle = D_n(B) \delta_{mn} + \langle D_m | H_1(B) | D_n(B) \rangle, \quad (5.1)$$

where $H_1(B)$ denotes the current off-diagonal part. Since a single point in the flow represents a possible Hamiltonian in the picture of Deutsch, the basis $|D_n(B)\rangle$ is used in the following part. However, when comparing quantities over flow, it does not matter, whether the energy density is considered with respect to $B = \infty$ or $B < \infty$, because they differ only by a slight margin.

This observation can be contrasted to the random unitary transformation, where the difference between the eigenvalues and the diagonal is huge (see Fig. 5.5).

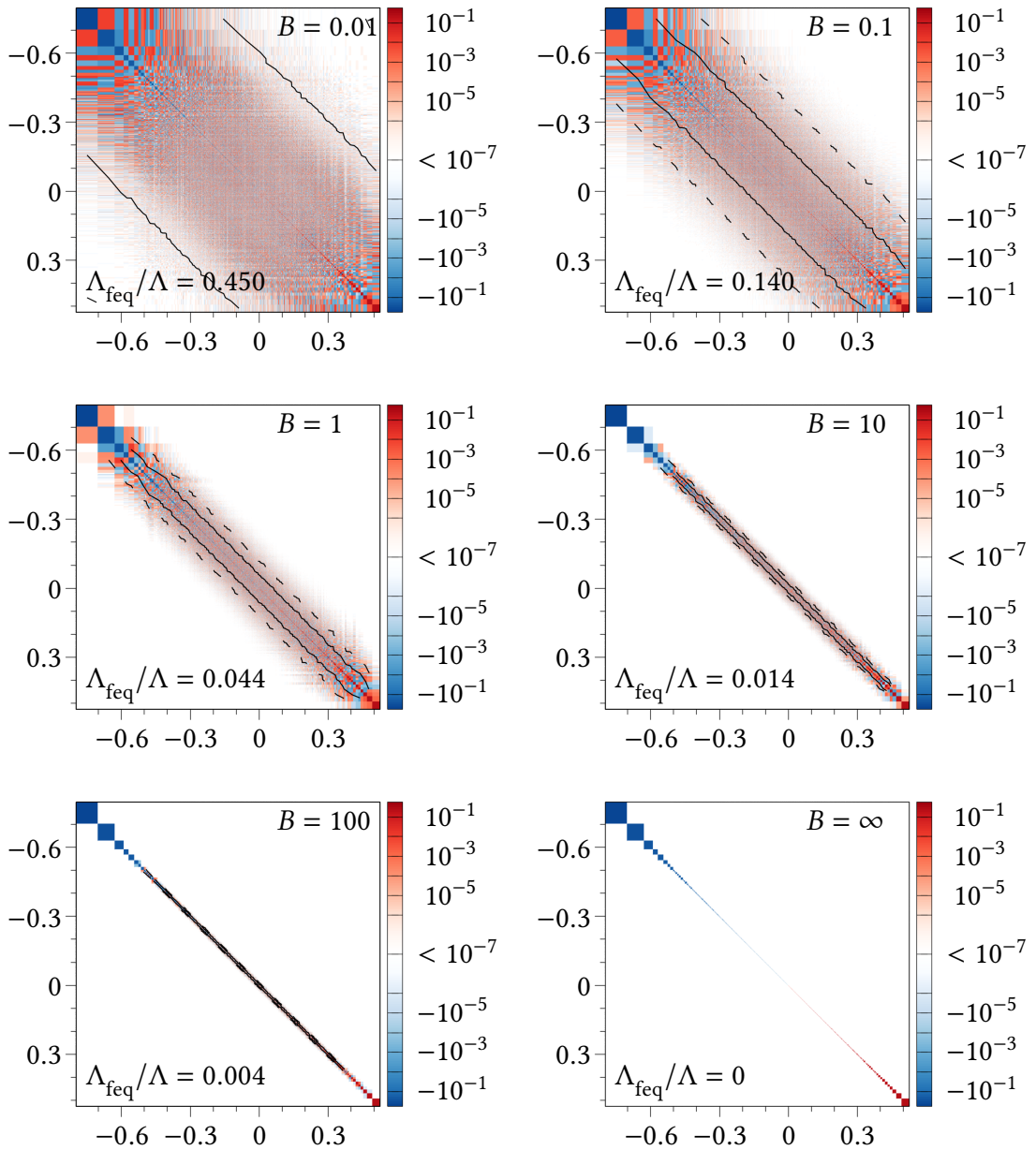


Figure 5.6: The Hamiltonian matrix $H(B)$ for parameters $t_1 = 1, V_1 = 1, V_2 = 0.96$, symmetry sector $(k, p, z) = (0, 1, 1)$ and lattice size $L = 18$ over the course of the flow that started in Fig. 5.1b. The axis have been recasted from $(m, n) \rightarrow (E_m/L, E_n/L)$. The size of matrix elements is enlarged to its neighboring sites, whereas the value is unchanged. Each matrix is sorted to give a sorted diagonal before display. Since the Wegner flow leads to an approximate exponential decay, the solid (dashed) line borders the region, which has approximately decayed to 33% (1%) of its initial value at $B = 0$. Similarly, $\Lambda_{\text{freq}}/\Lambda$ denotes the fraction of the Hamiltonian that still needs to be diagonalized. At $B = 10$ about 1.4% remains to be diagonalized. The matrix at $B = 100$ is so narrow that it almost looks like the diagonalized Hamiltonian ($B = \infty$).

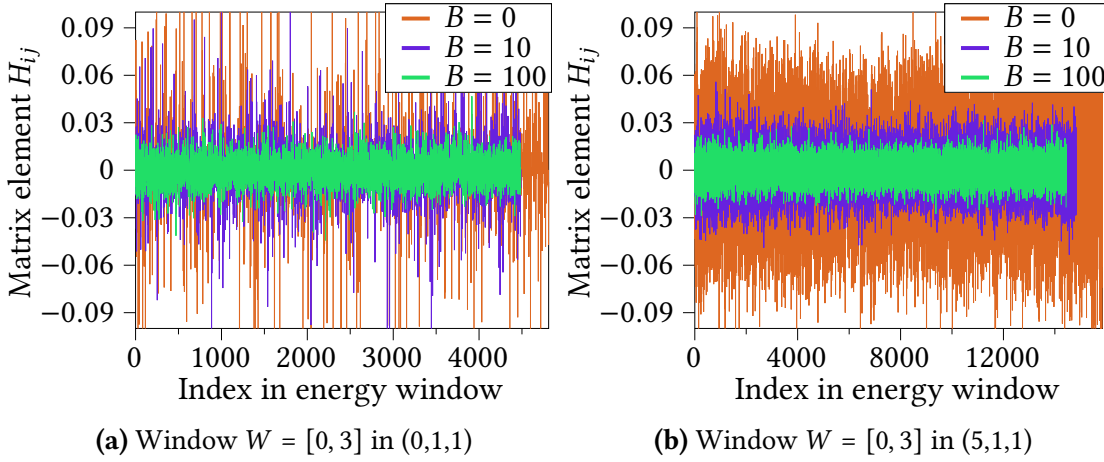


Figure 5.7: Matrix elements in the window $W = [0, 3]$ in units of level spacing of $L = 20$, $(0, 1, 1)$. It is (a) symmetry sector $(0,1,1)$ (b) symmetry sector $(5,1,1)$

5.1.4 Statistical analysis

This part deals with the statistical analysis of the Hamiltonian. In his argument, Deutsch assumed that the off-diagonal band consists of identically distributed, independent random variables, each with a Gaussian distribution of mean zero and the variance σ^2 (Deutsch 1991). Since the flow equation create band-diagonal matrices by construction, the bandedness of the Hamiltonian is already fulfilled. The Gaussianity of the matrix elements, however, is still to be verified. Although it might be obvious, it is important to stress that the flow cannot create true random variables, because it is deterministic. If the flow was repeated from the same point with the same conditions and parameters, it would end up at the same point. The only property, one can hope to find, is that the matrix elements are distributed *as if* they were drawn from a similar ensemble. In other words, if one was given a banded matrix and it was very difficult or impossible to tell that they result from a deterministic flow equation, one could reasonably argue that the properties must be close to identical to those of a real random matrix.

There are two arguments, why this can be expected to be true. The first argument is related to the level statistic, which shows a form predicted by the Wigner-Dyson distribution (see Fig. 5.2b). Since the Wigner-Dyson or Gaussian Orthogonal ensemble describes the level statistic of a typical random matrix under certain conditions, one could assume that other “typical” matrices with the same level statistic have similar properties (like the Gaussianity). However, it is necessary to be careful, because among the matrices in the GOE, there are also matrices like the Hamiltonian in the spatial basis or in the eigenbasis, which feature the same statistic (they are all connected via unitary transformations, i. e. the definition of the GOE). These matrices are rare, though, and can be assumed to have a vanishing measure.

The second argument is that the flow equation defines a set of highly coupled non-linear differential equations, which create a very complicated deterministic path. From

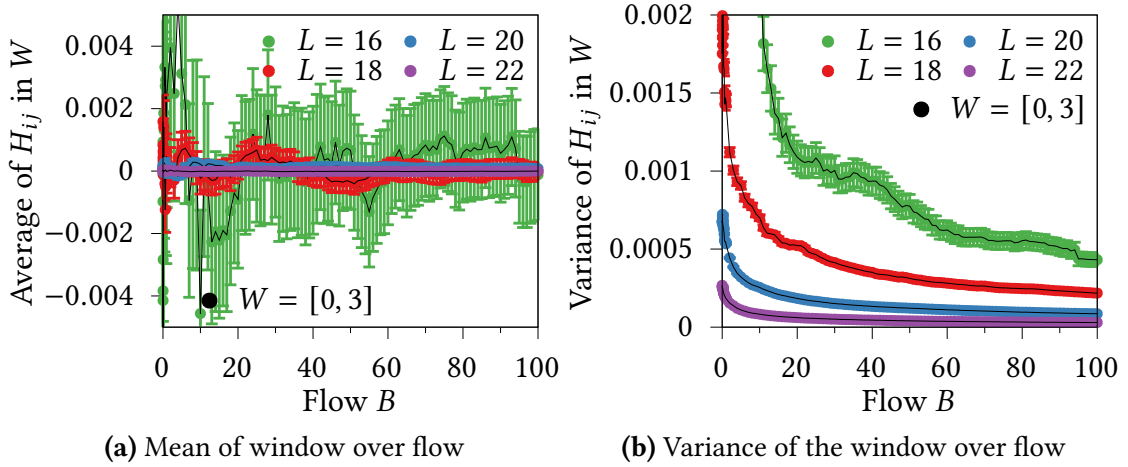


Figure 5.8: Mean and variance of all matrix elements in a window over flow for different lattice sizes in the symmetry sector $k = 0, \pi$. The window W is chosen to contain the elements of up to 3 times the average difference of neighboring eigenvalues of $L = 20$ in symm. sector $(0,1,1)$, i. e. approximately $[0, 0.0125]$. Therefore, for this lattice size and in this sector, the window comprises roughly the 3 first subdiagonals. For larger system sizes it will be more, for smaller less. A similar window in a different symmetry sector is depicted in Fig. 5.7a.

a numerical point of view, this is expressed in the fact that one matrix element at flow $B > 0$ is the result of thousands of large matrix-matrix multiplications, which mix matrix elements in a manner, which is, although not analytically, but *effectively* unpredictable. The central limit theorem then suggests that the matrix elements at later flows are normally distributed.

Due to the construction of the flow, off-diagonal matrix elements will shrink exponentially at points far away from the main diagonal. Therefore, it is necessary to look at regions parallel or close to parallel to the main diagonal, because in those regions the exponential falloff is approximately identical for all matrix elements. If the region is defined too large, a substantial number of elements will have fallen off by several magnitudes compared to the largest ones. This would include a huge number of “zeros”, which influence the statistic heavily. As a consequence, it is a more promising idea to consider regions that have a similar behavior with respect to first-order perturbation theory. Equation (3.13) suggests that one can group the matrix elements, whose differences of the corresponding main diagonal elements $|H_{ii}(B) - H_{jj}(B)|$ are within a chosen range $[s_l, s_u]$. The boundaries of the region can be defined using the average spacing of diagonal matrix elements with the distance $d = |i - j|$ in their indices via

$$s_d(B) := \frac{1}{N_{\text{elem}} - d} \sum_{i=1}^{N_{\text{elem}} - d} |H_{i,i}(B) - H_{i+d,i+d}(B)|. \quad (5.2)$$

By construction one can approximate that $s_d \approx ds_1$ and thus choose a *window*, which is defined to be the set of matrix elements

$$W(m, n) = \{H_{ij}(B) | ms_1 < |H_{ii}(B) - H_{jj}(B)| < ns_1\} \quad (5.3)$$

with $n > m$. As a consequence, the corresponding decay factor is within $[s_m, s_n] = [e^{-Bn^2s_1^2}, e^{-Bm^2s_1^2}]$. The thinnest window possible using this definition is when $n = m + 1$ and contains matrix elements mostly found around the subdiagonal m . The analysis in the following parts is done over subdiagonals and windows of off-diagonal matrix elements. In order to be able to compare different lattice sizes, the window is in most cases defined in units of the difference between neighboring energy eigenstates of $L = 20$ in the sector $(0, 1, 1)$. If the window is given in absolute numbers, the location of the matrix elements depend strongly on the system size. However, this ensures that matrix elements are included in the statistic, which have experienced the same decay, and which yields comparability between different lattice sizes.

Figure 5.7 shows the window $[0, 3]$ in units of 0.004167, i. e. $[0, 0.012501]$ for two different symmetry sectors for different flows. The dimension of the matrix of sector $(5, 1, 1)$ is approximately twice as large, which is why there are more elements in Fig. 5.7b. The matrix elements show the expected shrinking over the flow. Furthermore, a broad estimation by eye suggests that they become more even in size. Since there is no apparent reason, why positive or negative numbers should be preferred, it is expected that values are normal distributed with a vanishing mean. This can be studied in Fig. 5.8a, which shows the mean over the flow for different system sizes for the same window in all symmetry sectors $k = 0, \pi$. While the smaller lattice sizes still show fluctuations, the larger sizes like $L = 20$ and $L = 22$ feature a vanishing mean. In the neighboring plot in Fig. 5.8b contains the corresponding variance over flow.

5.1.5 Histograms

In order to study the “the degree of randomness” and “normality” the data sets are analyzed with two different methods: visual (also graphical) tests and a normality indicator.

First of all, a useful and necessary method, which cannot be neglected, is to use the studied eye to study the form of different histograms over the data ([Mohd Razali and Yap 2011](#)). Even though this could seem to be exposed to a subjective interpretation, this prevents the data from showing numerical artifacts. Together with an appropriate fit to different distribution functions this already provides a lot of information. The visual inspection and a consecutive estimation of the “degree of normality” is needed to get a first impression and to rule out numerical anomalies, which cannot be detected by later methods ([D’Agostino 1986](#)). The histograms are fitted to several standard distribution functions: the Gaussian distribution, the logistic distribution, which is more heavy-tailed than the Gaussian, an exponential to probe for the exponential decay, and a Lorentzian, which is more sharply peaked than the others. In addition, the Gaussian

is plotted, which would be predicted by the mean and variance of the data set (orange). The histogram for a band of the closest 1% of the subdiagonals is depicted in Fig. 5.10 for symmetry sectors $k = 0, \pi$ and in Fig. 5.11 for the other sectors. At very early flows (Appendix B) the histogram shows an overhang of small or zero values, which can be understood by the small number of matrix-matrix multiplications that have already been performed. Numerically, it is expected that speed with which normal distribution is reached grows with the system size, because larger matrices mean more elements that mix. Since the distribution is sharply peaked, the Lorentzian is the first, which fits adequately at $B = 1$ in Appendix B. Even later in flow, there seems to be a moment, when the exponential is the best fit (Appendix B). At very late flows, in Appendix B, the distribution is close to a logistic or Gaussian distribution. In this case, also the Gaussian, which is defined by the mean and the variance of the data set, is starting to be a useful guide. Overall, it can be stated that the behavior is complicated. Between the points in the flow the distribution changes a lot. However, at very large flows, a Gaussian can be regarded as a possible candidate. For the other symmetry sector the behavior is easier to interpret, because much more data is available. The histograms in Section 5.1.5 seem to follow a normal distribution everywhere. Moreover, the Gaussian defined by the data does agree with the histograms, as well. Since more than 2 million data points is a huge number, the next analysis focuses on the small window $W = [0, 3]$ (in units of nearest-neighbor eigenenergy difference of $L = 20$, $(0, 1, 1)$, see above). For the small band, where the matrix elements have been particularly chosen depending on their expected exponential decay, the fits in Fig. 5.9 seem to be satisfying, although the data set is much smaller than in Fig. 5.10. The same holds true for the corresponding analysis in the other symmetry sectors depicted in Fig. 5.12. The histograms for another window, which is farther from the main diagonal, are depicted in Fig. B.1 and Fig. B.2. They agree with the previous results.

5.1.6 Normality indicator

After the visual test has not rejected the hypothesis of normal distributed matrix values, the next step is to use more formal procedures, which means quantities, which can condense this information, such that it is not required to look at every histogram. A simple test for normality of a data set with elements x_i is to calculate the ratio

$$\Gamma = \overline{|x_i|^2} / |\overline{x_i}|^2 \quad (5.4)$$

of the average of the squared elements to the square of the average of the elements (Geary 1947). If the data is normally distributed with zero mean and standard deviation σ , the expectation value of the numerator is found to be $\overline{|x_i|^2} = \frac{\pi}{2}\sigma^2$, whereas the denominator value is σ^2 , such that $\Gamma = \pi/2$ (D'Agostino 1986). It has also seen application in condensed matter physics, namely in the verification of the ETH (LeBlond et al. 2019). The plots of Γ over the flow for different system sizes are depicted in Fig. 5.13. In Fig. 5.13a for $k = 0, \pi$ a clear tendency to $\pi/2$ is visible. However, the flow seems to be not far enough, yet, to truly converge to $\pi/2$. It is different, though, for the symmetry

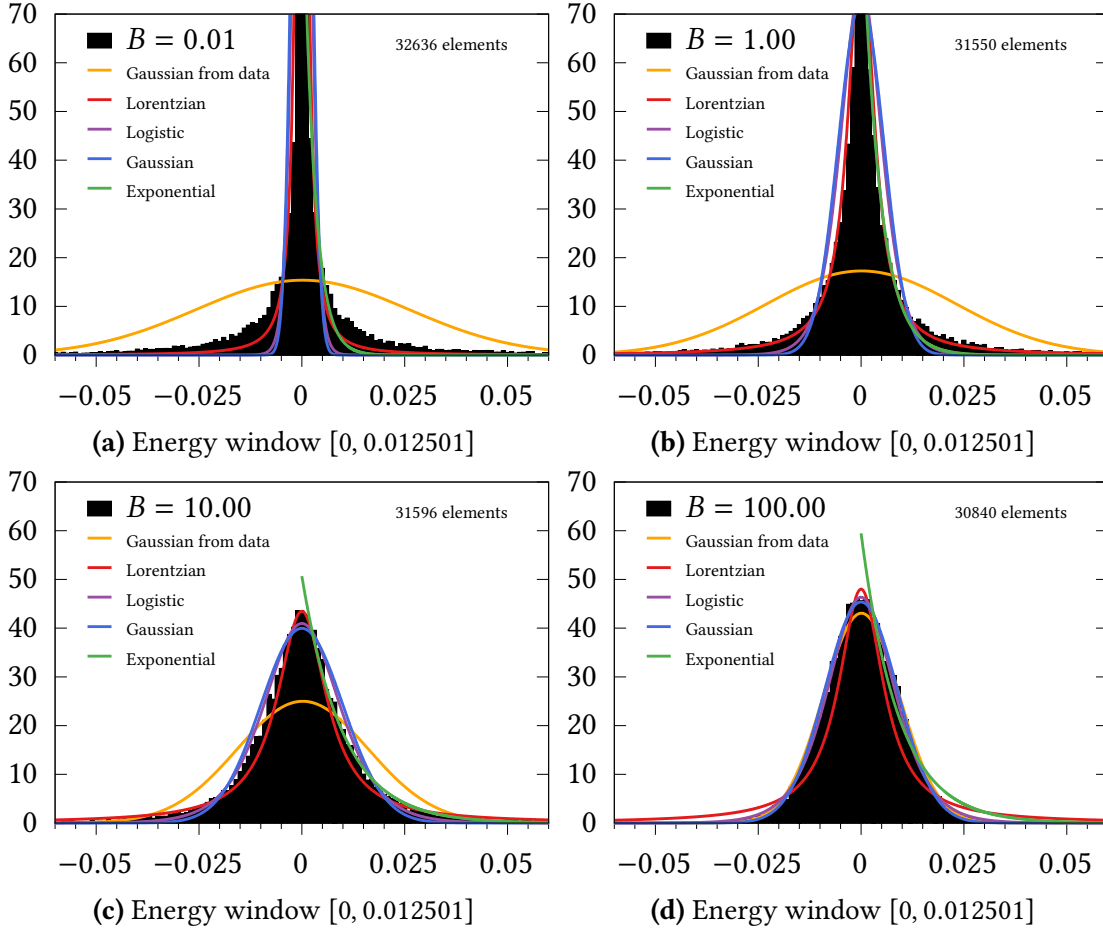


Figure 5.9: Histograms over the flow for energy window $[0, 0.012501]$ for the symmetry sectors $k = 0, L/2$ and both other symmetry quantum numbers, i. e. $p = \pm 1, z \pm 1$ and lattice size $L = 20$. Each shows the relative frequency over bins of size 0.001.

sectors $k \neq 0, \pi$ in Fig. 5.13b. There, the picture agrees with the expectation from the histograms that the set of the large number of data points is normally distributed. In this case, the value for Γ can not be distinguished from the corresponding value of a Hamiltonian transformed via a true random unitary, which is depicted in Fig. B.3. To use an even more formal procedure, a null hypothesis significance test (NHST) has been done for different normality tests for the data (Field 2013). The finding is, however, that the null hypothesis that the data is normally distributed is rejected almost all the time, which contradicts the previous findings. This is a well-known problem, though, which is called the “p-value problem” (Lin et al. 2013). Other alternatives one can use are normal probability plots (Altman and Bland 1995), but this has not been done here, because it is more important to rule out, whether the data contradicts normality and this has been done with a high degree of confidence (Elliott and Woodward 2007). Finally, it is known that regardless of the true shape, the distribution of large sets of data always look normal (Field 2013).

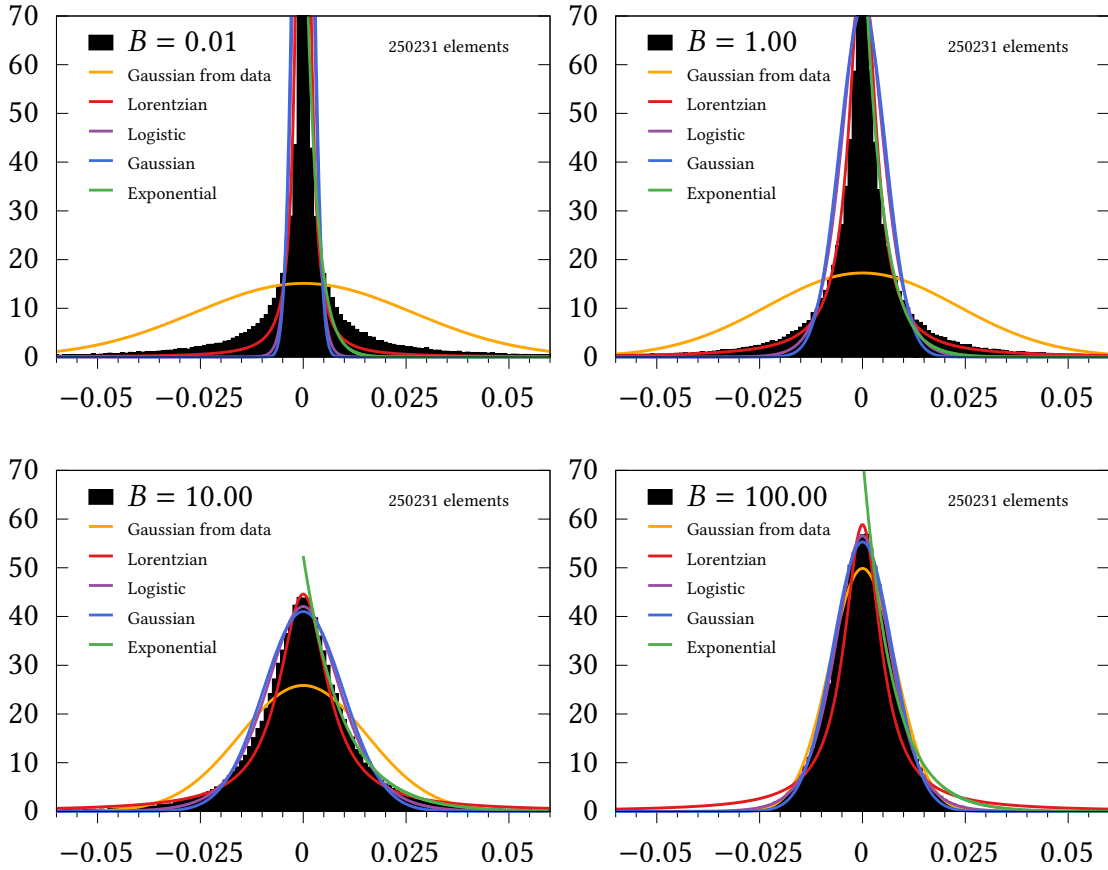


Figure 5.10: Histograms over the flow for a band comprising the closest 1% of sub-diagonals for the symmetry sectors $k = 0, L/2$ and both other symmetry quantum numbers, i. e. $p = \pm 1, z \pm 1$ and lattice size $L = 20$. Each shows the relative frequency over bins of size 0.001. Initially, the sparsity of the matrix creates a huge overhang of vanishing matrix elements. The peak then broadens and resembles a Lorentzian distribution ($B = 1$), then an exponential distribution ($B = 10$) until it approximates a Gaussian or a logistic distribution due to the heavy tails. The orange curve shows the Gaussian that is defined by the mean and standard deviation of the corresponding data set.

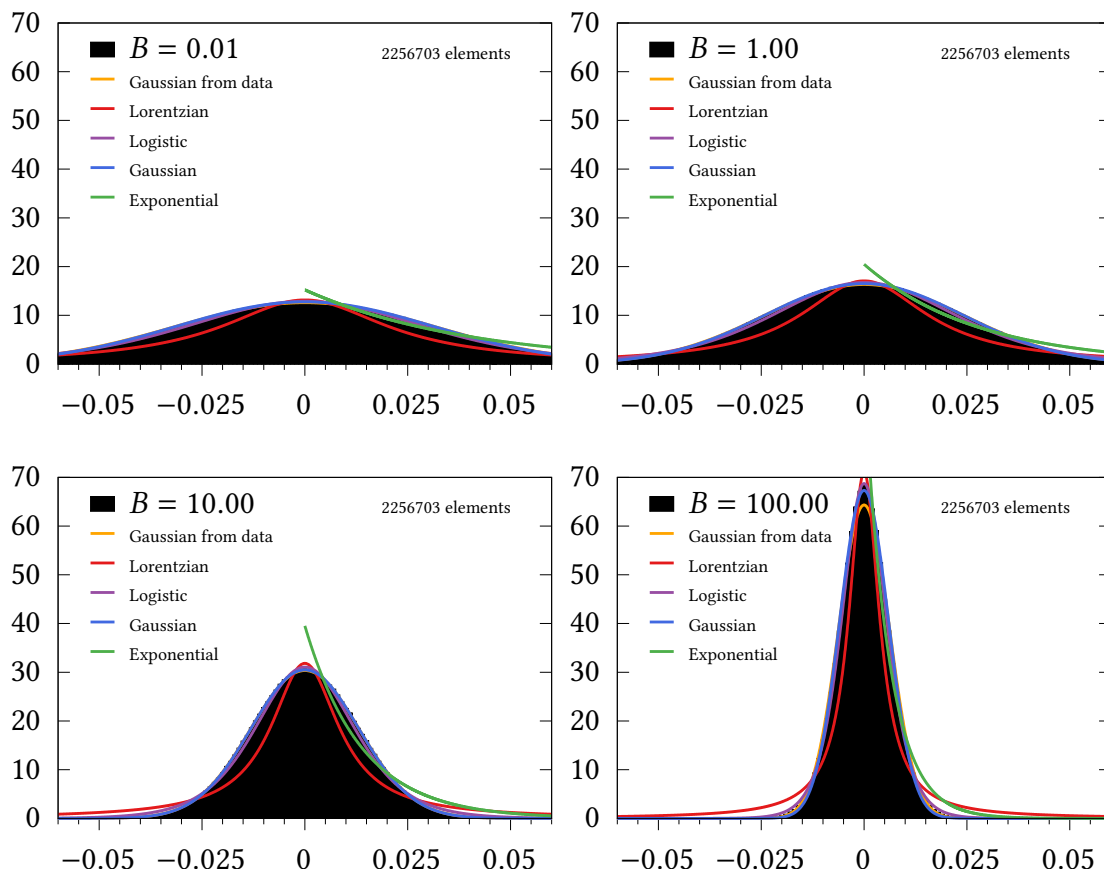


Figure 5.11: Histograms over the flow for a band comprising the closest 1% of subdiagonals for the symmetry sectors $k \neq 0, L/2$, so $k = \{1, 2, 3, 4, 5, 6, 7, 8, 9\}$, and both other symmetry quantum numbers, i. e. $p = \pm 1, z \pm 1$ and lattice size $L = 20$. Each shows the relative frequency over bins of size 0.001. Initially, the sparsity of the matrix creates a huge overhang of vanishing matrix elements. The peak then broadens and resembles a Lorentzian distribution ($B = 1$), then an exponential distribution ($B = 10$) until it approximates a Gaussian or a logistic distribution due to the heavy tails. The orange curve shows the Gaussian that is defined by the mean and standard deviation of the corresponding data set.

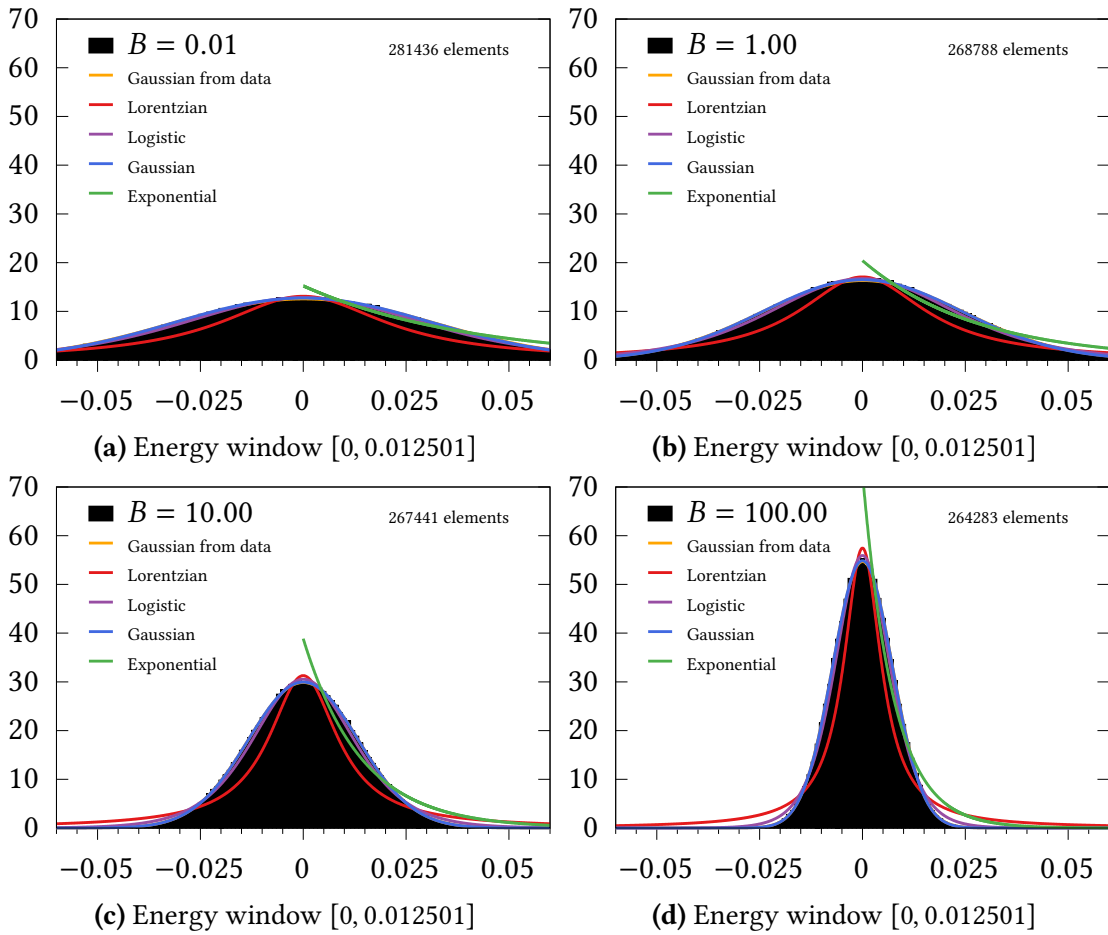


Figure 5.12: Histograms over the flow for energy window $[0, 0.012501]$ for the symmetry sectors $k \neq 0, L/2$ and both other symmetry quantum numbers, i. e. $p = \pm 1, z \pm 1$ and lattice size $L = 20$. Each shows the relative frequency over bins of size 0.001.

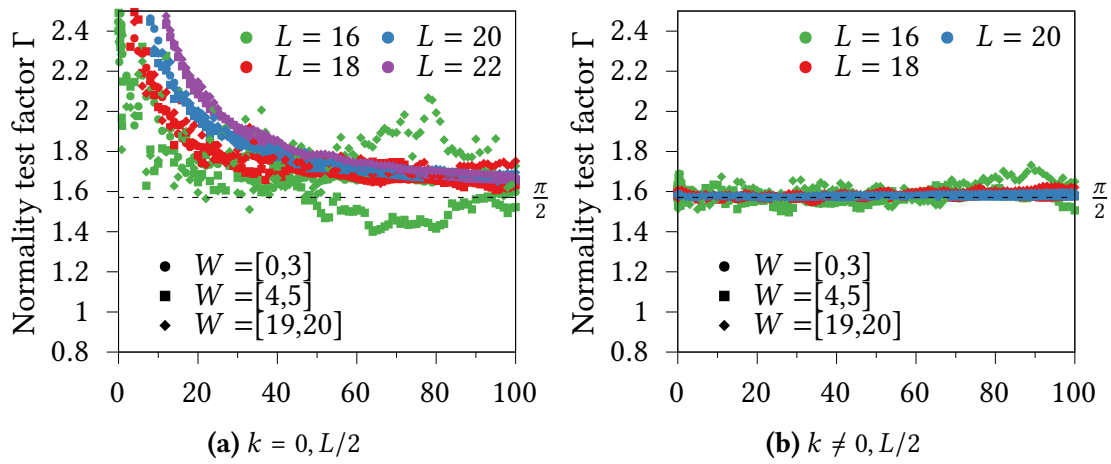


Figure 5.13: The Γ -normality indicator for three energy windows in units of s_1 over the course of the flow for different lattice sizes and the symmetry sectors (a) $k = 0, L/2$ and (b) $k \neq 0, L/2$ and all other combinations of symmetry quantum numbers, i. e. $p = \pm 1, z \pm 1$. The window contains approximately the closest 3 subdiagonals next to the main diagonal of the Hamiltonian for $L = 20$. For Gaussian distributed values it is $\Gamma = \frac{\pi}{2}$. It seems that the Γ -value of the data set asymptotically approaches $\pi/2$ from above for $k = 0, L/2$. For $k \neq 0, L/2$ the value for Γ seems to be converged to $\pi/2$ at $B = 0$ already. The Γ -indicator in the symmetry sectors $k \neq 0, \pi$ is almost undistinguishable from the corresponding value of a random unitary transformation (see Fig. B.3).

5.2 Localization of observables

This part treats the question whether the few-body structure of observables is retained over the flow. In the previous section it was found that the flow equation can indeed be used to transform the Hamiltonian into a basis, where its structure and statistical properties are similar to a banded random matrix. Since the main idea is to justify Deutsch’s argument, which is closely related to the ETH (see Section 2.2.2), and since the ETH is believed to hold for few-body observables, it remains to be shown that the flow does not destroy the few-body property of observables in order to make a viable justification of Deutsch’s argument (see Chapter 3). If, however, this transformation destroyed the few-body property of observables (see Section 4.2) in the sense that they populated an extensive part of the Hilbert space in the new basis, then it would not be possible to verify Deutsch’s argument numerically (Chapter 3).

In the following four observables as defined in Section 4.2 will be studied. They cover all combinations from local and non-local, one-body and two-body operators and represent the class of few-body observables. They are often used in numerical studies (e. g. by Santos and Rigol (2010a,b)).

To contrast the behavior of the observables another operator is studied, namely the projection operator $\mathcal{P}_{E=0}$, which is defined to be the operator that projects into the eigenstate with vanishing energy, which is in the bulk of the spectrum. It is defined via

$$\mathcal{P}_{E=0} := |E = 0\rangle\langle E = 0| \quad (5.5)$$

and can be constructed numerically in the energy eigenbasis, where it is just a single ‘1’ on the diagonal. It is then transformed back into the initial basis by the basis transformation that already diagonalizes the Hamiltonian, if written in the initial basis. When the energy eigenbasis is reached at flow $B = \infty$, the projector will be completely localized, because only one element is non-zero. The projection operator commutes with the Hamiltonian by construction and is therefore conserved, moreover, its projection onto a certain eigenstate prohibits thermalization in a mathematical sense (Section 2.2.2). It has been argued that they are neither few-body nor extensive (D’Alessio and Polkovnikov 2013). Finally, the properties of the observables over the regular flow are also compared to those obtained through a random unitary transformation U_{rand} as it has been done in the previous part.

To study the behavior of the few-body property over the flow two “localization measures” are used: the IPR and the Shannon entropy (see Section 4.4). However, one cannot simply calculate the quantity and interpret it, since its value depends on the chosen basis. In the basis, which diagonalizes an observable, the observable looks fully localized, whereas it can be more spread out in a different basis, e. g. in the spatial basis, as can be seen later. Therefore, one can only study “localization” by examining the scaling over different lattice sizes and by comparing it to the fully localized and delocalized limit (see Section 4.4). The delocalization limit is antiproportional to the Hilbert space dimension D , which grows exponentially with lattice size L , i. e. $D \propto \exp(L)$. Hence, it is possible to detect exponential growth of the number of the required basis

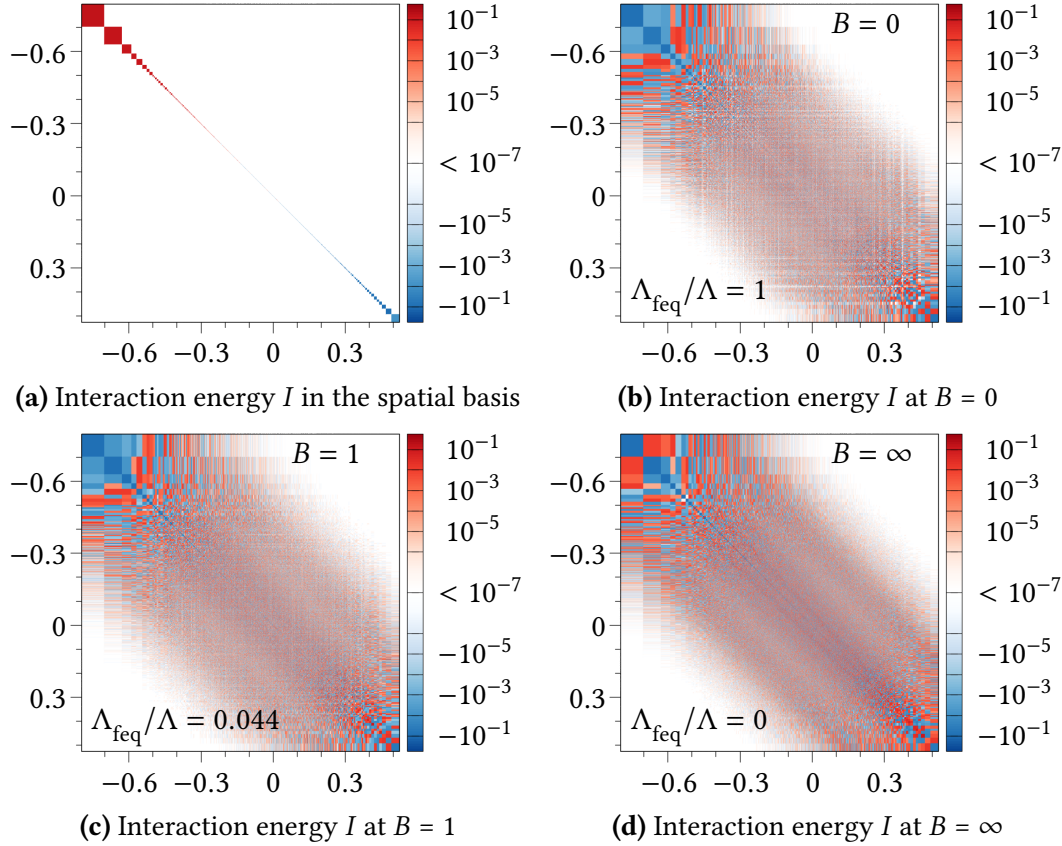


Figure 5.14: Interaction energy for $L = 18$ in the symmetry sector $(k, p, z) = (0, 1, 1)$ (a) in the spatial basis, (b) at $B = 0$, (c) at $B = 1$ and at $B = \infty$. In the spatial basis the matrix only consists of diagonal matrix element due to the fact that density operators cannot change the state they are acted upon. The later progress of the flow does not show easily visible developments in the center of the matrix, but only at the edges.

states of an observable by comparing the IPR to the delocalization limit. The opposite point of reference is the localized limit, where only one basis state is needed and therefore $\text{IPR} = 1$.

5.2.1 Behavior of the observables over the flow

Before the flow starts the observables receive a similar treatment as the Hamiltonian, which means that they are constructed in the same spatial basis and then transformed using the same basis transformation into the integrable basis. Then, any resorting of the basis states, which is performed on the Hamiltonian, is also performed on the observable. This procedure yields an observable (or operator), which is in the basis of the flow B , i. e. $O(B)$. To improve readability only the interaction energy is depicted here, while the other matrices can be found in the appendix showing all observables in the spatial basis in Fig. B.4, at early flows in Fig. B.7 and at late flows in Fig. B.8. If $B = \infty$, the basis is the eigenbasis of the Hamiltonian and the matrix elements $\langle E_m | O | E_n \rangle$,

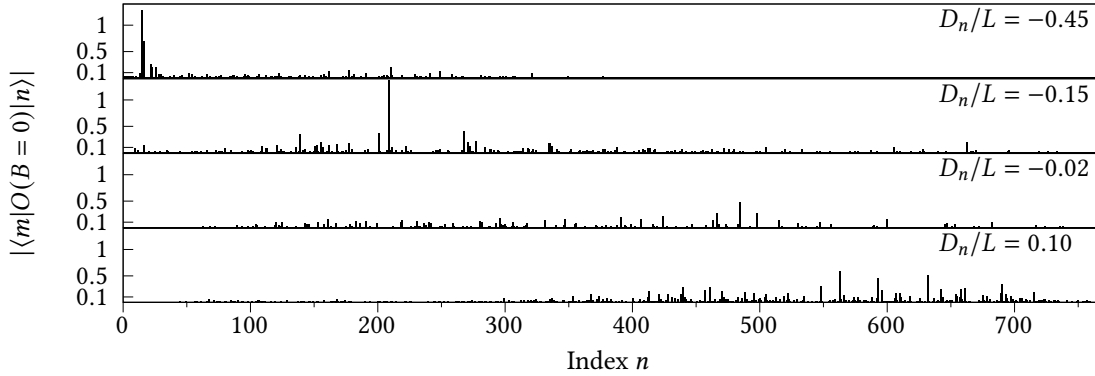


Figure 5.15: Vertical cuts through Fig. 5.14b at different energies per site D_n/L (for better visibility plotted over the indices n). The two top plots show all the matrix elements at the lower end ($D_n/L = -0.45$) and at the low-to-mid ($D_n/L = -0.15$) part of the bulk. Very few very large matrix elements dominate the picture. At the center of the bulk (bottom two plots) the matrix elements become smaller, but the number of matrix elements, which have an equally large value is higher.

which has been analyzed before (Santos and Rigol 2010a). As far as it can be compared, the findings from the literature agree with the ones here (e. g. Fig. 5.15).

To provide a better understanding of the structure of the observables over the flow the interaction energy I is depicted in the spatial basis, at $B = 0$, i. e. before the flow in the integrable basis, at intermediate flow $B = 1$ and at $B = \infty$, i. e. in the eigenbasis of the Hamiltonian. The matrix elements are not plotted with their indices, but over the corresponding value of the energy per site E_n/L , similar to the Hamiltonian. The first observation, which strikes the eye is that the interaction energy (as well as the other observables) already takes on a banded matrix form in the integrable basis, i. e. before the flow (Fig. 5.14b). Although one must be careful with the interpretation using the colored logscale for the matrix values, there are large white corners, which indicate exponentially small regions creating the band diagonal form. This becomes more clear, when the observables are compared to the observables in a random basis, i. e. in the basis, which is reached by a random unitary (see Fig. B.6a).

The localization measures are computed for a chosen column in the sense that they measure how many basis states are needed in order to express $O(B)|n\rangle$, where $|n\rangle$ corresponds to a chosen energy per site D_n/L . For $B = 0$ four vertical cuts are depicted in Fig. 5.15 for the four values of “energy per site”, which represent the lower end of the bulk, an intermediate region and the center of the bulk. It is not easy to capture all the matrix elements in one figure, because they vastly differ in size. Therefore, the cuts are also shown on a logscale in Fig. B.10, as well as for the other observables in Fig. B.9. The vertical cuts in Fig. 5.15 (see also the logscale plot in Fig. B.10a) show that at $B = 0$ and at the lower end of the bulk (top plot) very few very large matrix elements greatly outscale the majority of the rest, which means that the basis states at the energy, where the overlap is large, approximately describe the state $O|n\rangle$. Moreover, it is expected that these cases lead to a large localization, i. e. a large IPR and small Shannon entropy.

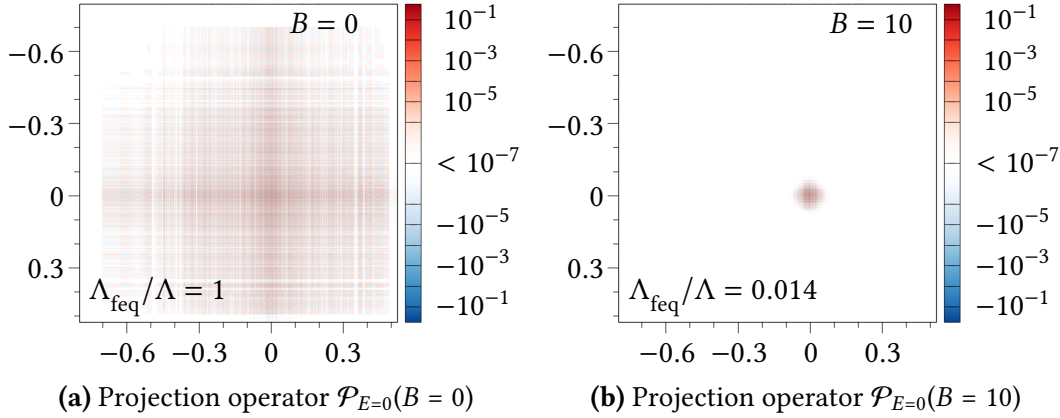


Figure 5.16: The projection operator $\mathcal{P}_{E=0}$ for the symmetry sector $(k, p, z) = (0, 1, 1)$ and $L = 18$ for the flows $B = 0$ and $B = 10$. (a) The dense structure that was present in the spatial basis (see Fig. B.5) is still visible at $B = 0$, although it appears to have lead to a strong concentration on the area, where the '1' can be seen at $B = \infty$ (The plot for $B = \infty$ is not shown, because a single 1 is not visible.) (b) At late flows the projection operator only consists of matrix elements in the vicinity of the projection.

In the bulk however, at $D_n/L = -0.02$ and $D_n/L = 0.1$, the number of equally large matrix elements increases, which in turn yields lower values of the localization.

A more detailed analysis shows that the dominating matrix elements are located on the main diagonal. This can be understood as the consequence of the construction of the flow and the fact that the sum of the kinetic and interaction energy is equal to the Hamiltonian. At late flows the Hamiltonian is approximately diagonal, such that the diagonal is very close to the eigenvalues of the system. Therefore, the absolute values of the Hamiltonian diagonal must be large in size compared to the rest of the matrix. Since $H = K + I$, the main diagonal elements of the kinetic and interaction energy must also be large in size with their off-diagonal elements having opposite signs (see also the IPR plot in Fig. B.12). Now, mathematically speaking, it could be that also the off-diagonal elements are large, but this is not to be expected, because both observables are found to fulfill ETH in the non-integrable case and therefore have exponentially small off-diagonal elements (Santos and Rigol 2010a). The work by Santos and Rigol (2010a) allows for a comparison of the vertical cuts through the observables here. The authors study the same observables in the EEV for the identical system at various next-to-nearest neighbor interaction V_2 . For $V_2 = 1$, which is close to $V_2 = 0.96$ used here, and a very large system ($L = 22$) they find at an energy density of approximately -0.15 that the EEV is extremely sharply peaked with respect to eigenstates, which are close in energy. This data point can be seen in Fig. 5.15 in the second plot, almost with the same amplitude, although it is for $B = 0$. However, as will be seen in the next part, the IPR seems to be stable over the flow indicating that this data point is related to the corresponding point in the energy eigenbasis at $B = \infty$. To contrast with results of the observables with an operator, which has no few-body structure, the projection operator is analyzed in the next parts, as well. It is shown in Fig. 5.16 and shows a

convergence to a singular '1' at the position of the eigenstate the projection is focused on (here $E = 0$).

5.2.2 Quantifying localization: IPR and Shannon entropy

This part addresses the analysis of the localization of the observables and the projection operator. The observation that the observables as depicted in Fig. 5.14 or the other observables in Fig. B.7 and Fig. B.8 do not change much over the flow is neither completely true nor wrong as it shall be explained in the following sections. But even more so, it is dangerous to deduce from the logscale plot and the very small dots in the center that a localization measure like the IPR or Shannon entropy as defined in Section 4.4 is constant everywhere. To study this in more detail the localization measure is computed for each column like the ones in Fig. 5.15, and plotted vs. the energy per site, e. g. $\text{IPR}(n) = \text{IPR}(D_n/L)$.

Inverse Participation Ratio IPR

The IPR for the four observables in the symmetry sectors $k = 0, L/2$ for the early flows $B = 0$ and $B = 1$ are depicted in Fig. 5.17 and for the late flows $B = 10$ and $B = \infty$ in Fig. 5.18. The other plots for the symmetry sectors $k \neq 0, L/2$ can be found in Fig. B.13 and Fig. B.14. The interpretation of the figures for $k = 0, \pi$ and $k \neq 0, \pi$ is similar, although the spread of the data points is reduced significantly for the symmetry sectors $k \neq 0, \pi$. The better convergence of the symmetry sectors $k \neq 0, \pi$ in the center of the spectrum has already been seen in other works, however, for the study of the IPR of an eigenstate in the momentum basis (Santos and Rigol 2010a).

The black lines denote moving averages of the different system sizes over windows of approx. 4% of the spectrum (dotted for $L = 16$, dash-dotted for $L = 18$, solid for $L = 20$ and dash-dash-dotted for $L = 22$). An immediate observation of looking at the overall picture of all 8 plots is that the moving averages of the IPRs of all observables are robust with respect to the flow. Even more so, it does not make a big difference, whether the flow is done or not, because the general behavior is often similar between $B = 0$ (before the flow) and $B = \infty$ (at the end of the flow). Besides a better convergence to the moving average, the IPR of early flows only differs from the IPR at $B = \infty$ in details, which shall be discussed in the following.

Interaction energy I The top row shows the interaction energy and displays an IPR, which heavily depends on the point in the spectrum that you look at. The majority of points near the lower end of the bulk of the spectrum have a larger IPR and, thus, are more localized than at the center of the bulk (infinite temperature). However, although the moving averages of the different system sizes do agree nicely, the variance around the mean is very large at early flows. It follows that for a single energy density D_n/L the vertical cut can look either very delocalized or localized. The variance is reduced over the course of the flow until the well-studied behavior in the energy eigenbasis (Santos and Rigol 2010a). Since the data points seem to converge

better the larger the system is, one expects that the IPR varies smoothly with the energy density in the thermodynamic limit. Finally, it can be seen that the center of the bulk becomes more delocalized the larger the system is. Later, in Section 5.2.4, a detailed discussion of this scaling is given. If the IPR is analyzed for an entire column $\langle m|O(B)|n \rangle$ without the largest element, it becomes clear that the largest element on the diagonal defines the form of the IPR (see Fig. B.12). Without it the IPR becomes flat.

Kinetic energy K The kinetic energy is very localized at the edges of the spectrum with a delocalized “dip” in a small region in the center of the bulk. The form of the IPR is heavily determined by the size of a single very large matrix element that is the diagonal element (see Fig. B.12b and also Fig. B.10b at $D_n/L = -0.45$). Since the matrix elements in the basis, which sorts the Hamiltonian, are also often sorted (as explained in Section 5.2.1), the IPR decreases with the shrinking matrix element on the diagonal (see second row in Fig. B.9b). A detailed analysis of the IPR without the dominating matrix element confirms this and yields a flat IPR (parallel to the x axis, not shown in this thesis). In the delocalized bulk section, where the sorted eigenvalues change from negative to positive, the diagonal matrix element is similar in size to the off-diagonals, such that no dominating element is present and the IPR is small (see Fig. B.10b).

Momentum distribution function $n(k = 0)$ The IPR of the momentum distribution function is more independent of where one looks at it. The value of the IPR indicates that no part of the spectrum is specifically localized or delocalized. Overall, the size suggests a delocalization, which does not change with the system size, hence hinting at no exponential growth of the occupied Hilbert space (see next section for the detailed analysis). The spread of the data points seem to reduce like for the other observables the larger the system is. It is remarkable, however, that the observable displays a similar behavior in both the integrable and the eigenbasis of the Hamiltonian. This can be understood as a degree of robustness against unitary transformations.

Density-density structure factor $N(k = \pi)$ The behavior of the density-density interaction is similar to the behavior of the momentum distribution function. The IPR suggests that the observable is delocalized to a certain extent and is very robust with respect to the present transformations.

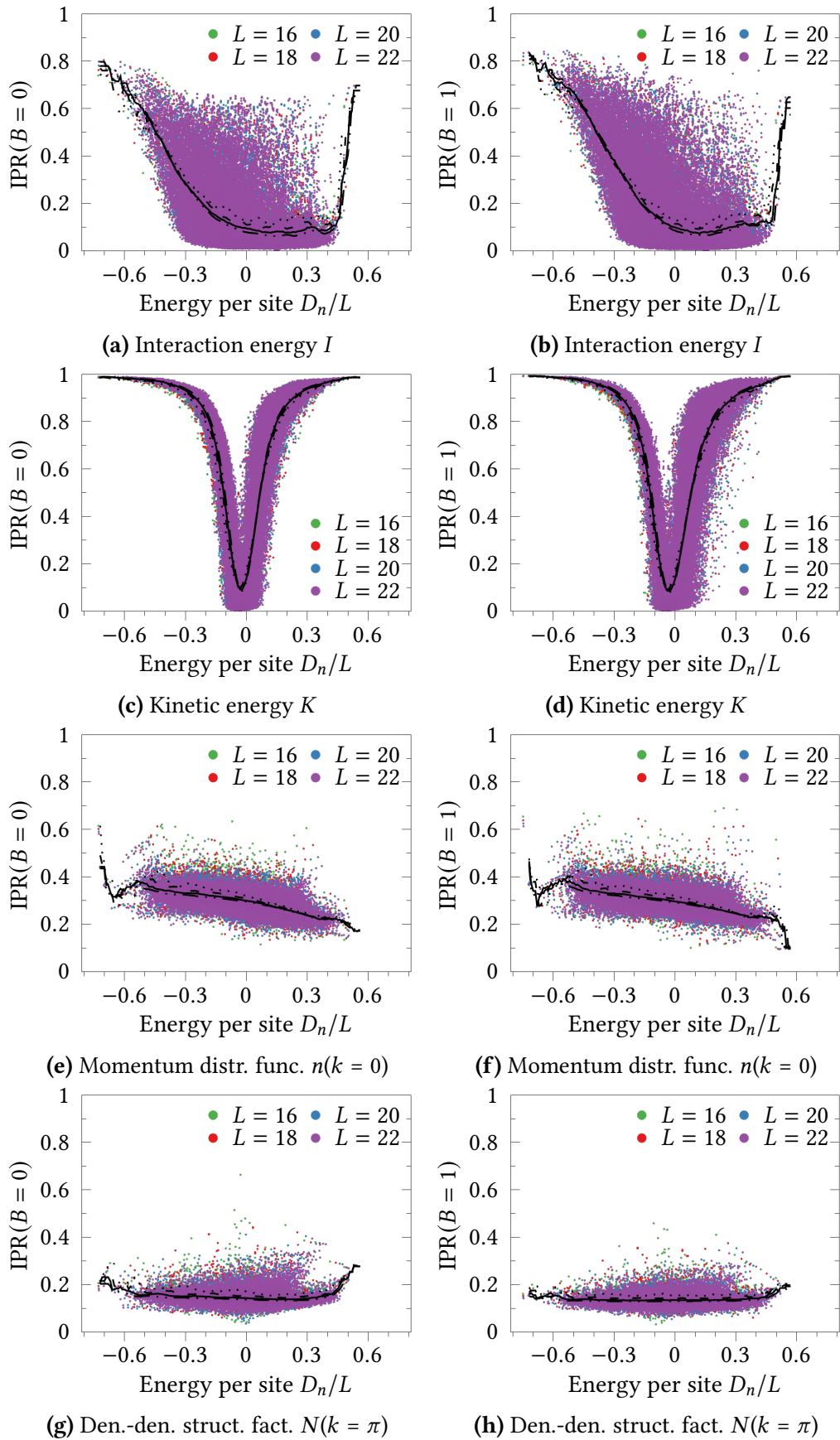


Figure 5.17: The IPR for all observables and a moving average (black) over a window of size 0.06 ($\approx 4\%$ of the spectrum) for the symm. sectors $n_k = 0, L/2$ and an early flow.

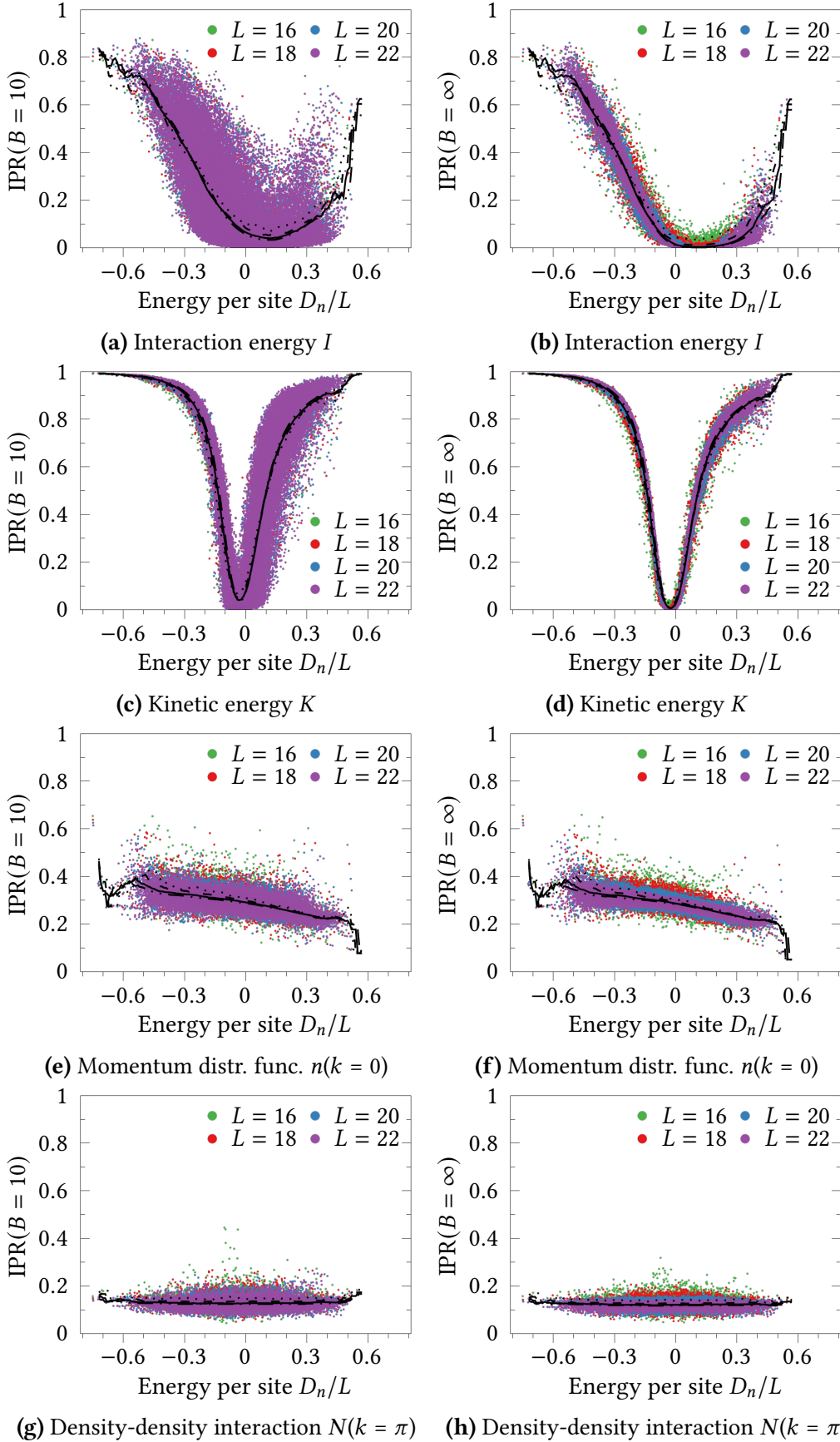


Figure 5.18: The IPR for all observables and a moving average (black) over a window of size 0.06 ($\approx 4\%$ of the spectrum) for the symm. sectors $n_k = 0, L/2$ and a late flow.

The only results from the literature these results for the IPR of the observables can be compared to is the analysis of the IPR of eigenstates in the momentum basis (Santos and Rigol 2010a), to the IPR of eigenstates in the integrable basis when t_2 is used as the integrability breaking term (Santos and Rigol 2010b) or to the same system with different parameters and filling (Rigol and Santos 2010). For states the IPR is defined in a slightly different way (see Eq. (4.28) in Section 4.4), however the interpretation remains identical. Santos and Rigol (2010a) have studied the IPR (specifically $1/\text{IPR}$ as defined here) for eigenstates in the momentum basis and find that the energy eigenstates delocalize in the center of the spectrum, whereas they are localized at the edges, i. e. in the low-energy region. Likewise it has been shown by Santos and Rigol (2010b) that the same behavior holds for the IPR of eigenstates in the integrable basis, if $t_2 > 0.96$ is used as the integrability breaking term (and not V_2 as here). This complexity, i. e. the delocalization of the eigenstates, in the center of the spectrum in the momentum or integrable basis, has been proposed to help achieving thermalization along the lines of Berry's conjecture (Santos and Rigol 2010b). Their results can be related to the study of the IPR in this work through the following argument. The observable in the flow or initial basis $|i\rangle$ is related to the eigenbasis $|E_n\rangle$ via

$$\langle i|O|j\rangle = \sum_{n,m} \langle i|E_m\rangle \langle E_m|O|E_n\rangle \langle E_n|j\rangle. \quad (5.6)$$

Since $\langle E_m|O|E_n\rangle$ is strongly peaked for eigenstates close in energy (Santos and Rigol 2010b; Rigol 2009a), a large delocalization of the eigenstates in the chosen basis, as e. g. observed by Santos and Rigol (2010b), means that $\langle i|O|j\rangle$ is very much delocalized, as well. To see this analytically, one can consider the artificial extreme case, where one assumes the perfect delocalization of the eigenstates $|\langle i|E_m\rangle| \propto 1/C$ for all i, E_m in the center of the spectrum and C large and $\langle E_m|O|E_n\rangle \approx O_{nn}\delta_{mn}$ neglecting the off-diagonal matrix elements. In this case, it follows that

$$\langle i|O|j\rangle \propto \frac{1}{|C|^2} \sum_n O_{nn} \quad (5.7)$$

would be delocalized in the center of the spectrum, as well. This could be the starting point for a further analysis. Overall, one can note that observables, which are closely related to the Hamiltonian and therefore to the eigenstates like the kinetic energy and the interaction energy, do show delocalization behavior in a related sense to the behavior that has been observed for the eigenstates in the momentum and integrable basis.

Projection operator

In the next step, the IPR of the observables is contrasted with the IPR of the projection operator. The projection operator neither thermalizes nor has a few-body structure (see Section 2.2 and D'Alessio and Polkovnikov (2013)). The IPR of the projection operator is depicted in Fig. 5.19 and indicates a strong delocalization in the integrable basis before the flow (for the other symmetry sectors see Fig. B.16). Over the course

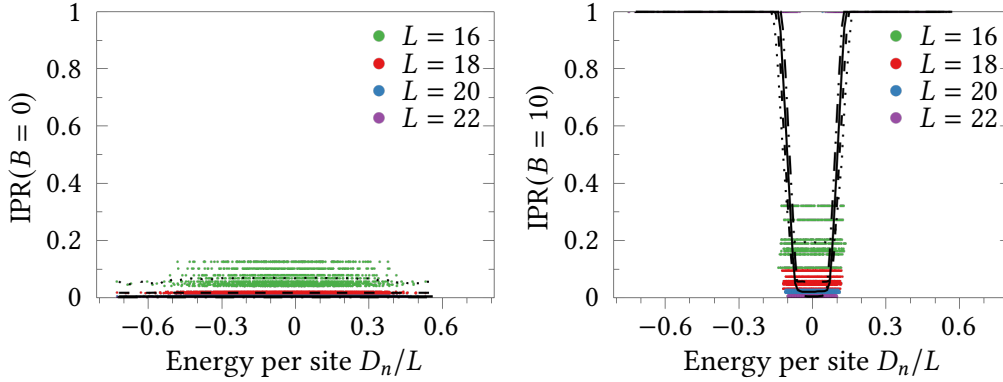


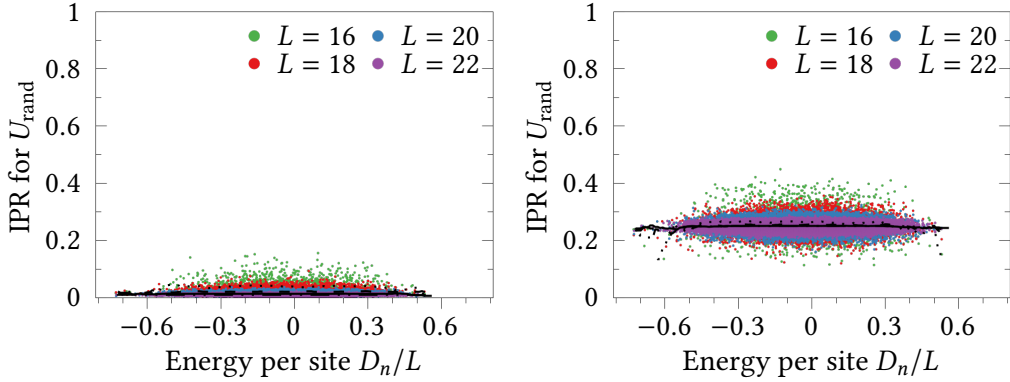
Figure 5.19: The IPR for the projection operator $\mathcal{P}_{E=0}$ and a moving average (black) over a window of size 0.06 ($\approx 4\%$ of the spectrum) before the flow ($B = 0$) and at $B = 10$ for the symm. sectors $n_k = 0, L/2$.

of the flow all other matrix elements rotate out leading to a complete localization beginning at the edges (The IPR of vanishing values is defined to be 1). The convergence to a small area around the singular '1' at $B = \infty$ (see Fig. 5.16b) does increase the IPR continuously until the entire matrix is fully localized.

Comparison to random unitary flow

Finally, the IPR of the four observables and the projection operator over the Wegner flow are compared to the IPR in a random basis reached via U_{rand} . Since a random unitary transformation yields a random sorting of the basis states, the IPR is expected to be flat, i. e. to barely depend on the energy per site D_n/L . This can be seen in Fig. 5.20, which shows the IPR of the interaction energy and the momentum distribution function in a random basis. It turns out that the flatness of the IPR is present for all observables (see Fig. B.15). How much an observable is delocalized, however, depends on the observable. The momentum distribution function in Fig. 5.20b and the density-density structure factor are more localized in the random basis than the interaction and kinetic energy, although not as much as over the flow (see Fig. 5.17 and Fig. 5.18). The difference of the IPR of the kinetic and interaction energy between the regular and the random flow is clearly visible. The scaling analysis in Section 5.2.4 will show, whether the delocalization is truly extensive (i. e. it grows with the Hilbert space dimension) or not.

The observation that the observables are affected by the random unitary transformation in different ways is surprising, because, without further knowledge, one could assume that all observables do differentiate a random basis from a distinguished basis like the eigenbasis of H (at $B = \infty$) or the integrable basis (at $B = 0$). However, the finding that the two observables $n(k = 0)$ and $N(k = \pi)$ demonstrate a high robustness of the IPR with respect to the underlying basis means that for them already a special basis like the eigenbasis is only slightly different from a random basis. This is different for the other two observables, where the IPR's behavior is completely destroyed. One



(a) Interaction energy I in a random basis ($n_k = 0, L/2$) (b) Mom. distr. func. $n(k = 0)$ in a random basis ($n_k = 0, L/2$)

Figure 5.20: (a) The interaction energy I in a random basis and (b) the momentum distribution function $n(k = 0)$. The IPR of the interaction energy takes on a complete different form compared to the one of the Wegner flow in Fig. 5.17a. (a) The transformation into a random basis via random unitary delocalizes the entire observable. The scaling with respect to the system size is studied later. (b) The momentum distribution function is robust with respect to the random transformation (see Fig. 5.17e. In that sense it can be understood of not distinguishing much between the integrable basis, the energy eigenbasis or a random basis.

explanation for this is that the close relation of the interaction and kinetic energy to the Hamiltonian defines the IPR of the regular flow. As it has been discussed before, one finds that the Hamiltonian maintains a main diagonal, which is very large in size compared to the off-diagonal matrix elements throughout the flow. As K and I , i. e. both parts of the Hamiltonian, must add up to yield the large diagonal, it is expected that the size of the diagonal matrix elements determines large IPRs at the edges of the spectrum for both K and I . In a random basis, this property is not required such that the delocalization can be strong.

The projection operator in the random basis does delocalize strongly (see Fig. B.17). There is no property, which would suggest a different behavior, because it is already very much delocalized in the initial integrable basis.

Shannon entropy

The other quantity, which is often used to measure localization, is the Shannon or information entropy as defined in Eq. (4.31) (Santos and Rigol 2010b; Rigol and Santos 2010). It is useful to look at the Shannon entropy, because in combination with the IPR (sometimes even defined together as the quantity *structural entropy*) both can discover information, which is inaccessible for the other quantity, especially in the delocalized region (Santos and Rigol 2010a). It is important to note that the Shannon entropy ranges between 0 (completely localized) and $\ln D$ (completely delocalized), where D denotes the dimension of the Hilbert space (Section 4.4). Broadly speaking, it can be

interpreted like $1/\text{IPR}$. As almost all results of the IPR do agree with the results of the Shannon entropy, they are only briefly discussed and can be found in the appendix. The Shannon entropy of the four observables before ($B = 0$) and after the flow ($B = \infty$) are depicted in Fig. B.18 for the symmetry sectors $k = 0, \pi$ and in Fig. B.19 for all other symmetry sectors. The interpretation of the Shannon entropy agrees with the previous findings for the IPR. All observables share the behavior that the spread of the data points is reduced over the flow to yield a smooth appearance, which is appropriately expressed by the moving averages. The values for the Shannon entropy in symmetry sectors $k \neq 0, \pi$ are already well converged at $B = \infty$, such that the development over the flow is even smaller (Fig. B.19).

The interaction energy at $B = \infty$ displays a very distinct scaling in the upper center of the bulk of the spectrum, which identifies a region where the observable becomes more delocalized over the flow. This has also been seen in the corresponding IPR plot in Fig. 5.18b. It grows over the flow and is studied in detail in the next section.

The same holds true for the kinetic energy, where a thin region in the bulk of the spectrum scales with the system size, whereas the edges remain localized.

The Shannon entropy of the momentum distribution function and the density-density structure factor, though, do not change much over the course of the flow. A behavior, which has already been seen in the IPR in Fig. 5.17 and Fig. 5.18. Beyond the smaller broadness of the data points both observables show a slight delocalization in the bulk of the spectrum.

Also the projection operator $\mathcal{P}_{E=0}$ in Fig. B.21 shows the expected behavior, which is reciprocal to the behavior for the IPR due to the definition of the Shannon entropy.

The Shannon entropy in the random basis displays flat regions like for the IPR, but this time in a reciprocal way as plateaus.

The important scaling over the lattice sizes is done in Section 5.2.4.

5.2.3 IPR over flow

The previous Section has shown that both localization measures are not expected to change much over the flow. Therefore, it is sufficient to show only the IPR over the course of the flow for the interaction energy and the kinetic energy, because in those cases the changes are largest. To show the development of the IPR the moving average of the IPR is plotted at different values of “energy per site”. Moreover, the moving average is rescaled to the value of $\text{IPR}(B = 0)$ of the system $L = 18$ in order to identify whether different lattice sizes converge to different points. The IPR over the flow for the interaction and kinetic energy is shown in Fig. 5.21. The other observables, as well as the projection operator, show a similar behavior, which is why they are not provided here. This holds also true for the Shannon entropy.

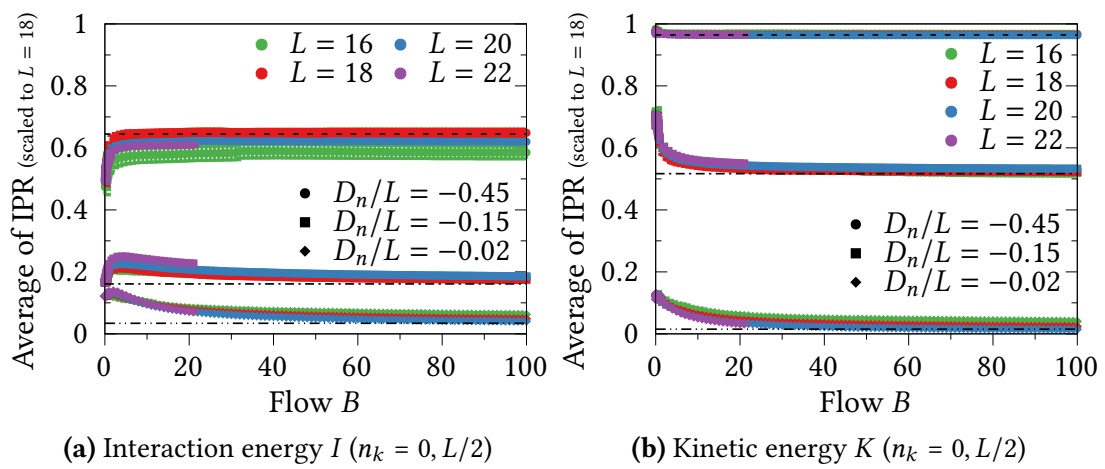


Figure 5.21: IPR over flow for (a) the interaction energy and (b) the kinetic energy for different values of energy per site D_n/L in the symmetry sectors $k = 0, \pi$. The displayed value is the moving average of the IPR in the figures of the previous section. All points are rescaled to the value $\text{IPR}(B = 0)$ of the system with $L = 18$ in order to identify different scalings. The black lines describes the value at the end of the flow, i. e. the $\text{IPR}(B = \infty)$. The energies per site $D_n/L = -0.45, -0.15, -0.02$ correspond to the low-end, low-to-mid, center of the bulk of the spectrum. The IPR can be seen to be quite stable over the course of the flow. The bad scaling in the left plot for $D_n/L = -0.45$ results from the energy density to be too low such that the moving average is not well defined (see Fig. 5.18a and Fig. 5.18b).

5.2.4 Scaling of the localization measures

It is believed that the ETH holds for few-body observables, which are observables that only contain terms with a limited product of operators (D'Alessio and Polkovnikov 2013). A term can only contain a number of operators, which is not extensive, i. e., which is not proportional to the system size. In the following the scaling for both the IPR and the Shannon entropy is analyzed to detect, whether the Hilbert space that an observable populates grows extensively or not. Since both measures have a distinct limit for localization and delocalization, it is possible to compare the numerical data with these limits. For the IPR the fully delocalized limit is given by 1 over the Hilbert space dimension D of the symmetry sectors, i. e. $\text{IPR} = 1/D$ (the Hilbert space dimensions are averaged over the included symmetry sectors). In this limit all elements are identical in size and hence the observable is completely delocalized. The localized limit occurs when only one element is non-zero, which leads to $\text{IPR} = 1$. For the Shannon entropy the corresponding limits are given by 0 (localized) and $\ln(D)$ (delocalized) (see Section 4.4). In the following figures the delocalized (localized) limit is depicted via a dash-dotted (dashed) line. In addition, one can compare the scaling to the scaling of a random matrix taken from the GOE, which is known to scale as $3/D$ for the IPR and $\ln(0.48D)$ for the Shannon entropy (Izrailev 1990; Zelevinsky et al. 1996) (see also Section 4.4).

Scaling of the IPR

Figure 5.22 shows the scaling of the averages of the IPR with respect to the lattice sizes for the four observables at (left) $B = 0$ and (right) $B = \infty$ over a logscale axis and the symmetry sectors $k = 0, \pi$. Additional plots for $B = 0$ (Fig. B.23), $B = 10$ (Fig. B.24) and $B = \infty$ (Fig. B.25) including all symmetry sectors can be found in Appendix B. Full points in Fig. 5.22 denote the Wegner flow, whereas star symbols describe the values obtained using a random unitary transformation U_{rand} . Since Hilbert space dimensions scale exponentially with system size, i. e. $D \propto \exp(L)$, the IPR is depicted using a logscale. It follows that if the IPR scales parallelly to the slope of the delocalized limit $1/D$ the number of elements that contribute to the IPR also grow exponentially with L , which indicating the loss of the few-body structure. On the other hand, if the IPR is parallel to the abscissa, i. e. constant, it does not scale with the growth of the Hilbert space dimension indicating that its structure does not change.

The scaling of the IPR is depicted for the same four different fractions of “energy per site” D_n/L , which have been analyzed in the previous parts. Hereby, $D_n/L = -0.45$ represents the lowest end of the bulk, $D_n/L = -0.15$ the low-to-mid part and $D_n/L = -0.02$ and $D_n/L = 0.1$ the central parts of the bulk behavior of the spectrum. The last two points are chosen, because the kinetic energy (interaction energy) delocalizes the most at $D_n/L = -0.02$ ($D_n/L = 0.1$) (see Section 5.2.2).

Comparing the left side of Fig. 5.22 to the right side means comparing the scaling of the IPR at $B = 0$ to $B = \infty$. The first impression one gets is that there are almost no differences between the the observables except for the bulk of the spectrum in the top two rows, which show the scaling of the IPR of the interaction energy and the kinetic energy. Hence, it can be concluded that in most cases it does not matter at what flow value B the scaling is studied. In the following, the details of the scaling are discussed. It follows that neither the Wegner nor the random unitary flow do destroy the localization of the observables by much. Since this Section analyzes the scaling of the localization measures, it is sufficient to mainly focus on a single flow B .

Interaction energy I The interaction energy I (top row) shows ambiguous behavior, because at the lower end of the bulk of the spectrum ($D_n/L = -0.45$ and $D_n/L = -0.15$) the IPR scales as the localized limit, i. e. parallel to 1. However, at $B = \infty$ and in the center of the bulk at $D_n/L = 0.1$, where I has been seen to be delocalized, the scaling of the IPR is parallel to the delocalized limit (triangular shaped points). The intermediate value at $D_n/L = -0.02$ fills the gap. Although close to parallel at $B = 0$, the slope for $D_n/L = -0.15$ shrinks over the flow, but not to an extent that it falls off like the delocalization limit. In contrast, it seems to follow the behavior of the random unitary transformation (empty points), which has a clear convex development to the localization axis indicating a polynomial behavior. It is, however, striking that the random unitary transformation does not yield the scaling of a delocalized observable. It seems as if the structure of the interaction energy is too robust to be changed by any transformation. In the symmetry sector $k \neq 0, \pi$ the center of the bulk is already delocalized at $B = 0$ (Fig. 5.23a). This means that in this case the flow barely changes the structure of the observable.

Kinetic energy K The kinetic energy K (second row) does not lose its few-body structure over the flow, because for the more central parts of the bulk of the spectrum the IPR scales as the localized limit, i. e. parallel to 1. The only cut, which behaves slightly different, occurs at the energy per site $D_n/L = -0.02$, where the observable is delocalized the most. Although parallel at $B = 0$, the slope shrinks over the flow, but displays a subexponential falloff.

Another striking feature is that the IPR of the kinetic energy in a random basis is identical to the IPR of a random matrix and therefore falls off exponentially. This means that the kinetic energy in a random basis loses its few-body structure and looks like a random matrix of the GOE. The structure of the kinetic energy seems to be much more susceptible to a transformation into a random basis. In the symmetry sector $k \neq 0, \pi$ the momentum distribution function seems to be more delocalized in the center of the spectrum, however, without an extensive population of the Hilbert space.

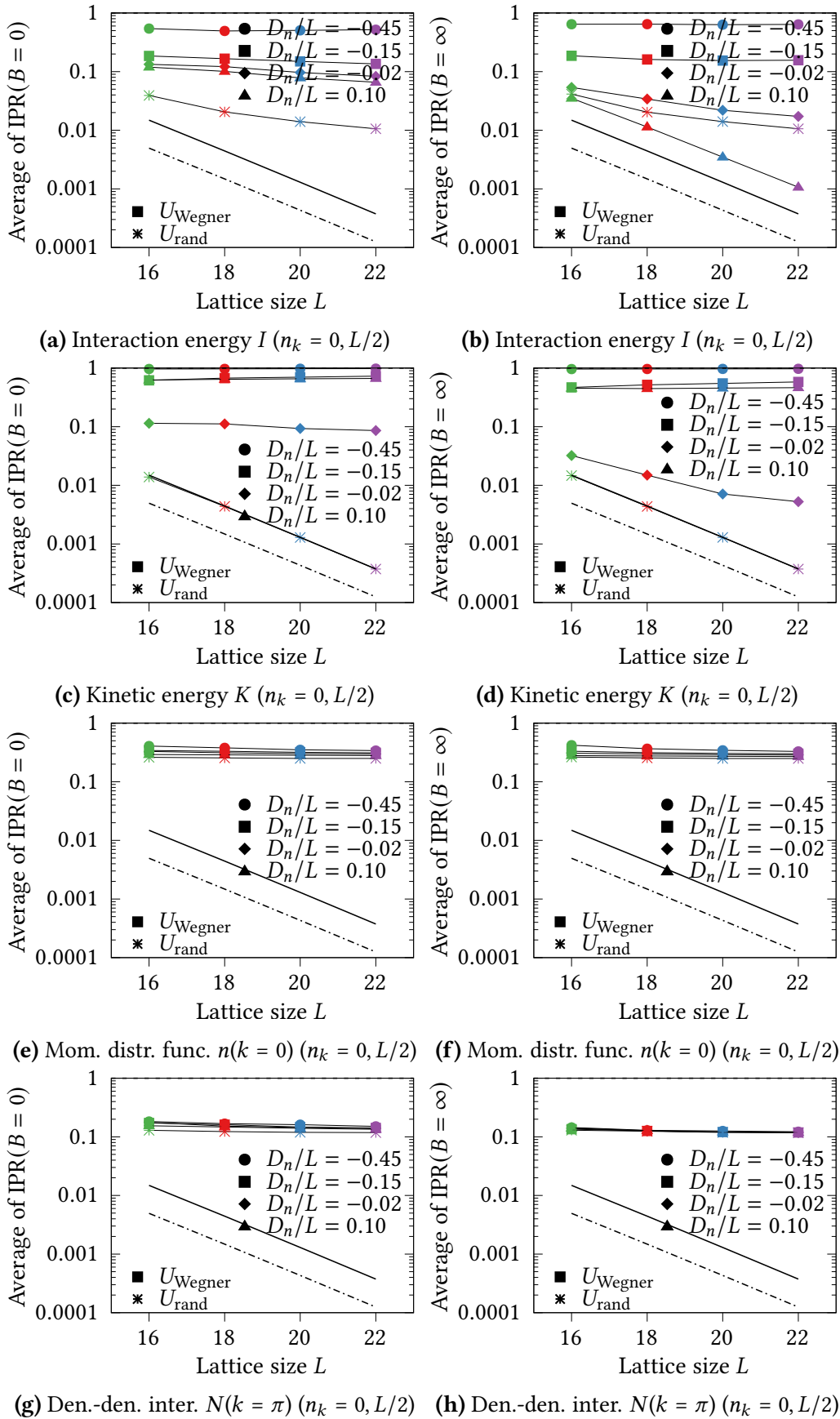


Figure 5.22: The scaling of the IPR over lattice sizes for different energy densities and all observables and the symmetry sectors $n_k = 0, L/2$ at (left) $B = 0$ and (right) $B = \infty$.

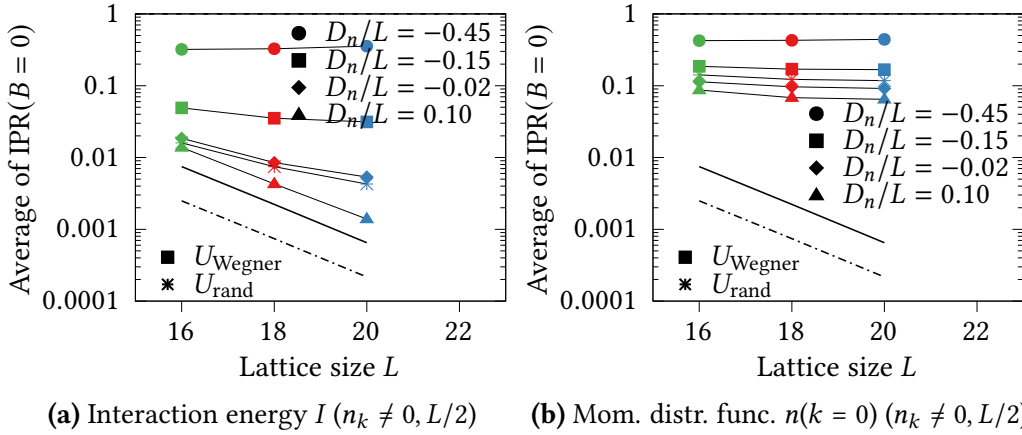


Figure 5.23: The scaling of the IPR over lattice sizes of the (left) interaction energy and (right) momentum distribution function for different energies per site and in the symmetry sectors $n_k \neq 0, L/2$ at $B = 0$. (a) In all other symmetry sectors than $k = 0, \pi$ the scaling of the IPR is already extensive at $B = 0$ in the center of the spectrum (compare with Fig. B.23a). (b) The center of the bulk of the spectrum is more delocalized than the edges of the bulk. The scaling is not parallel to the delocalization limit and, hence, not extensive (compare with Fig. B.23e).

Momentum distribution function $n(k = 0)$ The momentum distribution function remains localized throughout the flow and does not lose its few-body structure. Moreover, it seems as if the amount of delocalization is independent from the position in the spectrum in the symmetry sectors $k = 0, \pi$. In all other symmetry sectors, however, it becomes more delocalized in the bulk of the spectrum as depicted in Fig. B.23 ($B = 0$), Fig. B.24 ($B = 10$) and Fig. B.25 ($B = \infty$). The scaling is not extensive, though. In summary, one finds that the “few-bodiness” is not lost through a random transformation. The observable looks more delocalized in a random basis (logscale) for all areas in the spectrum in all symmetry sectors, except for the center of the bulk of the spectrum if $k \neq 0, \pi$.

Density-density structure factor $N(k = \pi)$ The same holds true for the density-density structure factor. Here, the flow causes the same amount of delocalization as a random unitary transformation in the symmetry sectors $k = 0, \pi$, because the plots lie on top of each other. If $k \neq 0, \pi$, though, the bulk displays a larger delocalization.

Projection operator $\mathcal{P}_{E=0}$ The scaling of the IPR of the four observables in Fig. B.23 is clearly different from the scaling of the IPR of the projection operator $\mathcal{P}_{E=0}$ in Fig. 5.24. While the observables clearly show their few-body structure at $B = 0$, the projection operator is completely delocalized as expected. Later, when more and more regions are rotated out by the flow, only a small region around the projection survives, which leads to full localization of a growing part of the spectrum (IPR of zeros is defined as 1). At $B = \infty$ only a single matrix element is non-zero: the ‘1’ at energy per

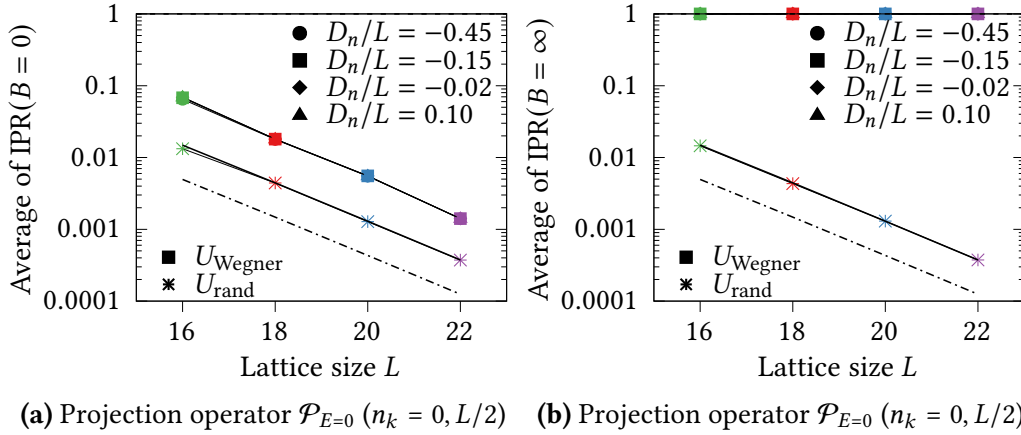


Figure 5.24: The scaling of the IPR over lattice sizes for the projection operator $\mathcal{P}_{E=0}$ for different energy densities and the symmetry sectors $n_k = 0, L/2$ at (left) $B = 0$ and (right) $B = \infty$.

site $D_n/L = 0$, which means full localization.

The IPR of the projection operator in a random basis lies on top of the line indicating the IPR of a matrix from the GOE. As the projection operator is simple, this is a rare case, where one can find analytical arguments for this behavior. When performing a random unitary transformation the starting basis does not matter, because any other basis transformation could be seen as a consecutive transformation of the random transformation. Hence, one could also begin in the basis at $B = \infty$, where only a single '1' is present at index l in the matrix. If this is transformed via a random unitary matrix with matrix elements u_{mn} , the resulting transformed matrix has the matrix elements $u_{lm}u_{ln}$, where m and n denote the row and column and l is fixed by the position of the '1'. Thus, one ends up with a full matrix, which elements are products of random variables, which need to fulfill the unitarity of U_{rand} , though (Brody et al. 1981). Since u_{ln} is present in every element in column n and can be factorized, one finds that the IPR is that of a random unitary matrix, which is $3/D$ (Zelevinsky et al. 1996).

Scaling of the Shannon entropy

The figures for all observables and symmetry sectors can be found in Fig. B.28 for $B = 0$ and in Fig. B.29 for $B = \infty$. The interpretation of the plots agrees in many cases with the interpretation of the IPR in the previous chapter, although they can be less conclusive for the Shannon entropy. As an example the scaling of the Shannon entropy of the kinetic energy, which is depicted in Fig. 5.25 at (a) $B = 0$ and (b) $B = \infty$ in the symmetry sector $k = 0, \pi$, is discussed. The corresponding scaling of the IPR in Fig. B.29c is found to signal localization everywhere in the spectrum and at all flows. The Shannon entropy in this case, however, boasts a line already at $B = 0$, which, albeit not being parallel to the delocalization limit, seems to lack any curvature. Even more so, at $B = \infty$ in Figs. B.29c and B.29d, it seems to be almost parallel to the delocalization limit. Thus, it is not clear, whether the data for this part of the spectrum can be completely trusted.

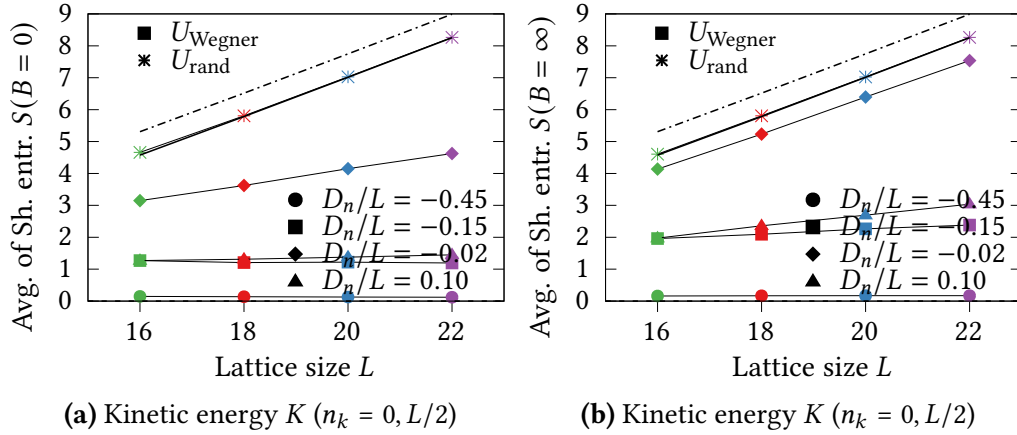


Figure 5.25: The scaling of the Shannon entropy of the kinetic energy versus lattice size for different regions in the spectrum and in the symmetry sectors $k = 0, \pi$ at (left) $B = 0$ and (right) $B = \infty$. The delocalized limit is depicted with the dash-dotted black line and the GOE value by the solid black line. A concave form of the scaling would indicate a subexponential scaling of the Shannon entropy, hence, signaling localization. The data points for $D_n/L = -0.45$ and $D_n/L = -0.15$ have this behavior, whereas the center of the spectrum is parallel or close to parallel to the delocalization limit.

The cuts at the lower end of the spectrum including the lower end of the bulk, though, confirm the interpretation of the IPR results that the observables retain their few-body structure throughout the flow.

The same interpretation can be applied to the interaction energy in Fig. B.29a and Fig. B.29b. Only at $D_n/L = -0.45$ and $D_n/L = -0.15$ a concave curvature hinting at subexponential scaling can be assumed.

For the other observables the picture is identical. They also feature the interesting fact that some regions in the spectrum delocalize more than the same observable in a random unitary basis, if $k \neq 0, \pi$ (see e. g. Fig. B.19f).

5.2.5 Summary of the localization scaling analysis

The analysis of the scaling of both localization measures is summarized as follows. The IPR data suggests that the interaction energy and the kinetic energy retain their few-body structure except for the center of the bulk of the spectrum, i. e. for high energy eigenstates. This can also be seen in the case of the momentum distribution function and the density-density structure factor. In general, it is found that the observables in the symmetry sectors $k = 0, \pi$ are always more localized than in the other symmetry sectors, i. e. $k \neq 0, \pi$. This has also been seen in other works, although for the IPR of different quantities (IPR of eigenstates in a specific basis) (Santos and Rigol 2010a). The explanation for this is that the symmetry sectors $k \neq 0, \pi$ are larger, in fact approximately twice as large, as their pendants at $k = 0, \pi$, which means that a bigger Hilbert space is available for possible delocalization. Following this line of thought, the curvature of the IPR observed in the symmetry sector $k \neq 0, \pi$ at large system sizes,

which is interpreted as signaling localization, can be regarded as a strong indicator for localization.

The scaling of the localization measures of the observables in a random basis offers additional insights beyond being a benchmark test. First of all, it is seen that the level of delocalization of the interaction energy, the momentum distribution function and the density-density structure factor in a random basis does not coincide with the corresponding value of a random matrix from the GOE (solid black lines). This is not completely surprising, because a random matrix consists of independent random variables, which do not have any correlation like one can assume for any physical observable. This does not only include the setup in the spatial basis, but also the preflow transformation with a matrix of orthonormal basis states. At the same time, though, it is visible that these three observables in a random basis often show a similar behavior like their counterparts obtained through the Wegner flow. The level of delocalization is often comparable, but mostly smaller in random basis. Hence, it can be concluded that the observables do not strongly distinguish the Wegner flow from random unitary transformation. Here, the only exception is the kinetic energy in the random basis, which displays a drastically different form of the IPR. Primarily, the scaling is found to be extensive in Hilbert space and thus the few-body structure of the kinetic energy is destroyed in the random basis. In fact, this is also the only case, where the localization measures in a random basis agree with the GOE prediction. In other words, it can be deduced that the kinetic energy takes on a form in a random basis, where its matrix elements appear to have no correlation among each other and look like a random matrix. While this behavior can be demonstrated analytically for the projection operator (see below), no such methods are known for this case. It remains an open question, which requires further studies.

Finally, it remains to summarize the analysis of the projection operator, which matches the expectation. Initially, the operator is delocalized over an extensive region of the Hilbert space until the flow converges and a fully localized '1' is left. In a random basis the operator delocalizes to the GOE value, which can be understood using analytical arguments (see Section 5.2.4).

5.3 Preflow transformation to the momentum basis

The basis of the Hamiltonian before the flow (preflow) in the previous chapters has been the integrable (mean-field) basis. In this basis the Hamiltonian consists of an integrable diagonal part and an off-diagonal part, which is proportional V_2 and breaks the integrability. Another possibility, which is often used, is to transform the Hamiltonian into the momentum basis ([Santos and Rigol 2010a,b](#)). In the momentum basis the kinetic energy of the Hamiltonian is diagonal, such that the off-diagonals are determined by the interaction V_1 and V_2 . To provide a full picture the results of a flow starting in the momentum basis are presented in this chapter.

5.3.1 Statistical analysis of the Hamiltonian

As in the previous case, a statistical analysis is performed with respect to the Hamiltonian at different points of the flow. The histograms over the matrix elements of a band of 1% of the dimension of the matrix is depicted in Fig. 5.27 for $k = 0, \pi$ and in Fig. B.30 for $k \neq 0, \pi$. The visual check confirms that similar to the previous case, where the Hamiltonian started in the integrable basis, the matrix elements show a Gaussian distribution at later flows. To probe the normality of the data the Γ -quantity is computed like in the previous case. It is depicted in Fig. 5.26 and suggests normality for flows from $B = 20$. There is one major detectable difference to the previous case in Fig. 5.13. This time also the symmetry sector $k = 0, \pi$ shows clear normal distributed subdiagonals. Although this requires further analysis, it is proposed for the moment that in the momentum basis more “weight” is put on the off-diagonal, because it is not proportional to V_2 , but also to V_1 . In the integrable basis, only terms proportional to V_2 were “rotated out” to the off-diagonal, while all terms proportional to t_1 and V_1 are on the main diagonal only. In the momentum basis, both V_1 and V_2 terms are transformed to the off-diagonal, which might lead to a larger number of large values. These large values compare better to the main diagonal and lead to a normal distribution for only some iteration steps. Beyond this difference, the analysis does not show differences to the case studied in Section 5.1.5.

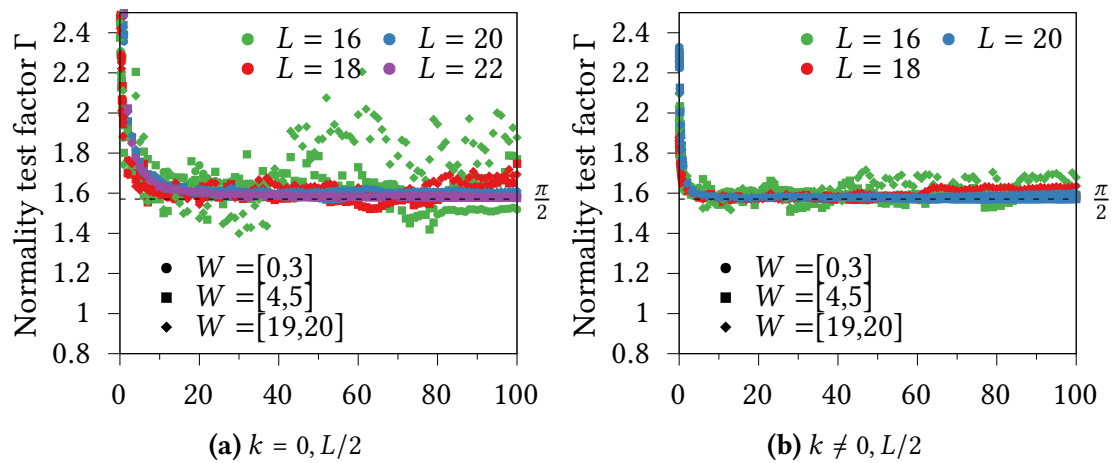


Figure 5.26: The Γ -normality indicator for three energy windows in units of s_1 over the course of the flow where the initial basis is the momentum basis in the symmetry sectors (a) $k = 0, L/2$ and (b) $k \neq 0, \pi$. For Gaussian distributed values it is $\Gamma = \frac{\pi}{2}$. It seems that the Γ -value of the data sets quickly converges to $\pi/2$ from above for all momenta sectors. The convergence seems to be better than in the case, when the Hamiltonian starts in the integrable basis.

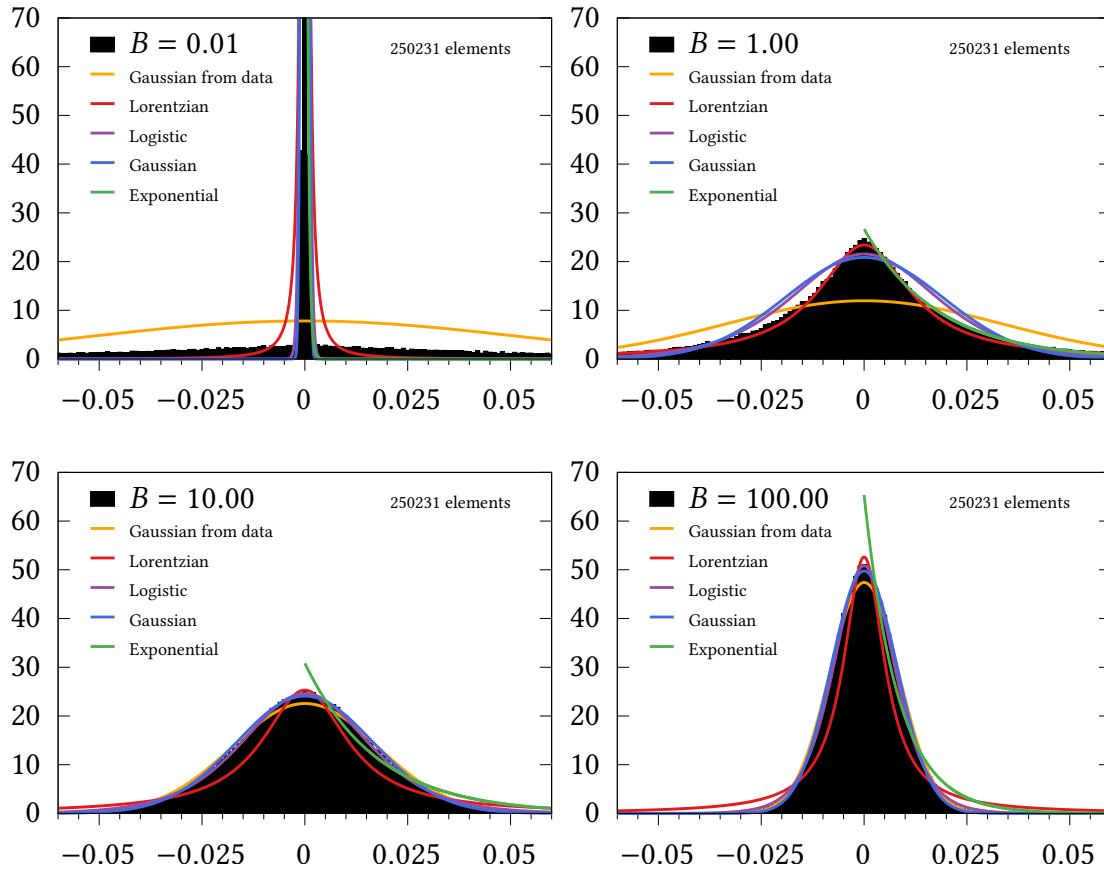


Figure 5.27: The preflow basis is the momentum basis. Histograms over the flow for a band comprising the closest 1% of subdiagonals for the symmetry sectors $k = 0, L/2$ and both other symmetry quantum numbers, i. e. $p = \pm 1, z \pm 1$ and lattice size $L = 20$. Each shows the relative frequency over bins of size 0.001. Initially, the sparsity of the matrix creates a huge overhang of vanishing matrix elements. The peak then broadens and resembles a Lorentzian distribution ($B = 1$), then an exponential distribution ($B = 10$) until it approximates a Gaussian or a logistic distribution due to the heavy tails. The orange curve shows the Gaussian that is defined by the mean and standard deviation of the corresponding data set.

5.3.2 Scaling of the IPR

The situation is identical for the analysis of the scaling of the IPR in Fig. B.32 and Fig. B.33, where extracts are depicted here for the interaction and kinetic energy in ???. While the scaling at $B = \infty$ does not differ from the corresponding counterpart for the integrable basis as the preflow basis (see Fig. B.23c), it features complete localization at $B = 0$. Since the preflow basis is the momentum basis, i. e. the eigenbasis of the kinetic energy, this is well expected. Overall, it turns out that a different preflow basis does not reveal any different behavior. In this way, it is similar to the localization analysis of the eigenstates in the integrable and momentum basis by Santos and Rigol (2010a) and other works (Rigol and Santos 2010; Santos and Rigol 2010b).

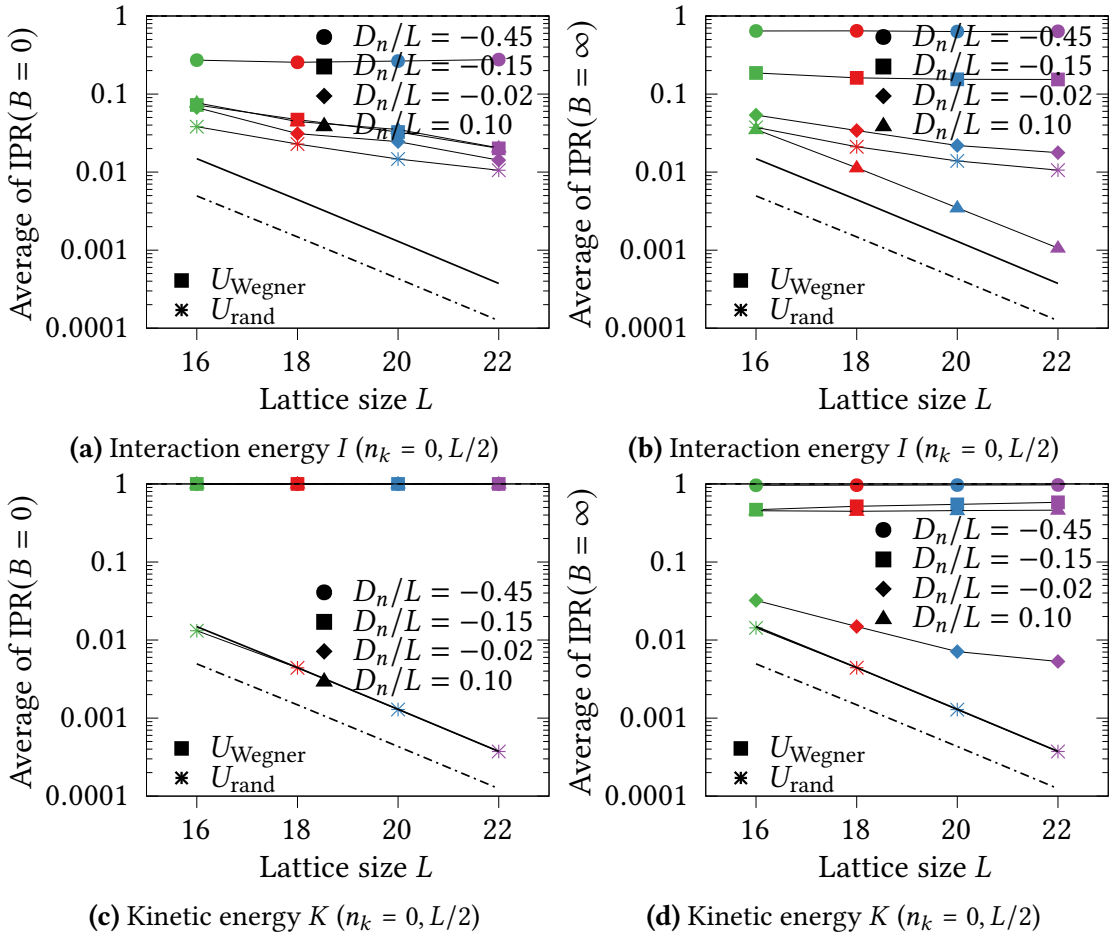


Figure 5.28: Scaling of the IPR for the interaction energy and the kinetic energy K at (left) $B = 0$ and (right) $B = \infty$ in the symmetry sectors $k = 0, \pi$. The preflow basis is the momentum basis. The interaction energy looks similar to the case in the integrable preflow basis. (c) The kinetic energy is diagonal and fully localized at $B = 0$, because it is initially in its eigenbasis. At the end of the flow there is no difference to the case in Fig. 5.22 for the integrable preflow basis.

Chapter 6

Conclusions

The project of this work was to justify the ETH for generic models using Deutsch's argument. The idea was to study, whether a microscopic Hamiltonian can fulfill the assumptions of Deutsch, such that his analytical reasoning for thermalization would be applicable. To demonstrate the requirements the Hamiltonian has to be brought into a banded form with specific statistical properties. Since a deterministic calculation can not yield true randomness, it is argued that a pseudo-random appearance, which can not be distinguished from the random version, is sufficient. Since the ETH is believed to hold for few-body observables, the structure of several observables is analyzed in the second part of the argument. If the observables display few-body properties, which are tested using localization measures, throughout the flow, the line of argument is complete and the thermalization of a generic model along the lines of Deutsch has been successfully motivated. The banded shape of the Hamiltonian of consideration is created using continuous unitary transformations defined by the flow equation. The starting point of the flow is the Hamiltonian of the full Hilbert space, which has been set up using exact diagonalization techniques. The flow is then performed numerically using the stable unitary integrator algorithm to preserve unitarity.

The chosen model is a one-dimensional lattice, which is half-filled with hardcore bosons. Together with periodic boundary conditions, this allows for taking advantage of all symmetries to split the exponentially large Hilbert space into feasible dimensions. Before the flow the Hamiltonian is transformed from the spatial basis to a preflow basis to comply with Deutsch's ansatz. Two initial basis are compared, i. e. the integrable and the momentum basis. Finally, all results are compared to the case of a random unitary transformation.

6.1 Banded pseudo-random Hamiltonian

The analysis of the Hamiltonian contained several steps. First of all, it was illustrated how fast the flow converges. After the initial depictions of fundamental statistical properties including the level statistics and how they develop over the flow, histograms over various windows and subdiagonals were analyzed visually. It was

shown that the symmetrically distributed data approximates different distributions depending on the flow and the chosen symmetry sector. At late flows the normal distribution is a satisfying fit to the data. In addition, the Γ test indicator has been computed. It suggested a normal distribution for late flows in the smaller symmetry sectors and already for early flows in the larger symmetry sectors. This was attributed to the huge data set, which was available through the consideration of all symmetry sectors. The comparison to the case of a random unitary transformation showed a very good agreement. Lastly, it was argued that more formal tests like the null hypothesis significance tests are not useful to underline the hypothesis of normality of the studied data. Overall, it was justified that the Hamiltonian can be transformed into a banded pseudo-random form matching Deutsch's requirements.

6.2 Few-body structure of the observables

In the second part, the few-body structure of four observables were studied. The main question was, whether the few-body structure is retained over the flow. As an appropriate tool to quantify this property, the Inverse Participation Ratio (IPR) and the Shannon entropy were introduced. The different depictions revealed similarities and distinctions among the observables. To distinguish the results from a case, where the hypothesis is not believed to be correct, the projection operator was included in the analysis.

The first main finding was that the flow does not have a profound effect on the localization in many regions of the spectrum. The data suggests that in many cases even the level of localization remains comparable throughout the flow. Only in specific regions like in the center of the bulk, the interaction energy and kinetic energy showed delocalization at very late flows, which has been suggested to be related to results for a different quantity from the literature (Santos and Rigol 2010a,b). It has been demonstrated that the IPR can be rather small, although large matrix elements are present like in the case of the momentum distribution function and the density-density structure factor (see also Fig. B.9 and Fig. B.10). Similar to the statistical analysis of the Hamiltonian, the finding that larger symmetry sectors, i.e. $k \neq 0, \pi$, tend to have more delocalized observables, has been attributed to the larger space, to which a state $O(B) |D_n(B)\rangle$ can spread to.

In the next step, the conservation of the few-body structure of the observables was studied using the scaling of the localization measures over lattice sizes. One finds that for all observables the low to mid-energy regions in the spectrum do not show the extensive population of the Hilbert space, thereby retaining their few-body structure. In the case of the momentum distribution function and the density-density structure factor, this is true for the entire energy range. The kinetic energy in the center of the bulk delocalizes more over the flow, although it is not losing its "few-bodiedness". The only case, where the obtained numerical data suggests an extensive scaling of the IPR is observed for the interaction energy in the bulk center. There, the localization mea-

tures show similar behavior as found for the projection operator before localization (compare with Fig. B.26a). It is unclear, however, whether the numerics are sufficient, because, in this case, the kinetic energy has been shown to obey ETH (Santos and Rigol 2010a).

In this context, it is important to note that the ETH is believed to hold for the bulk of the spectrum, i. e. high-energy states away from the edges (D'Alessio and Polkovnikov 2013). The EEVs of observables for low-energy eigenstates are generally not expected to be equal to the thermal distribution (Santos and Rigol 2010a). This has also been verified numerically in the identical model as studied here, where large fluctuations of the EEVs of the momentum distribution function and the density-density structure factor indicate a breakdown of thermalization at low energies (Rigol 2009a). How this relates to Deutsch's argument requires further investigations. A better understanding could also shine light on the difficult interpretation of the scaling of the other localization measure, the Shannon entropy.

Overall, one can conclude that, in general, the scaling analysis showed that the flow does not destroy the few-body structure. In the case, where a violation of this claim was observed, i. e. center of spectrum for the interaction energy, arguments like that in this case ETH is fulfilled, contribute to the assessment that a more elaborate analysis is required.

Interestingly, it turns out that all observables, except the kinetic energy, feature a high degree of robustness against basis transformations, because a random unitary transformation does not destroy few-body property either. It follows that for these observables a random basis must "feel" similar to a specific basis like the eigenbasis. It is not known, why the kinetic energy loses its few-body structure in a random basis and delocalizes to the value of a GOE-matrix like the projection operator.

In conclusion, it can be summarized that the hypothesis of this work that a generic system can be brought to a form, such that Deutsch's argument is applicable without destroying the properties of the observables, was justified successfully.

6.3 Outlook

The numerics that were displayed in this work were comprehensive, although not perfect. Especially the question of the interpretation of the Shannon entropy might benefit from additional effort.

To extend the scope of the considered models, the natural choice is to use different system parameters to probe, e. g. other phases like the strongly interacting case, where a very large V_2 is expected to put more weight on the off-diagonals.

Beyond the hardcore boson model, other models, especially the closely related spinless fermion model, could be worth studying. Although some properties are identical, there are some observables like the momentum distribution function, which show distinct fermionic properties (e. g. $n^2(k) = n(k)$). Moreover, it has been shown that the off-diagonal matrix elements of the flow endpoint $\langle E_m | n(k=0) | E_n \rangle$ are larger for fermions than for bosons, especially close to the main diagonal (Rigol 2009a). This can

be interpreted that also the earlier flow is different and features a better delocalization. Without a doubt, the holy grail would be an analytic argument, which is nowhere in sight.

Appendix A

Symmetries and basis construction

This appendix contains further explanations and calculations, which can be helpful when understanding the symmetries used in this work. Moreover, it treats the construction of the basis, which is dependent on the present symmetries, in greater detail. It specifically deals with the challenge of handling the signs, which appear in the case of fermions due to the anticommutation relation (see Eq. (4.2)). For spins and hardcore bosons this is not a problem, because the commutation relation is much simpler (see Eq. (4.3)).

A.1 Translational symmetry

The translation generating operator \mathcal{T} , which has been defined via Eq. (4.16), is the most essential symmetry operator, because it allows the splitting of the Hilbert space into many smaller subspaces each defined by a momentum.

First of all, it is helpful for the following parts to evaluate the action of the translation operator on a creation or annihilation operator. Therefore, one calculates

$$\begin{aligned}\mathcal{T} a_j^\dagger |n_1, \dots, n_L\rangle &= \mathcal{T} (-1)^{\sum_{l=1}^{j-1} n_l} |n_1, \dots, 1_j, \dots, n_L\rangle \\ &= (-1)^{N n_L} (-1)^{\sum_{l=1}^{j-1} n_l} |n_L, n_1, \dots, 1_j, \dots\rangle.\end{aligned}\quad (\text{A.1})$$

Comparing the last result with

$$\begin{aligned}a_{j+1}^\dagger \mathcal{T} |n_1, \dots, n_L\rangle &= (-1)^{(N-1)n_L} |n_L, n_1, \dots, n_{L-1}\rangle \\ &= (-1)^{(N-1)n_L} (-1)^{n_L + \sum_{l=1}^{j-1} n_l} |n_L, n_1, \dots, 1_j, \dots\rangle,\end{aligned}\quad (\text{A.2})$$

it follows that

$$\mathcal{T} a_j^\dagger \mathcal{T}^\dagger = a_{j+1}^\dagger \quad (\text{A.3})$$

for both fermions and hardcore bosons. It is straight forward to show that the relation also holds for the annihilation operator.

In order to find the expression for the eigenvectors of the translation operator defined in Eq. (4.16) an ansatz is made, which consists of a superposition of a chosen reference state $|a\rangle$ and all its translations:

$$|a(k)\rangle = \frac{1}{\sqrt{L_a}} \sum_{r=0}^{L-1} e^{-ikr} \mathcal{T}^r |a\rangle. \quad (\text{A.4})$$

The constant L_a is introduced to ensure the correct normalization $\langle a(k)|a(k)\rangle = 1$ and will be determined below. As one can easily show, it is indeed $\mathcal{T} |a(k)\rangle = e^{ik} |a(k)\rangle$ as required by Eq. (4.17).

The main goal is to use the states to form a complete orthonormalized basis. However, a state $|a(k)\rangle$ is not necessarily orthogonal to a state $|b(k)\rangle$ unless their representatives can not be mapped onto each other via any number of translations, i. e. $\mathcal{T}^r |a\rangle \neq |b\rangle$ for all r . If this is ensured, the basis can be used and only a small set of representatives $\{|a\rangle\}$ is needed to cover all states. The calculation of the normalization constant L_a is connected to the number of truly different states in the sum in Eq. (A.4), because it can happen that the state $|a\rangle$ maps onto itself after R_a translations, i. e. $\mathcal{T}^{R_a} |a\rangle = |a\rangle$ with $R_a < L$. A simple example is the state $|001001001\rangle$, for which it is $\mathcal{T}^3 |a\rangle = |a\rangle$ and therefore $R_a = 3$. As a consequence, there are multiple instances of the same state in the sum, which needs to be taken care of. The number R_a is called *periodicity* with $R_a \in \{1, \dots, L\}$ ¹. It plays an important role in the following calculation of the normalization L_a , because instead of adjusting the sum to only run until $R_a - 1$, it is better to alter the norm to take this into account.

If the system describes fermions, a fermionic commutation sign due to Eq. $|0101\rangle$, for which $\mathcal{T}^2 |0101\rangle = -|0101\rangle$ and the periodicity is $R_a = 2$ with an additional minus sign. In more general terms, it is defined that $\mathcal{T}^{R_a} |a\rangle = s_a |a\rangle$ with $s_a \in \{-1, 1\}$ (XXZ, hardcore bosons: $s_a = 1 \forall |a\rangle$).

¹According to Lagrange's theorem R_a must be a divisor of L , such that $R_a \in \{1, \dots, \frac{L}{4}, \frac{L}{3}, \frac{L}{2}, L\}$.

To determine the normalization factor L_a one calculates

$$\begin{aligned}
\langle a(k)|a(k')\rangle &= \frac{1}{L_a} \sum_{r,s=0}^{L-1} e^{-ik'r+iks} \langle a|\mathcal{T}^{-s}\mathcal{T}^r|a\rangle \\
&= \frac{1}{L_a} \sum_{r=0}^{L-1} \left[\sum_{s=0}^r e^{-ik'r+iks} \langle a|\mathcal{T}^{r-s}|a\rangle + \sum_{s=r+1}^{L-1} e^{-ik'r+iks} \langle a|\mathcal{T}^{r-s}|a\rangle \right] \\
&= \frac{1}{L_a} \sum_{r=0}^{L-1} \left[\sum_{u=r}^0 e^{-ik'r} e^{ik(r-u)} \langle a|\mathcal{T}^u|a\rangle + \sum_{u=L-1}^{r+1} e^{-ik'r} e^{ik(r-u+L)} \langle a|\mathcal{T}^{(u-L)}|a\rangle \right] \\
&= \frac{1}{L_a} \sum_{r=0}^{L-1} \left[\sum_{u=0}^r e^{-ik'r} e^{ik(r-u)} \langle a|\mathcal{T}^u|a\rangle + \sum_{u=r+1}^{L-1} e^{-ik'r} e^{ik(r-u)} \langle a|\mathcal{T}^u|a\rangle \right] \\
&= \frac{L}{L_a} \frac{1}{L} \underbrace{\sum_{r=0}^{L-1} e^{i(k-k')r}}_{=\delta_{kk'}} \sum_{u=0}^{L-1} e^{-iku} \langle a|\mathcal{T}^u|a\rangle \\
&= \delta_{kk'} \frac{L}{L_a} \sum_{n=0}^{L/R_a-1} e^{-iknR_a} \langle a|\mathcal{T}^{nR_a}|a\rangle = \delta_{kk'} \frac{L}{L_a} \sum_{n=0}^{L/R_a-1} e^{-iknR_a} s_a^n \tag{A.5}
\end{aligned}$$

where it was used that everytime $r - s$ is a multiple of R_a , i. e. $r - s = nR_a$ with $n = 0, 1, \dots, L/R_a - 1$, one gets a contribution ($\langle a|a\rangle = 1$) with an additional sign s_a for fermions. The remaining geometric sum in Eq. (A.5) can be determined, which yields

$$\sum_{n=0}^{L/R_a-1} e^{\pm iknR_a} s_a^n = \begin{cases} \sum_{n=0}^{L/R_a-1} e^{\pm iknR_a} = \frac{L}{R_a} & \text{if } kR_a = 2\pi m \quad \text{and } s_a = 1 \\ \sum_{n=0}^{L/R_a-1} e^{\pm iknR_a + i\pi n} = \frac{L}{R_a} & \text{if } kR_a = (2m+1)\pi \quad \text{and } s_a = -1 \\ 0 & \text{otherwise}^2 \end{cases} \tag{A.6}$$

where $m \in \mathbb{Z}$. The vanishing sum in Eq. (A.6) defines what representatives are allowed to describe the basis state $|a(k)\rangle$. A representative $|a\rangle$ is only permitted, if the equation

$$k = \frac{2\pi}{R_a} \left(m + \frac{1-s_a}{4} \right), \quad m = 0, 1, \dots, R_a - 1 \tag{A.7}$$

that connects the momentum, as given in Eq. (4.18), to the representative $|a\rangle$ is fulfilled. The norm then reads

$$L_a = \frac{L^2}{R_a}. \tag{A.8}$$

²To show this one requires some additional effort. One calculates the geometric sum to be $(1 - \exp(\pm ikL))/(1 - \exp(\pm ikR_a))$ for $s_a = 1$ and $(1 - \exp(\pm ikL + i\pi L/R_a))/(1 - \exp(\pm ikR_a + i\pi))$ for $s_a = -1$. In order to vanish the numerator must be zero. For the case $s_a = 1$, where the second summand in the exponential is not there, this is trivially fulfilled via $kL = 2\pi m$ (Eq. (4.18)). In the second case, however one needs that if $s_a = -1$, L/R_a is always an even number, which can be derived from $|a\rangle = \mathcal{T}^L |a\rangle = (\mathcal{T}^{R_a})^{L/R_a} |a\rangle = s_a^{L/R_a} |a\rangle$.

If a momentum state has a vanishing norm or, equivalently, a representative is not conform with the momentum, it cannot be used for the basis. Moreover, the periodicity is reflected in the formula, such that one can be sure that only one representative is included in the sum in Eq. (A.4). For states with no smaller periodicity than the full cycle, i. e. $R_a = L$, the norm reduces to the intuitive form $L_a = L$. The orthonormality of the basis follows naturally, since $\langle b|a\rangle = \delta_{ab}$ by construction and hence $\langle b(k')|a(k)\rangle = \delta_{ab}\delta_{kk'}$. The completeness of the basis results from the fact that a representative $|a\rangle$ appears in R_a different k -sectors (Eq. (A.7)) and that each representative represents R_a different states in $|a(k)\rangle$.

A.1.1 Commutation with the Hamiltonian

As a last step, it must be demonstrated that the translation operator commutes with the Hamiltonian, i. e. $[H, \mathcal{T}] = 0$. The kinetic part contains hopping terms like $c_{j+1}^\dagger c_j$, which describes the shift of the particle from site j to $j+1$. With Eq. (4.7a) and Eq. (4.7b), it becomes clear that the permutation sign for fermions vanishes, because j and $j+1$ are neighboring sites, unless the jump is across the boundary. Hence, one can show that

$$c_{j+1}^\dagger c_j |n_1, n_2, \dots, n_L\rangle = \begin{cases} s_{\mathcal{T}} |1, n_2, \dots, 0\rangle & \text{if } j = L \\ |n_1, \dots, 0_j, 1_{j+1}, \dots\rangle & \text{otherwise} \end{cases} \quad (\text{A.9})$$

where the abbreviated notation $n_{j+1} = 1_j$ and $n_j - 1 = 0_i$ was used. For the purpose of improved brevity most vanishing contributions are not explicitly mentioned (Reminder: $c_j |0_j\rangle = c_j^\dagger |1_j\rangle = 0$, see Section 4.0.1). Acting with \mathcal{T} on the state Eq. (A.9) yields

$$\mathcal{T} c_{j+1}^\dagger c_j |n_1, \dots, n_L\rangle = \begin{cases} s_{\mathcal{T}} |0, 1, \dots, n_{L-1}\rangle & \text{if } j = L \\ s_{\mathcal{T}} |1, n_1, \dots, 0\rangle & \text{if } j = L - 1 \\ s_{\mathcal{T}}^{n_L} |n_L, \dots, 0_{j+1}, 1_{j+2}, \dots\rangle & \text{otherwise} \end{cases}$$

Now the order of the operators is swapped and one calculates

$$\begin{aligned} c_{j+1}^\dagger c_j \mathcal{T} |n_1, \dots, n_L\rangle &= c_{j+1}^\dagger c_j s_{\mathcal{T}}^{n_L} |n_L, n_1, \dots, n_{L-1}\rangle \\ &= \begin{cases} s_{\mathcal{T}} |0, 1, \dots, n_{L-1}\rangle & \text{if } j = 1 \\ s_{\mathcal{T}} |1, n_1, \dots, 0\rangle & \text{if } j = L \\ s_{\mathcal{T}}^{n_L} |n_L, \dots, 0_{j-1}, 1_j, \dots\rangle & \text{otherwise} \end{cases} \end{aligned}$$

It is important to note that the numbering of the operators is done with respect to the underlying lattice, which is also used to name the initial occupations. Since the kinetic energy part of the fermionic Hamiltonian with periodic boundary conditions contains sums over all lattice sites, a short calculation using the results from above shows that

$$\mathcal{T} \sum_{j=1}^L c_{j+1}^\dagger c_j = \sum_{j=1}^L c_{j+1}^\dagger c_j \mathcal{T}. \quad (\text{A.10})$$

Likewise, one can show the same for the hermitian conjugate part $\sum c_j^\dagger c_{j+1}$. For the XXZ- and hardcore boson-model, there are no fermionic signs, of course, and the commutation relation is trivially fulfilled. The interaction energy consists of density-density terms as $n_i n_{i+x}$, where each $n_i = c_i^\dagger c_i$ consists of two operators acting on the same site. Therefore, it is clear that no fermionic sign can appear and the operator pair is translationally invariant. In conclusion, one finds that $[H, \mathcal{T}] = 0$.

A.1.2 Matrix elements in the momentum eigenbasis

With the results above and the fact that the Hamiltonian can be written as a big sum as for example in Eq. (??), it is straightforward to calculate the action of H on $|a(k)\rangle$:

$$H|a(k)\rangle = \frac{1}{\sqrt{L_a}} \sum_{r=0}^{L-1} e^{-ikr} \mathcal{T}^r H|a\rangle = \frac{1}{\sqrt{L_a}} \sum_{j=0}^L \sum_{r=0}^{L-1} e^{-ikr} \mathcal{T}^r h_j|a\rangle, \quad (\text{A.11})$$

where L_a , as defined in Eq. (A.8), is the normalization factor of the state and $|a\rangle$ is the chosen reference state. The application of h_j on $|a\rangle$ for $0 < j < L$ yields $h_j|a\rangle = h_j(a)|b'_j\rangle$, where $h_j(a)$ is the scalar according to the definitions of the Hamiltonian (e. g. $h_{j>0}(a) = -t$ for the spinless fermion model, see Eq. (??)). If the hopping is across the boundary (e. g. for $j = L$ and a NN-hopping), the usual translational sign factor $s_{h_L} = (-1)^{n_L(N-1)}$ can appear in the previous equation depending on the exact form of $|a\rangle$. The resulting state $|b'_j\rangle$, which is not necessarily a reference state, can be transformed to one by a suitable number of translations, i. e. $|b_j\rangle = s_{l_j} \mathcal{T}^{l_j} |b'_j\rangle$, where $l_j \in \{0, 1, \dots, L-1\}$ and s_{l_j} denotes the sign, which appears due to the l_j translations of fermionic operators. Moreover, it must be ensured that $|b_j\rangle$ is compatible with the momentum k , i. e. it must fulfill Eq. (A.7). If this holds, it follows that $h_j|a\rangle = h_j(a)s_{l_j} \mathcal{T}^{-l_j} |b_j\rangle$. If it does not, the overlap is zero.

The action of h_0 , which contains all the interaction part, is purely diagonal in the sense that it does not change the state. Together, this allows for the calculation of all matrix elements via the formulas

$$\langle b_0(k)|h_0|a(k)\rangle = \delta_{ab} \langle a|H_1|a\rangle \quad (\text{A.12})$$

$$\langle b_j(k)|h_{j>0}|a(k)\rangle = \sqrt{\frac{L_{b_j}}{L_a}} s_j h_j(a) s_{l_j} e^{-ikl_j} \quad (\text{A.13})$$

where

$$s_j = \begin{cases} (-1)^{n_L(N-1)} & \text{if } j = L \\ 1 & \text{otherwise.} \end{cases}$$

In general, it often occurs that multiple contributions like Eq. (A.13) contribute to one matrix element, because it can be that $H|a\rangle = s_{l_j} \mathcal{T}^{-l_j} |b_j\rangle$ and, additionally, $H|a\rangle = s_{l'_j} \mathcal{T}^{-l'_j} |b_j\rangle$ with $l_j \neq l'_j$. For bosonic systems both s_j and s_{l_j} are always 1, because the ladder operators commute.

A.2 Reflection symmetry and semi-momentum

Like in the case of the translation operator, it is easier to calculate only with operators, whenever possible. Therefore, one studies the transformation of a ladder operator under reflection, when both act on a Fock state with a certain normal order. It is

$$\begin{aligned} \mathcal{P} a_j^\dagger |n_1, \dots, n_L\rangle &= \mathcal{P} (-1)^{\sum_{l=1}^{j-1} n_l} |n_1, \dots, 1_j, \dots, n_L\rangle \\ &= (-1)^{N(N+1)/2} (-1)^{\sum_{l=1}^{j-1} n_l} |n_L, \dots, 1_j, \dots, n_1\rangle \end{aligned} \quad (\text{A.14})$$

and, similarly,

$$\begin{aligned} a_{L-j+1}^\dagger \mathcal{P} |n_1, \dots, n_L\rangle &= a_{L-j+1}^\dagger (-1)^{N(N-1)/2} |n_L, \dots, n_1\rangle \\ &= (-1)^{N(N-1)/2} (-1)^{\sum_{l=L-j+2}^L n_l} |n_L, \dots, 1_{L-j+1}, \dots, n_1\rangle \\ &= (-1)^{N(N-1)/2} (-1)^{N - \sum_{l=1}^{j-1} n_l} |n_L, \dots, 1_{L-j+1}, \dots, n_1\rangle \\ &= (-1)^{N(N+1)/2} (-1)^{\sum_{l=1}^{j-1} n_l} |n_L, \dots, 1_j, \dots, n_1\rangle. \end{aligned} \quad (\text{A.15})$$

Hence, it follows that

$$\mathcal{P} a_j^\dagger \mathcal{P}^\dagger = a_{L-j+1}^\dagger \quad (\text{A.16})$$

and analogous for a_j .

The motivation to build the semi-momentum states is to create states without any designated direction, which are invariant under space inversion or reflection symmetry defined by the reflection operator \mathcal{P} . In a first step the states with $\pm k$ are combined by summation ($\sigma = 1$) and subtraction ($\sigma = -1$) to yield

$$|a^\sigma(k)\rangle = \frac{1}{\sqrt{L_a}} \sum_{r=0}^{L-1} C_k^\sigma(r) \mathcal{T}^r |a\rangle. \quad (\text{A.17})$$

Here, the function $C_k(r)$ reads $C_k^1(r) = \cos(kr)$ and $C_k^{-1}(r) = \sin(kr)$. Since the sum of the combination contains two states (even two times the same if $k = 0, \pi$), the normalization requires a rescaling to

$$L_a = \frac{L^2 g_k}{2R_a}, \quad (\text{A.18})$$

where the factor $g_k = 1$ if $0 < k < \pi$ and $g_k = 2$ if $k = 0$ or π . The general overlap $\langle a^\tau(k) | a^\sigma(k') \rangle$ can be determined in a similar manner as in Eq. (A.5) by splitting the sums appropriately through index substitutions and trigonometric identities. While some terms vanish, because $\sum_n C_k^-(nR_a) s_a^n = 0$, the term $\sum_n C_k^+(nR_a) s_a^n$ yields exactly

the same result as in Eq. (A.6). One way to resolve the remaining sums, which are combinations of $C_k^\tau(r)C_{k'}^\sigma(r)$ is to use the following formulas:

$$\begin{aligned} \sum_{r=0}^{L-1} C_k^+(r)C_{k'}^+(r) &= \sum_{r=0}^{L-1} \cos(kr) \cos(k'r) = \sum_{r=0}^{L-1} \frac{1}{2} (\cos((k-k')r) + \cos((k+k')r)) \\ &= \delta_{kk'} \begin{cases} L & \text{if } kL = m\pi, m \in \mathbb{Z} \\ \frac{L}{2} & \text{otherwise} \end{cases} \end{aligned} \quad (\text{A.19})$$

$$\begin{aligned} \sum_{r=0}^{L-1} C_k^-(r)C_{k'}^-(r) &= \sum_{r=0}^{L-1} \sin(kr) \sin(k'r) = \sum_{r=0}^{L-1} \frac{1}{2} (\cos((k-k')r) - \cos((k+k')r)) \\ &= \delta_{kk'} \begin{cases} L & \text{if } kL = m\pi, m \in \mathbb{Z} \\ \frac{L}{2} & \text{otherwise} \end{cases} \end{aligned} \quad (\text{A.20})$$

$$\sum_{r=0}^{L-1} C_k^+(r)C_{k'}^-(r) = \sum_{r=0}^{L-1} \cos(kr) \sin(k'r) = \sum_{r=0}^{L-1} \frac{1}{2} (\sin((k-k')r) + \sin((k+k')r)) = 0 \quad (\text{A.21})$$

where it was used that $\cos^2(x) = (1 + \cos(2x))/2$.

In a second step one extends the semi-momentum states to incorporate the parity operation and defines

$$|a^\sigma(k, p)\rangle = \frac{1}{\sqrt{L_a^\sigma}} \sum_{r=0}^{L-1} C_k^\sigma(r) (1 + p\mathcal{P}) \mathcal{T}^r |a\rangle \quad (\text{A.22})$$

for $0 \leq k \leq \pi$. Using trigonometric functions it is straightforward to express Eq. (A.22) in terms of the pure momentum basis given by Eq. (A.17):

$$|a^\sigma(k, p)\rangle = \sqrt{\frac{L_a}{L_a^\sigma}} [(1 + \sigma p C_k^+(m)) |a^\sigma(k)\rangle - p C_k^-(m) |a^{-\sigma}(k)\rangle] \quad (\text{A.23})$$

This equation shows that the states $|a^\sigma(k, p)\rangle$ and $|a^{-\sigma}(k, p)\rangle$ are not generally orthogonal to each other. This can be dealt with by changing the normalization in Eq. (A.18) to be dependent on σ . To calculate the norm one simply exchanges the exponential phase factor in Eq. (A.5) for the combined factor $C^\sigma(k)$ and finds that

$$\langle a^\tau(k) | a^\sigma(k) \rangle = \frac{1}{L_a} \sum_{r,s=0}^{L-1} C_k^\tau(s) C_k^\sigma(r) \langle a | \mathcal{T}^{r-s} | a \rangle \quad (\text{A.24})$$

It is important to note that the normalization now depends on the indicator σ , because it might be that $\mathcal{T}^m \mathcal{P} |a\rangle = |a\rangle$. As required, the states fulfill $\mathcal{P} |a^\sigma(k, p)\rangle = p |a^\sigma(k, p)\rangle$.

A.2.1 Commutation with the Hamiltonian

$$\begin{aligned}
\mathcal{P}c_j^\dagger |n_1, \dots, n_L\rangle &= \mathcal{P}(-1)^{\sum_{l=1}^{j-1} n_l} |n_1, \dots, 1_j, \dots, n_L\rangle \\
&= (-1)^{N(N+1)/2} (-1)^{\sum_{l=1}^{j-1} n_l} |n_L, \dots, 1_{L-j+1}, \dots, n_1\rangle \\
c_{L-j+1}^\dagger \mathcal{P} |n_1, \dots, n_L\rangle &= c_{L-j+1}^\dagger (-1)^{N(N-1)/2} |n_L, \dots, n_1\rangle \\
&= (-1)^{N(N-1)/2} (-1)^{\sum_{l=1}^{L-j} n_l} |n_L, \dots, 1_{L-j+1}, \dots, n_1\rangle \\
&= (-1)^{N(N-1)/2} (-1)^{N - \sum_{l=1}^{j-1} n_l} |n_L, \dots, 1_{L-j+1}, \dots, n_1\rangle \quad (\text{A.25})
\end{aligned}$$

Therefore, $\mathcal{P}c_j^\dagger \mathcal{P}^\dagger = c_{L-j+1}^\dagger$. Again, it must be shown that $[H, \mathcal{P}] = 0$. As before, one finds that the interaction part is trivially commuting, because it counts all the nearest-neighbor or next-to-nearest-neighbor particle pairs, which do not change under a space inversion. For the kinetic energy part one calculates

$$\begin{aligned}
\mathcal{P}c_{j+1}^\dagger c_j |n_1, \dots, n_L\rangle &= \mathcal{P} |n_1, \dots, 0_j, 1_{j+1}, \dots, n_L\rangle \\
&= \begin{cases} s\mathcal{P}s\mathcal{T} |0, n_{L-1}, \dots, 1\rangle & \text{if } j = L \\ s\mathcal{P} |n_L, \dots, 1_{L-j}, 0_{L-j+1}, \dots\rangle & \text{otherwise} \end{cases}
\end{aligned}$$

and likewise

$$\begin{aligned}
c_{L-j}^\dagger c_{L-j+1} \mathcal{P} |n_1, \dots, n_L\rangle &= c_{L-j}^\dagger c_{L-j+1} s\mathcal{P} |n_L, n_{L-1}, \dots, n_1\rangle \\
&= \begin{cases} s\mathcal{P}s\mathcal{T} |0, n_{L-1}, \dots, 1\rangle & \text{if } j = L \\ s\mathcal{P} |n_L, \dots, 1_{L-j}, 0_{L-j+1}, \dots\rangle & \text{otherwise.} \end{cases}
\end{aligned}$$

$$\begin{aligned}
c_j^\dagger c_{j+1} \mathcal{P} |n_1, \dots, n_L\rangle &= c_j^\dagger c_{j+1} s\mathcal{P} |n_L, n_{L-1}, \dots, n_1\rangle \\
&= \begin{cases} s\mathcal{P}s\mathcal{T} |0, n_{L-1}, \dots, 1\rangle & \text{if } j = L \\ s\mathcal{P} |n_L, \dots, 1_{L-j}, 0_{L-j+1}, \dots\rangle & \text{otherwise.} \end{cases}
\end{aligned}$$

In conclusion, one finds that $\mathcal{P} \sum_j c_{j+1}^\dagger c_j = \mathcal{P} \sum_j c_j^\dagger c_{j+1}$. Together with the missing hermitean conjugate (see e. g. Eq. (??)), it becomes clear that the kinetic energy part commutes with the parity operator. The interaction term does not introduce any new sign, as in the translational case, so the proof is complete.

A.2.2 Matrix elements in the semi-momentum basis

A.3 Particle-hole inversion symmetry

$$\mathcal{Z} = \prod_{j=1}^L \left(a_j^\dagger + (-1)^j a_j \right), \quad (\text{A.26})$$

A.3.1 Commutation with the Hamiltonian

Again, it must be shown that $[H, \mathcal{Z}] = 0$. This time, it is the kinetic energy part, which is the one that is easier to tackle: With Eq. (??) one finds that $\mathcal{Z}c_{i+1}^\dagger c_i = -c_i^\dagger c_{i+1} \mathcal{Z}$. This means that the hopping to the left becomes the hopping to the right and vice versa.

As before, one finds that the interaction part is trivially commuting, because it counts all the nearest-neighbor or next-to-nearest-neighbor particle pairs, which do not change under a space inversion. For the kinetic energy part one calculates

$$\begin{aligned} \mathcal{Z}c_{i+1}^\dagger c_i |n_1, \dots, n_L\rangle &= \dots \left(c_i^\dagger + c_i \right) \left(c_{i+1}^\dagger + c_{i+1} \right) \dots c_{i+1}^\dagger c_i |n_1, \dots, n_L\rangle \\ &= \dots \left(c_i^\dagger c_{i+1}^\dagger + c_i^\dagger c_{i+1} + c_i c_{i+1}^\dagger + c_i c_{i+1} \right) \dots c_{i+1}^\dagger c_i |n_1, \dots, n_L\rangle \\ &= n_{i+1} |n_1, \dots, n_L\rangle \end{aligned} \quad (\text{A.27})$$

and likewise

$$\begin{aligned} c_i^\dagger c_{i+1} \mathcal{P} |n_1, \dots, n_L\rangle &= c_i^\dagger c_{i+1} (-1)^{N(N-1)/2} |n_L, n_{L-1}, \dots, n_1\rangle \\ &= \begin{cases} (-1)^{N(N-1)/2} (-1)^{N-1} |0, n_{L-1}, \dots, 1\rangle & \text{if } i = L \\ (-1)^{N(N-1)/2} |n_L, \dots, 1_{L-i}, 0_{L-i+1}, \dots\rangle & \text{otherwise.} \end{cases} \end{aligned}$$

$$\begin{aligned} \mathcal{Z} |n_1, n_2, \dots, n_L\rangle &= \prod_{j=1}^L \left(c_j^\dagger + (-1)^j c_j \right) |n_1, n_2, \dots, n_L\rangle \\ &= \left(c_1^\dagger - c_1 \right) \left(c_2^\dagger + c_2 \right) \dots \left(c_L^\dagger + c_L \right) \left(c_1^\dagger \right)^{n_1} \left(c_2^\dagger \right)^{n_2} \dots \left(c_L^\dagger \right)^{n_L} |0\rangle \\ &= \left(c_1^\dagger - c_1 \right) \dots \left(c_{L-1}^\dagger - c_{L-1} \right) \left(c_1^\dagger \right)^{n_1} \left(c_2^\dagger \right)^{n_2} \dots \underbrace{\left(c_L^\dagger + c_L \right) \left(c_L^\dagger \right)^{n_L}}_{=n_L+1 \pmod{2}} |0\rangle \\ &= \prod_{j=1}^L (-1)^{jn_j + \sum_{l=1}^{j-1} n_l} |1 - n_1, 1 - n_2, \dots, 1 - n_L\rangle \end{aligned}$$

The sign of \mathcal{Z} when acting on a Fock state is 1, because

$$s_Z = \prod_{j=1}^L (-1)^{jn_j + \sum_{l=1}^{j-1} n_l} = (-1)^{\sum_{j=1}^L \left(jn_j + \sum_{l=1}^{j-1} n_l \right)} \quad (\text{A.28})$$

$$= (-1)^{\sum_{j=1}^L (jn_j + (L-j)n_j)} = (-1)^{\sum_{j=1}^L n_j} = (-1)^{2N^2} = 1. \quad (\text{A.29})$$

The problem is, however, that in the case of spinless fermions a special ordering is required. Moreover, some observables like the momentum distribution function do not commute with the particle hole exchange operator \mathcal{Z} such that these observables cannot be formulated in the chosen basis easily. They would require different symmetry

sectors which contradicts the benefits one gets from the chosen basis.

Commutation with the Hamiltonian

$$\begin{aligned} \mathcal{Z} \sum_{j=1}^L (c_{j+1}^\dagger c_j + c_j^\dagger c_{j+1}) &= \sum_{j=1}^L \left((-1)^{j+1} (-1)^j c_{j+1} c_j^\dagger + (-1)^{j+1} (-1)^j c_j c_{j+1}^\dagger \right) \mathcal{Z} \\ &= \sum_{j=1}^L (c_j^\dagger c_{j+1} + c_{j+1}^\dagger c_j) \mathcal{Z} \end{aligned} \quad (\text{A.30})$$

A.4 Observables

This Appendix contains the verifications that the observables as introduced in Section 4.2 do obey the symmetries as explained. The chosen basis as explained in the previous part exploits the invariance of the Hamiltonian under several symmetry operators. This is equivalent to saying that the action of the Hamiltonian leaves the momentum untouched, i. e. there are no matrix elements connecting different k -sectors. Analogously, the space inversion and particle-hole exchange symmetry can be used. In order to retain the block structure of the basis only observables which obey the same symmetries can be implemented. In the fermionic system only observables, which commute with the fermionic parity operator (also called *superselection rule*), are allowed. This is related to the fact that any Hilbert space containing fermions can be decomposed into a direct sum of a two parts with an even and odd number of fermions, respectively, using Majorana fermions. full basis which considers all necessary momenta. An example for an operator that does not reflect the translation symmetry is the occupation number operator at site j :

$$n_j = \frac{1}{L} \sum_{k,k'} e^{i(k'-k)j} a_k^\dagger a_{k'}. \quad (\text{A.31})$$

A.4.1 Momentum distribution function

If this operator is Fourier transformed and hence brought to the momentum basis, it becomes the momentum distribution function operator n_k , which obeys the translation symmetry. This can be shown by acting with the translation operator on n_k

$$\mathcal{T} n(k) = \frac{1}{L} \sum_{l,m=0}^{L-1} e^{ik(l-m)} \mathcal{T} c_l^\dagger c_m = \frac{1}{L} \sum_{l,m=0}^{L-1} e^{ik(l-m)} c_{l+1}^\dagger c_{m+1} \mathcal{T}, \quad (\text{A.32})$$

where a final renaming of the summation indices yields $[\mathcal{T}, n(k)] = 0$. The operator is then split up into cases where $m < l$, $m = l$ and $m > l$.

$$n(k) = \frac{1}{L} \sum_{l=0}^{L-1} \sum_{m=0}^{l-1} e^{ik(l-m)} c_l^\dagger c_m + \frac{1}{L} \sum_{l=0}^{L-1} c_l^\dagger c_l + \frac{1}{L} \sum_{l=0}^{L-1} \sum_{m=l+1}^{L-1} e^{ik(l-m)} c_l^\dagger c_m \quad (\text{A.33})$$

The first term can be rewritten swapping the sums such that

$$n(k) = \frac{1}{L} \sum_{m=0}^{L-1} \sum_{l=m+1}^{L-1} e^{ik(l-m)} c_l^\dagger c_m + \frac{1}{L} \sum_{l=0}^{L-1} c_l^\dagger c_l + \frac{1}{L} \sum_{l=0}^{L-1} \sum_{m=l+1}^{L-1} e^{ik(l-m)} c_l^\dagger c_m \quad (\text{A.34})$$

$$= \frac{1}{L} \sum_{m=0}^{L-1} \sum_{R=1}^{L-1-m} e^{ikR} c_{m+R}^\dagger c_m + \frac{1}{L} \sum_{l=0}^{L-1} c_l^\dagger c_l + \frac{1}{L} \sum_{l=0}^{L-1} \sum_{R=1}^{L-1-l} e^{-ikR} c_l^\dagger c_{l+R} \quad (\text{A.35})$$

$$= \frac{1}{L} \sum_{l=0}^{L-1} c_l^\dagger c_l + \frac{1}{L} \sum_{l=0}^{L-1} \sum_{R=1}^{L-1-l} (e^{ikR} c_{l+R}^\dagger c_l + e^{-ikR} c_l^\dagger c_{l+R}) \quad (\text{A.36})$$

In the last step we introduced the distance R to condense the sums to one. The operator then becomes

$$n(k) = \sum_{l=0}^{L-1} \tilde{n}_k(l) \quad \text{with} \quad \tilde{n}_k(j) = \frac{1}{L} c_l^\dagger c_l + \frac{1}{L} \sum_{R=1}^{L-1-l} (e^{ikR} c_{l+R}^\dagger c_l + e^{-ikR} c_l^\dagger c_{l+R}) \quad (\text{A.37})$$

The remaining part is to study the action of $c_l^\dagger c_m$ acting on a reference state which has the form $|n_0, n_1, \dots, n_{L-1}\rangle$. If $l < m$ one leaves the order, whereas if $l > m$ one swaps the operators into $c_l^\dagger c_m = -c_m c_l^\dagger$. One then finds that for $l < m$

$$c_l^\dagger c_m |n_0, n_1, \dots, n_l, \dots, n_m, \dots, n_{L-1}\rangle \quad (\text{A.38})$$

$$= c_l^\dagger (-1)^{\sum_{j=0}^{m-1} n_j} |n_0, n_1, \dots, 0_l, \dots, 0_m, \dots, n_{L-1}\rangle \quad (\text{A.39})$$

$$= (-1)^{\sum_{j=0}^{l-1} n_j} (-1)^{\sum_{j=0}^{m-1} n_j} |n_0, n_1, \dots, 1_l, \dots, 0_m, \dots, n_{L-1}\rangle \quad (\text{A.40})$$

$$= (-1)^{\sum_{j=l}^{m-1} n_j} |n_0, n_1, \dots, 1_l, \dots, 0_m, \dots, n_{L-1}\rangle \quad (\text{A.41})$$

Technically, we measure the entire section $\sum_{j=l}^m n_j$ including l and m of the original state and then add 1, because initially $n_m = 1$. Accordingly, for $l > m$:

$$c_l^\dagger c_m |n_0, n_1, \dots, n_{L-1}\rangle = -c_m (-1)^{\sum_{j=0}^{l-1} n_j} |n_0, n_1, \dots, 1_m, \dots, 1_l, \dots, n_{L-1}\rangle \quad (\text{A.42})$$

$$= -(-1)^{\sum_{j=0}^{m-1} n_j} (-1)^{\sum_{j=0}^{l-1} n_j} |n_0, n_1, \dots, 0_m, \dots, 1_l, \dots, n_{L-1}\rangle \quad (\text{A.43})$$

$$= -(-1)^{\sum_{j=m}^{l-1} n_j} |n_0, n_1, \dots, 1_l, \dots, 0_m, \dots, n_{L-1}\rangle \quad (\text{A.44})$$

Using the measured section $\sum_{j=l}^m n_j$ as before, this time initially $n_l = 0$, such that no additional minus sign is required.

Action of the reflection operator

$$\begin{aligned} \mathcal{P}n(k)\mathcal{P}^\dagger &= \frac{1}{L} \sum_{l,m=1}^L e^{ik(l-m)} \mathcal{P} c_l^\dagger c_m \mathcal{P}^\dagger = \frac{1}{L} \sum_{l,m=1}^L e^{ik(l-m)} c_{L-l+1}^\dagger c_{L-m+1} \\ &= \frac{1}{L} \sum_{l,m=1}^L e^{ik(L-l+1-(L-m+1))} c_l^\dagger c_m = \frac{1}{L} \sum_{l,m=1}^L e^{-ik(l-m)} c_l^\dagger c_m \\ &= n(-k) \end{aligned} \quad (\text{A.45})$$

Action of the particle-hole exchange operator

$$\begin{aligned}\mathcal{Z}n(k)\mathcal{Z}^\dagger &= \frac{1}{L} \sum_{l,m=1}^L e^{ik(l-m)} \mathcal{Z}c_l^\dagger c_m \mathcal{Z}^\dagger \\ &= \frac{1}{L} \sum_{l,m=1}^L e^{ik(l-m)} (-1)^l c_l (-1)^m c_m^\dagger = \frac{1}{L} \sum_{l,m=1}^L e^{ik(l-m)+i\pi(l-m)} \left(\delta_{lm} - c_m^\dagger c_l \right) \quad (\text{A.46})\end{aligned}$$

$$= \frac{1}{L} \sum_{l,m=1}^L e^{i(k+\pi)(l-m)} \left(\delta_{lm} - c_m^\dagger c_l \right) = 1 - \frac{1}{L} \sum_{l,m=1}^L e^{-i(k+\pi)(m-l)} c_m^\dagger c_l \quad (\text{A.47})$$

$$= 1 - n(-k - \pi) \quad (\text{A.48})$$

$$\begin{aligned}\mathcal{Z}n(k)\mathcal{Z}^\dagger &= \frac{1}{L} \sum_{l,m=1}^L e^{ik(l-m)} \mathcal{Z}b_l^\dagger b_m \mathcal{Z}^\dagger = \frac{1}{L} \sum_{l,m=1}^L e^{ik(l-m)} b_l b_m^\dagger \\ &= \frac{1}{L} \sum_{l=1}^L \left(1 - b_l^\dagger b_l \right) + \frac{1}{L} \sum_{\substack{l,m=1 \\ l \neq m}}^L e^{ik(l-m)} b_m^\dagger b_l \\ &= \frac{1}{L} \sum_{l=1}^L (1 - 2n_l) + \frac{1}{L} \sum_{l,m=1}^L e^{-ik(m-l)} b_m^\dagger b_l \\ &= \frac{L - 2N}{L} + n(-k) \quad (\text{A.49})\end{aligned}$$

Similarly, for hardcore bosons one finds

$$\begin{aligned}\mathcal{Z}n(k)\mathcal{Z}^\dagger &= \frac{1}{L} \sum_{l,m=1}^L e^{ik(l-m)} \mathcal{Z}b_l^\dagger b_m \mathcal{Z}^\dagger = \frac{1}{L} \sum_{l,m=1}^L e^{ik(l-m)} b_l b_m^\dagger \\ &= \frac{1}{L} \sum_{\substack{l,m=1 \\ l \neq m}}^L e^{ik(l-m)} b_m^\dagger b_l + \frac{1}{L} \sum_{l=1}^L b_l b_l^\dagger \\ &= \frac{1}{L} \sum_{\substack{l,m=1 \\ l \neq m}}^L e^{ik(l-m)} b_m^\dagger b_l + \frac{1}{L} \sum_{l=1}^L b_l^\dagger b_l + \frac{1}{L} \sum_{l=1}^L (b_l b_l^\dagger - b_l^\dagger b_l) \\ &= n(-k) + \frac{1}{L} \sum_{l=1}^L (1 - 2b_l^\dagger b_l) = n(-k) + 1 - \frac{2N}{L} \quad (\text{A.50})\end{aligned}$$

In the case of half-filling it is $N = L/2$, such that the additional summand in Eq. (A.50) vanishes and it is simply $\mathcal{Z}n(k)\mathcal{Z}^\dagger = n(-k)$.

A.4.2 Density-density correlation structure factor

It is evident that it only contains diagonal matrix elements in the spatial basis, because the product $n_l n_m$ does not alter the state. Both sites l and m need to be occupied to give

a contribution, which is then hit twice (double sum), unless $l = m$. It follows that the exponentials add up to a real cosine, which is also expected, because the observable is hermitean. Hence, this simplifies to

$$D(k) = \frac{N}{L} + \frac{2}{L} \sum_{l=0}^{L-1} \sum_{R=1}^{L-1-l} \cos(kR) n_l n_{l+R}. \quad (\text{A.51})$$

The observable $D(k)$ commutes with the translation operator \mathcal{T} , because any shift in the index $(l, m) \rightarrow (l+1, m+1)$ cancels through the minus sign. Moreover, it also commutes with \mathcal{P} , since n

A.4.3 Momentum distribution function

The chosen basis as explained in the previous section exploits the invariance under translations of the Hamilton operator. This is equivalent to saying that the action of the Hamiltonian leaves the momentum untouched, i. e. there are no matrix elements connecting different k -sectors. Analogously, the space inversion and particle-hole exchange symmetry can be used. In order to retain the block structure of the basis only observables which obey the same symmetries can be implemented. In the fermionic system only observables, which commute with the fermionic parity operator (also called *superselection rule*), are allowed. This is related to the fact that any Hilbert space containing fermions can be decomposed into a direct sum of a two parts with an even and odd number of fermions, respectively, using Majorana fermions. full basis which considers all necessary momenta. An example is the occupation number at site j

$$n_j = \frac{1}{L} \sum_{k, k'} e^{i(k'-k)j} a_k^\dagger a_{k'}, \quad (\text{A.52})$$

However, since n_k

$$\mathcal{T} n_k = \frac{1}{L} \sum_{l, m=0}^{L-1} e^{ik(l-m)} \mathcal{T} c_l^\dagger c_m = \frac{1}{L} \sum_{l, m=0}^{L-1} e^{ik(l-m)} c_{l+1}^\dagger c_{m+1} \mathcal{T}, \quad (\text{A.53})$$

a renaming of the summation indices yields $[\mathcal{T}, n_k] = 0$. The operator is then split up into cases where $m < l$, $m = l$ and $m > l$.

$$n_k = \frac{1}{L} \sum_{l=0}^{L-1} \sum_{m=0}^{l-1} e^{ik(l-m)} c_l^\dagger c_m + \frac{1}{L} \sum_{l=0}^{L-1} c_l^\dagger c_l + \frac{1}{L} \sum_{l=0}^{L-1} \sum_{m=l+1}^{L-1} e^{ik(l-m)} c_l^\dagger c_m \quad (\text{A.54})$$

The first term can be rewritten swapping the sums such that

$$n_k = \frac{1}{L} \sum_{m=0}^{L-1} \sum_{l=m+1}^{L-1} e^{ik(l-m)} c_l^\dagger c_m + \frac{1}{L} \sum_{l=0}^{L-1} c_l^\dagger c_l + \frac{1}{L} \sum_{l=0}^{L-1} \sum_{m=l+1}^{L-1} e^{ik(l-m)} c_l^\dagger c_m \quad (\text{A.55})$$

$$= \frac{1}{L} \sum_{m=0}^{L-1} \sum_{R=1}^{L-1-m} e^{ikR} c_{m+R}^\dagger c_m + \frac{1}{L} \sum_{l=0}^{L-1} c_l^\dagger c_l + \frac{1}{L} \sum_{l=0}^{L-1} \sum_{R=1}^{L-1-l} e^{-ikR} c_l^\dagger c_{l+R} \quad (\text{A.56})$$

$$= \frac{1}{L} \sum_{l=0}^{L-1} c_l^\dagger c_l + \frac{1}{L} \sum_{l=0}^{L-1} \sum_{R=1}^{L-1-l} (e^{ikR} c_{l+R}^\dagger c_l + e^{-ikR} c_l^\dagger c_{l+R}) \quad (\text{A.57})$$

In the last step we introduced the distance R to condense the sums to one. The operator then becomes

$$n_k = \sum_{l=0}^{L-1} \tilde{n}_k(l) \quad \text{with} \quad \tilde{n}_k(j) = \frac{1}{L} c_l^\dagger c_l + \frac{1}{L} \sum_{R=1}^{L-1-l} (e^{ikR} c_{l+R}^\dagger c_l + e^{-ikR} c_l^\dagger c_{l+R}) \quad (\text{A.58})$$

The remaining part is to study the action of $c_l^\dagger c_m$ acting on a reference state which has the form $|n_0, n_1, \dots, n_{L-1}\rangle$. If $l < m$ one leaves the order, whereas if $l > m$ one swaps the operators into $c_l^\dagger c_m = -c_m c_l^\dagger$. One then finds that for $l < m$

$$c_l^\dagger c_m |n_0, n_1, \dots, n_l, \dots, n_m, \dots, n_{L-1}\rangle \quad (\text{A.59})$$

$$= c_l^\dagger (-1)^{\sum_{j=0}^{m-1} n_j} |n_0, n_1, \dots, 0_l, \dots, 0_m, \dots, n_{L-1}\rangle \quad (\text{A.60})$$

$$= (-1)^{\sum_{j=0}^{l-1} n_j} (-1)^{\sum_{j=0}^{m-1} n_j} |n_0, n_1, \dots, 1_l, \dots, 0_m, \dots, n_{L-1}\rangle \quad (\text{A.61})$$

$$= (-1)^{\sum_{j=l}^{m-1} n_j} |n_0, n_1, \dots, 1_l, \dots, 0_m, \dots, n_{L-1}\rangle \quad (\text{A.62})$$

Technically, we measure the entire section $\sum_{j=l}^m n_j$ including l and m of the original state and then add 1, because initially $n_m = 1$. Accordingly, for $l > m$:

$$c_l^\dagger c_m |n_0, n_1, \dots, n_{L-1}\rangle = -c_m (-1)^{\sum_{j=0}^{l-1} n_j} |n_0, n_1, \dots, 1_m, \dots, 1_l, \dots, n_{L-1}\rangle \quad (\text{A.63})$$

$$= -(-1)^{\sum_{j=0}^{m-1} n_j} (-1)^{\sum_{j=0}^{l-1} n_j} |n_0, n_1, \dots, 0_m, \dots, 1_l, \dots, n_{L-1}\rangle \quad (\text{A.64})$$

$$= -(-1)^{\sum_{j=m}^{l-1} n_j} |n_0, n_1, \dots, 1_l, \dots, 0_m, \dots, n_{L-1}\rangle \quad (\text{A.65})$$

Using the measured section $\sum_{j=l}^m n_j$ as before, this time initially $n_l = 0$, such that no additional minus sign is required.

A.4.4 Density-density correlation structure factor

It is evident that the density-density correlation structure factor as defined in Eq. (4.14) only contains diagonal matrix elements in the spatial basis, because the product $n_l n_m$ does not alter the state. Both sites l and m need to be occupied to give a contribution, which is then hit twice (double sum), unless $l = m$. It follows that the exponentials

add up to a real cosine, which is also expected, because the observable is hermitean. Hence, this simplifies to

$$D(k) = \frac{N}{L} + \frac{2}{L} \sum_{l=0}^{L-1} \sum_{R=1}^{L-1-l} \cos(kR) n_l n_{l+R}. \quad (\text{A.66})$$

A.5 Implementation

When the basis is implemented, it is chosen to take the smallest integer of all translations as the reference state $|a\rangle$.

A.5.1 Momentum distribution function

The chosen basis as explained in the previous section exploits the invariance under translations of the Hamilton operator. This is equivalent to saying that the action of the Hamiltonian leaves the momentum untouched, i. e. there are no matrix elements connecting different k -sectors. Analogously, the space inversion and particle-hole exchange symmetry can be used. In order to retain the block structure of the basis only observables which obey the same symmetries can be implemented. In the fermionic system only observables, which commute with the fermionic parity operator (also called *superselection rule*), are allowed. This is related to the fact that any Hilbert space containing fermions can be decomposed into a direct sum of a two parts with an even and odd number of fermions, respectively, using Majorana fermions. full basis which considers all necessary momenta. An example is the occupation number at site j

$$n_j = \frac{1}{L} \sum_{k,k'} e^{i(k'-k)j} a_k^\dagger a_{k'}. \quad (\text{A.67})$$

However, since n_k

$$\mathcal{T} n_k = \frac{1}{L} \sum_{l,m=0}^{L-1} e^{ik(l-m)} \mathcal{T} c_l^\dagger c_m = \frac{1}{L} \sum_{l,m=0}^{L-1} e^{ik(l-m)} c_{l+1}^\dagger c_{m+1} \mathcal{T}, \quad (\text{A.68})$$

a renaming of the summation indices yields $[\mathcal{T}, n_k] = 0$. The operator is then split up into cases where $m < l$, $m = l$ and $m > l$.

$$n_k = \frac{1}{L} \sum_{l=0}^{L-1} \sum_{m=0}^{l-1} e^{ik(l-m)} c_l^\dagger c_m + \frac{1}{L} \sum_{l=0}^{L-1} c_l^\dagger c_l + \frac{1}{L} \sum_{l=0}^{L-1} \sum_{m=l+1}^{L-1} e^{ik(l-m)} c_l^\dagger c_m \quad (\text{A.69})$$

The first term can be rewritten swapping the sums such that

$$n_k = \frac{1}{L} \sum_{m=0}^{L-1} \sum_{l=m+1}^{L-1} e^{ik(l-m)} c_l^\dagger c_m + \frac{1}{L} \sum_{l=0}^{L-1} c_l^\dagger c_l + \frac{1}{L} \sum_{l=0}^{L-1} \sum_{m=l+1}^{L-1} e^{ik(l-m)} c_l^\dagger c_m \quad (\text{A.70})$$

$$= \frac{1}{L} \sum_{m=0}^{L-1} \sum_{R=1}^{L-1-m} e^{ikR} c_{m+R}^\dagger c_m + \frac{1}{L} \sum_{l=0}^{L-1} c_l^\dagger c_l + \frac{1}{L} \sum_{l=0}^{L-1} \sum_{R=1}^{L-1-l} e^{-ikR} c_l^\dagger c_{l+R} \quad (\text{A.71})$$

$$= \frac{1}{L} \sum_{l=0}^{L-1} c_l^\dagger c_l + \frac{1}{L} \sum_{l=0}^{L-1} \sum_{R=1}^{L-1-l} (e^{ikR} c_{l+R}^\dagger c_l + e^{-ikR} c_l^\dagger c_{l+R}) \quad (\text{A.72})$$

In the last step we introduced the distance R to condense the sums to one. The operator then becomes

$$n_k = \sum_{l=0}^{L-1} \tilde{n}_k(l) \quad \text{with} \quad \tilde{n}_k(j) = \frac{1}{L} c_l^\dagger c_l + \frac{1}{L} \sum_{R=1}^{L-1-l} (e^{ikR} c_{l+R}^\dagger c_l + e^{-ikR} c_l^\dagger c_{l+R}) \quad (\text{A.73})$$

The remaining part is to study the action of $c_l^\dagger c_m$ acting on a reference state which has the form $|n_0, n_1, \dots, n_{L-1}\rangle$. If $l < m$ one leaves the order, whereas if $l > m$ one swaps the operators into $c_l^\dagger c_m = -c_m c_l^\dagger$. One then finds that for $l < m$

$$c_l^\dagger c_m |n_0, n_1, \dots, n_l, \dots, n_m, \dots, n_{L-1}\rangle \quad (\text{A.74})$$

$$= c_l^\dagger (-1)^{\sum_{j=0}^{m-1} n_j} |n_0, n_1, \dots, 0_l, \dots, 0_m, \dots, n_{L-1}\rangle \quad (\text{A.75})$$

$$= (-1)^{\sum_{j=0}^{l-1} n_j} (-1)^{\sum_{j=0}^{m-1} n_j} |n_0, n_1, \dots, 1_l, \dots, 0_m, \dots, n_{L-1}\rangle \quad (\text{A.76})$$

$$= (-1)^{\sum_{j=l}^{m-1} n_j} |n_0, n_1, \dots, 1_l, \dots, 0_m, \dots, n_{L-1}\rangle \quad (\text{A.77})$$

Technically, we measure the entire section $\sum_{j=l}^m n_j$ including l and m of the original state and then add 1, because initially $n_m = 1$. Accordingly, for $l > m$:

$$c_l^\dagger c_m |n_0, n_1, \dots, n_{L-1}\rangle = -c_m (-1)^{\sum_{j=0}^{l-1} n_j} |n_0, n_1, \dots, 1_m, \dots, 1_l, \dots, n_{L-1}\rangle \quad (\text{A.78})$$

$$= -(-1)^{\sum_{j=0}^{m-1} n_j} (-1)^{\sum_{j=0}^{l-1} n_j} |n_0, n_1, \dots, 0_m, \dots, 1_l, \dots, n_{L-1}\rangle \quad (\text{A.79})$$

$$= -(-1)^{\sum_{j=m}^{l-1} n_j} |n_0, n_1, \dots, 1_l, \dots, 0_m, \dots, n_{L-1}\rangle \quad (\text{A.80})$$

Using the measured section $\sum_{j=l}^m n_j$ as before, this time initially $n_l = 0$, such that no additional minus sign is required.

A.5.2 Density-density correlation structure factor

It is evident that the density-density correlation structure factor as defined in Eq. (4.14) only contains diagonal matrix elements in the spatial basis, because the product $n_l n_m$ does not alter the state. Both sites l and m need to be occupied to give a contribution, which is then hit twice (double sum) or once, if $l = m$. It follows that the exponentials

add up to a real cosine, which is also expected, because the observable is hermitean. Hence, the observable simplifies to

$$D(k) = \frac{N}{L} + \frac{2}{L} \sum_{l=1}^L \sum_{R=1}^{L-l} \cos(kR) n_l n_{l+R}. \quad (\text{A.81})$$

The observable $D(k)$ commutes with the translation operator \mathcal{T} , because any shift in the index $(l, m) \rightarrow (l + 1, m + 1)$ cancels through the minus sign. Moreover, it also commutes with \mathcal{P} , since $D(-k) = D(k)$. Furthermore, one finds that $D(k = 0) = N/L + 2/L(N(N - 1)/2) = N^2/L$. Finally, one calculates that

$$\begin{aligned} \mathcal{Z}D(k)\mathcal{Z}^\dagger &= \frac{1}{L} \sum_{l,m=1}^L e^{ik(l-m)} (1 - n_l)(1 - n_m) \\ &= \frac{1}{L} \sum_{l,m=1}^L e^{ik(l-m)} - \frac{1}{L} \sum_{m=1}^L e^{-ikm} \sum_{l=1}^L e^{ikl} n_l - \frac{1}{L} \sum_{l=1}^L e^{ikl} \sum_{m=1}^L e^{-ikm} n_m + D(k) \\ &= L\delta_{k,0} - 2\delta_{k,0}N + D(k), \end{aligned} \quad (\text{A.82})$$

and hence $\mathcal{Z}D(k)\mathcal{Z}^\dagger = D(k)$ at half-filling.

Appendix B

Supplementary plots

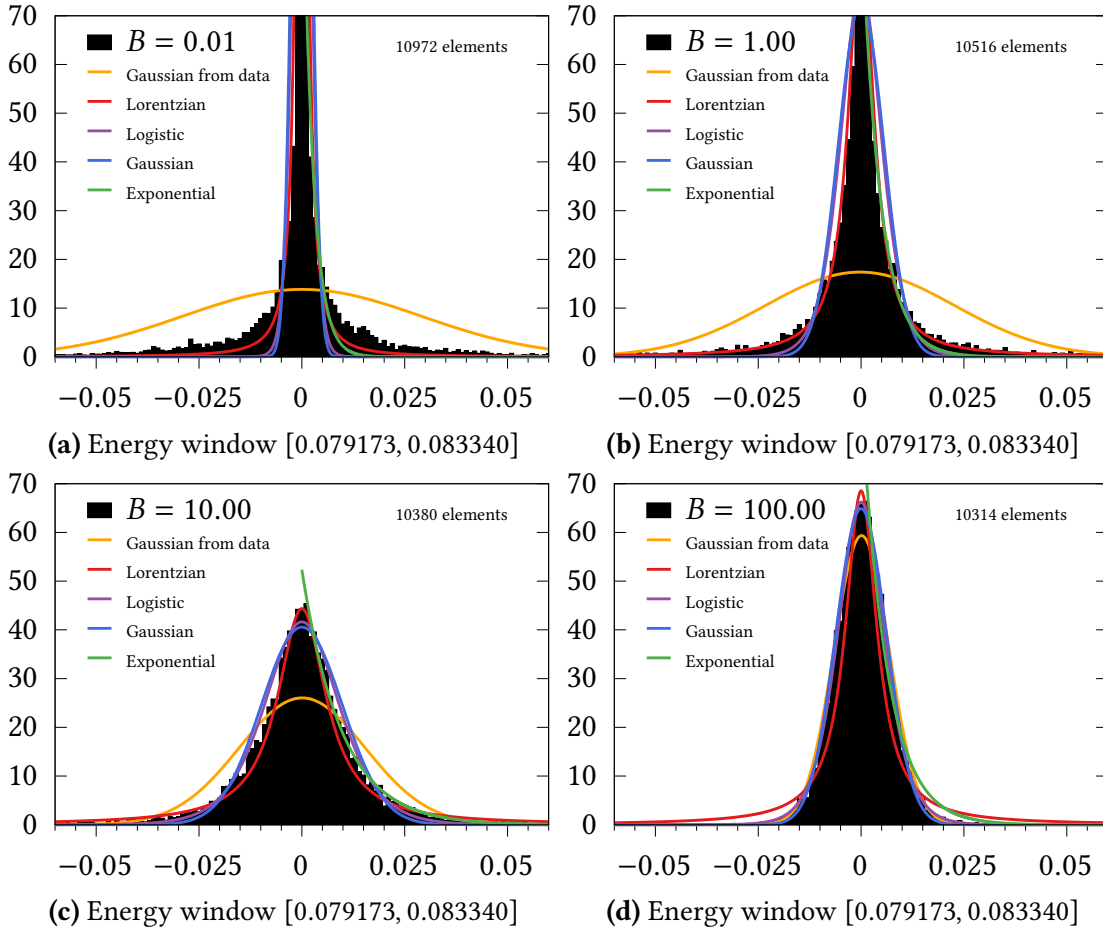


Figure B.1: Histograms over the flow for energy window $[0.079173, 0.083340]$ for the symmetry sectors $k = 0, L/2$ and both other symmetry quantum numbers, i. e. $p = \pm 1, z \pm 1$ and lattice size $L = 20$. Each shows the relative frequency over bins of size 0.001.

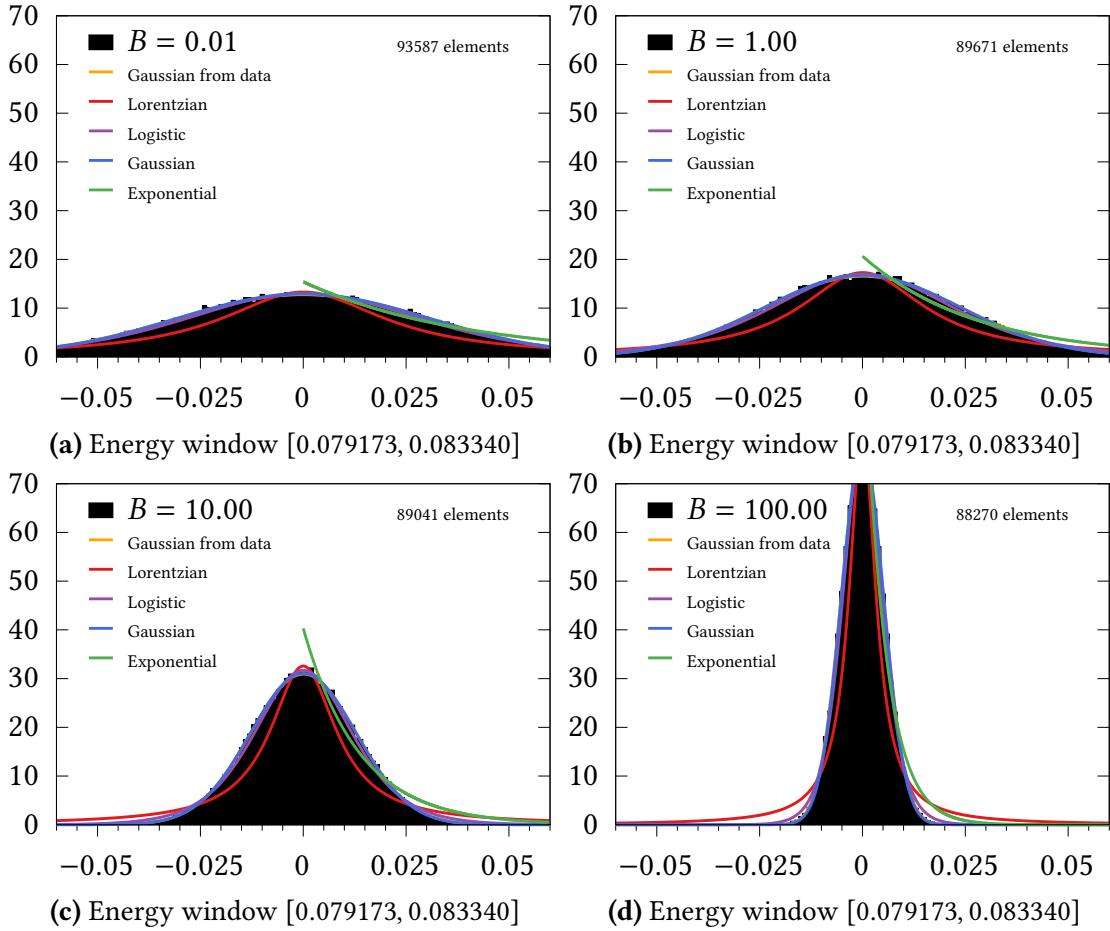


Figure B.2: Histograms over the flow for energy window [0.079173, 0.083340] for the symmetry sectors $k \neq 0, L/2$ and both other symmetry quantum numbers, i. e. $p = \pm 1, z \pm 1$ and lattice size $L = 20$. Each shows the relative frequency over bins of size 0.001.

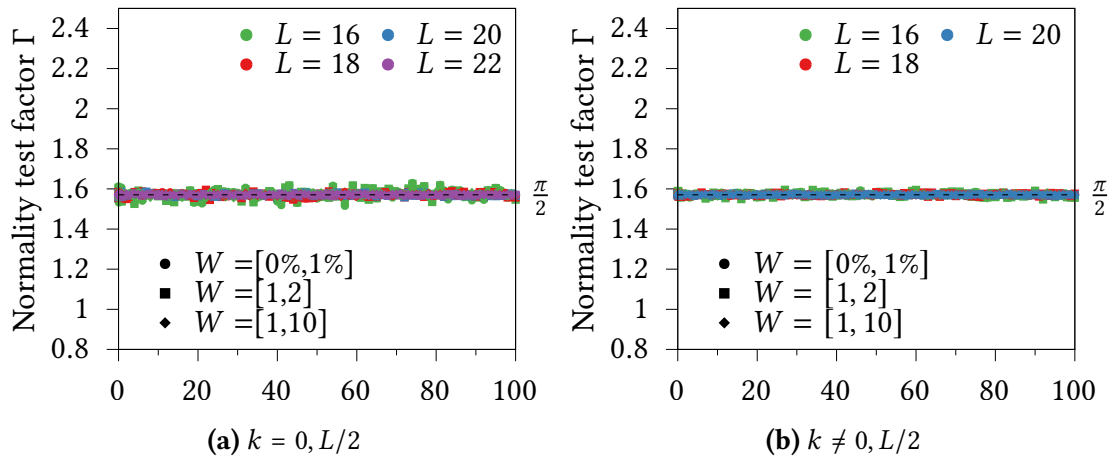


Figure B.3: The Γ -normality indicator for three different windows over subdiagonals for a true random flow, i. e. for transformations with 100 different random unitary matrices. Different lattice sizes and the symmetry sectors (a) $k = 0, L/2$ and (b) $k \neq 0, L/2$. For Gaussian distributed values it is $\Gamma = \frac{\pi}{2}$. The Γ -value of the data is always very close to the normality value $\pi/2$ from above for all momenta k as expected.

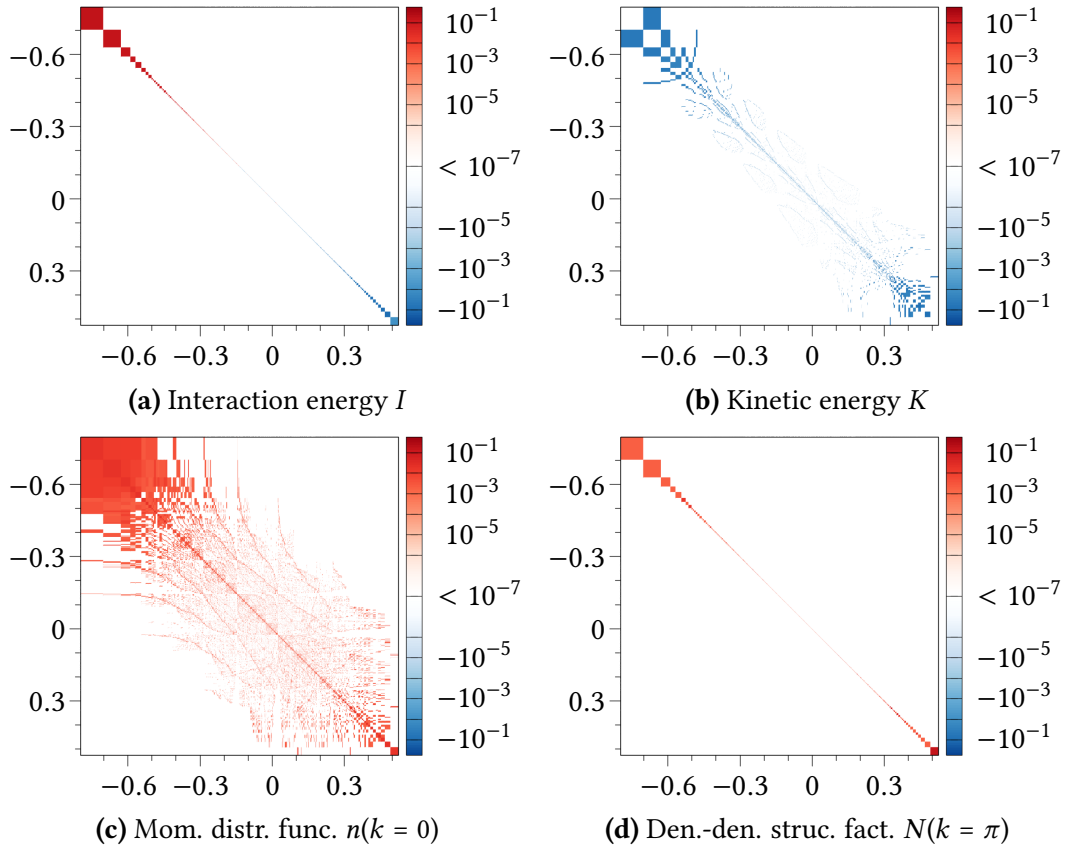


Figure B.4: Observables for the symmetry sector $(k, p, z) = (0, 1, 1)$ and $L = 18$ in the spatial basis. Since both the interaction I and the den.-den. struc. fact. $N(k = \pi)$ only contain density operators, they cannot change a basis state and are confined to the main diagonal. The kinetic energy K is always negative, because of the negative sign in front of t_1 ($t_1 > 0$). The mom. distribution function $n(k = 0)$ only accumulates successful hoppings from site m to l and is therefore positive (see ??).

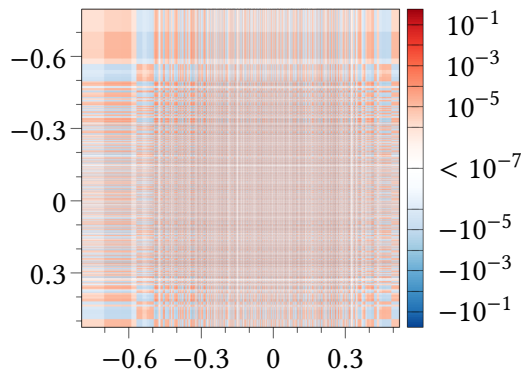


Figure B.5: The projection operator $\mathcal{P}_{E=0}$ in the spatial basis. This operator can be computed by using the transformation, which diagonalizes the Hamiltonian in the spatial basis, to reversely transform a diagonal, which only contains a '1' at the chosen site. In the spatial basis it yields a densely populated form.

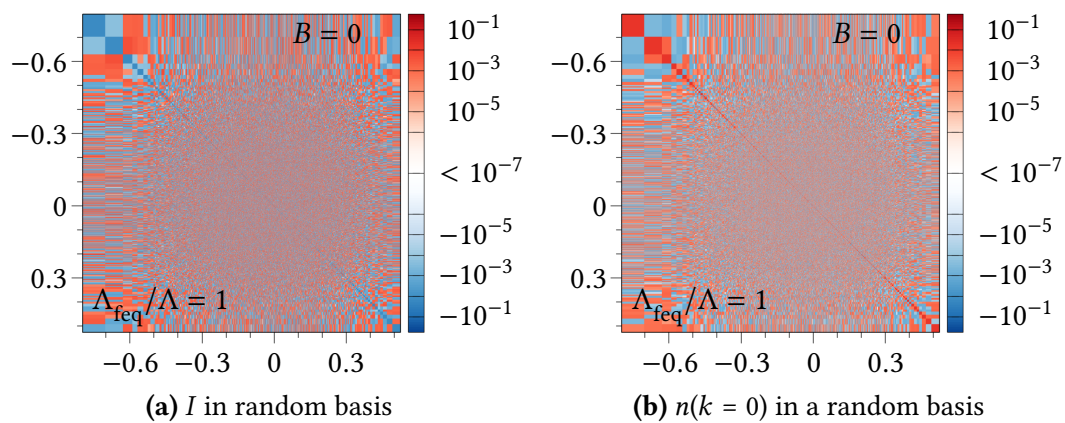


Figure B.6: The interaction energy and the mom. distr. func. for the symmetry sector $(k, p, z) = (0, 1, 1)$ and $L = 18$ in a random basis. The other two observables look similar. One can clearly see the difference compared to the Wegner flow pendants (see e. g. Fig. B.7b and Fig. B.7f).

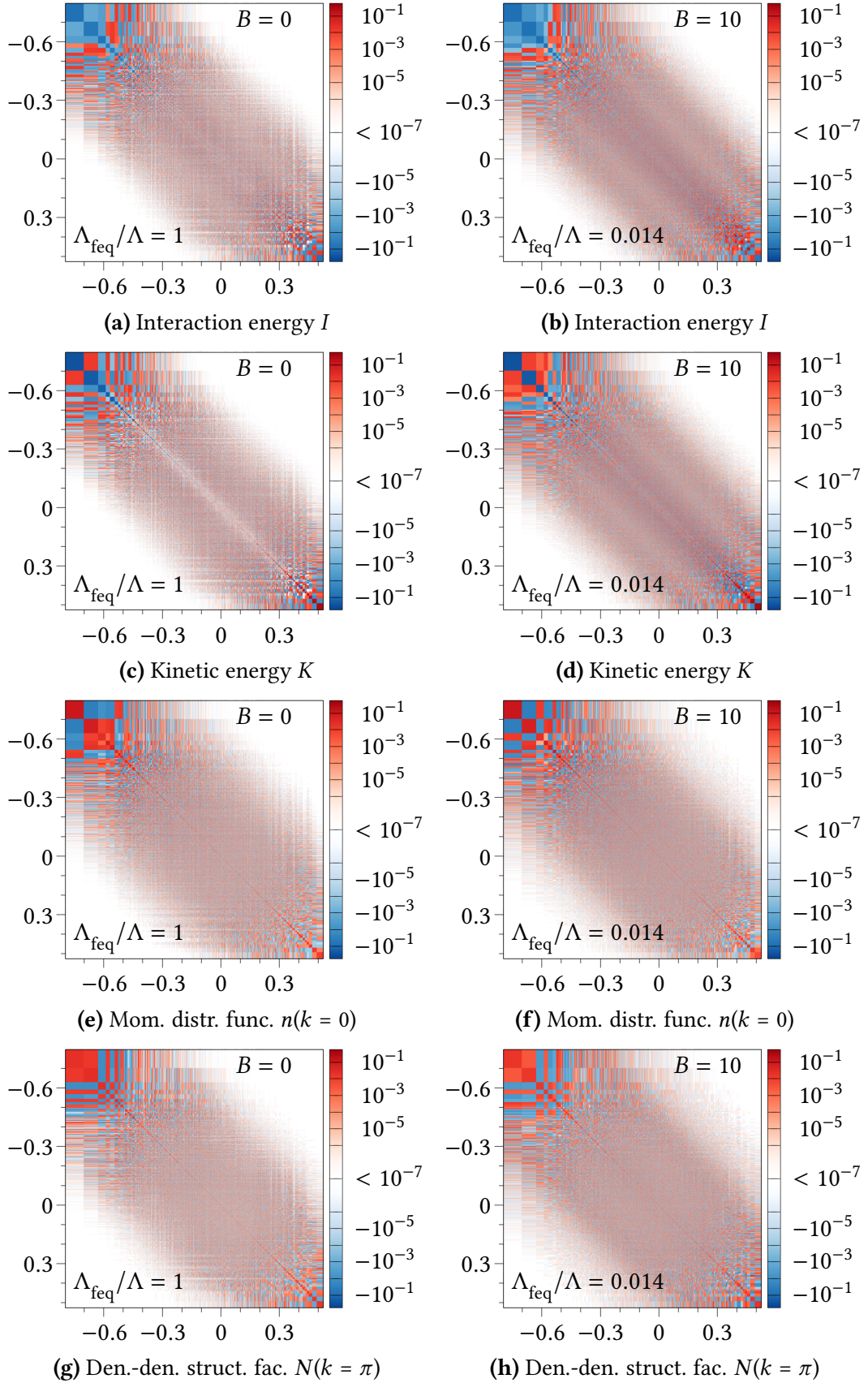


Figure B.7: Observables for the symmetry sector $(k, p, z) = (0, 1, 1)$ and $L = 18$

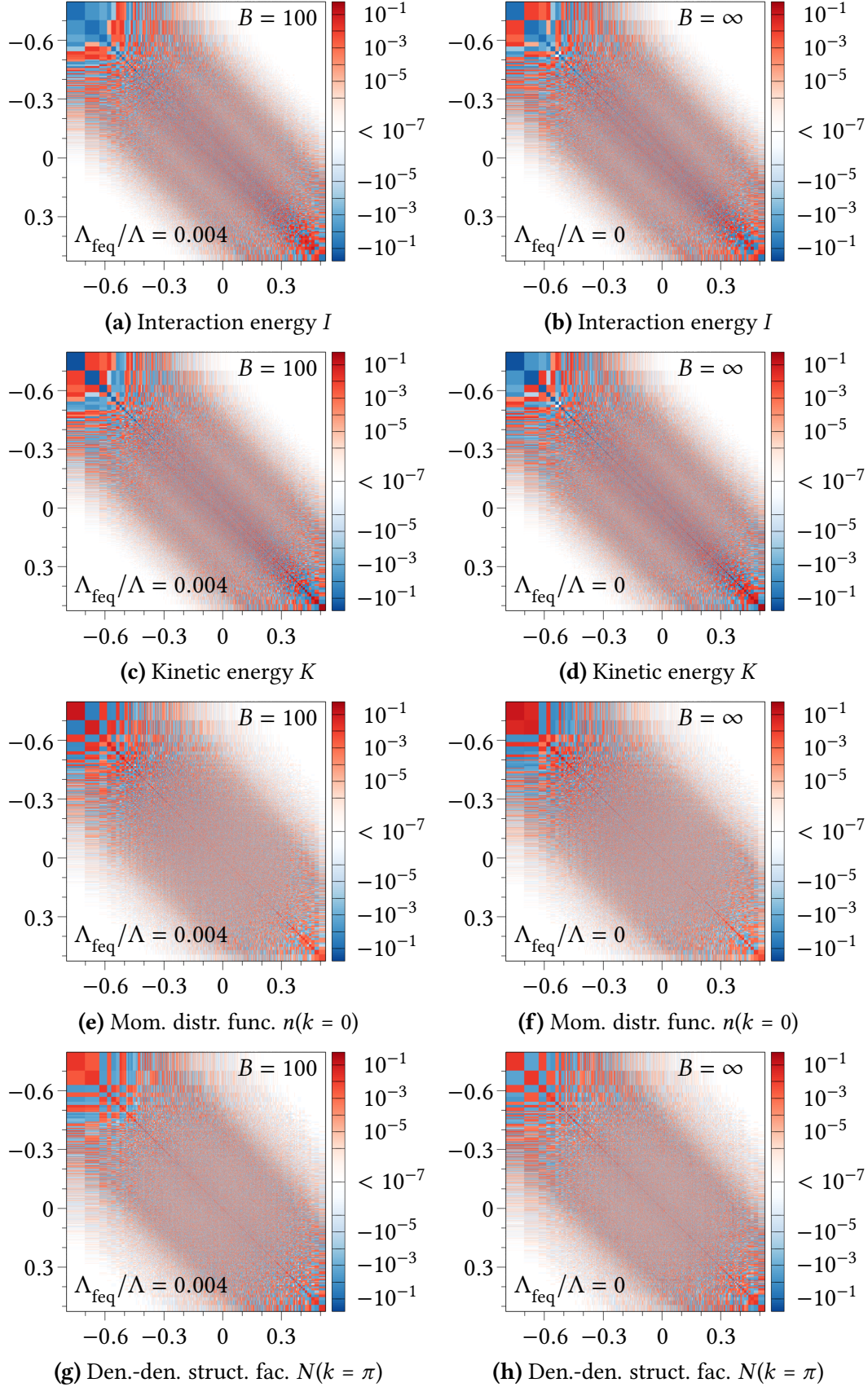


Figure B.8: Observables for the symmetry sector $(k, p, z) = (0, 1, 1)$ and $L = 18$

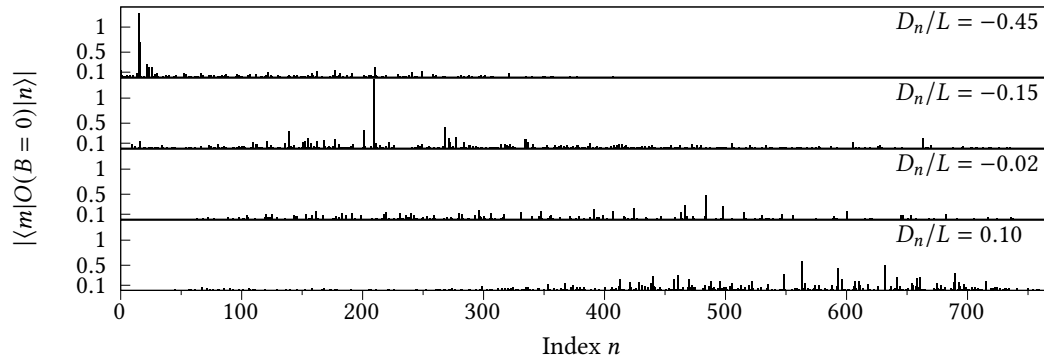
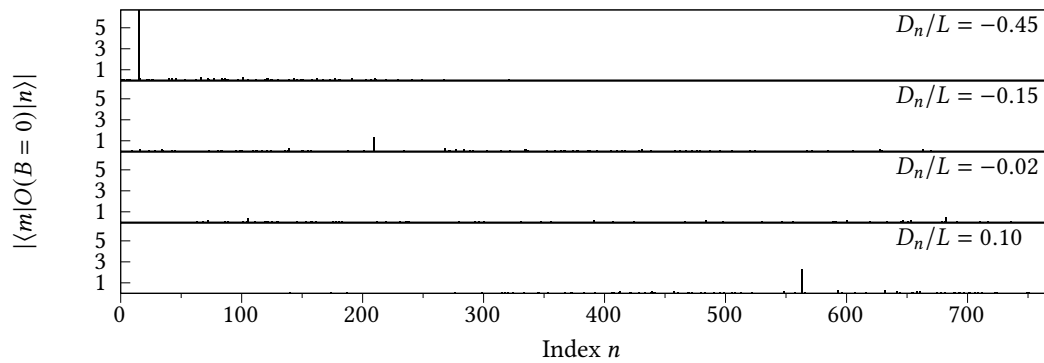
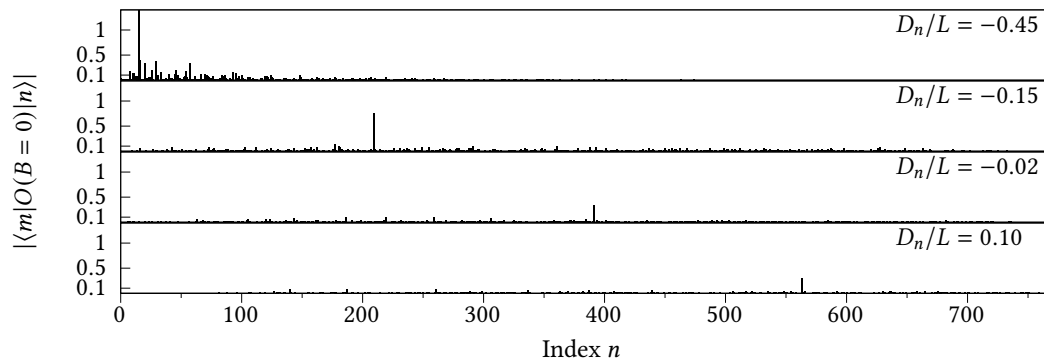
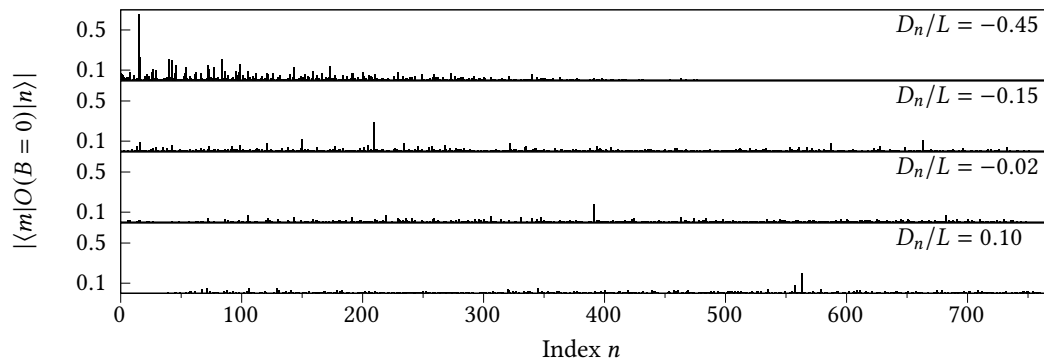
(a) Interaction energy I (b) Kinetic energy K (c) Mom. distr. func. $n(k=0)$ (d) Den.-den. struct. fact. $N(k=\pi)$

Figure B.9: Matrix elements of the observables in the basis of $B = 0$ for different energies per site, i. e. cuts through the spectrum.

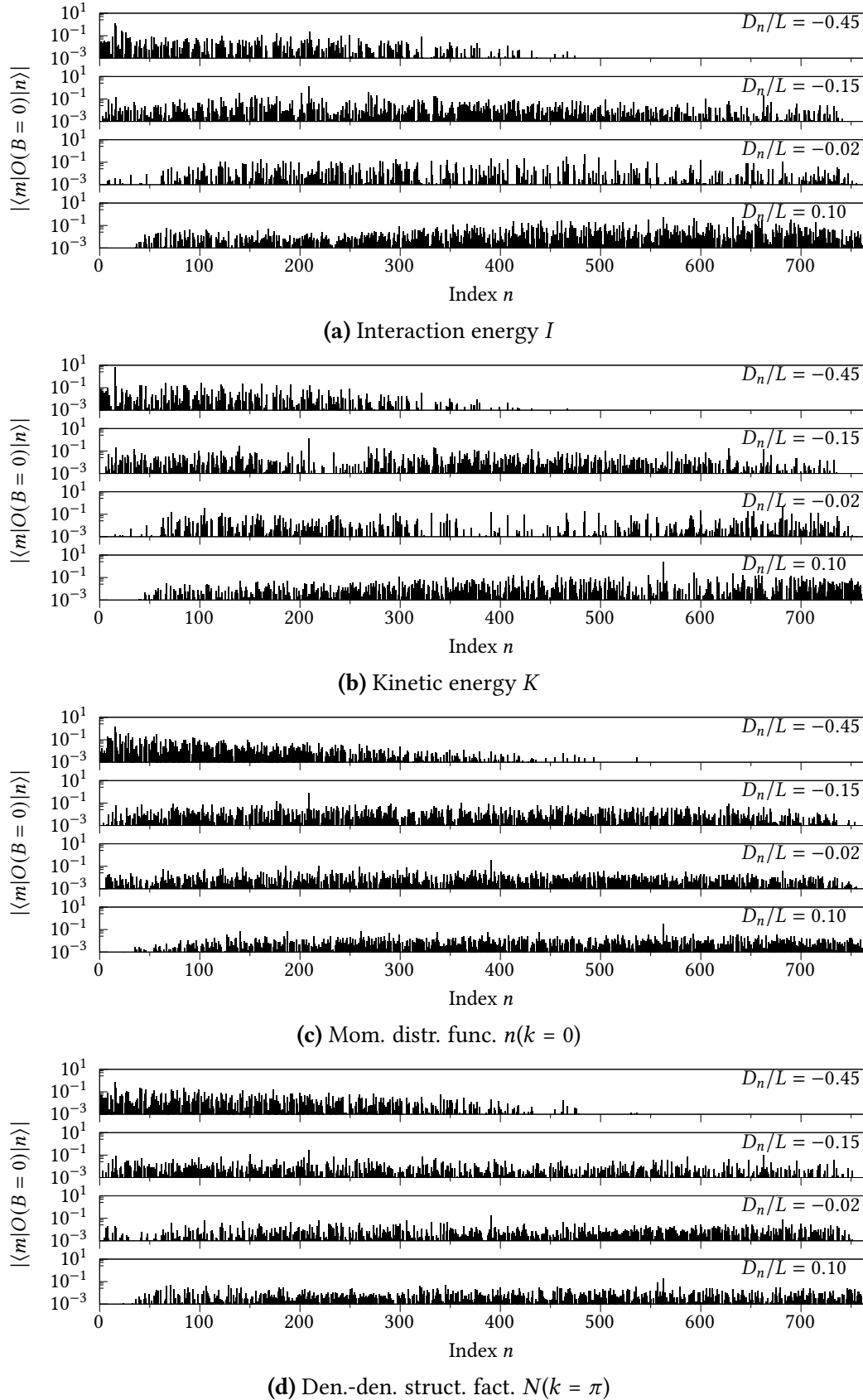


Figure B.10: Matrix elements of the observables in the basis of $B = 0$ for different energies per site, i. e. cuts through the spectrum. The data is identical to the data in Fig. B.9, this time, however, plotted over a logscale.

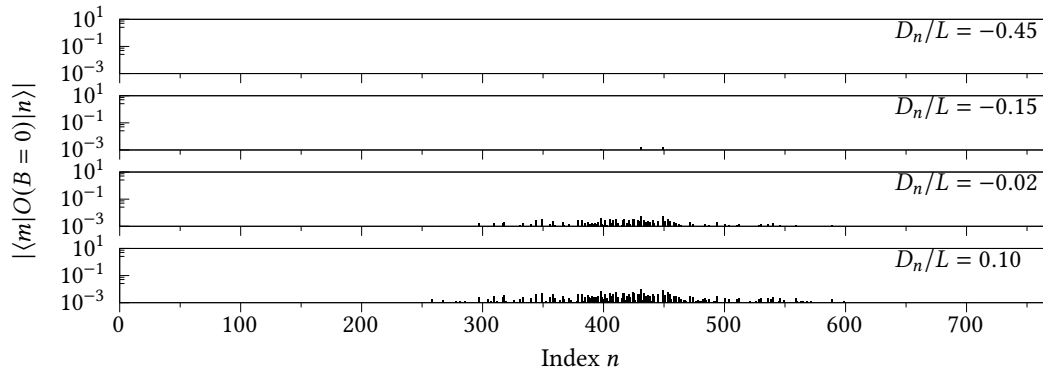
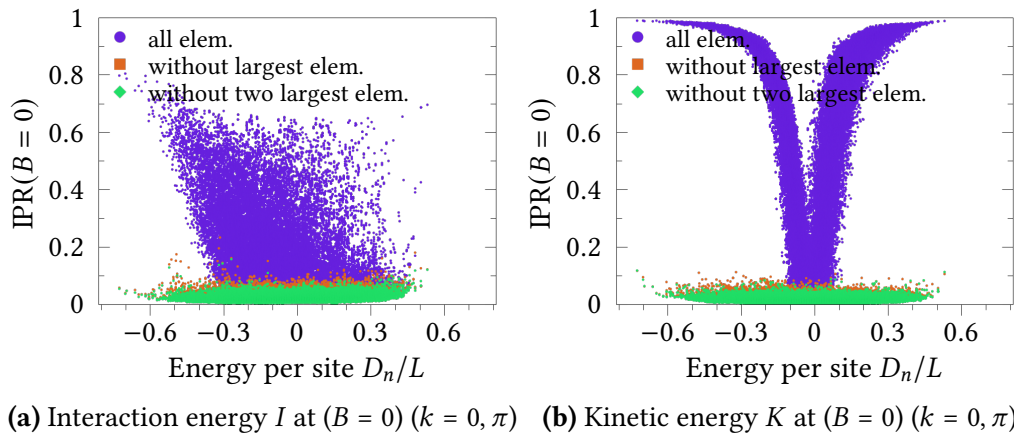


Figure B.11: Matrix elements $|\langle m|\mathcal{P}_{E=0}|n\rangle|$ at $B = 0$ of the Projection operator $\mathcal{P}_{E=0}$ for different energies per site.



(a) Interaction energy I at $(B = 0)$ ($k = 0, \pi$) **(b)** Kinetic energy K at $(B = 0)$ ($k = 0, \pi$)

Figure B.12: The IPR for the (a) interaction energy and (b) kinetic energy for three different data sets ($L = 22, k = 0, \pi$). The IPR is computed not only for all matrix elements (blue), but also for all but the largest (orange), all but the largest two (green) matrix elements. It turns out that the largest element defines the overall form of the IPR and that without it the IPR is flat also for I and K .

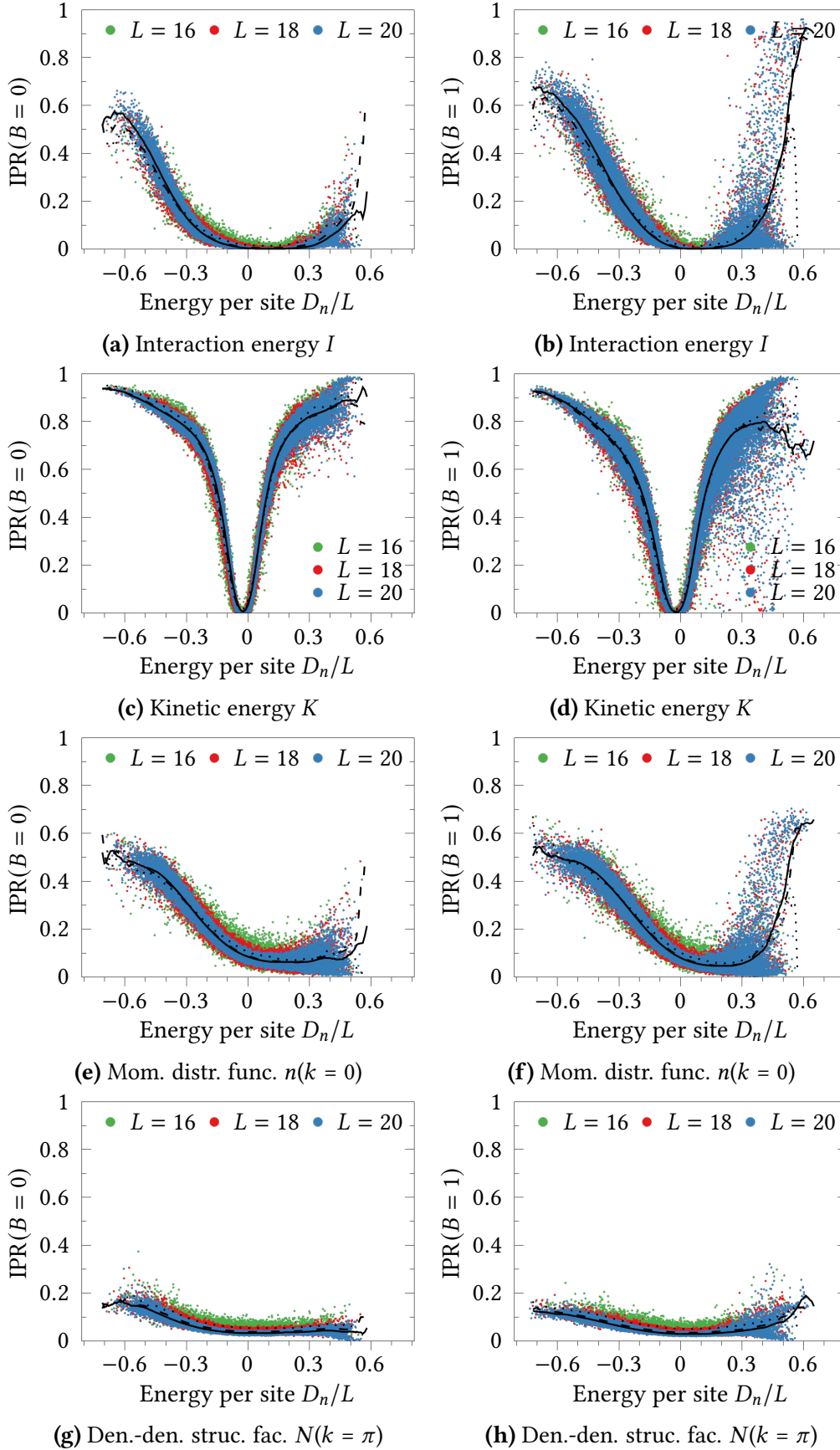


Figure B.13: The IPR for all observables and a mov. avg. (black) over a 0.06 window ($\approx 4\%$ of the spectrum) for the symm. sectors $n_k \neq 0, L/2$ and and early flow.

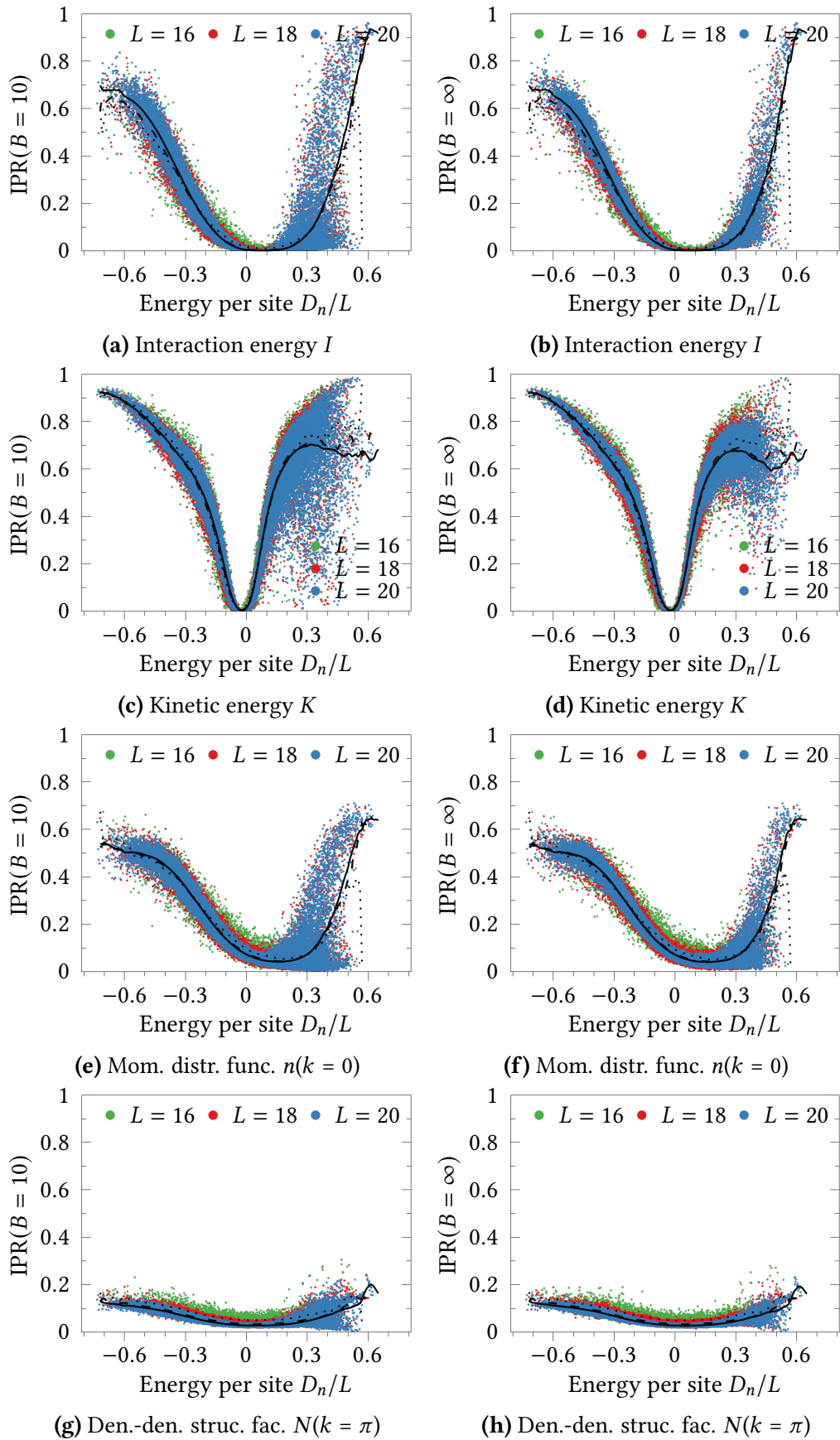


Figure B.14: The IPR for all observables and a mov. avg. (black) over a 0.06 window ($\approx 4\%$ of the spectrum) for the symm. sectors $n_k \neq 0, L/2$ and late flows.

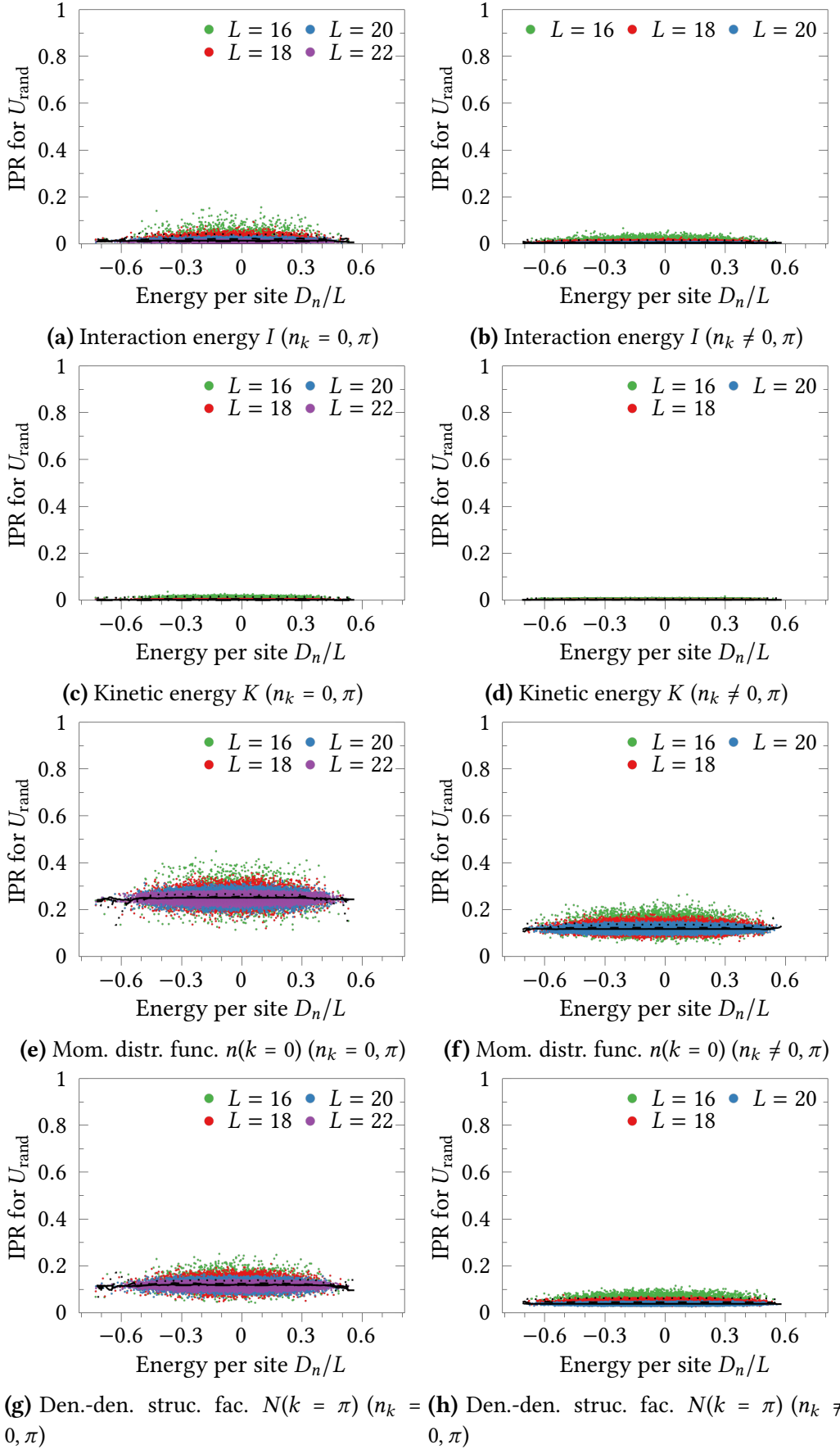


Figure B.15: The IPR for all observables and mov. avg.s (black) over a 0.06 window ($\approx 4\%$ of the spectrum) for all symm. sectors and a random unitary transformation.

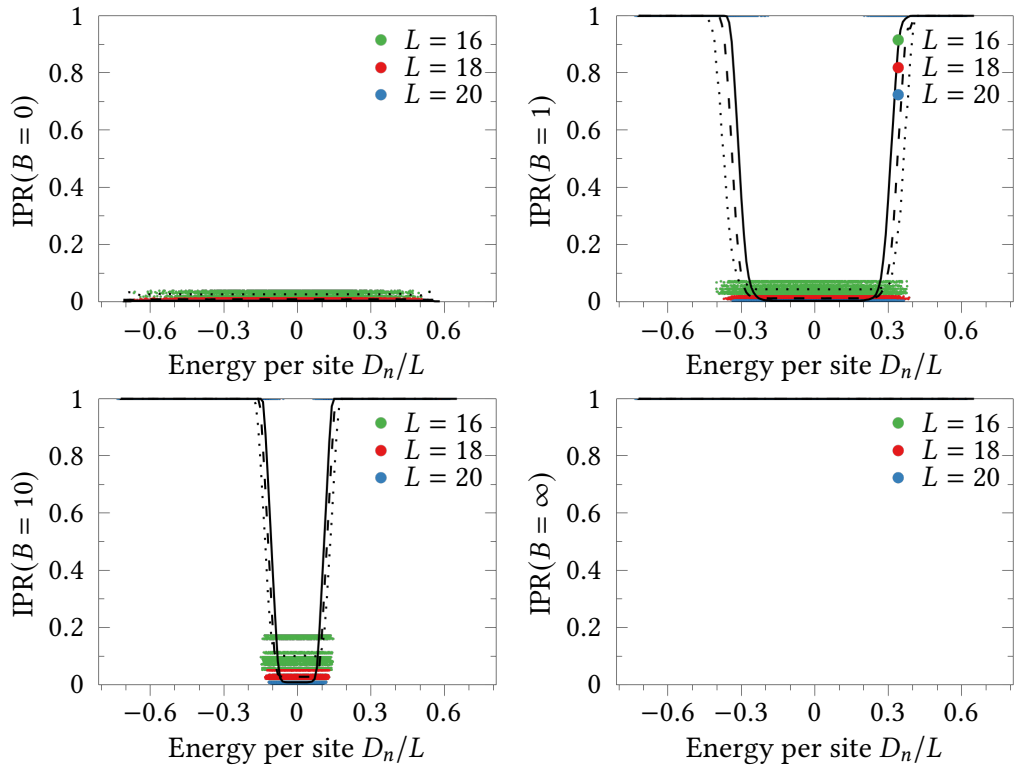
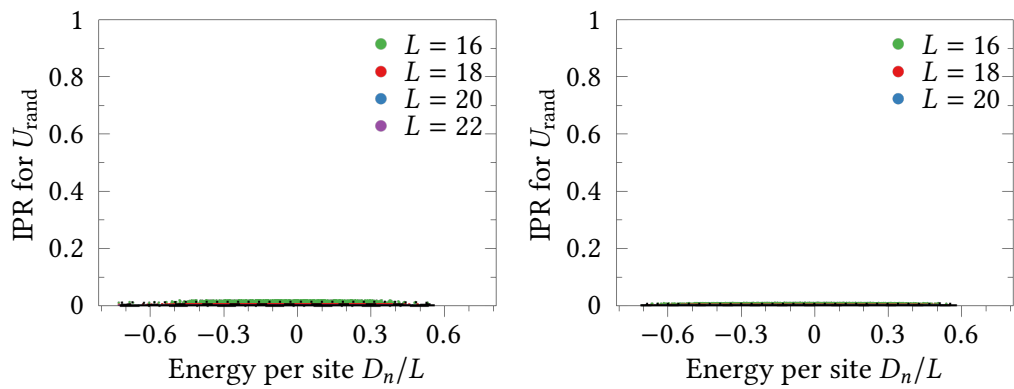


Figure B.16: The IPR of the projection operator $\mathcal{P}_{E=0}$ and moving averages (black) for different flows B over a 0.06 window ($\approx 4\%$ of the spectrum) for the symm. sectors $n_k \neq 0, L/2$.



(a) Projection operator $\mathcal{P}_{E=0}$ ($n_k = 0, L/2$) (b) Projection operator $\mathcal{P}_{E=0}$ ($n_k \neq 0, L/2$)

Figure B.17: The IPR for the projection operator $\mathcal{P}_{E=0}$ and a mov. avg. (black) over a 0.06 window ($\approx 4\%$ of the spectrum) for the symm. sectors (left) $n_k = 0, L/2$ and (right) $n_l \neq 0, L/2$ and a random unitary transformation.

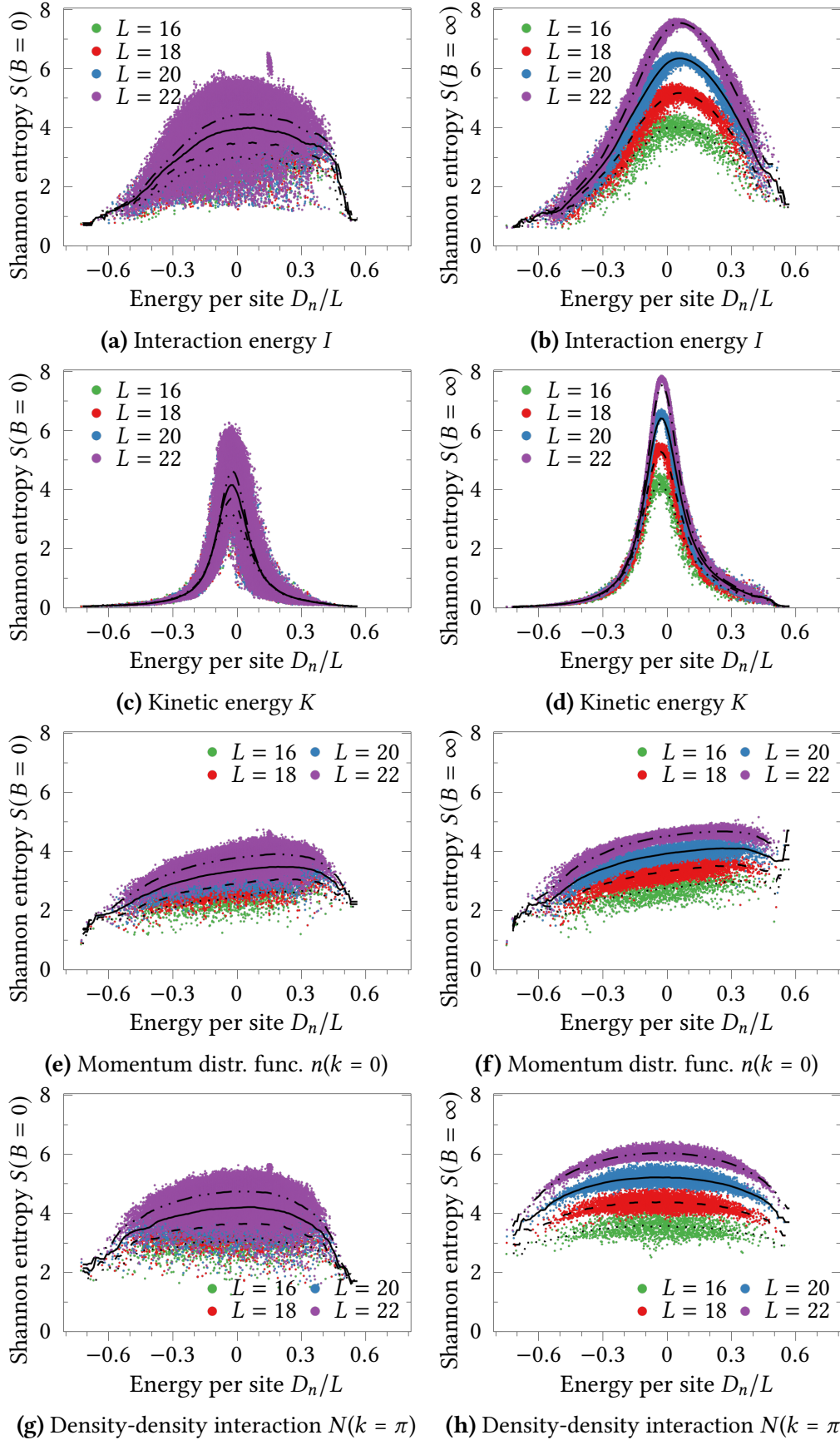


Figure B.18: The Shannon entropy for all observables and a mov. avg. (black) over a 0.06 window ($\approx 4\%$ of the spectrum) for $B = 0$ and $B = \infty$ in the symm. sectors $n_k = 0, L/2$.

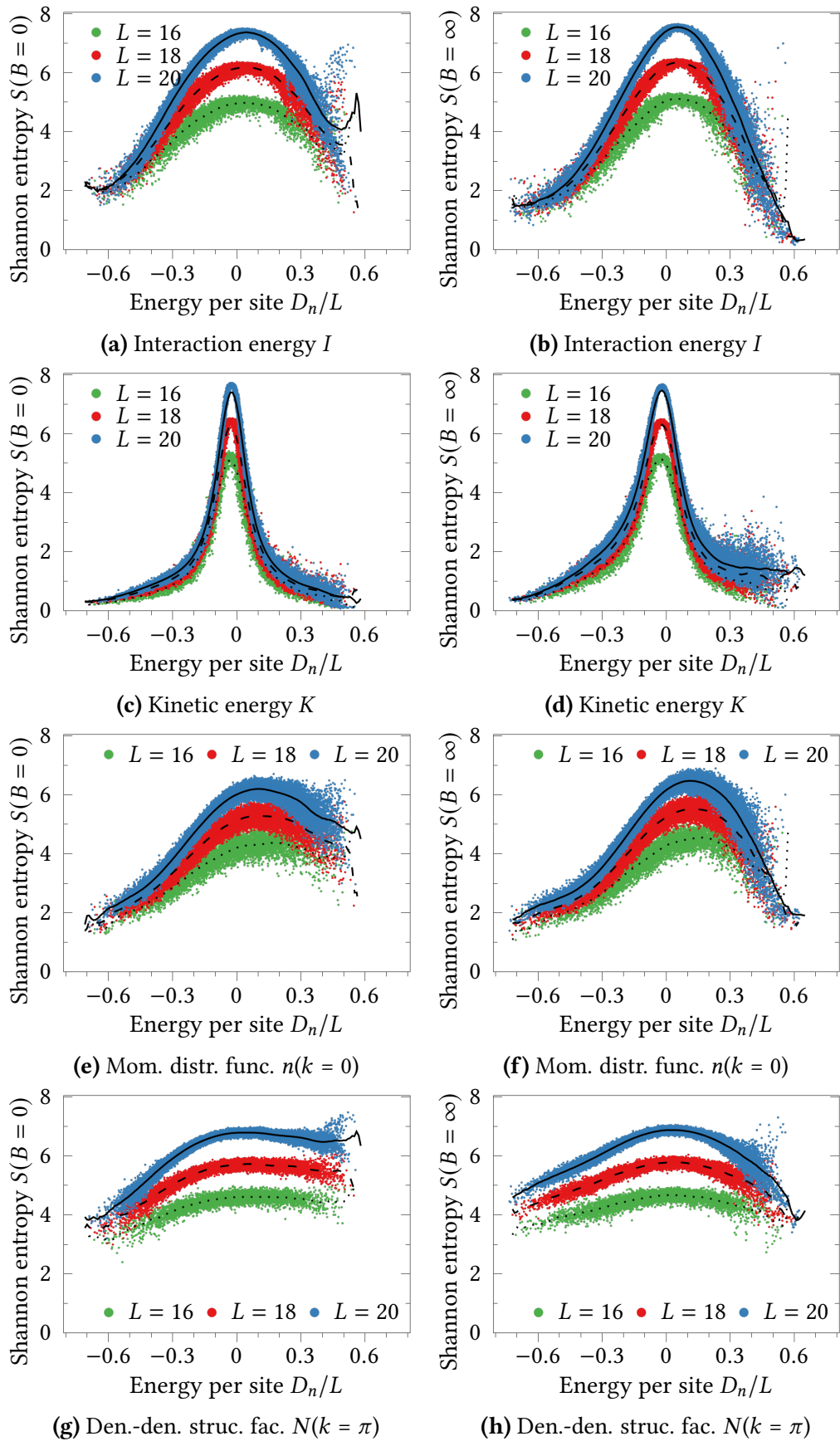


Figure B.19: The Shannon entropy for all observables and a mov. avg. (black) over a window 0.06 ($\approx 4\%$ of the spectrum) for (left) $B = 0$ and (right) $B = \infty$ in the symm. sectors $n_k \neq 0, L/2$.

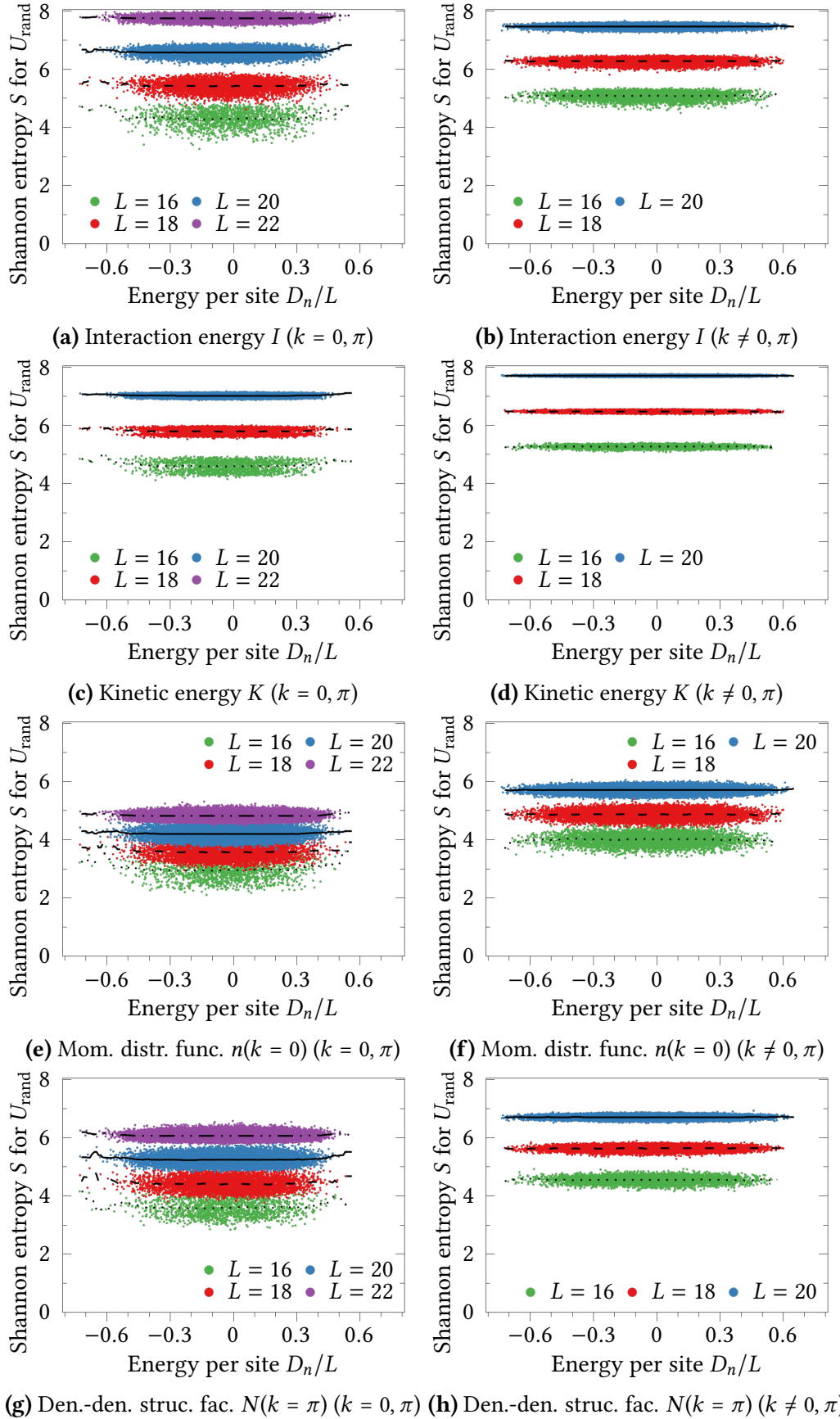


Figure B.20: The Shannon entropy for all observables and a mov. avg. (black) over a 0.06 window ($\approx 4\%$ of the spectrum) in a random basis for the sectors (left) $n = 0, \pi$ and (right) $n_k \neq 0, L/2$.

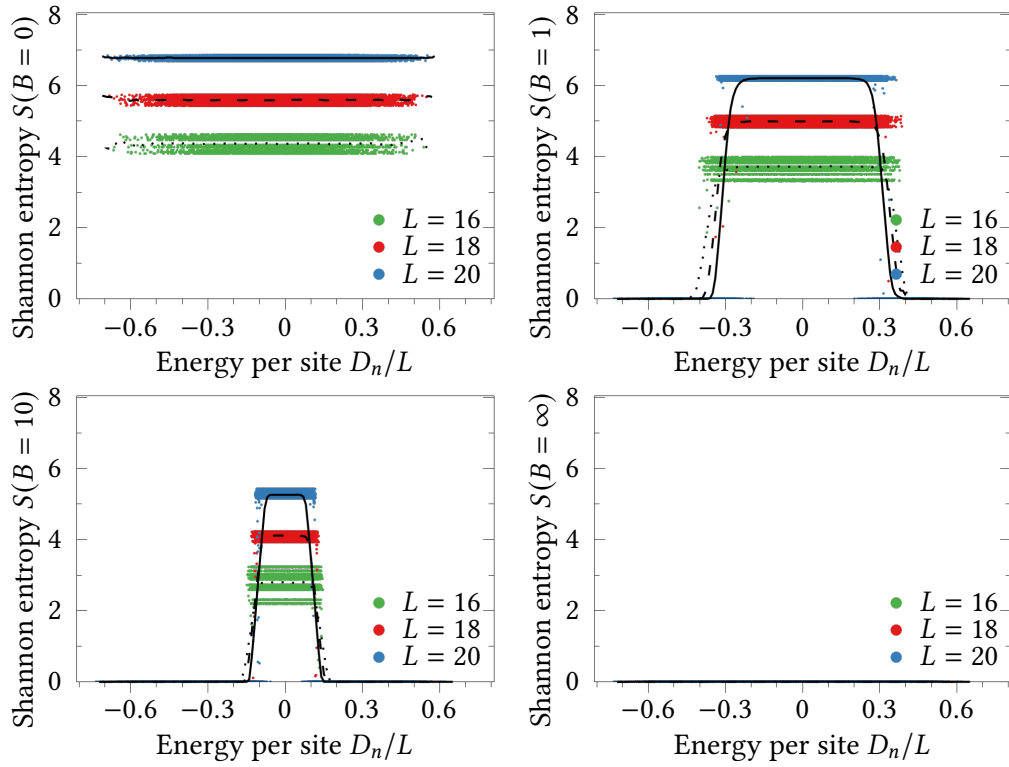
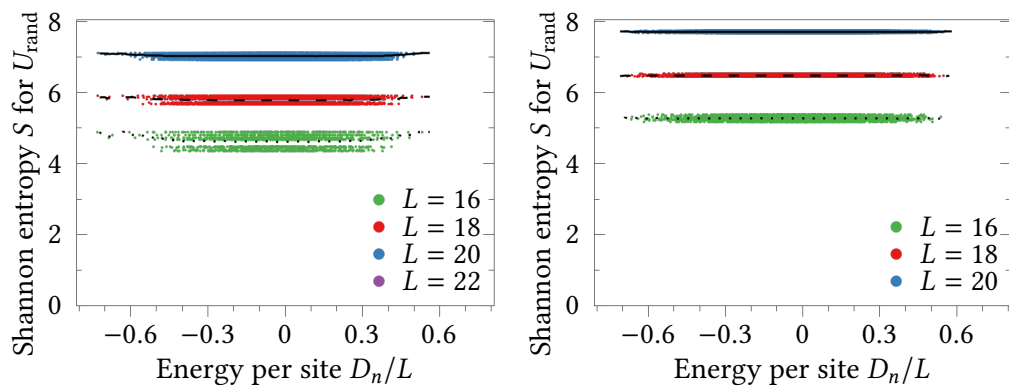


Figure B.21: The Shannon entropy of the projection operator $\mathcal{P}_{E=0}$ and a mov. avg.s (black) for different flows B over a 0.06 window ($\approx 4\%$ of the spectrum) for the symm. sectors $n_k \neq 0, L/2$.



(a) Projection operator $\mathcal{P}_{E=0}$ ($n_k = 0, L/2$) (b) Projection operator $\mathcal{P}_{E=0}$ ($n_k \neq 0, L/2$) and a random unitary transformation.

Figure B.22: The Shannon entropy for the projection operator $\mathcal{P}_{E=0}$ and a mov. avg.s (black) over a window of size 0.06 ($\approx 4\%$ of the spectrum) for the symm. sectors (left) $n_k = 0, L/2$ and (right) $n_l \neq 0, L/2$ and a random unitary transformation.

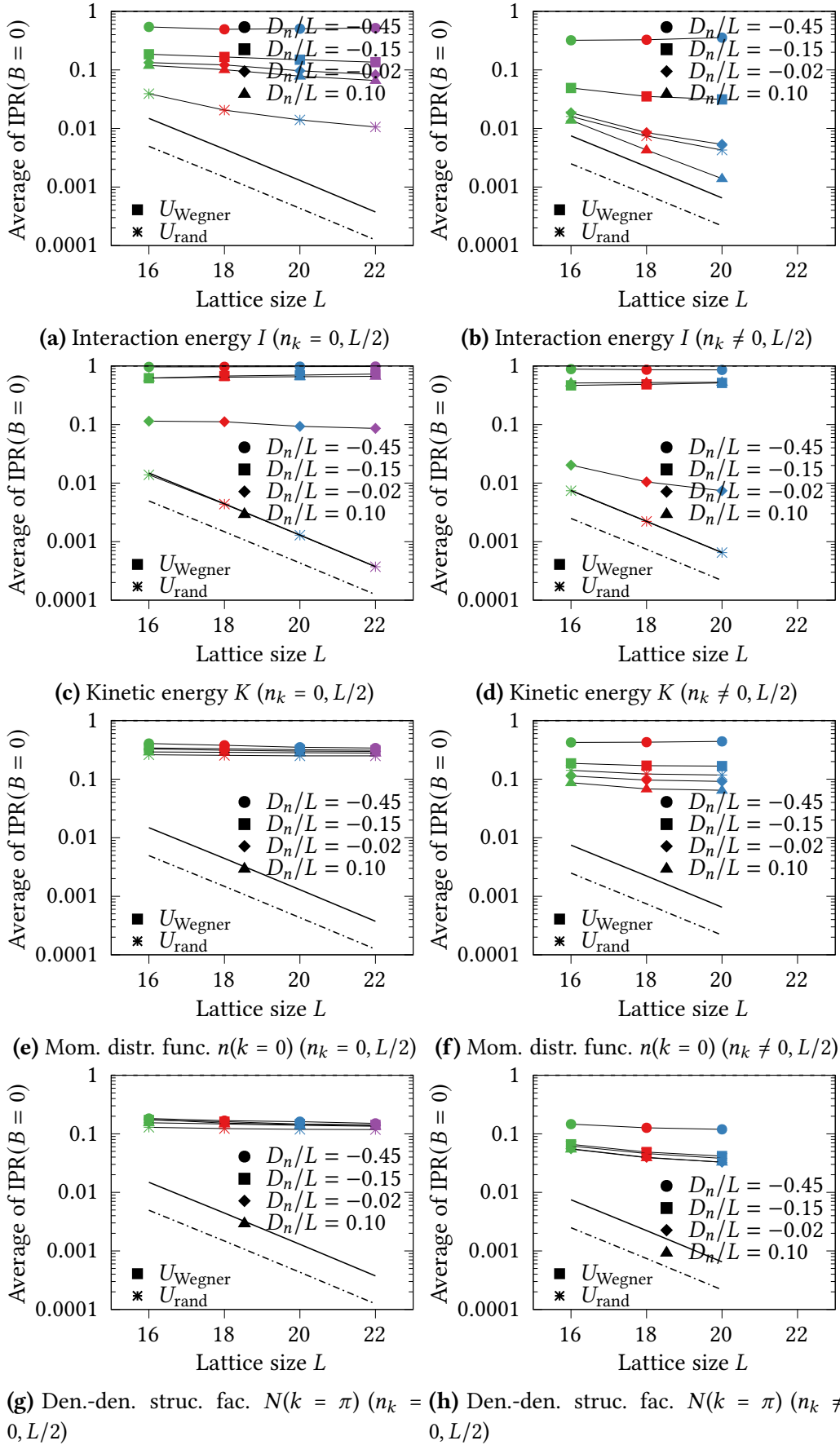


Figure B.23: Scaling of the Shannon entropy over lattice sizes of all observables for different energy densities in all symmetry sectors at $B = 0$.

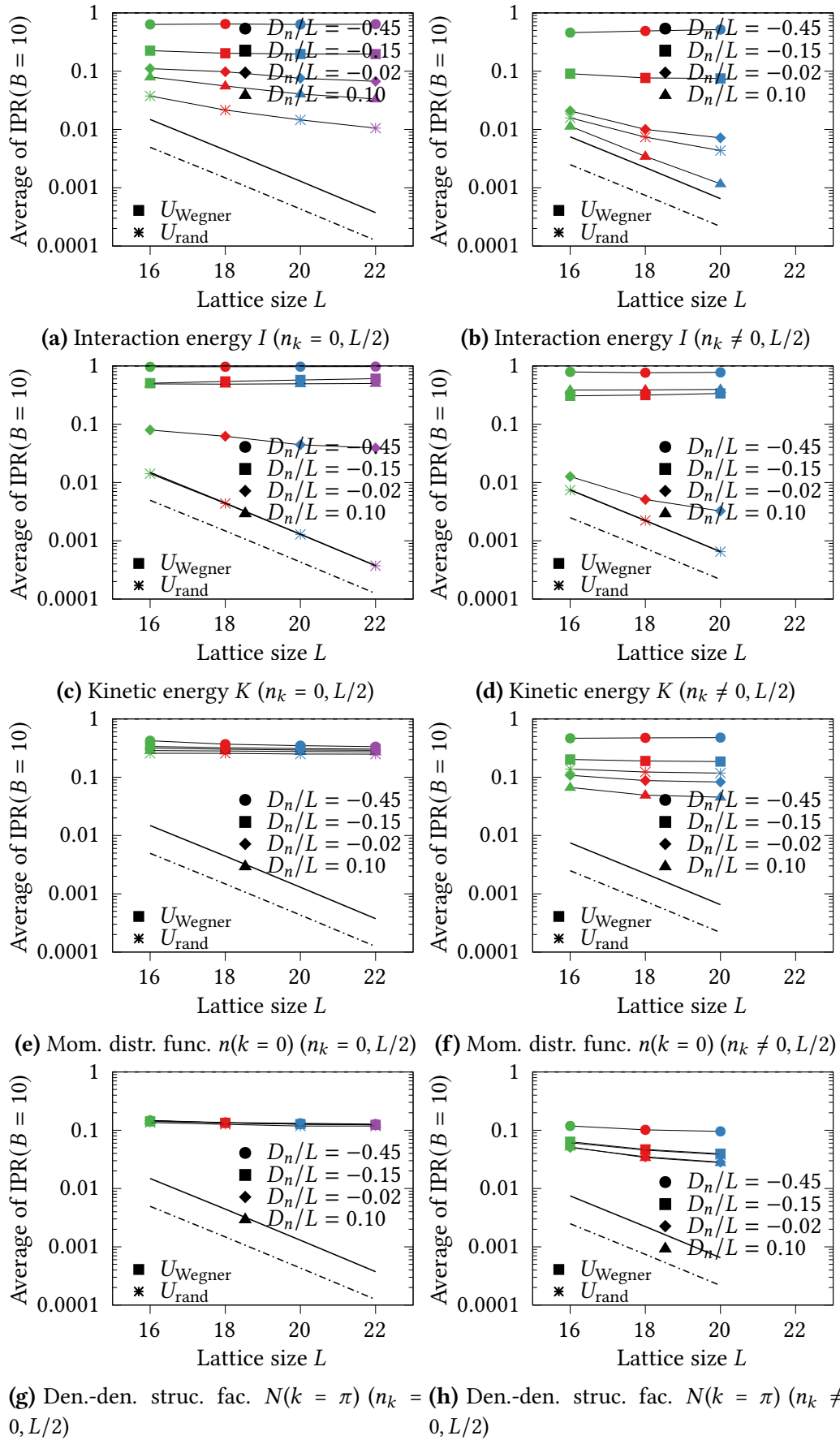


Figure B.24: Scaling of the Shannon entropy over lattice sizes of all observables for different energy densities in all symmetry sectors at $B = 10$.

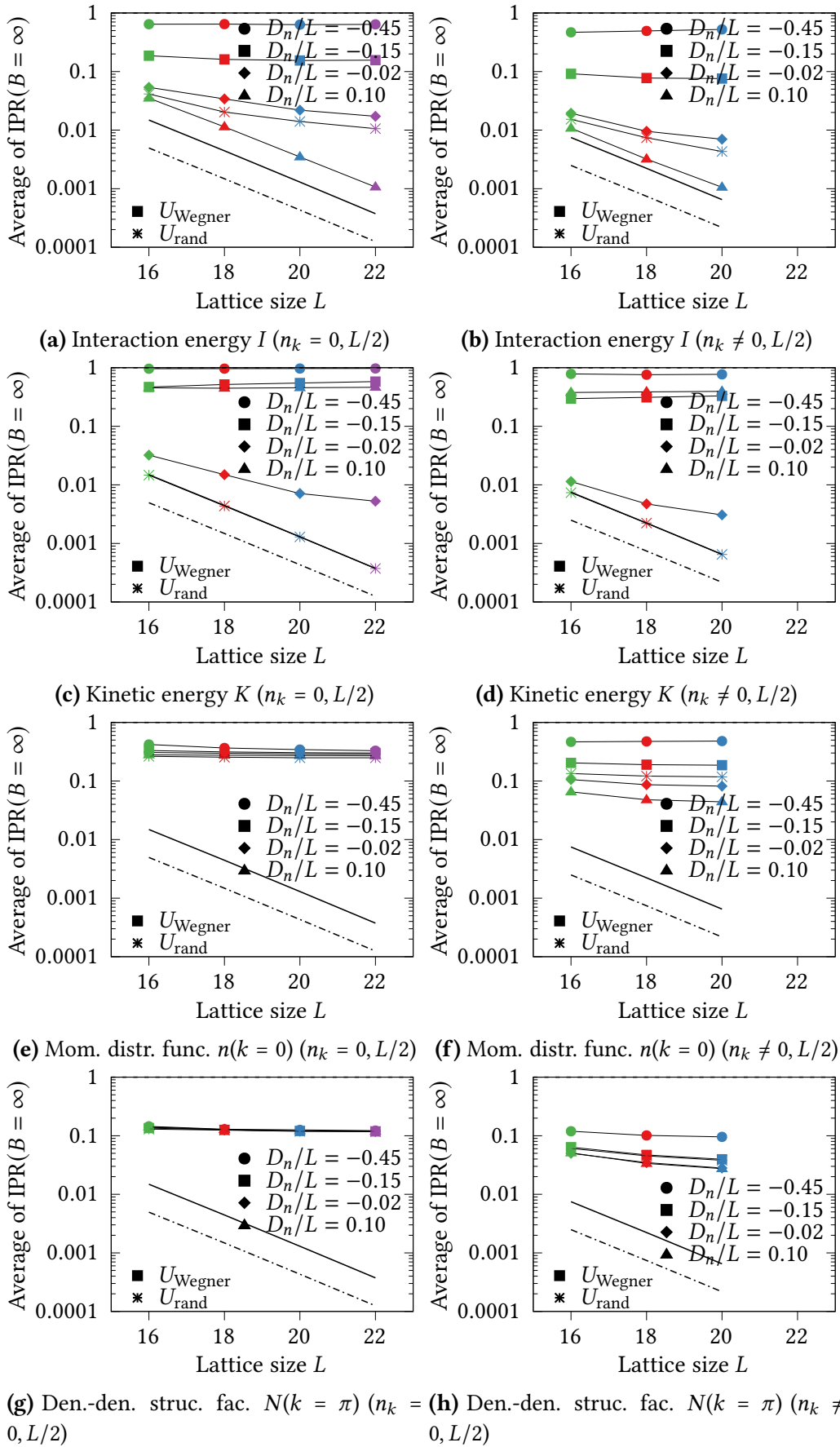


Figure B.25: Scaling of the Shannon entropy over lattice sizes of all observables for different energy densities in all symmetry sectors at $B = \infty$.

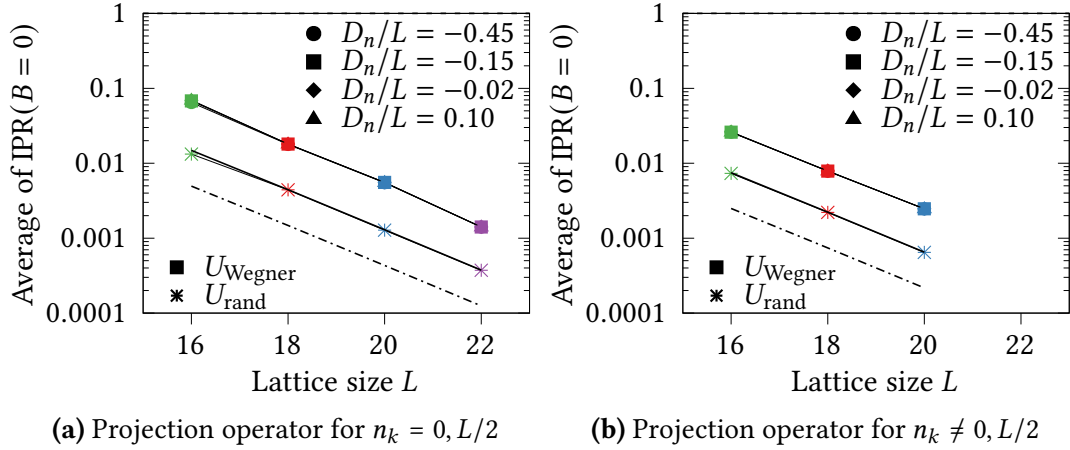


Figure B.26: The scaling of the IPR over lattice sizes for three energy densities and for the projection operator $\mathcal{P}_{E=0}$ into the energy eigenstate with $E = 0$ and all symmetry sectors at $B = 0$. The identical quantity but for a *random* unitary flow is depicted with star shaped symbols.

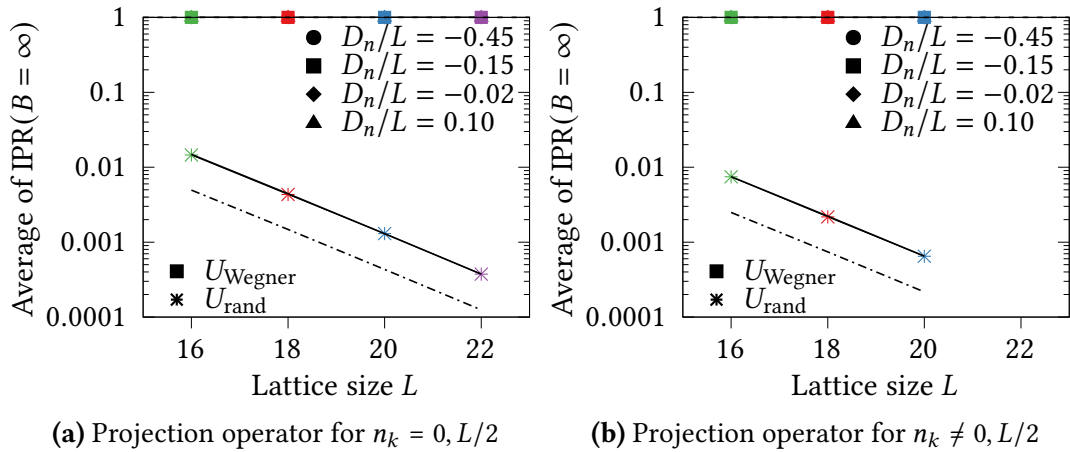


Figure B.27: Scaling of the IPR over lattice sizes for three energy densities and for the projection operator $\mathcal{P}_{E=0}$ into the energy eigenstate with $E = 0$ and all symmetry sectors at $B = \infty$. The identical quantity but for a *random* unitary flow is depicted with star shaped symbols.

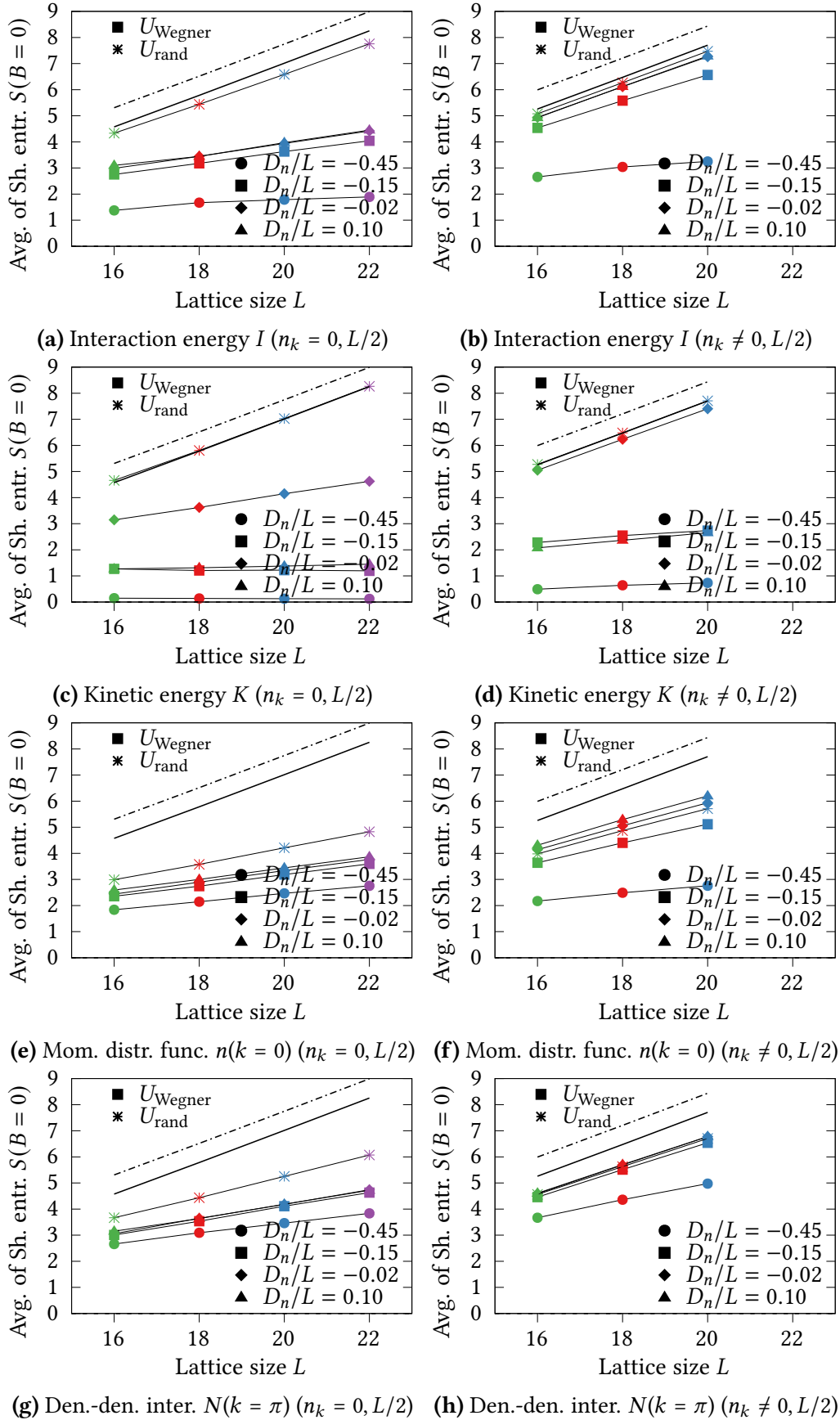


Figure B.28: Scaling of the Shannon entropy over lattice sizes of all observables for different energy densities in all symmetry sectors at $B = 0$.

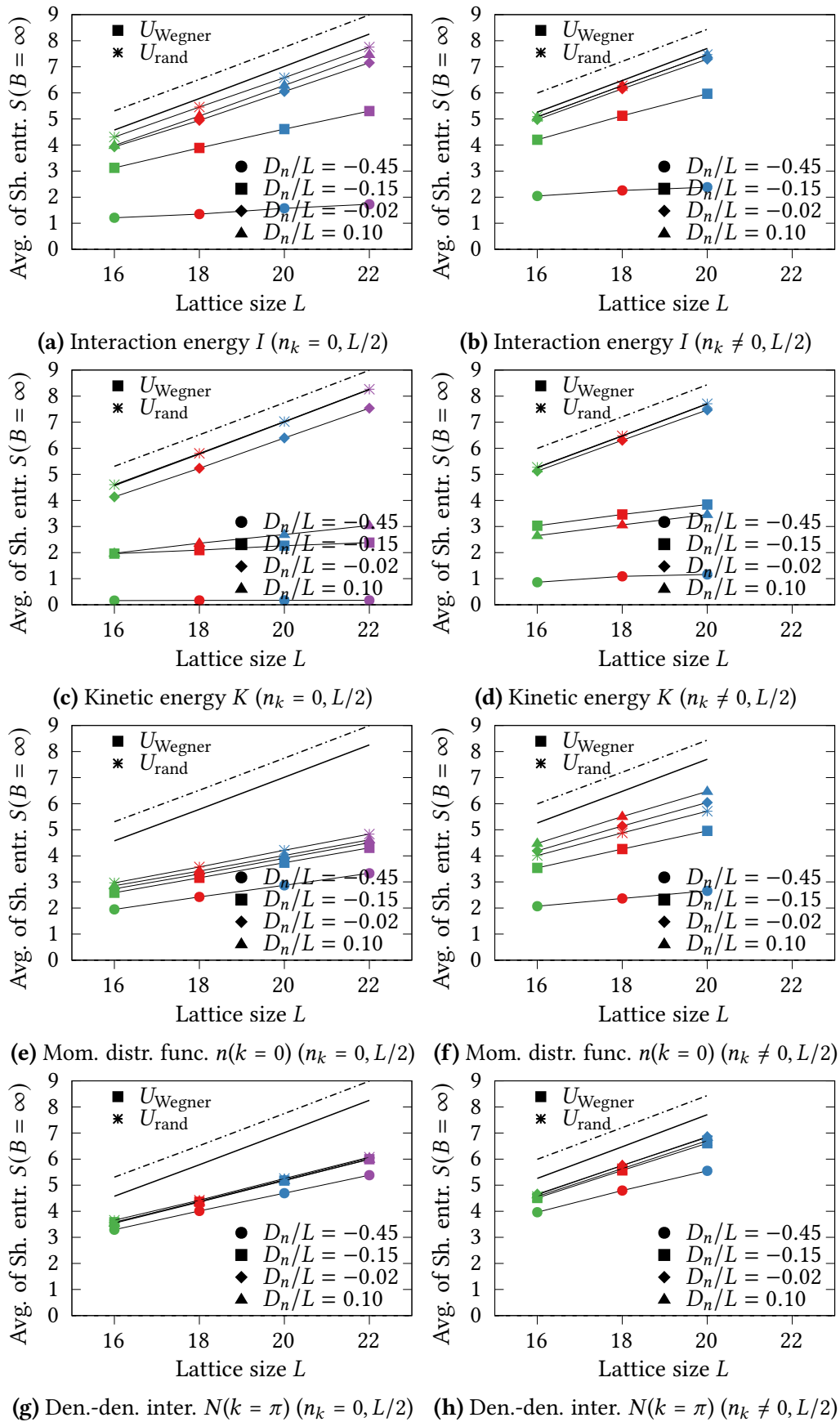


Figure B.29: Scaling of the Shannon entropy over lattice sizes of all observables for different energy densities in all symmetry sectors at $B = \infty$.

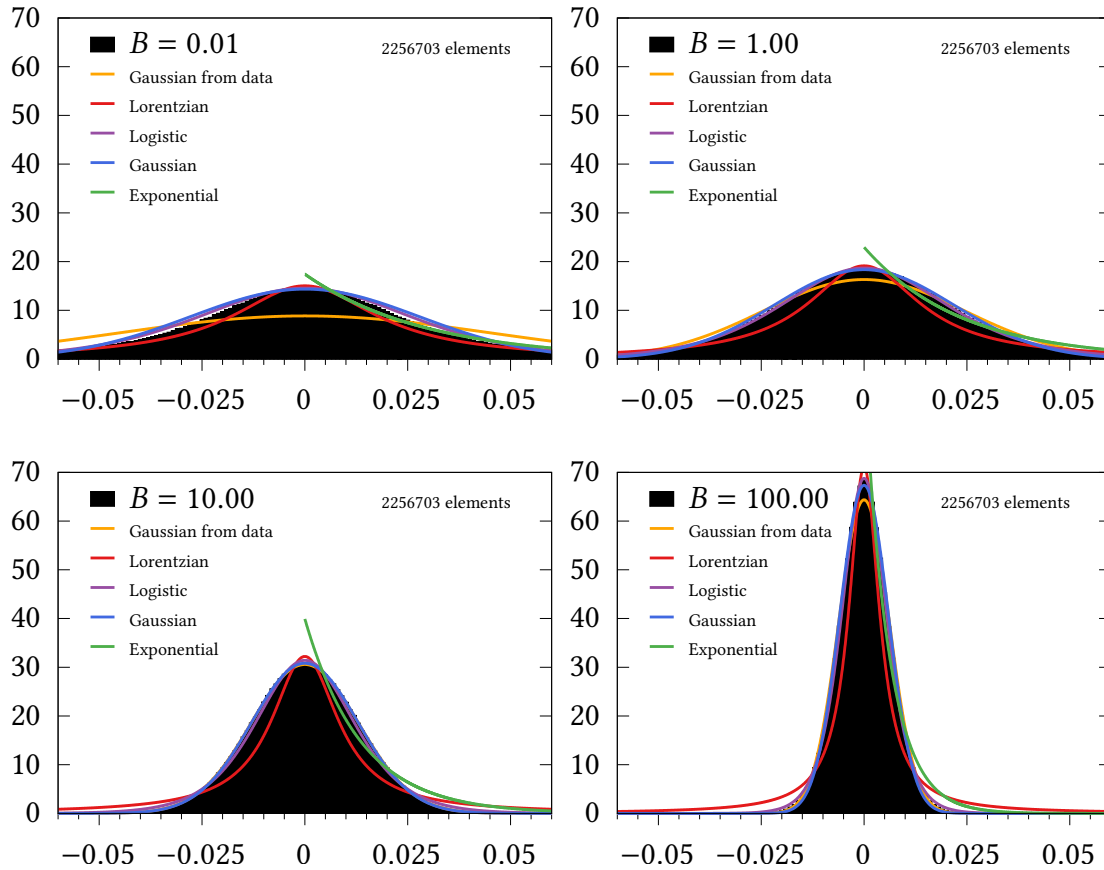


Figure B.30: Histograms over the flow for a band comprising the closest 1% of sub-diagonals for the symmetry sectors $k \neq 0, \pi$, so $n_k = \{1, 2, 3, 4, 5, 6, 7, 8, 9\}$ and lattice size $L = 20$. The preflow basis is the momentum basis. Each figure shows the relative frequency over bins of size 0.001. Initially, the number of large matrix elements in the subdiagonal window is huge, which leads to a very broad shape. At flow $B = 1$ it looks more like a Gaussian or a logistic distribution, which is due to the heavy tails. Even later in the flow, the distribution seems to be well approximated by a Gaussian distribution. The orange curve shows the Gaussian that is defined by the mean and standard deviation of the corresponding data set.

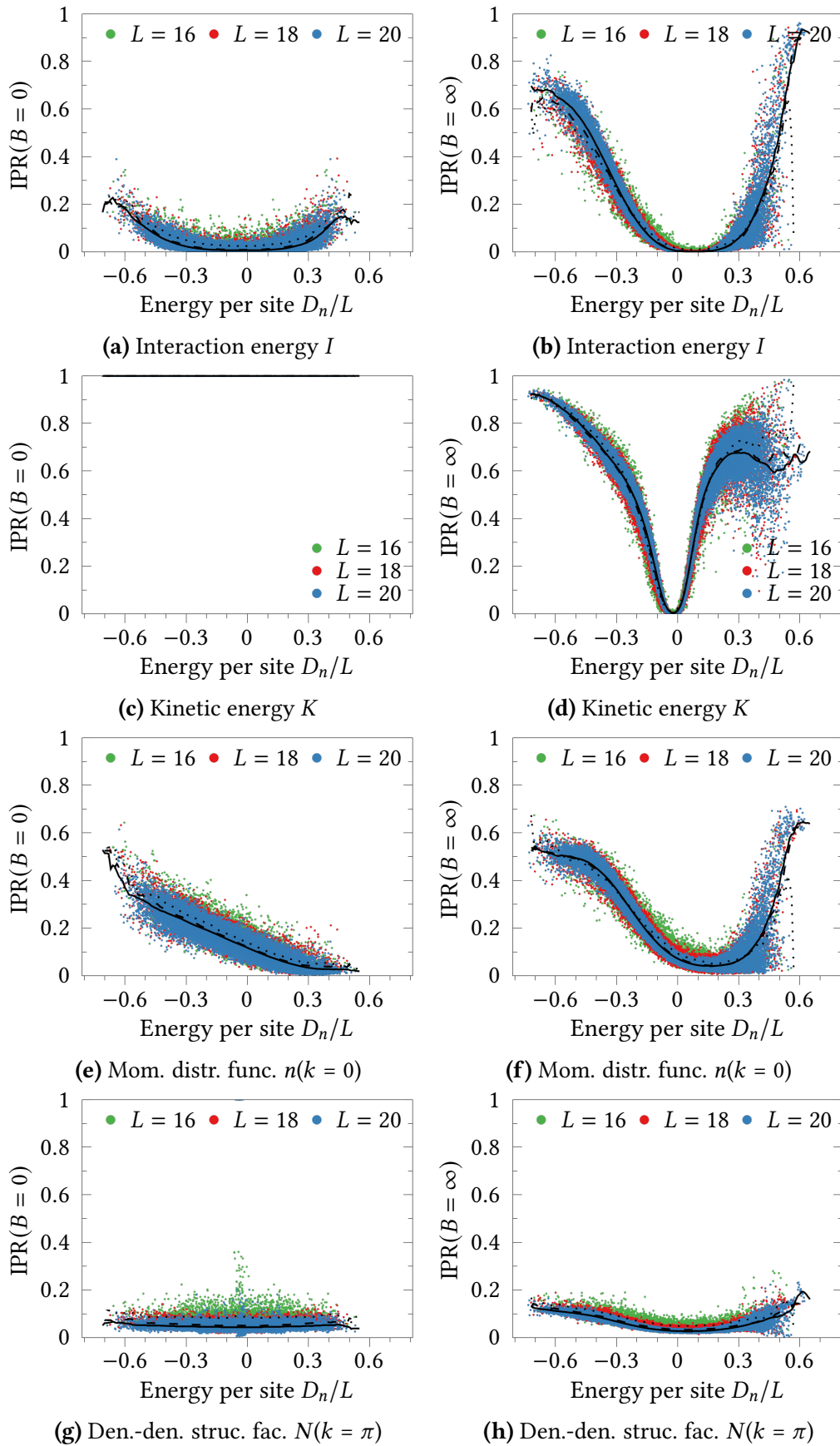


Figure B.31: The IPR for all observables and a mov. avg. (black) over a 0.06 window ($\approx 4\%$ of the spectrum) for the symm. sectors $n_k = 0, L/2$ and at flow (left) $B = 0$ and (right) $B = \infty$.

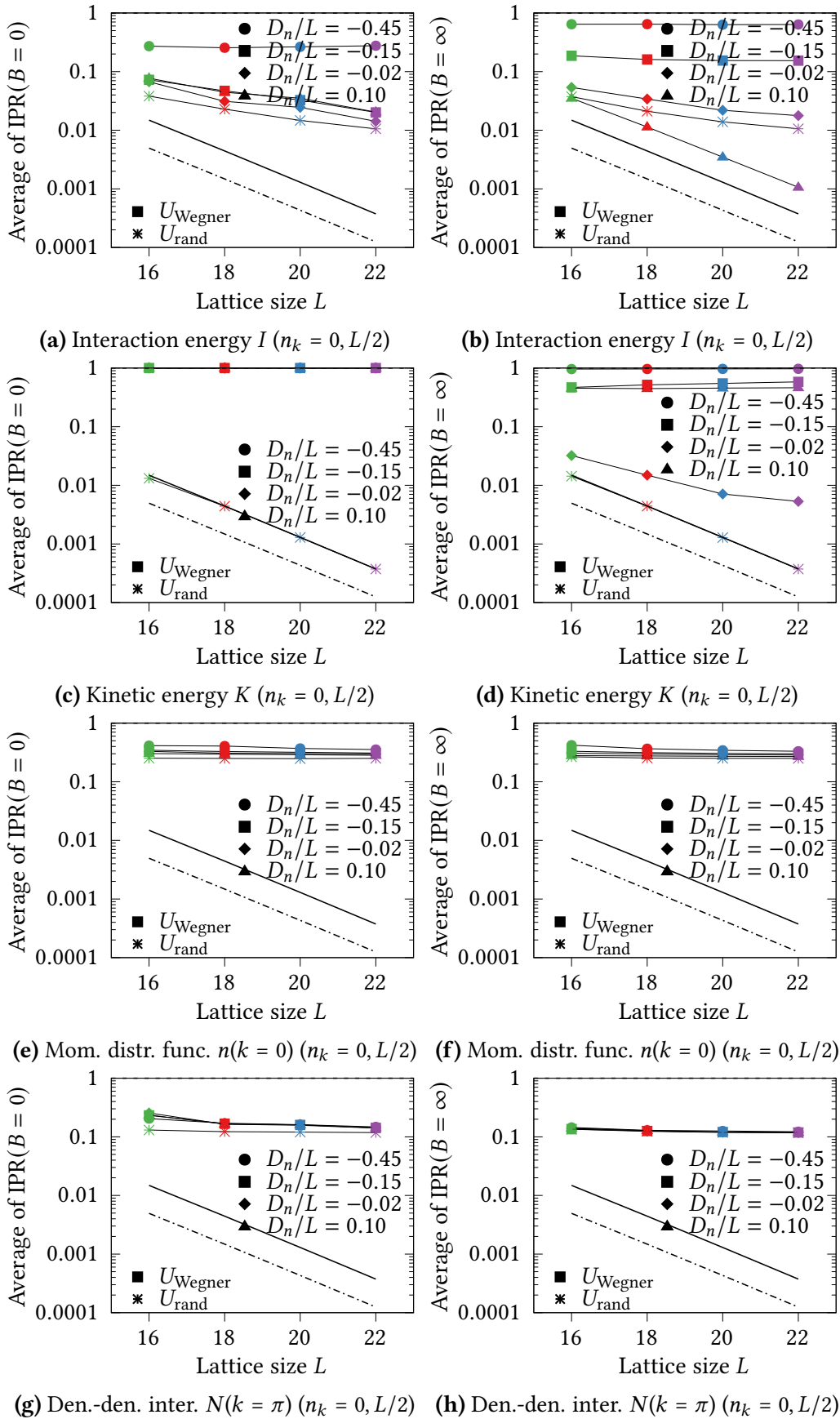


Figure B.32: Scaling of the IPR over lattice size of all observables, when the preflow basis is the momentum basis. Symm. sect. $n_k = 0, L/2$ at (left) $B = 0$ and (right) $B = \infty$.

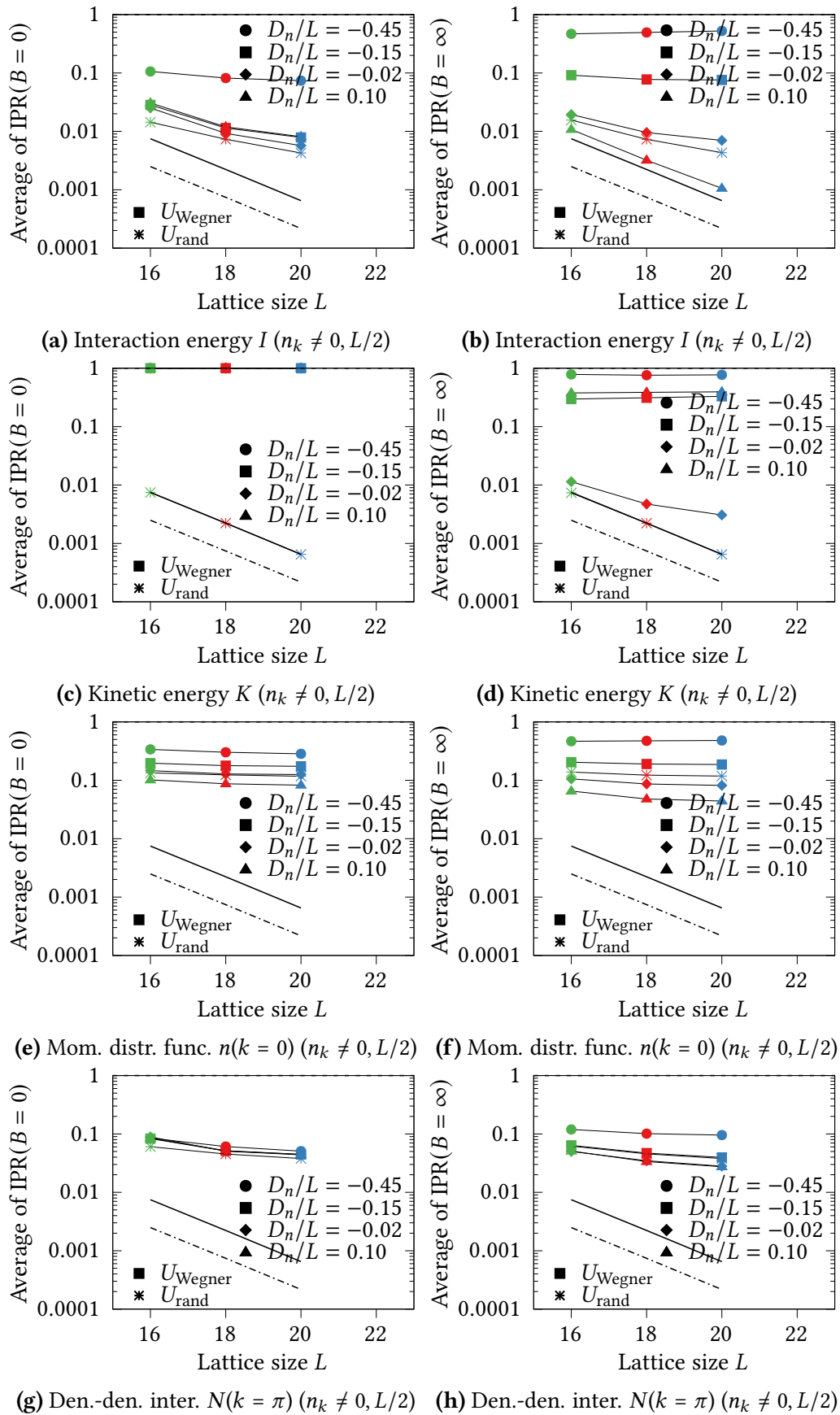


Figure B.33: Scaling of the IPR over lattice size of all observables, when the preflow basis is the momentum basis. Symm. sect. $n_k \neq 0, L/2$ at (left) $B=0$ and (right) $B=\infty$.

Appendix C

Spectral analysis

It is believed that the level statistics is an immediate indicator of whether a system is integrable or non-integrable (see Section 2.2). One of the most popular ways is to study the level spacings or level ratios. In particular, one is interested in the distribution or probability density of the level spacings. The interpretation is then simple: a vanishing value at zero spacing means that *level repulsion* is present. This was first studied by [von Neumann and Wigner \(1929\)](#), after it had been observed by [Hund \(1927\)](#). In order to analyze the levels it is beneficial to not simply look at the energy eigenvalues E_i and the spacings of neighboring levels $\Delta E_i = E_{i+1} - E_i$ (with E_i sorted in ascending order). This is, because the model might have a special energy density, which also depends on the chosen parameters of the system. Since the goal is to study the generic behavior of the levels, one would like to remove the influence of the system-specific level density, instead. The canonical way of approaching this is to perform the so-called *unfolding* procedure ([Brody et al. 1981](#); [Bohigas 1991](#)). This method ensures that the mean level spacing is approximately 1, independent of the considered model. It is discussed in more detail in the appendix in Appendix C.1.

C.1 Unfolding procedure

In a first step, one calculates the cumulative spectral function $N(E)$, which is a staircase-function that counts the number of levels below a given level. The edges of the spectrum are usually dominated by large fluctuations, which e. g. reflect a different low-energy behavior, which is why they are neglected (usually 20% of the spectrum is cut off on both ends). The remaining levels of the bulk then form

$$N(E) = \sum_i \theta(E - E_i) = \sum_{E_i \leq E} 1. \quad (\text{C.1})$$

The function $N(E)$ consists of a smooth (or average) part plus a fluctuating contribution on top of it. In the next step, the smooth part is computed by fitting a high-degree polynomial to it (in our case: usually of degree 13). The fitted function $\tilde{N}(E)$ is then used to define new energies $\tilde{E}_i = \tilde{N}(E_i)$, which have an average spacing unity and are dimensionless. Based on the new variables one defines the level spacing $s_i = \tilde{E}_{i+1} - \tilde{E}_i$.

Its derivative is the density of states

$$\rho(E) = \frac{dN}{dE} = \sum_{i=1}^{\infty} \delta(E - E_i). \quad (\text{C.2})$$

Level spacing distribution for chaotic or non-integrable systems is the so-called *Wigner surmise*, also called Wigner-Dyson distribution:

$$P_{\text{WD}}(s) = \frac{\pi s}{2} \exp\left(-\frac{\pi s^2}{4}\right) \quad (\text{C.3})$$

$$P_{\text{Poisson}}(s) = e^{-s} \quad (\text{C.4})$$

Appendix D

Dimensions of symmetry sectors

			L	16	18	20	22
k	p	z					
0	1	1		257	765	2518	8359
0	1	-1		183	622	2234	7800
0	-1	1		158	602	2136	7721
0	-1	-1		212	715	2364	8186
1	1	1		392	1336	4587	
1	1	-1		408	1364	4638	
2	1	1		411	1364	4649	
2	1	-1		397	1336	4601	
3	1	1		392	1337	4587	
3	1	-1		408	1366	4638	
4	1	1		413	1364	4652	
4	1	-1		396	1336	4598	
5	1	1		392	1336	4587	
5	1	-1		408	1364	4639	
6	1	1		411	1366	4649	
6	1	-1		397	1337	4601	
7	1	1		392	1336	4587	
7	1	-1		408	1364	4638	
8	1	1		239	1364	4652	
8	1	-1		166	1336	4598	
9	1	1			715	4587	
9	1	-1			602	4638	
10	1	1				2453	
10	1	-1				2173	
11	1	1					8186
11	1	-1					7721
$L/2$	-1	1		175	622	2197	7800
$L/2$	-1	-1		230	765	2429	8359

Table D.1: Dimensions of the Hilbert spaces

Bibliography

- Daniel S. Abrams and Seth Lloyd. Simulation of many-body fermi systems on a universal quantum computer. *Phys. Rev. Lett.*, 79:2586–2589, Sep 1997. doi: 10.1103/PhysRevLett.79.2586. URL <https://link.aps.org/doi/10.1103/PhysRevLett.79.2586>.
- D. G. Altman and J. M. Bland. Statistics notes: the normal distribution. *BMJ (Clinical research ed.)*, 310(6975):298–298, Feb 1995. ISSN 0959-8138. doi: 10.1136/bmj.310.6975.298. URL <https://doi.org/10.1136/bmj.310.6975.298.7866172>[pmid].
- GA Askar’yan. *Sov. Phys. JETP*, 15:1088, 1962.
- R. Balescu. *Equilibrium and nonequilibrium statistical mechanics*. 1975.
- R. Balian, D. Haar, and J.F. Gregg. *From Microphysics to Macrophysics: Methods and Applications of Statistical Physics*. Number Bd. 1 in Theoretical and Mathematical Physics. Springer Berlin Heidelberg, 2006. ISBN 9783540454694. URL <https://books.google.de/books?id=xsQzLxiatyMC>.
- Roger Balian. Random matrices and information theory. *Il Nuovo Cimento B (1965-1970)*, 57(1):183–193, 1968.
- John S Bell. On the einstein podolsky rosen paradox. *Physics Physique Fizika*, 1(3):195, 1964. URL <https://link.aps.org/pdf/10.1103/PhysicsPhysiqueFizika.1.195>.
- R. J. Bell and P. Dean. Atomic vibrations in vitreous silica. *Discuss. Faraday Soc.*, 50:55–61, 1970. doi: 10.1039/DF9705000055. URL <http://dx.doi.org/10.1039/DF9705000055>.
- Paul Benioff. The computer as a physical system: A microscopic quantum mechanical hamiltonian model of computers as represented by turing machines. *Journal of Statistical Physics*, 22(5):563–591, May 1980. ISSN 1572-9613. doi: 10.1007/BF01011339. URL <https://doi.org/10.1007/BF01011339>.
- C. H. Bennett, J. I. Cirac, M. S. Leifer, D. W. Leung, N. Linden, S. Popescu, and G. Vidal. Optimal simulation of two-qubit hamiltonians using general local operations. *Phys.*

- Rev. A*, 66:012305, Jul 2002. doi: 10.1103/PhysRevA.66.012305. URL <https://link.aps.org/doi/10.1103/PhysRevA.66.012305>.
- T. Bergeman, Gidon Erez, and Harold J. Metcalf. Magnetostatic trapping fields for neutral atoms. *Phys. Rev. A*, 35:1535–1546, Feb 1987. doi: 10.1103/PhysRevA.35.1535. URL <https://link.aps.org/doi/10.1103/PhysRevA.35.1535>.
- J. Berges, Sz. Borsányi, and C. Wetterich. Prethermalization. *Phys. Rev. Lett.*, 93:142002, Sep 2004. doi: 10.1103/PhysRevLett.93.142002. URL <https://link.aps.org/doi/10.1103/PhysRevLett.93.142002>.
- M. V. Berry. Semi-classical mechanics in phase space: A study of wigner’s function. *Philosophical Transactions of the Royal Society of London A: Mathematical, Physical and Engineering Sciences*, 287(1343):237–271, 1977a. ISSN 0080-4614. doi: 10.1098/rsta.1977.0145. URL <http://rsta.royalsocietypublishing.org/content/287/1343/237>.
- M. V. Berry. Regular and irregular semiclassical wavefunctions. *Journal of Physics A: Mathematical and General*, 10(12):2083, 1977b. URL <http://stacks.iop.org/0305-4470/10/i=12/a=016>.
- Michael Victor Berry, M. Tabor, and John Michael Ziman. Level clustering in the regular spectrum. *Proceedings of the Royal Society of London. A. Mathematical and Physical Sciences*, 356(1686):375–394, 1977. doi: 10.1098/rspa.1977.0140. URL <https://royalsocietypublishing.org/doi/abs/10.1098/rspa.1977.0140>.
- M.V. Berry. Quantizing a classically ergodic system: Sinai’s billiard and the kkr method. *Annals of Physics*, 131(1):163–216, 1981. ISSN 0003-4916. doi: [https://doi.org/10.1016/0003-4916\(81\)90189-5](https://doi.org/10.1016/0003-4916(81)90189-5). URL <https://www.sciencedirect.com/science/article/pii/0003491681901895>.
- H. Bethe. Zur theorie der metalle. *Zeitschrift für Physik*, 71(3):205–226, Mar 1931. ISSN 0044-3328. doi: 10.1007/BF01341708. URL <https://doi.org/10.1007/BF01341708>.
- W. Beugeling, R. Moessner, and Masudul Haque. Finite-size scaling of eigenstate thermalization. *Phys. Rev. E*, 89:042112, Apr 2014. doi: 10.1103/PhysRevE.89.042112. URL <https://link.aps.org/doi/10.1103/PhysRevE.89.042112>.
- Giulio Biroli, Corinna Kollath, and Andreas M. Läuchli. Effect of rare fluctuations on the thermalization of isolated quantum systems. *Phys. Rev. Lett.*, 105:250401, Dec 2010. doi: 10.1103/PhysRevLett.105.250401. URL <https://link.aps.org/doi/10.1103/PhysRevLett.105.250401>.
- J. E. Bjorkholm, R. R. Freeman, A. Ashkin, and D. B. Pearson. Observation of focusing of neutral atoms by the dipole forces of resonance-radiation pressure. *Phys. Rev.*

- Lett.*, 41:1361–1364, Nov 1978. doi: 10.1103/PhysRevLett.41.1361. URL <https://link.aps.org/doi/10.1103/PhysRevLett.41.1361>.
- S. Blanes, F. Casas, J.A. Oteo, and J. Ros. The magnus expansion and some of its applications. *Physics Reports*, 470(5):151 – 238, 2009. ISSN 0370-1573. doi: <https://doi.org/10.1016/j.physrep.2008.11.001>. URL <http://www.sciencedirect.com/science/article/pii/S0370157308004092>.
- R. Blatt and C. F. Roos. Quantum simulations with trapped ions. *Nature Physics*, 8:277 EP –, 04 2012. URL <https://doi.org/10.1038/nphys2252>.
- Rainer Blatt and David Wineland. Entangled states of trapped atomic ions. *Nature*, 453: 1008 EP –, 06 2008. URL <https://doi.org/10.1038/nature07125>.
- Immanuel Bloch, Jean Dalibard, and Wilhelm Zwerger. Many-body physics with ultracold gases. *Rev. Mod. Phys.*, 80:885–964, Jul 2008. doi: 10.1103/RevModPhys.80.885. URL <https://link.aps.org/doi/10.1103/RevModPhys.80.885>.
- Immanuel Bloch, Jean Dalibard, and Sylvain Nascimbène. Quantum simulations with ultracold quantum gases. *Nature Physics*, 8:267 EP –, 04 2012. URL <https://doi.org/10.1038/nphys2259>.
- O Bohigas, RU Haq, and A Pandey. Nuclear data for science and technology. *Research Reports in Physics (Springer Berlin Heidelberg, 1992)*, 1, 1983.
- O. Bohigas, M. J. Giannoni, and C. Schmit. Characterization of chaotic quantum spectra and universality of level fluctuation laws. *Phys. Rev. Lett.*, 52:1–4, Jan 1984. doi: 10.1103/PhysRevLett.52.1. URL <https://link.aps.org/doi/10.1103/PhysRevLett.52.1>.
- Oriol Bohigas. Random matrix theories and chaotic dynamics. Technical report, Paris-11 Univ., 1991.
- Ludwig Boltzmann. *Über die mechanische Bedeutung des zweiten Hauptsatzes der Wärmetheorie:(vorgelegt in der Sitzung am 8. Februar 1866)*. Staatsdruckerei, 1866.
- Ludwig Boltzmann. Weitere Studien über das Wärmegleichgewicht unter Gasmolekülen. *K. Acad. Wiss.(Wein) Sitzb., II Abt*, 66, 1872.
- F. Borgonovi, F.M. Izrailev, L.F. Santos, and V.G. Zelevinsky. Quantum chaos and thermalization in isolated systems of interacting particles. *Physics Reports*, 626: 1 – 58, 2016. ISSN 0370-1573. doi: <https://doi.org/10.1016/j.physrep.2016.02.005>. URL <http://www.sciencedirect.com/science/article/pii/S0370157316000831>. Quantum chaos and thermalization in isolated systems of interacting particles.

- P Braun-Munzinger, D Magestro, K Redlich, and J Stachel. Hadron production in au–au collisions at rhic. *Physics Letters B*, 518(1):41 – 46, 2001. ISSN 0370-2693. doi: [https://doi.org/10.1016/S0370-2693\(01\)01069-3](https://doi.org/10.1016/S0370-2693(01)01069-3). URL <http://www.sciencedirect.com/science/article/pii/S0370269301010693>.
- Gavin K. Brennen, Carlton M. Caves, Poul S. Jessen, and Ivan H. Deutsch. Quantum logic gates in optical lattices. *Phys. Rev. Lett.*, 82:1060–1063, Feb 1999. doi: 10.1103/PhysRevLett.82.1060. URL <https://link.aps.org/doi/10.1103/PhysRevLett.82.1060>.
- T. A. Brody, J. Flores, J. B. French, P. A. Mello, A. Pandey, and S. S. M. Wong. Random-matrix physics: spectrum and strength fluctuations. *Rev. Mod. Phys.*, 53:385–479, Jul 1981. doi: 10.1103/RevModPhys.53.385. URL <https://link.aps.org/doi/10.1103/RevModPhys.53.385>.
- Iulia Buluta and Franco Nori. Quantum simulators. *Science*, 326(5949):108–111, 2009. ISSN 0036-8075. doi: 10.1126/science.1177838. URL <http://science.sciencemag.org/content/326/5949/108>.
- Leonid A Bunimovich. On the ergodic properties of nowhere dispersing billiards. *Communications in Mathematical Physics*, 65(3):295–312, 1979.
- N.Del Buono and L Lopez. Numerical methods for hermitian unitary differential systems. *Journal of Computational and Applied Mathematics*, 111(1):133 – 145, 1999. ISSN 0377-0427. doi: [https://doi.org/10.1016/S0377-0427\(99\)00137-5](https://doi.org/10.1016/S0377-0427(99)00137-5). URL <http://www.sciencedirect.com/science/article/pii/S0377042799001375>.
- Pasquale Calabrese and John Cardy. Evolution of entanglement entropy in one-dimensional systems. *Journal of Statistical Mechanics: Theory and Experiment*, 2005 (04):P04010, 2005. URL <http://stacks.iop.org/1742-5468/2005/i=04/a=P04010>.
- Pasquale Calabrese and John Cardy. Time dependence of correlation functions following a quantum quench. *Phys. Rev. Lett.*, 96:136801, Apr 2006. doi: 10.1103/PhysRevLett.96.136801. URL <https://link.aps.org/doi/10.1103/PhysRevLett.96.136801>.
- H. S. Camarda and P. D. Georgopoulos. Statistical behavior of atomic energy levels: Agreement with random-matrix theory. *Phys. Rev. Lett.*, 50:492–495, Feb 1983. doi: 10.1103/PhysRevLett.50.492. URL <https://link.aps.org/doi/10.1103/PhysRevLett.50.492>.
- Amy C. Cassidy, Charles W. Clark, and Marcos Rigol. Generalized thermalization in an integrable lattice system. *Phys. Rev. Lett.*, 106:140405, Apr 2011. doi: 10.1103/PhysRevLett.106.140405. URL <https://link.aps.org/doi/10.1103/PhysRevLett.106.140405>.

- Jean-Sébastien Caux and Fabian H. L. Essler. Time evolution of local observables after quenching to an integrable model. *Phys. Rev. Lett.*, 110:257203, Jun 2013. doi: 10.1103/PhysRevLett.110.257203. URL <https://link.aps.org/doi/10.1103/PhysRevLett.110.257203>.
- M. A. Cazalilla, R. Citro, T. Giamarchi, E. Orignac, and M. Rigol. One dimensional bosons: From condensed matter systems to ultracold gases. *Rev. Mod. Phys.*, 83:1405–1466, Dec 2011. doi: 10.1103/RevModPhys.83.1405. URL <https://link.aps.org/doi/10.1103/RevModPhys.83.1405>.
- Steven Chu, J. E. Bjorkholm, A. Ashkin, and A. Cable. Experimental observation of optically trapped atoms. *Phys. Rev. Lett.*, 57:314–317, Jul 1986. doi: 10.1103/PhysRevLett.57.314. URL <https://link.aps.org/doi/10.1103/PhysRevLett.57.314>.
- J. I. Cirac and P. Zoller. Quantum computations with cold trapped ions. *Phys. Rev. Lett.*, 74:4091–4094, May 1995. doi: 10.1103/PhysRevLett.74.4091. URL <https://link.aps.org/doi/10.1103/PhysRevLett.74.4091>.
- John F. Clauser, Michael A. Horne, Abner Shimony, and Richard A. Holt. Proposed experiment to test local hidden-variable theories. *Phys. Rev. Lett.*, 23:880–884, Oct 1969. doi: 10.1103/PhysRevLett.23.880. URL <https://link.aps.org/doi/10.1103/PhysRevLett.23.880>.
- Rudolf Clausius. Über die anwendung der mechanischen wärmetheorie auf die dampfmaschine. *Annalen der Physik*, 173(3):441–476, 1856.
- Predrag Cvitanovic, Roberto Artuso, Ronnie Mainieri, Gregor Tanner, Gábor Vattay, Niall Whelan, and Andreas Wirzba. Chaos: classical and quantum. *Chaos-Book.org (Niels Bohr Institute, Copenhagen 2005)*, 69, 2005. URL <http://www.chaosbook.org/chapters/OUPbook.pdf>.
- R.B. D’Agostino. *Goodness-of-Fit-Techniques*. Statistics: A Series of Textbooks and Monographs. Taylor & Francis, 1986. ISBN 9780824774875. URL <https://books.google.de/books?id=1BSEaGVBj5QC>.
- Luca D’Alessio, Yariv Kafri, Anatoli Polkovnikov, and Marcos Rigol. From quantum chaos and eigenstate thermalization to statistical mechanics and thermodynamics. *Advances in Physics*, 65(3):239–362, 2016. doi: 10.1080/00018732.2016.1198134. URL <https://doi.org/10.1080/00018732.2016.1198134>.
- A J Daley, C Kollath, U Schollwöck, and G Vidal. Time-dependent density-matrix renormalization-group using adaptive effective hilbert spaces. *Journal of Statistical Mechanics: Theory and Experiment*, 2004(04):P04005, 2004a. URL <http://stacks.iop.org/1742-5468/2004/i=04/a=P04005>.

- A J Daley, C Kollath, U Schollwöck, and G Vidal. Time-dependent density-matrix renormalization-group using adaptive effective hilbert spaces. *Journal of Statistical Mechanics: Theory and Experiment*, 2004(04):P04005, apr 2004b. doi: 10.1088/1742-5468/2004/04/P04005. URL <https://dx.doi.org/10.1088/1742-5468/2004/04/P04005>.
- Philippe de Forcrand. Localization properties of fermions and bosons. *AIP Conference Proceedings*, 892(1):29–35, 2007. doi: 10.1063/1.2714343. URL <https://aip.scitation.org/doi/abs/10.1063/1.2714343>.
- H.G. Dehmelt. Radiofrequency spectroscopy of stored ions i: Storage**part ii: Spectroscopy is now scheduled to appear in volume v of this series. volume 3 of *Advances in Atomic and Molecular Physics*, pages 53 – 72. Academic Press, 1968. doi: [https://doi.org/10.1016/S0065-2199\(08\)60170-0](https://doi.org/10.1016/S0065-2199(08)60170-0). URL <http://www.sciencedirect.com/science/article/pii/S0065219908601700>.
- H.G. Dehmelt. Radiofrequency spectroscopy of stored ions ii: Spectroscopy**part i, sections 1 and 2 of this article appear in volume 3 of this series. volume 5 of *Advances in Atomic and Molecular Physics*, pages 109 – 154. Academic Press, 1969. doi: [https://doi.org/10.1016/S0065-2199\(08\)60156-6](https://doi.org/10.1016/S0065-2199(08)60156-6). URL <http://www.sciencedirect.com/science/article/pii/S0065219908601566>.
- Jacques Des Cloizeaux and Michel Gaudin. Anisotropic linear magnetic chain. *Journal of Mathematical Physics*, 7(8):1384–1400, 1966. doi: 10.1063/1.1705048. URL <https://doi.org/10.1063/1.1705048>.
- David Deutsch and Richard Jozsa. Rapid solution of problems by quantum computation. *Proceedings of the Royal Society of London. Series A: Mathematical and Physical Sciences*, 439(1907):553–558, 1992. doi: 10.1098/rspa.1992.0167. URL <https://royalsocietypublishing.org/doi/abs/10.1098/rspa.1992.0167>.
- David Deutsch and Roger Penrose. Quantum theory, the church–turing principle and the universal quantum computer. *Proceedings of the Royal Society of London. A. Mathematical and Physical Sciences*, 400(1818):97–117, 1985. doi: 10.1098/rspa.1985.0070. URL <https://royalsocietypublishing.org/doi/abs/10.1098/rspa.1985.0070>.
- J. M. Deutsch. A closed quantum system giving ergodicity. Website. Online accessible under <https://deutsch.physics.ucsc.edu/pdf/quantumstat.pdf>; accessed February 5, 2019.
- J. M. Deutsch. Quantum statistical mechanics in a closed system. *Phys. Rev. A*, 43: 2046–2049, Feb 1991. doi: 10.1103/PhysRevA.43.2046. URL <https://link.aps.org/doi/10.1103/PhysRevA.43.2046>.

- Joshua M Deutsch. Eigenstate thermalization hypothesis. *Reports on Progress in Physics*, 81(8):082001, jul 2018. doi: 10.1088/1361-6633/aac9f1. URL <https://doi.org/10.1088%2F1361-6633%2Faac9f1>.
- Paul Adrien Maurice Dirac. *The principles of quantum mechanics*. Number 27. Oxford university press, 1981.
- Jennifer L. Dodd, Michael A. Nielsen, Michael J. Bremner, and Robert T. Thew. Universal quantum computation and simulation using any entangling hamiltonian and local unitaries. *Phys. Rev. A*, 65:040301, Apr 2002. doi: 10.1103/PhysRevA.65.040301. URL <https://link.aps.org/doi/10.1103/PhysRevA.65.040301>.
- John R Dormand and Peter J Prince. A family of embedded runge-kutta formulae. *Journal of computational and applied mathematics*, 6(1):19–26, 1980.
- Jiangfeng Du, Nanyang Xu, Xinhua Peng, Pengfei Wang, Sanfeng Wu, and Dawei Lu. Nmr implementation of a molecular hydrogen quantum simulation with adiabatic state preparation. *Phys. Rev. Lett.*, 104:030502, Jan 2010. doi: 10.1103/PhysRevLett.104.030502. URL <https://link.aps.org/doi/10.1103/PhysRevLett.104.030502>.
- Shawn Dubey, Luciano Silvestri, Justin Finn, Sai Vinjanampathy, and Kurt Jacobs. Approach to typicality in many-body quantum systems. *Phys. Rev. E*, 85:011141, Jan 2012. doi: 10.1103/PhysRevE.85.011141. URL <https://link.aps.org/doi/10.1103/PhysRevE.85.011141>.
- Freeman J. Dyson. Statistical theory of the energy levels of complex systems. ii. *Journal of Mathematical Physics*, 3(1):157–165, 1962a. doi: 10.1063/1.1703774. URL <https://doi.org/10.1063/1.1703774>.
- Freeman J. Dyson. Statistical theory of the energy levels of complex systems. iii. *Journal of Mathematical Physics*, 3(1):166–175, 1962b. doi: 10.1063/1.1703775. URL <https://doi.org/10.1063/1.1703775>.
- Freeman J. Dyson. A brownian-motion model for the eigenvalues of a random matrix. *Journal of Mathematical Physics*, 3(6):1191–1198, 1962c. doi: 10.1063/1.1703862. URL <https://doi.org/10.1063/1.1703862>.
- Freeman J. Dyson. Statistical theory of the energy levels of complex systems. i. *Journal of Mathematical Physics*, 3(1):140–156, 1962d. doi: 10.1063/1.1703773. URL <https://doi.org/10.1063/1.1703773>.
- Luca D'Alessio and Anatoli Polkovnikov. Many-body energy localization transition in periodically driven systems. *Annals of Physics*, 333:19 – 33, 2013. ISSN 0003-4916. doi: <https://doi.org/10.1016/j.aop.2013.02.011>. URL <http://www.sciencedirect.com/science/article/pii/S0003491613000389>.

- Martin Eckstein, Marcus Kollar, and Philipp Werner. Thermalization after an interaction quench in the hubbard model. *Phys. Rev. Lett.*, 103:056403, Jul 2009. doi: 10.1103/PhysRevLett.103.056403. URL <https://link.aps.org/doi/10.1103/PhysRevLett.103.056403>.
- Dirk Eddebuettel and Conrad Sanderson. Rcpparmadillo: Accelerating r with high-performance c++ linear algebra. *Computational Statistics & Data Analysis*, 71: 1054 – 1063, 2014. ISSN 0167-9473. doi: <https://doi.org/10.1016/j.csda.2013.02.005>. URL <http://www.sciencedirect.com/science/article/pii/S0167947313000492>.
- A. Eddington. *The Nature of the Physical World: Gifford Lectures (1927)*. Cambridge University Press, 2012. ISBN 9781107663855. URL <https://books.google.de/books?id=MRPCG8qgnUAC>.
- Alan Edelman and N Raj Rao. Random matrix theory. *Acta numerica*, 14:233, 2005.
- J T Edwards and D J Thouless. Numerical studies of localization in disordered systems. *Journal of Physics C: Solid State Physics*, 5(8):807, 1972. URL <http://stacks.iop.org/0022-3719/5/i=8/a=007>.
- Paul Ehrenfest and Tatiana Ehrenfest. *The conceptual foundations of the statistical approach in mechanics*. Courier Corporation, 2002.
- A. Einstein, B. Podolsky, and N. Rosen. Can quantum-mechanical description of physical reality be considered complete? *Phys. Rev.*, 47:777–780, May 1935. doi: 10.1103/PhysRev.47.777. URL <https://link.aps.org/doi/10.1103/PhysRev.47.777>.
- J. Eisert, M. Friesdorf, and C. Gogolin. Quantum many-body systems out of equilibrium. *Nature Physics*, 11:124 EP –, 02 2015. URL <https://doi.org/10.1038/nphys3215>.
- Alan C Elliott and Wayne A Woodward. *Statistical analysis quick reference guidebook: With SPSS examples*. Sage, 2007.
- Fabian HL Essler, Holger Frahm, Frank Göhmann, Andreas Klümper, and Vladimir E Korepin. *The one-dimensional Hubbard model*. Cambridge University Press, 2005.
- Tilman Esslinger. Fermi-hubbard physics with atoms in an optical lattice. *Annual Review of Condensed Matter Physics*, 1(1):129–152, 2010. doi: 10.1146/annurev-conmatphys-070909-104059. URL <https://doi.org/10.1146/annurev-conmatphys-070909-104059>.
- Mario Feingold and Asher Peres. Distribution of matrix elements of chaotic systems. *Phys. Rev. A*, 34:591–595, Jul 1986a. doi: 10.1103/PhysRevA.34.591. URL <https://link.aps.org/doi/10.1103/PhysRevA.34.591>.

- Mario Feingold and Asher Peres. Distribution of matrix elements of chaotic systems. *Physical Review A*, 34(1):591, 1986b.
- Mario Feingold, David M. Leitner, and Oreste Piro. Semiclassical structure of hamiltonians. *Phys. Rev. A*, 39:6507–6514, Jun 1989a. doi: 10.1103/PhysRevA.39.6507. URL <https://link.aps.org/doi/10.1103/PhysRevA.39.6507>.
- Mario Feingold, David M Leitner, and Oreste Piro. Semiclassical structure of hamiltonians. *Physical Review A*, 39(12):6507, 1989b.
- Mario Feingold, David M. Leitner, and Michael Wilkinson. Spectral statistics in semiclassical random-matrix ensembles. *Phys. Rev. Lett.*, 66:986–989, Feb 1991. doi: 10.1103/PhysRevLett.66.986. URL <https://link.aps.org/doi/10.1103/PhysRevLett.66.986>.
- C. D. Fertig, K. M. O’Hara, J. H. Huckans, S. L. Rolston, W. D. Phillips, and J. V. Porto. Strongly inhibited transport of a degenerate 1d bose gas in a lattice. *Phys. Rev. Lett.*, 94:120403, Apr 2005. doi: 10.1103/PhysRevLett.94.120403. URL <https://link.aps.org/doi/10.1103/PhysRevLett.94.120403>.
- Richard P. Feynman. Simulating physics with computers. *International Journal of Theoretical Physics*, 21(6):467–488, Jun 1982. ISSN 1572-9575. doi: 10.1007/BF02650179. URL <https://doi.org/10.1007/BF02650179>.
- Andy Field. *Discovering statistics using IBM SPSS statistics*. sage, 2013.
- Matthew P. A. Fisher, Peter B. Weichman, G. Grinstein, and Daniel S. Fisher. Boson localization and the superfluid-insulator transition. *Phys. Rev. B*, 40:546–570, Jul 1989. doi: 10.1103/PhysRevB.40.546. URL <https://link.aps.org/doi/10.1103/PhysRevB.40.546>.
- P J Forrester, N C Snaith, and J J M Verbaarschot. Developments in random matrix theory. *Journal of Physics A: Mathematical and General*, 36(12):R1–R10, mar 2003. doi: 10.1088/0305-4470/36/12/201. URL <https://doi.org/10.1088/0305-4470/36/12/201>.
- W. M. C. Foulkes, L. Mitas, R. J. Needs, and G. Rajagopal. Quantum monte carlo simulations of solids. *Rev. Mod. Phys.*, 73:33–83, Jan 2001. doi: 10.1103/RevModPhys.73.33. URL <https://link.aps.org/doi/10.1103/RevModPhys.73.33>.
- Giovanni Gallavotti. *Statistical mechanics: A short treatise*. Springer Science & Business Media, 2013.
- James R. Garrison and Tarun Grover. Does a single eigenstate encode the full hamiltonian? *Phys. Rev. X*, 8:021026, Apr 2018. doi: 10.1103/PhysRevX.8.021026. URL <https://link.aps.org/doi/10.1103/PhysRevX.8.021026>.

- Roy Charles Geary. Testing for normality. *Biometrika*, 34(3/4):209–242, 1947. URL <https://www.jstor.org/stable/pdf/2332434.pdf>.
- S. Genway, A. F. Ho, and D. K. K. Lee. Thermalization of local observables in small hubbard lattices. *Phys. Rev. A*, 86:023609, Aug 2012. doi: 10.1103/PhysRevA.86.023609. URL <https://link.aps.org/doi/10.1103/PhysRevA.86.023609>.
- I. M. Georgescu, S. Ashhab, and Franco Nori. Quantum simulation. *Rev. Mod. Phys.*, 86:153–185, Mar 2014. doi: 10.1103/RevModPhys.86.153. URL <https://link.aps.org/doi/10.1103/RevModPhys.86.153>.
- Scott D. Geraedts, Rahul Nandkishore, and Nicolas Regnault. Many-body localization and thermalization: Insights from the entanglement spectrum. *Phys. Rev. B*, 93:174202, May 2016. doi: 10.1103/PhysRevB.93.174202. URL <https://link.aps.org/doi/10.1103/PhysRevB.93.174202>.
- J Willard Gibbs. *Elementary principles in statistical mechanics*. Courier Corporation, 2014.
- Stanisław D Głazek and Kenneth G Wilson. Renormalization of hamiltonians. *Physical Review D*, 48(12):5863, 1993.
- Christian Gogolin and Jens Eisert. Equilibration, thermalisation, and the emergence of statistical mechanics in closed quantum systems. *Reports on Progress in Physics*, 79(5):056001, 2016. URL <http://stacks.iop.org/0034-4885/79/i=5/a=056001>.
- N. Goldman, J. C. Budich, and P. Zoller. Topological quantum matter with ultracold gases in optical lattices. *Nature Physics*, 12:639 EP –, 06 2016. URL <https://doi.org/10.1038/nphys3803>.
- Markus Greiner, Olaf Mandel, Tilman Esslinger, Theodor W. Hänsch, and Immanuel Bloch. Quantum phase transition from a superfluid to a mott insulator in a gas of ultracold atoms. *Nature*, 415:39 EP –, 01 2002a. URL <https://doi.org/10.1038/415039a>.
- Markus Greiner, Olaf Mandel, Theodor W. Hänsch, and Immanuel Bloch. Collapse and revival of the matter wave field of a bose–einstein condensate. *Nature*, 419:51 EP –, 09 2002b. URL <https://doi.org/10.1038/nature00968>.
- Rudolf Grimm, Matthias Weidemüller, and Yurii B. Ovchinnikov. Optical dipole traps for neutral atoms. volume 42 of *Advances In Atomic, Molecular, and Optical Physics*, pages 95 – 170. Academic Press, 2000. doi: [https://doi.org/10.1016/S1049-250X\(08\)60186-X](https://doi.org/10.1016/S1049-250X(08)60186-X). URL <http://www.sciencedirect.com/science/article/pii/S1049250X0860186X>.

- M. Gring, M. Kuhnert, T. Langen, T. Kitagawa, B. Rauer, M. Schreitl, I. Mazets, D. Adu Smith, E. Demler, and J. Schmiedmayer. Relaxation and prethermalization in an isolated quantum system. *Science*, 337(6100):1318–1322, 2012. ISSN 0036-8075. doi: 10.1126/science.1224953. URL <http://science.sciencemag.org/content/337/6100/1318>.
- H.J. Groenewold. On the principles of elementary quantum mechanics. *Physica*, 12(7):405 – 460, 1946. ISSN 0031-8914. doi: [https://doi.org/10.1016/S0031-8914\(46\)80059-4](https://doi.org/10.1016/S0031-8914(46)80059-4). URL <http://www.sciencedirect.com/science/article/pii/S0031891446800594>.
- Christian Gross and Immanuel Bloch. Quantum simulations with ultracold atoms in optical lattices. *Science*, 357(6355):995–1001, 2017. ISSN 0036-8075. doi: 10.1126/science.aal3837. URL <http://science.sciencemag.org/content/357/6355/995>.
- Lov K. Grover. Quantum mechanics helps in searching for a needle in a haystack. *Phys. Rev. Lett.*, 79:325–328, Jul 1997. doi: 10.1103/PhysRevLett.79.325. URL <https://link.aps.org/doi/10.1103/PhysRevLett.79.325>.
- I.I. Gurevich and M.I. Pevsner. Repulsion of nuclear levels. *Nuclear Physics*, 2(5):575–581, 1956. ISSN 0029-5582. doi: [https://doi.org/10.1016/0029-5582\(57\)90069-X](https://doi.org/10.1016/0029-5582(57)90069-X). URL <https://www.sciencedirect.com/science/article/pii/002955825790069X>.
- Martin C. Gutzwiller. Effect of correlation on the ferromagnetism of transition metals. *Phys. Rev. Lett.*, 10:159–162, Mar 1963. doi: 10.1103/PhysRevLett.10.159. URL <https://link.aps.org/doi/10.1103/PhysRevLett.10.159>.
- E. Haller, H. Köppel, and L.S. Cederbaum. On the statistical behaviour of molecular vibronic energy levels. *Chemical Physics Letters*, 101(3):215–220, 1983. ISSN 0009-2614. doi: [https://doi.org/10.1016/0009-2614\(83\)87001-8](https://doi.org/10.1016/0009-2614(83)87001-8). URL <https://www.sciencedirect.com/science/article/pii/0009261483870018>.
- R. U. Haq, A. Pandey, and O. Bohigas. Fluctuation properties of nuclear energy levels: Do theory and experiment agree? *Phys. Rev. Lett.*, 48:1086–1089, Apr 1982. doi: 10.1103/PhysRevLett.48.1086. URL <https://link.aps.org/doi/10.1103/PhysRevLett.48.1086>.
- M. Hénon. Integrals of the toda lattice. *Phys. Rev. B*, 9:1921–1923, Feb 1974. doi: 10.1103/PhysRevB.9.1921. URL <https://link.aps.org/doi/10.1103/PhysRevB.9.1921>.
- B. Hensen, H. Bernien, A. E. Dréau, A. Reiserer, N. Kalb, M. S. Blok, J. Ruitenbergh, R. F. L. Vermeulen, R. N. Schouten, C. Abellán, W. Amaya, V. Pruneri, M. W. Mitchell, M. Markham, D. J. Twitchen, D. Elkouss, S. Wehner, T. H. Taminiau, and R. Hanson.

- Loophole-free bell inequality violation using electron spins separated by 1.3 kilometres. *Nature*, 526:682 EP –, 10 2015. URL <https://doi.org/10.1038/nature15759>.
- S. Hofferberth, I. Lesanovsky, B. Fischer, T. Schumm, and J. Schmiedmayer. Non-equilibrium coherence dynamics in one-dimensional bose gases. *Nature*, 449:324 EP –, 09 2007. URL <https://doi.org/10.1038/nature06149>.
- P. Hohenberg and W. Kohn. Inhomogeneous electron gas. *Phys. Rev.*, 136:B864–B871, Nov 1964. doi: 10.1103/PhysRev.136.B864. URL <https://link.aps.org/doi/10.1103/PhysRev.136.B864>.
- T. Holstein and H. Primakoff. Field dependence of the intrinsic domain magnetization of a ferromagnet. *Phys. Rev.*, 58:1098–1113, Dec 1940. doi: 10.1103/PhysRev.58.1098. URL <https://link.aps.org/doi/10.1103/PhysRev.58.1098>.
- Michał Horodecki, Paweł Horodecki, and Ryszard Horodecki. *Mixed-State Entanglement and Quantum Communication*, pages 151–195. Springer Berlin Heidelberg, Berlin, Heidelberg, 2001. ISBN 978-3-540-44678-1. doi: 10.1007/3-540-44678-8_5. URL https://doi.org/10.1007/3-540-44678-8_5.
- Pavan Hosur and Xiao-Liang Qi. Characterizing eigenstate thermalization via measures in the fock space of operators. *Phys. Rev. E*, 93:042138, Apr 2016. doi: 10.1103/PhysRevE.93.042138. URL <https://link.aps.org/doi/10.1103/PhysRevE.93.042138>.
- J. Hubbard and Brian Hilton Flowers. Electron correlations in narrow energy bands. *Proceedings of the Royal Society of London. Series A. Mathematical and Physical Sciences*, 276(1365):238–257, 1963. doi: 10.1098/rspa.1963.0204. URL <https://royalsocietypublishing.org/doi/abs/10.1098/rspa.1963.0204>.
- F. Hund. Zur Deutung der Molekelspektren. I. *Zeitschrift für Physik*, 40:742–764, Oct 1927. ISSN 0044-3328. doi: 10.1007/BF01400234. URL <https://doi.org/10.1007/BF01400234>.
- David A. Huse, Rahul Nandkishore, and Vadim Oganesyan. Phenomenology of fully many-body-localized systems. *Phys. Rev. B*, 90:174202, Nov 2014. doi: 10.1103/PhysRevB.90.174202. URL <https://link.aps.org/doi/10.1103/PhysRevB.90.174202>.
- H. Häffner, C.F. Roos, and R. Blatt. Quantum computing with trapped ions. *Physics Reports*, 469(4):155 – 203, 2008. ISSN 0370-1573. doi: <https://doi.org/10.1016/j.physrep.2008.09.003>. URL <http://www.sciencedirect.com/science/article/pii/S0370157308003463>.

- T.W. Hänsch and A.L. Schawlow. Cooling of gases by laser radiation. *Optics Communications*, 13(1):68 – 69, 1975. ISSN 0030-4018. doi: [https://doi.org/10.1016/0030-4018\(75\)90159-5](https://doi.org/10.1016/0030-4018(75)90159-5). URL <http://www.sciencedirect.com/science/article/pii/0030401875901595>.
- Tatsuhiko N. Ikeda, Yu Watanabe, and Masahito Ueda. Eigenstate randomization hypothesis: Why does the long-time average equal the microcanonical average? *Phys. Rev. E*, 84:021130, Aug 2011. doi: 10.1103/PhysRevE.84.021130. URL <https://link.aps.org/doi/10.1103/PhysRevE.84.021130>.
- Felix M. Izrailev. Simple models of quantum chaos: Spectrum and eigenfunctions. *Physics Reports*, 196(5):299–392, 1990. ISSN 0370-1573. doi: [https://doi.org/10.1016/0370-1573\(90\)90067-C](https://doi.org/10.1016/0370-1573(90)90067-C). URL <https://www.sciencedirect.com/science/article/pii/037015739090067C>.
- F.M. Izrailev. Quantum localization and statistics of quasienergy spectrum in a classically chaotic system. *Physics Letters A*, 134(1):13–18, 1988. ISSN 0375-9601. doi: [https://doi.org/10.1016/0375-9601\(88\)90538-5](https://doi.org/10.1016/0375-9601(88)90538-5). URL <https://www.sciencedirect.com/science/article/pii/0375960188905385>.
- F.M. Izrailev. Scaling properties of spectra and eigenfunctions for quantum dynamical and disordered systems. *Chaos, Solitons & Fractals*, 5(7):1219–1234, 1995. ISSN 0960-0779. doi: [https://doi.org/10.1016/0960-0779\(94\)E0063-U](https://doi.org/10.1016/0960-0779(94)E0063-U). URL <https://www.sciencedirect.com/science/article/pii/0960077994E0063U>. Quantum Chaos: Present and Future.
- D. Jaksch, C. Bruder, J. I. Cirac, C. W. Gardiner, and P. Zoller. Cold bosonic atoms in optical lattices. *Phys. Rev. Lett.*, 81:3108–3111, Oct 1998. doi: 10.1103/PhysRevLett.81.3108. URL <https://link.aps.org/doi/10.1103/PhysRevLett.81.3108>.
- Enric Jané, Guifre Vidal, Wolfgang Dür, Peter Zoller, and J. Ignacio Cirac. Simulation of quantum dynamics with quantum optical systems. *Quantum Information & Computation*, 3(1):15–37, 2003. URL <http://portal.acm.org/citation.cfm?id=2011510>.
- E. T. Jaynes. Information theory and statistical mechanics. *Phys. Rev.*, 106:620–630, May 1957a. doi: 10.1103/PhysRev.106.620. URL <https://link.aps.org/doi/10.1103/PhysRev.106.620>.
- E. T. Jaynes. Information theory and statistical mechanics. ii. *Phys. Rev.*, 108:171–190, Oct 1957b. doi: 10.1103/PhysRev.108.171. URL <https://link.aps.org/doi/10.1103/PhysRev.108.171>.
- R. V. Jensen and R. Shankar. Statistical behavior in deterministic quantum systems with few degrees of freedom. *Phys. Rev. Lett.*, 54:1879–1882, Apr 1985.

- doi: 10.1103/PhysRevLett.54.1879. URL <https://link.aps.org/doi/10.1103/PhysRevLett.54.1879>.
- Kevin M. Jones, Eite Tiesinga, Paul D. Lett, and Paul S. Julienne. Ultracold photoassociation spectroscopy: Long-range molecules and atomic scattering. *Rev. Mod. Phys.*, 78:483–535, May 2006. doi: 10.1103/RevModPhys.78.483. URL <https://link.aps.org/doi/10.1103/RevModPhys.78.483>.
- P. Jordan and E. Wigner. Über das paulische äquivalenzverbot. *Zeitschrift für Physik*, 47(9):631–651, Sep 1928. ISSN 0044-3328. doi: 10.1007/BF01331938. URL <https://doi.org/10.1007/BF01331938>.
- Robert Jördens, Niels Strohmaier, Kenneth Günter, Henning Moritz, and Tilman Esslinger. A mott insulator of fermionic atoms in an optical lattice. *Nature*, 455: 204 EP –, 09 2008. URL <https://doi.org/10.1038/nature07244>.
- P. Jurcevic, B. P. Lanyon, P. Hauke, C. Hempel, P. Zoller, R. Blatt, and C. F. Roos. Quasiparticle engineering and entanglement propagation in a quantum many-body system. *Nature*, 511:202 EP –, 07 2014. URL <https://doi.org/10.1038/nature13461>.
- P. Jurcevic, H. Shen, P. Hauke, C. Maier, T. Brydges, C. Hempel, B. P. Lanyon, M. Heyl, R. Blatt, and C. F. Roos. Direct observation of dynamical quantum phase transitions in an interacting many-body system. *Phys. Rev. Lett.*, 119:080501, Aug 2017. doi: 10.1103/PhysRevLett.119.080501. URL <https://link.aps.org/doi/10.1103/PhysRevLett.119.080501>.
- Alex Kamenev and Anton Andreev. Electron-electron interactions in disordered metals: Keldysh formalism. *Phys. Rev. B*, 60:2218–2238, Jul 1999. doi: 10.1103/PhysRevB.60.2218. URL <https://link.aps.org/doi/10.1103/PhysRevB.60.2218>.
- Junjiro Kanamori. Electron correlation and ferromagnetism of transition metals. *Progress of Theoretical Physics*, 30(3):275–289, 1963. doi: 10.1143/PTP.30.275. URL <http://dx.doi.org/10.1143/PTP.30.275>.
- Adam M. Kaufman, M. Eric Tai, Alexander Lukin, Matthew Rispoli, Robert Schittko, Philipp M. Preiss, and Markus Greiner. Quantum thermalization through entanglement in an isolated many-body system. *Science*, 353(6301):794–800, 2016. ISSN 0036-8075. doi: 10.1126/science.aaf6725. URL <http://science.sciencemag.org/content/353/6301/794>.
- S. Kehrein. *The Flow Equation Approach to Many-Particle Systems*. Springer Tracts in Modern Physics. Springer Berlin Heidelberg, 2007. ISBN 9783540340683. URL <https://books.google.de/books?id=haH1BwAAQBAJ>.

- Hyungwon Kim, Tatsuhiko N. Ikeda, and David A. Huse. Testing whether all eigenstates obey the eigenstate thermalization hypothesis. *Phys. Rev. E*, 90:052105, Nov 2014. doi: 10.1103/PhysRevE.90.052105. URL <https://link.aps.org/doi/10.1103/PhysRevE.90.052105>.
- K. Kim, M.-S. Chang, R. Islam, S. Korenblit, L.-M. Duan, and C. Monroe. Entanglement and tunable spin-spin couplings between trapped ions using multiple transverse modes. *Phys. Rev. Lett.*, 103:120502, Sep 2009. doi: 10.1103/PhysRevLett.103.120502. URL <https://link.aps.org/doi/10.1103/PhysRevLett.103.120502>.
- Toshiya Kinoshita, Trevor Wenger, and David S. Weiss. A quantum newton's cradle. *Nature*, 440:900 EP –, 04 2006. URL <https://doi.org/10.1038/nature04693>.
- Arnaud Koetsier, R. A. Duine, Immanuel Bloch, and H. T. C. Stoof. Achieving the néel state in an optical lattice. *Phys. Rev. A*, 77:023623, Feb 2008. doi: 10.1103/PhysRevA.77.023623. URL <https://link.aps.org/doi/10.1103/PhysRevA.77.023623>.
- Lev Kofman, Andrei Linde, and Alexei A. Starobinsky. Nonthermal phase transitions after inflation. *Phys. Rev. Lett.*, 76:1011–1014, Feb 1996. doi: 10.1103/PhysRevLett.76.1011. URL <https://link.aps.org/doi/10.1103/PhysRevLett.76.1011>.
- Michael Köhl, Henning Moritz, Thilo Stöferle, Kenneth Günter, and Tilman Esslinger. Fermionic atoms in a three dimensional optical lattice: Observing fermi surfaces, dynamics, and interactions. *Phys. Rev. Lett.*, 94:080403, Mar 2005. doi: 10.1103/PhysRevLett.94.080403. URL <https://link.aps.org/doi/10.1103/PhysRevLett.94.080403>.
- W. Kohn and L. J. Sham. Self-consistent equations including exchange and correlation effects. *Phys. Rev.*, 140:A1133–A1138, Nov 1965. doi: 10.1103/PhysRev.140.A1133. URL <https://link.aps.org/doi/10.1103/PhysRev.140.A1133>.
- Corinna Kollath, Andreas M. Läuchli, and Ehud Altman. Quench dynamics and nonequilibrium phase diagram of the bose-hubbard model. *Phys. Rev. Lett.*, 98:180601, Apr 2007. doi: 10.1103/PhysRevLett.98.180601. URL <https://link.aps.org/doi/10.1103/PhysRevLett.98.180601>.
- Jindřich Kolorenč and Lubos Mitas. Applications of quantum monte carlo methods in condensed systems. *Reports on Progress in Physics*, 74(2):026502, 2011. URL <http://stacks.iop.org/0034-4885/74/i=2/a=026502>.
- T. D. Ladd, F. Jelezko, R. Laflamme, Y. Nakamura, C. Monroe, and J. L. O'Brien. Quantum computers. *Nature*, 464:45 EP –, 03 2010. URL <https://doi.org/10.1038/nature08812>.

- L. Landau. Das dämpfungsproblem in der wellenmechanik. *Zeitschrift für Physik*, 45 (5):430–441, May 1927. ISSN 0044-3328. doi: 10.1007/BF01343064. URL <https://doi.org/10.1007/BF01343064>.
- A. M. Lane, R. G. Thomas, and E. P. Wigner. Giant resonance interpretation of the nucleon-nucleus interaction. *Phys. Rev.*, 98:693–701, May 1955. doi: 10.1103/PhysRev.98.693. URL <https://link.aps.org/doi/10.1103/PhysRev.98.693>.
- T. Langen, R. Geiger, M. Kuhnert, B. Rauer, and J. Schmiedmayer. Local emergence of thermal correlations in an isolated quantum many-body system. *Nature Physics*, 9: 640 EP –, 09 2013. URL <https://doi.org/10.1038/nphys2739>.
- Tim Langen, Remi Geiger, and Jörg Schmiedmayer. Ultracold atoms out of equilibrium. *Annual Review of Condensed Matter Physics*, 6(1):201–217, 2015. doi: 10.1146/annurev-conmatphys-031214-014548. URL <https://doi.org/10.1146/annurev-conmatphys-031214-014548>.
- Tyler LeBlond, Krishnanand Mallayya, Lev Vidmar, and Marcos Rigol. Entanglement and matrix elements of observables in interacting integrable systems. *Phys. Rev. E*, 100:062134, Dec 2019. doi: 10.1103/PhysRevE.100.062134. URL <https://link.aps.org/doi/10.1103/PhysRevE.100.062134>.
- Joel L Lebowitz and Oliver Penrose. Modern ergodic theory. *Physics Today*, 26(2): 23–29, 1973.
- David M. Leitner and L.S. Cederbaum. Invariant random matrix ensembles as models for ergodic and nonergodic hamiltonian systems. *Journal of Molecular Structure*, 292:197–205, 1993. ISSN 0022-2860. doi: [https://doi.org/10.1016/0022-2860\(93\)80100-A](https://doi.org/10.1016/0022-2860(93)80100-A). URL <https://www.sciencedirect.com/science/article/pii/002228609380100A>.
- VS Letokhov. *JETP Lett.*, 7:272, 1968.
- VS Letokhov. Nonlinear high resolution laser spectroscopy. *Science*, 190(4212):344–351, 1975. URL <https://www.jstor.org/stable/1741065>.
- Maciej Lewenstein, Anna Sanpera, Veronica Ahufinger, Bogdan Damski, Aditi Sen(De), and Ujjwal Sen. Ultracold atomic gases in optical lattices: mimicking condensed matter physics and beyond. *Advances in Physics*, 56(2):243–379, 2007. doi: 10.1080/00018730701223200. URL <https://doi.org/10.1080/00018730701223200>.
- Allen J Lichtenberg and Michael A Lieberman. Regular and chaotic dynamics, vol. 38 of. *Applied Mathematical Sciences*, 1992.

- Elliott Lieb, Theodore Schultz, and Daniel Mattis. Two soluble models of an antiferromagnetic chain. *Annals of Physics*, 16(3):407 – 466, 1961. ISSN 0003-4916. doi: [https://doi.org/10.1016/0003-4916\(61\)90115-4](https://doi.org/10.1016/0003-4916(61)90115-4). URL <http://www.sciencedirect.com/science/article/pii/0003491661901154>.
- Mingfeng Lin, Henry C. Lucas, and Galit Shmueli. Research commentary—too big to fail: Large samples and the p-value problem. *Information Systems Research*, 24(4):906–917, 2013. doi: 10.1287/isre.2013.0480. URL <https://doi.org/10.1287/isre.2013.0480>.
- Seth Lloyd. Universal quantum simulators. *Science*, 273(5278):1073–1078, 1996. ISSN 0036-8075. doi: 10.1126/science.273.5278.1073. URL <http://science.sciencemag.org/content/273/5278/1073>.
- J Loschmidt. J. loschmidt, wien. ber. 75, 67 (1877). *Wien. Ber.*, 75:67, 1877.
- Yuri I. Manin. The computable and not computable, 1980. URL https://web.archive.org/web/20130510173823/http://publ.lib.ru/ARCHIVES/M/MANIN_Yuriy_Ivanovich/Manin_Yu.I._Vychislimoe_i_nevychislimoe.%281980%29.%5Bdjv%5D.zip.
- S. R. Manmana, S. Wessel, R. M. Noack, and A. Muramatsu. Strongly correlated fermions after a quantum quench. *Phys. Rev. Lett.*, 98:210405, May 2007. doi: 10.1103/PhysRevLett.98.210405. URL <http://link.aps.org/doi/10.1103/PhysRevLett.98.210405>.
- Salvatore R. Manmana, Alejandro Muramatsu, and Reinhard M. Noack. Time evolution of one-dimensional quantum many body systems. *AIP Conference Proceedings*, 789(1):269–278, 2005. doi: 10.1063/1.2080353. URL <https://aip.scitation.org/doi/abs/10.1063/1.2080353>.
- E. Manousakis. A quantum-dot array as model for copper-oxide superconductors: A dedicated quantum simulator for the many-fermion problem. *Journal of Low Temperature Physics*, 126(5):1501–1513, Mar 2002. ISSN 1573-7357. doi: 10.1023/A:1014295416763. URL <https://doi.org/10.1023/A:1014295416763>.
- Ll. Masanes, G. Vidal, and J. I. Latorre. Time-optimal hamiltonian simulation and gate synthesis using homogeneous local unitaries. *Quantum Info. Comput.*, 2(4):285–296, June 2002. ISSN 1533-7146. URL <http://dl.acm.org/citation.cfm?id=2011477.2011479>.
- Takeo Matsubara and Hirotugu Matsuda. A lattice model of liquid helium, i. *Progress of Theoretical Physics*, 16(6):569–582, 1956. doi: 10.1143/PTP.16.569. URL <http://dx.doi.org/10.1143/PTP.16.569>.

- James Clerk Maxwell. Ii. illustrations of the dynamical theory of gases. *The London, Edinburgh, and Dublin Philosophical Magazine and Journal of Science*, 20(130):21–37, 1860a.
- James Clerk Maxwell. V. illustrations of the dynamical theory of gases.—part i. on the motions and collisions of perfectly elastic spheres. *The London, Edinburgh, and Dublin Philosophical Magazine and Journal of Science*, 19(124):19–32, 1860b.
- Steven W. McDonald and Allan N. Kaufman. Spectrum and eigenfunctions for a hamiltonian with stochastic trajectories. *Phys. Rev. Lett.*, 42:1189–1191, Apr 1979. doi: 10.1103/PhysRevLett.42.1189. URL <https://link.aps.org/doi/10.1103/PhysRevLett.42.1189>.
- W. L. McMillan. Ground state of liquid he⁴. *Phys. Rev.*, 138:A442–A451, Apr 1965. doi: 10.1103/PhysRev.138.A442. URL <https://link.aps.org/doi/10.1103/PhysRev.138.A442>.
- Madan Lal Mehta. *Random matrices*, volume 142. Elsevier, 2004.
- Alan L. Migdall, John V. Prodan, William D. Phillips, Thomas H. Bergeman, and Harold J. Metcalf. First observation of magnetically trapped neutral atoms. *Phys. Rev. Lett.*, 54:2596–2599, Jun 1985. doi: 10.1103/PhysRevLett.54.2596. URL <https://link.aps.org/doi/10.1103/PhysRevLett.54.2596>.
- M. Mitrano, A. Cantaluppi, D. Nicoletti, S. Kaiser, A. Perucchi, S. Lupi, P. Di Pietro, D. Pontiroli, M. Riccò, S. R. Clark, D. Jaksch, and A. Cavalleri. Possible light-induced superconductivity in k₃c₆₀ at high temperature. *Nature*, 530:461 EP –, 02 2016. URL <https://doi.org/10.1038/nature16522>.
- Michael Moeckel and Stefan Kehrein. Crossover from adiabatic to sudden interaction quenches in the hubbard model: prethermalization and non-equilibrium dynamics. *New Journal of Physics*, 12(5):055016, 2010. URL <http://stacks.iop.org/1367-2630/12/i=5/a=055016>.
- Nornadiah Mohd Razali and Bee Yap. Power comparisons of shapiro-wilk, kolmogorov-smirnov, lilliefors and anderson-darling tests. *J. Stat. Model. Analytics*, 2, 01 2011. URL https://www.researchgate.net/publication/267205556_Power_Comparisons_of_Shapiro-Wilk_Kolmogorov-Smirnov_Lilliefors_and_Anderson-Darling_Tests.
- C. Moler and C. Van Loan. Nineteen dubious ways to compute the exponential of a matrix, twenty-five years later. *SIAM Review*, 45(1):3–49, 2003. doi: 10.1137/S00361445024180. URL <https://doi.org/10.1137/S00361445024180>.

- Rubem Mondaini, Keith R. Fratus, Mark Srednicki, and Marcos Rigol. Eigenstate thermalization in the two-dimensional transverse field ising model. *Phys. Rev. E*, 93:032104, Mar 2016. doi: 10.1103/PhysRevE.93.032104. URL <https://link.aps.org/doi/10.1103/PhysRevE.93.032104>.
- C. Monroe, D. M. Meekhof, B. E. King, W. M. Itano, and D. J. Wineland. Demonstration of a fundamental quantum logic gate. *Phys. Rev. Lett.*, 75:4714–4717, Dec 1995. doi: 10.1103/PhysRevLett.75.4714. URL <https://link.aps.org/doi/10.1103/PhysRevLett.75.4714>.
- T. D. Morris, N. M. Parzuchowski, and S. K. Bogner. Magnus expansion and in-medium similarity renormalization group. *Phys. Rev. C*, 92:034331, Sep 2015. doi: 10.1103/PhysRevC.92.034331. URL <https://link.aps.org/doi/10.1103/PhysRevC.92.034331>.
- J. E. Moyal. Quantum mechanics as a statistical theory. *Mathematical Proceedings of the Cambridge Philosophical Society*, 45(1):99–124, 1949. doi: 10.1017/S0305004100000487.
- Rahul Nandkishore and David A. Huse. Many-body localization and thermalization in quantum statistical mechanics. *Annual Review of Condensed Matter Physics*, 6(1):15–38, 2015. doi: 10.1146/annurev-conmatphys-031214-014726. URL <https://doi.org/10.1146/annurev-conmatphys-031214-014726>.
- Charlie Nation and Diego Porrás. Off-diagonal observable elements from random matrix theory: distributions, fluctuations, and eigenstate thermalization. *New Journal of Physics*, 20(10):103003, oct 2018. doi: 10.1088/1367-2630/aae28f. URL <https://doi.org/10.1088/1367-2630/aae28f>.
- W. Neuhauser, M. Hohenstatt, P. Toschek, and H. Dehmelt. Optical-sideband cooling of visible atom cloud confined in parabolic well. *Phys. Rev. Lett.*, 41:233–236, Jul 1978. doi: 10.1103/PhysRevLett.41.233. URL <https://link.aps.org/doi/10.1103/PhysRevLett.41.233>.
- J. v. Neumann. Beweis des ergodensatzes und des h-theorems in der neuen mechanik. *Zeitschrift für Physik*, 57(1):30–70, Jan 1929. ISSN 0044-3328. doi: 10.1007/BF01339852. URL <https://doi.org/10.1007/BF01339852>.
- J. v. Neumann. Proof of the quasi-ergodic hypothesis. *Proceedings of the National Academy of Sciences*, 18(1):70–82, 1932. ISSN 0027-8424. doi: 10.1073/pnas.18.1.70. URL <http://www.pnas.org/content/18/1/70>.
- M.A. Nielsen and I.L. Chuang. *Quantum Computation and Quantum Information: 10th Anniversary Edition*. Cambridge University Press, 2010. ISBN 9781107002173. URL <https://books.google.de/books?id=j2ULnwEACAAJ>.

- Jeremy L. O'Brien. Optical quantum computing. *Science*, 318(5856):1567–1570, 2007. ISSN 0036-8075. doi: 10.1126/science.1142892. URL <http://science.sciencemag.org/content/318/5856/1567>.
- Arijeet Pal and David A. Huse. Many-body localization phase transition. *Phys. Rev. B*, 82:174411, Nov 2010. doi: 10.1103/PhysRevB.82.174411. URL <https://link.aps.org/doi/10.1103/PhysRevB.82.174411>.
- Oliver Penrose. *Foundations of statistical mechanics: a deductive treatment*. Courier Corporation, 2005.
- János Pipek and Imre Varga. Universal classification scheme for the spatial-localization properties of one-particle states in finite, d-dimensional systems. *Phys. Rev. A*, 46:3148–3163, Sep 1992. doi: 10.1103/PhysRevA.46.3148. URL <https://link.aps.org/doi/10.1103/PhysRevA.46.3148>.
- Dmitry Podolsky, Gary N. Felder, Lev Kofman, and Marco Peloso. Equation of state and beginning of thermalization after preheating. *Phys. Rev. D*, 73:023501, Jan 2006. doi: 10.1103/PhysRevD.73.023501. URL <https://link.aps.org/doi/10.1103/PhysRevD.73.023501>.
- Anatoli Polkovnikov. Phase space representation of quantum dynamics. *Annals of Physics*, 325(8):1790–1852, 2010. ISSN 0003-4916. doi: <https://doi.org/10.1016/j.aop.2010.02.006>. URL <https://www.sciencedirect.com/science/article/pii/S0003491610000382>.
- Anatoli Polkovnikov, Krishnendu Sengupta, Alessandro Silva, and Mukund Vengalattore. Colloquium: Nonequilibrium dynamics of closed interacting quantum systems. *Rev. Mod. Phys.*, 83:863–883, Aug 2011. doi: 10.1103/RevModPhys.83.863. URL <https://link.aps.org/doi/10.1103/RevModPhys.83.863>.
- D. Porras and J. I. Cirac. Effective quantum spin systems with trapped ions. *Phys. Rev. Lett.*, 92:207901, May 2004. doi: 10.1103/PhysRevLett.92.207901. URL <https://link.aps.org/doi/10.1103/PhysRevLett.92.207901>.
- C E Porter and N Rosenzweig. Statistical properties of atomic and nuclear spectra. *Ann. Acad. Sci. Fennicae. Ser. A VI*, Vol: No. 44, 1 1960. URL <https://www.osti.gov/biblio/4147616>.
- J. F. Poyatos, J. I. Cirac, and P. Zoller. Quantum reservoir engineering with laser cooled trapped ions. *Phys. Rev. Lett.*, 77:4728–4731, Dec 1996. doi: 10.1103/PhysRevLett.77.4728. URL <https://link.aps.org/doi/10.1103/PhysRevLett.77.4728>.
- John Preskill. Quantum information and physics: Some future directions. *Journal of Modern Optics*, 47(2-3):127–137, 2000. doi: 10.1080/09500340008244031. URL <https://www.tandfonline.com/doi/abs/10.1080/09500340008244031>.

- William H Press, Saul A Teukolsky, William T Vetterling, and Brian P Flannery. *Numerical recipes 3rd edition: The art of scientific computing*. Cambridge university press, 2007.
- D. E. Pritchard, E. L. Raab, V. Bagnato, C. E. Wieman, and R. N. Watts. Light traps using spontaneous forces. *Phys. Rev. Lett.*, 57:310–313, Jul 1986. doi: 10.1103/PhysRevLett.57.310. URL <https://link.aps.org/doi/10.1103/PhysRevLett.57.310>.
- E. L. Raab, M. Prentiss, Alex Cable, Steven Chu, and D. E. Pritchard. Trapping of neutral sodium atoms with radiation pressure. *Phys. Rev. Lett.*, 59:2631–2634, Dec 1987. doi: 10.1103/PhysRevLett.59.2631. URL <https://link.aps.org/doi/10.1103/PhysRevLett.59.2631>.
- L.E. Reichl. *A modern course in statistical physics*. University of Texas Press, 1980. ISBN 9780292750517. URL <https://books.google.de/books?id=GDa2DAEACAAJ>.
- Peter Reimann. Eigenstate thermalization: Deutsch’s approach and beyond. *New Journal of Physics*, 17(5):055025, may 2015. doi: 10.1088/1367-2630/17/5/055025. URL <https://doi.org/10.1088/1367-2630/17/5/055025>.
- Peter Reimann and Lennart Dabelow. Refining deutsch’s approach to thermalization. *Phys. Rev. E*, 103:022119, Feb 2021. doi: 10.1103/PhysRevE.103.022119. URL <https://link.aps.org/doi/10.1103/PhysRevE.103.022119>.
- Marcos Rigol. Quantum quenches and thermalization in one-dimensional fermionic systems. *Phys. Rev. A*, 80:053607, Nov 2009a. doi: 10.1103/PhysRevA.80.053607. URL <https://link.aps.org/doi/10.1103/PhysRevA.80.053607>.
- Marcos Rigol. Breakdown of thermalization in finite one-dimensional systems. *Phys. Rev. Lett.*, 103:100403, Sep 2009b. doi: 10.1103/PhysRevLett.103.100403. URL <https://link.aps.org/doi/10.1103/PhysRevLett.103.100403>.
- Marcos Rigol and Lea F. Santos. Quantum chaos and thermalization in gapped systems. *Phys. Rev. A*, 82:011604, Jul 2010. doi: 10.1103/PhysRevA.82.011604. URL <https://link.aps.org/doi/10.1103/PhysRevA.82.011604>.
- Marcos Rigol and Mark Srednicki. Alternatives to eigenstate thermalization. *Phys. Rev. Lett.*, 108:110601, Mar 2012. doi: 10.1103/PhysRevLett.108.110601. URL <https://link.aps.org/doi/10.1103/PhysRevLett.108.110601>.
- Marcos Rigol, Vanja Dunjko, Vladimir Yurovsky, and Maxim Olshanii. Relaxation in a completely integrable many-body quantum system: An ab initio study of the dynamics of the highly excited states of 1d lattice hard-core bosons. *Phys. Rev. Lett.*, 98:050405, Feb 2007. doi: 10.1103/PhysRevLett.98.050405. URL <https://link.aps.org/doi/10.1103/PhysRevLett.98.050405>.

- Marcos Rigol, Vanja Dunjko, and Maxim Olshanii. Thermalization and its mechanism for generic isolated quantum systems. *Nature*, 452:854 EP –, 04 2008. URL <https://doi.org/10.1038/nature06838>.
- Norbert Rosenzweig and Charles E. Porter. "Repulsion of Energy Levels" in Complex Atomic Spectra. *Phys. Rev.*, 120(5):1698–1714, Dec 1960. ISSN 1536-6065. doi: 10.1103/PhysRev.120.1698.
- Conrad Sanderson and Ryan Curtin. Armadillo: a template-based c++ library for linear algebra. *Journal of Open Source Software*, 2016.
- Anders W. Sandvik. Computational studies of quantum spin systems. *AIP Conference Proceedings*, 1297(1):135–338, 2010. doi: 10.1063/1.3518900. URL <https://aip.scitation.org/doi/abs/10.1063/1.3518900>.
- L. F. Santos, F. Borgonovi, and F. M. Izrailev. Chaos and statistical relaxation in quantum systems of interacting particles. *Phys. Rev. Lett.*, 108:094102, Mar 2012a. doi: 10.1103/PhysRevLett.108.094102. URL <http://link.aps.org/doi/10.1103/PhysRevLett.108.094102>.
- Lea F. Santos and Marcos Rigol. Localization and the effects of symmetries in the thermalization properties of one-dimensional quantum systems. *Phys. Rev. E*, 82:031130, Sep 2010a. doi: 10.1103/PhysRevE.82.031130. URL <https://link.aps.org/doi/10.1103/PhysRevE.82.031130>.
- Lea F. Santos and Marcos Rigol. Onset of quantum chaos in one-dimensional bosonic and fermionic systems and its relation to thermalization. *Phys. Rev. E*, 81:036206, Mar 2010b. doi: 10.1103/PhysRevE.81.036206. URL <https://link.aps.org/doi/10.1103/PhysRevE.81.036206>.
- Lea F. Santos, Anatoli Polkovnikov, and Marcos Rigol. Weak and strong typicality in quantum systems. *Phys. Rev. E*, 86:010102, Jul 2012b. doi: 10.1103/PhysRevE.86.010102. URL <http://link.aps.org/doi/10.1103/PhysRevE.86.010102>.
- Samuel Savitz and Gil Refael. Stable unitary integrators for the numerical implementation of continuous unitary transformations. *Physical Review B*, 96(11):115129, 2017.
- R Schmied, T Roscilde, V Murg, D Porras, and J I Cirac. Quantum phases of trapped ions in an optical lattice. *New Journal of Physics*, 10(4):045017, 2008. URL <http://stacks.iop.org/1367-2630/10/i=4/a=045017>.
- Peter Schmitteckert and Ralph Werner. Charge-density-wave instabilities driven by multiple umklapp scattering. *Phys. Rev. B*, 69:195115, May 2004. doi: 10.1103/PhysRevB.69.195115. URL <https://link.aps.org/doi/10.1103/PhysRevB.69.195115>.

- U. Schneider, L. Hackermüller, S. Will, Th. Best, I. Bloch, T. A. Costi, R. W. Helmes, D. Rasch, and A. Rosch. Metallic and insulating phases of repulsively interacting fermions in a 3d optical lattice. *Science*, 322(5907):1520–1525, 2008. doi: 10.1126/science.1165449. URL <https://www.science.org/doi/abs/10.1126/science.1165449>.
- U. Schollwöck. The density-matrix renormalization group. *Rev. Mod. Phys.*, 77:259–315, Apr 2005. doi: 10.1103/RevModPhys.77.259. URL <https://link.aps.org/doi/10.1103/RevModPhys.77.259>.
- Ulrich Schollwöck. The density-matrix renormalization group in the age of matrix product states. *Annals of Physics*, 326(1):96 – 192, 2011. ISSN 0003-4916. doi: <https://doi.org/10.1016/j.aop.2010.09.012>. URL <http://www.sciencedirect.com/science/article/pii/S0003491610001752>. January 2011 Special Issue.
- Michael Schreiber, Sean S. Hodgman, Pranjal Bordia, Henrik P. Lüschen, Mark H. Fischer, Ronen Vosk, Ehud Altman, Ulrich Schneider, and Immanuel Bloch. Observation of many-body localization of interacting fermions in a quasirandom optical lattice. *Science*, 349(6250):842–845, 2015. ISSN 0036-8075. doi: 10.1126/science.aaa7432. URL <http://science.sciencemag.org/content/349/6250/842>.
- E. Schrödinger. Quantisierung als eigenwertproblem. *Annalen der Physik*, 384(4): 361–376, a. doi: 10.1002/andp.19263840404. URL <https://onlinelibrary.wiley.com/doi/abs/10.1002/andp.19263840404>.
- E. Schrödinger. Quantisierung als eigenwertproblem. *Annalen der Physik*, 384(6): 489–527, b. doi: 10.1002/andp.19263840602. URL <https://onlinelibrary.wiley.com/doi/abs/10.1002/andp.19263840602>.
- E. Schrödinger. Quantisierung als eigenwertproblem. *Annalen der Physik*, 385(13): 437–490, c. doi: 10.1002/andp.19263851302. URL <https://onlinelibrary.wiley.com/doi/abs/10.1002/andp.19263851302>.
- E. Schrödinger. Quantisierung als eigenwertproblem. *Annalen der Physik*, 386(18): 109–139, d. doi: 10.1002/andp.19263861802. URL <https://onlinelibrary.wiley.com/doi/abs/10.1002/andp.19263861802>.
- J. Sebby-Strabley, B. L. Brown, M. Anderlini, P. J. Lee, W. D. Phillips, J. V. Porto, and P. R. Johnson. Preparing and probing atomic number states with an atom interferometer. *Phys. Rev. Lett.*, 98:200405, May 2007. doi: 10.1103/PhysRevLett.98.200405. URL <https://link.aps.org/doi/10.1103/PhysRevLett.98.200405>.
- Maksym Serbyn, Z. Papić, and Dmitry A. Abanin. Universal slow growth of entanglement in interacting strongly disordered systems. *Phys. Rev. Lett.*, 110:260601, Jun

- 2013a. doi: 10.1103/PhysRevLett.110.260601. URL <https://link.aps.org/doi/10.1103/PhysRevLett.110.260601>.
- Maksym Serbyn, Z. Papić, and Dmitry A. Abanin. Local conservation laws and the structure of the many-body localized states. *Phys. Rev. Lett.*, 111:127201, Sep 2013b. doi: 10.1103/PhysRevLett.111.127201. URL <https://link.aps.org/doi/10.1103/PhysRevLett.111.127201>.
- B. A. Shadwick and W. F. Buell. Unitary integration: A numerical technique preserving the structure of the quantum liouville equation. *Phys. Rev. Lett.*, 79:5189–5193, Dec 1997. doi: 10.1103/PhysRevLett.79.5189. URL <https://link.aps.org/doi/10.1103/PhysRevLett.79.5189>.
- P. W. Shor. Algorithms for quantum computation: discrete logarithms and factoring. In *Proceedings 35th Annual Symposium on Foundations of Computer Science*, pages 124–134, Nov 1994. doi: 10.1109/SFCS.1994.365700.
- Yakov Grigor'evich Sinai. On the foundations of the ergodic hypothesis for a dynamical system of statistical mechanics. In *Doklady Akademii Nauk*, volume 153, pages 1261–1264. Russian Academy of Sciences, 1963.
- Yakov Grigor'evich Sinai. Dynamical systems with elastic reflections. *Russian Mathematical Surveys*, 25(2):137–189, 1970.
- Navinder Singh. On the foundations of statistical mechanics: A brief review. *Modern Physics Letters B*, 27(06):1330003, 2013. doi: 10.1142/S0217984913300032. URL <https://doi.org/10.1142/S0217984913300032>.
- Lawrence Sklar. *Physics and chance: Philosophical issues in the foundations of statistical mechanics*. Cambridge University Press, 1995.
- S. Somaroo, C. H. Tseng, T. F. Havel, R. Laflamme, and D. G. Cory. Quantum simulations on a quantum computer. *Phys. Rev. Lett.*, 82:5381–5384, Jun 1999. doi: 10.1103/PhysRevLett.82.5381. URL <https://link.aps.org/doi/10.1103/PhysRevLett.82.5381>.
- R. Somma, G. Ortiz, J. E. Gubernatis, E. Knill, and R. Laflamme. Simulating physical phenomena by quantum networks. *Phys. Rev. A*, 65:042323, Apr 2002. doi: 10.1103/PhysRevA.65.042323. URL <https://link.aps.org/doi/10.1103/PhysRevA.65.042323>.
- Mark Srednicki. Chaos and quantum thermalization. *Phys. Rev. E*, 50:888–901, Aug 1994. doi: 10.1103/PhysRevE.50.888. URL <https://link.aps.org/doi/10.1103/PhysRevE.50.888>.
- Mark Srednicki. Thermal fluctuations in quantized chaotic systems. *Journal of Physics A: Mathematical and General*, 29(4):L75, 1996. URL <http://stacks.iop.org/0305-4470/29/i=4/a=003>.

- Mark Srednicki. The approach to thermal equilibrium in quantized chaotic systems. *Journal of Physics A: Mathematical and General*, 32(7):1163, 1999. URL <http://stacks.iop.org/0305-4470/32/i=7/a=007>.
- Andrew Steane. Quantum computing. *Reports on Progress in Physics*, 61(2):117, 1998. URL <http://stacks.iop.org/0034-4885/61/i=2/a=002>.
- R. Steinigeweg, J. Herbrych, and P. Prelovšek. Eigenstate thermalization within isolated spin-chain systems. *Phys. Rev. E*, 87:012118, Jan 2013. doi: 10.1103/PhysRevE.87.012118. URL <https://link.aps.org/doi/10.1103/PhysRevE.87.012118>.
- H. Stöckmann. Microwave billiards and quantum chaos. *Scholarpedia*, 5(10):10243, 2010. doi: 10.4249/scholarpedia.10243. revision #127194.
- M. Suzuki. *Quantum Monte Carlo Methods in Condensed Matter Physics*. World Scientific, 1993. ISBN 9789810236830. URL <https://books.google.de/books?id=OUsqJuE0nZ8C>.
- Terence Tao. Topics in random matrix theory. vol. 132 of graduate studies in mathematics. *American Mathematical Society, Providence, RI*, 2012.
- Hal Tasaki. The hubbard model - an introduction and selected rigorous results. *Journal of Physics: Condensed Matter*, 10(20):4353, 1998. URL <http://stacks.iop.org/0953-8984/10/i=20/a=004>.
- S. J. Thomson and M. Schiró. Time evolution of many-body localized systems with the flow equation approach. *Phys. Rev. B*, 97:060201, Feb 2018. doi: 10.1103/PhysRevB.97.060201. URL <https://link.aps.org/doi/10.1103/PhysRevB.97.060201>.
- Richard Chace Tolman. *The principles of statistical mechanics*. Courier Corporation, 1979.
- S. Trotzky, Y-A. Chen, A. Flesch, I. P. McCulloch, U. Schollwöck, J. Eisert, and I. Bloch. Probing the relaxation towards equilibrium in an isolated strongly correlated one-dimensional bose gas. *Nature Physics*, 8:325 EP –, 02 2012. URL <https://doi.org/10.1038/nphys2232>.
- Matthias Troyer and Uwe-Jens Wiese. Computational complexity and fundamental limitations to fermionic quantum monte carlo simulations. *Phys. Rev. Lett.*, 94:170201, May 2005. doi: 10.1103/PhysRevLett.94.170201. URL <https://link.aps.org/doi/10.1103/PhysRevLett.94.170201>.
- A. K. Tuchman, C. Orzel, A. Polkovnikov, and M. A. Kasevich. Nonequilibrium coherence dynamics of a soft boson lattice. *Phys. Rev. A*, 74:051601, Nov 2006. doi: 10.1103/PhysRevA.74.051601. URL <https://link.aps.org/doi/10.1103/PhysRevA.74.051601>.

- Jos Uffink. Compendium of the foundations of classical statistical physics, March 2006. URL <http://philsci-archive.pitt.edu/2691/>. Chapter for "Handbook for Philosophy of Physics", J. Butterfield and J. Earman (eds) to appear.
- Alexander van Oudenaarden and J. E. Mooij. One-dimensional mott insulator formed by quantum vortices in josephson junction arrays. *Phys. Rev. Lett.*, 76:4947–4950, Jun 1996. doi: 10.1103/PhysRevLett.76.4947. URL <https://link.aps.org/doi/10.1103/PhysRevLett.76.4947>.
- Pragya Verma and Donald G. Truhlar. Status and challenges of density functional theory. *Trends in Chemistry*, 2(4):302–318, 2020. ISSN 2589-5974. doi: <https://doi.org/10.1016/j.trechm.2020.02.005>. URL <https://www.sciencedirect.com/science/article/pii/S2589597420300411>. Special Issue - Laying Groundwork for the Future.
- Guifré Vidal. Efficient simulation of one-dimensional quantum many-body systems. *Phys. Rev. Lett.*, 93:040502, Jul 2004. doi: 10.1103/PhysRevLett.93.040502. URL <https://link.aps.org/doi/10.1103/PhysRevLett.93.040502>.
- J. von Neumann and E. P. Wigner. Über das Verhalten von Eigenwerten bei adiabatischen Prozessen. *Physikalische Zeitschrift*, 30:467–470, 1929. doi: 10.1007/978-3-662-02781-3_20. URL https://doi.org/10.1007/978-3-662-02781-3_20.
- John von Neumann. Wahrscheinlichkeitstheoretischer aufbau der quantenmechanik. *Nachrichten von der Gesellschaft der Wissenschaften zu Göttingen, Mathematisch-Physikalische Klasse*, 1927:245–272, 1927.
- G. Wallis and M. C. Gutzwiller. Chaos in classical and quantum mechanics. *ZAMM - Journal of Applied Mathematics and Mechanics / Zeitschrift für Angewandte Mathematik und Mechanik*, 72(12):684–684, 1990. doi: 10.1002/zamm.19920721221. URL <https://onlinelibrary.wiley.com/doi/abs/10.1002/zamm.19920721221>.
- F. Wegner. Inverse participation ratio in $2+\epsilon$ dimensions. *Zeitschrift für Physik B Condensed Matter*, 36(3):209–214, Sep 1980. ISSN 1431-584X. doi: 10.1007/BF01325284. URL <https://doi.org/10.1007/BF01325284>.
- Franz Wegner. Flow-equations for hamiltonians. *Annalen der Physik*, 506(2):77–91. doi: 10.1002/andp.19945060203. URL <https://onlinelibrary.wiley.com/doi/abs/10.1002/andp.19945060203>.
- H. Weyl. Quantenmechanik und gruppentheorie. *Zeitschrift für Physik*, 46(1):1–46, Nov 1927. ISSN 0044-3328. doi: 10.1007/BF02055756. URL <https://doi.org/10.1007/BF02055756>.

- Steven R. White. Density matrix formulation for quantum renormalization groups. *Phys. Rev. Lett.*, 69:2863–2866, Nov 1992. doi: 10.1103/PhysRevLett.69.2863. URL <https://link.aps.org/doi/10.1103/PhysRevLett.69.2863>.
- Steven R. White. Density-matrix algorithms for quantum renormalization groups. *Phys. Rev. B*, 48:10345–10356, Oct 1993. doi: 10.1103/PhysRevB.48.10345. URL <https://link.aps.org/doi/10.1103/PhysRevB.48.10345>.
- Steven R. White. Numerical canonical transformation approach to quantum many-body problems. *The Journal of Chemical Physics*, 117(16):7472–7482, 2002. doi: 10.1063/1.1508370. URL <https://doi.org/10.1063/1.1508370>.
- Steven R. White and Adrian E. Feiguin. Real-time evolution using the density matrix renormalization group. *Phys. Rev. Lett.*, 93:076401, Aug 2004. doi: 10.1103/PhysRevLett.93.076401. URL <https://link.aps.org/doi/10.1103/PhysRevLett.93.076401>.
- E. Wigner. On the quantum correction for thermodynamic equilibrium. *Phys. Rev.*, 40:749–759, Jun 1932. doi: 10.1103/PhysRev.40.749. URL <https://link.aps.org/doi/10.1103/PhysRev.40.749>.
- Eugene P. Wigner. On a class of analytic functions from the quantum theory of collisions. *Annals of Mathematics*, 53(1):36–67, 1951a. ISSN 0003486X. URL <http://www.jstor.org/stable/1969342>.
- Eugene P. Wigner. On the statistical distribution of the widths and spacings of nuclear resonance levels. *Mathematical Proceedings of the Cambridge Philosophical Society*, 47(4):790–798, 1951b. doi: 10.1017/S0305004100027237.
- Eugene P. Wigner. Characteristic vectors of bordered matrices with infinite dimensions. *Annals of Mathematics*, 62(3):548–564, 1955. ISSN 0003486X. URL <http://www.jstor.org/stable/1970079>.
- Eugene P. Wigner. Characteristic vectors of bordered matrices with infinite dimensions ii. *Annals of Mathematics*, 65(2):203–207, 1957a. ISSN 0003486X. URL <http://www.jstor.org/stable/1969956>.
- Eugene Paul Wigner. Gruppentheorie und ihre anwendung auf die quantenmechanik der atomspektren. 1931.
- Eugene Paul Wigner. *Statistical properties of real symmetric matrices with many dimensions*. Princeton University, 1957b.
- William Thomson. Kinetic theory of the dissipation of energy. *Nature*, 9:441, April 1874. doi: <https://doi.org/10.1038/009441c010.1038/009441c0>.

- D. J. Wineland, R. E. Drullinger, and F. L. Walls. Radiation-pressure cooling of bound resonant absorbers. *Phys. Rev. Lett.*, 40:1639–1642, Jun 1978. doi: 10.1103/PhysRevLett.40.1639. URL <https://link.aps.org/doi/10.1103/PhysRevLett.40.1639>.
- D J Wineland, C Monroe, W M Itano, D Leibfried, B E King, and D M Meekhof. Experimental issues in coherent quantum-state manipulation of trapped atomic ions. *Journal of research of the National Institute of Standards and Technology*, 103(3):259–328, May-Jun 1998. doi: 10.6028/jres.103.019. URL <https://www.ncbi.nlm.nih.gov/pubmed/28009379>.
- D.J. Wineland, Wayne M. Itano, and R.S. Van Dyck. High-resolution spectroscopy of stored ions. volume 19 of *Advances in Atomic and Molecular Physics*, pages 135 – 186. Academic Press, 1983. doi: [https://doi.org/10.1016/S0065-2199\(08\)60253-5](https://doi.org/10.1016/S0065-2199(08)60253-5). URL <http://www.sciencedirect.com/science/article/pii/S0065219908602535>.
- John Wishart. THE GENERALISED PRODUCT MOMENT DISTRIBUTION IN SAMPLES FROM A NORMAL MULTIVARIATE POPULATION. *Biometrika*, 20A(1-2): 32–52, 12 1928. ISSN 0006-3444. doi: 10.1093/biomet/20A.1-2.32. URL <https://doi.org/10.1093/biomet/20A.1-2.32>.
- C. N. Yang and C. P. Yang. One-dimensional chain of anisotropic spin-spin interactions. i. proof of bethe’s hypothesis for ground state in a finite system. *Phys. Rev.*, 150:321–327, Oct 1966. doi: 10.1103/PhysRev.150.321. URL <https://link.aps.org/doi/10.1103/PhysRev.150.321>.
- Vladimir Zelevinsky, B.Alex Brown, Njema Frazier, and Mihai Horoi. The nuclear shell model as a testing ground for many-body quantum chaos. *Physics Reports*, 276(2):85 – 176, 1996. ISSN 0370-1573. doi: [https://doi.org/10.1016/S0370-1573\(96\)00007-5](https://doi.org/10.1016/S0370-1573(96)00007-5). URL <http://www.sciencedirect.com/science/article/pii/S0370157396000075>.
- J. Zhang, P. W. Hess, A. Kyprianidis, P. Becker, A. Lee, J. Smith, G. Pagano, I. D. Potirniche, A. C. Potter, A. Vishwanath, N. Y. Yao, and C. Monroe. Observation of a discrete time crystal. *Nature*, 543:217 EP –, 03 2017. URL <https://doi.org/10.1038/nature21413>.
- A. K. Zhuravlev, M. I. Katsnelson, and A. V. Trefilov. Electronic phase transitions in a one-dimensional spinless fermion model with competing interactions. *Phys. Rev. B*, 56:12939–12946, Nov 1997. doi: 10.1103/PhysRevB.56.12939. URL <https://link.aps.org/doi/10.1103/PhysRevB.56.12939>.

Acknowledgements

I thank my supervisor Stefan Kehrein for giving me the opportunity for this project and for the support throughout the years. Whenever I was lost in the deep jungle of ideas and possibilities, he pointed out the important paths. With an endless patience, he helped me in many discussions to make this work a success. Furthermore, I am very grateful for the financial support over many years and the encouragement to present my results at several scientific conferences and the participation in multiple schools and workshops.

I also thank Fabian Heidrich-Meisner for assuming the duties as Second Referee and the daily words of cheer.

Next, I would like to thank all the past and present office mates over the years, namely Mirco, Markus, Ronny, Florian, Manuel, Michael and Ingo. The many discussions over all topics, be it Physics or Non-Physics, made it enjoyable to spend many hours there. I especially mention Markus, my initial PhD companion and travel mate, with whom I shared most of the experiences in Göttingen and abroad beginning with our Master's. I am very grateful to the colleagues of the CMT group in the Institute, who often became friends. For the sake of brevity only some moments can be mentioned here. Among others, I thank Thomas and Isa for the continuous support over many years in various topics and ways, be it technical or proof-reading, great Pizzas or sending a Swedish care package, Florian for housing me and, together with Michael and Christin, for helping me use the free time in an enjoyable way, Jan for all the relaxed moments when cooking on Sunday night, and Lorenzo, Ingo, Davide, Johannes, Sebastian, Constantin, Laura, Kai, Alexander, Niklas, David, Simon and others for all the happy moments spent together.

Above all, I would like to thank my family for their unconditional and never-ending support and love. They helped me getting through the good and bad times of my PhD time and were always there for me.